Investigating Viral Glycosylation Pathways for Drug and Vaccine Development

Juliane Brun

St Edmunds Hall

University of Oxford

A thesis submitted for the degree of

Doctor of Philosophy

Hilary Term 2021

To my mother

Abstract

Glycosylation is the most common protein co- and post-translational modification. It has crucial functions for glycoprotein folding, structure, trafficking, localisation and stability. Glycosylation is not only critical for eukaryotic cell function but vital for many enveloped viruses which have evolved to exploit the host cell glycosylation pathway in order to fold their proteins correctly and coat many of their surface proteins with glycans that can contribute to viral pathogenesis. Vaccines often focus on the viral fusion glycoproteins that protrude from the virion envelope as they are among the most immunogenic biomolecules and can elicit a humoral immune response. A robust vaccine antigen needs to mimic viral glycosylation to produce an appropriate and strong B-cell response, as many neutralising antibodies incorporate glycans as part of their binding epitopes, and other epitopes are shielded by sugars and inducing antibodies against those would lead to a less relevant antibody response.

The current COVID-19 pandemic has highlighted the urgent need for vaccines and antiviral drugs. The principal topic of my DPhil centres on addressing these needs for viral infection. Chapter 4 focuses on the site-specific glycosylation occupancy, and N- and O-glycan structures attached to virion derived SARS-CoV-2 spike glycoproteins. This glycan signature was compared to a stabilised prefusion trimeric spike, to a monomeric subunit of spike (S1) and to an antigen of a non-stabilised vaccine candidate, revealing subunit shedding of the S1 glycoprotein for the vaccine candidate. Whether or not monomeric S1 shedding has an effect on the vaccine antibody response or could be implicated in the observed rare side effects, remains to be investigated but

evidence from other studies implicates this occurrence as detrimental in animal models.

The COVID-19 pandemic highlighted again the lack of broad-spectrum antivirals available to patients before thorough investigation of an emergent virus, such as its genome or target host receptor. Chapter 5 discusses the establishment of a medium-throughput drug screening platform against SARS-CoV-2. FDA-approved compounds were prioritised and triaged within the screen for clinical committees such as the UK steering group for therapeutics for COVID-19. Compounds of a global anti-COVID-19 effort called the "Moonshot project" targeting the main protease of SARS-CoV-2 were also screened and promising compounds were progressed further to produce a specific direct-acting SARS-CoV-2 antiviral compound. Iminosugars, which inhibit N-linked glycan processing enzymes such as endoplasmic reticulum alpha-glucosidase I and II of the glycoprotein quality control pathway, constituted one of the two most promising groups of drugs in this antiviral cellular screen that have not entered clinical trials yet.

The second part of this thesis focuses on ER alpha-glucosidase I as a key antiviral target to develop a broad-spectrum antiviral. Previously, it had been observed that a single high-dose treatment with the iminosugar M*O*N-DNJ led to long-lasting antiviral effects in lethal dengue mouse models via alpha-glucosidase I inhibition. In Chapter 6 the mechanism of action was investigated in an *in cellulo* model recapitulating the *in vivo* data. This led to preliminary results and the hypothesis that the unfolded protein response might play a fundamental role in activating the apoptosis pathway in dengue-infected and high-dose treated cells alone. This warrants further investigation in a more relevant cell type, precipitating the development of the human induced pluripotent

stem cell knockouts of the unfolded protein response constituents. This chapter also describes how I produced these cells.

An important factor that warrants consideration is that inhibition of the alpha-glucosidases in the ER by iminosugars as glucose mimetics can lead to unintended side-effects as many host enzymes can recognise glucose molecules. In Chapter 7, I describe attempts towards identification of a specific alpha-glucosidase I inhibitor. X-ray crystallisation of ER alpha-glucosidase I with the iminosugar *N*B-DNJ bound in the active site, led to one crystal which was analysed, but the crystallisation process was not reproducible enough to be useful for fragment or drug screening. Further methods such as thermal shift assay screening of 1600 FDA-approved compounds did not reveal any compounds that bound to the soluble enzyme. Screening of a library of 2.9 billion DNA-tagged molecules against the soluble enzyme found 937 potential binders. This needs further validation to establish the binding mode and inhibitory activity.

Overall, this thesis describes the unique influence of glycan analysis in the rational design of vaccines and how subtle changes in glycosylation help interpret large-scale changes in the structure of an antigen, or the foundation for a totally new type of broad-spectrum antiviral that functions through inhibiting the host glycosylation pathway – collectively these outputs will help preparedness for future pandemics.

Acknowledgements

First and foremost, I would like to acknowledge my supervisors Nicole Zitzmann and Bridget Wills. Both are brilliant scientists, group leaders and mentors. They taught me that science is more than just publications, but rather growing as a scientist and trying to do good in the world with our science. I am excited to have you both as mentors for my onward scientific journey. To Nicole, for always having an open door to discuss any matter in science, in life and being always open to my ideas. Your optimism, support, and trust in me helped me to explore my own ideas and showed me again how fascinated I am about viruses. To Bridget, for supporting me through-out this DPhil with lots and lots of meetings with you in Vietnam. Giving me the perspective of how to work in a country in which dengue is endemic and your insight into clinical dengue work, has made me more passionate about my work. I am so thankful that you agreed to be my second supervisor!

To Raymond Dwek, for his exceptional support during my time in Glycobiology. His dedication to science is inspiring, and our daily chats over the coffee break always ended up in captivating scientific discussions which helped me to (re)-think my science. To Norica Branza-Nichita and Mark Wormald for examining this thesis. To Wellcome Trust for funding my DPhil and to the course directors, Chris Tang, Jan Rehwinkel and Nicole, and our administrators Dawn Gibbons and Louise Samson, for making IITM an incredible supportive program. To Sally Cowley, who introduced me into the world of stem cells and taught me everything about them. To Annette von Delft for her help working on the SARS-Cov-2 Cellular Tracker.

My time during my DPhil would not have been the same without the past and present members of the Zitzmann laboratory. To Anu, Beatrice, Bevin, Dina, Dom, Fergus, Jo, Johan, Mario, Michelle, Natassa, Nilanka, Pietro, Re'em, Snezi, Steve, Tehmi and to our honorary members Andrea, Mark, Olivia and Weston. Their helpful discussions have helped to shape not only the progress of my research, but more importantly, have helped to create a great environment to work in. I especially want to say thanks to Anu and Pietro for introducing me to structural biology. To Re'em, you are always there for me and time with you is always fun. To Nilanka, we shared many hours discussing our science, when experiments failed or buddying each other during late hours in the dengue lab. Our friendship is something I will always value. To

Weston, for unintentionally entertaining Snezi and me, for helping to bring this thesis to the finish line. To Michelle, working with you is always a blast. I cannot believe how many hours we spent together in the dengue lab and then in the Covid lab. To Dom, your passion for glycans and HPLC infected me, so that I enjoy discussing every single peak in a HPLC trace with you. Thank you for being a good friend. To JL, I cannot and want to imagine how this DPhil would have gone without you. You always listen to my problems, supported me in every aspect and kept me company watching 'good' TV shows. To my Snezi, I still remember our first interaction in the TC lab. Since then, you are an important figure in my life. Inside and outside of the lab you are supporting me in everything and working with you showed me what a real scientist is. Your passion about your science and how to live life to the fullest inspires me. We both know which role you played in this DPhil and life, and I am happy to call you my lab-mum!

To all my friends in Oxford outside of the lab, without you I would not have made it to this point. To my beloved Brunch Club: Athena, Johannes, Jonny, Felix and Sarah – for our weekly brunches, dinners and time together. To my B-Friends: Rob and Steve – for always making me laugh. To Alun, my stem cells would have not made it without you. To Iva for a friend going through our first year together. To Cherrelle, for having the best college mum. Thanks for the support from all of you through-out this DPhil and for making Oxford a fun place to live in. I also want to thank my friends outside of Oxford. To Javier, Carol, Dalma, Lourdes, Marina, Manuel, I will never forget our time and will be always thankful to have you on my side. A special thanks to Lena and Andres, two remarkable people who are always there for me at day and night. Even after being away for so long from home, I do not want miss thanking my friends from back home. To Amel, Gerrit, Jo, Karin, Laura, Miri, Sophia, Tanja and Tobi, you all helped me to get there where I am now. A special thanks to my closest friends Aldina and Sarah, you are with me since we are 16 years old, we went through so much together and will always have each other's backs. I don't think I could have maintained my sanity without you!

Finally, I would like to thank my family. In honour of my father who inspired me to go for this DPhil. To my brother, who always has my back in every situation. I want to acknowledge my mother. She has been there for me in every situation from good to bad times, supported me in every decision I have ever made and always believed in me. She taught me how to go through life even if there are obstacles and to never give up. She is my role model. Thank you, mum!

Statement of Authorship

The experiments presented in this thesis were undertaken in Prof. Nicole Zitzmann's laboratory, Oxford Glycobiology Institute, Department of Biochemistry, University of Oxford.

I, Juliane Brun, declare that all the work described here is my own with following exceptions. In Chapter 4, mass spectrometry was performed by Dr Bevin Gangadharan and mass photometry by Dr Weston Struwe. In Chapter 5, all work in the SARS-CoV-2 category 3 laboratory was performed in a buddy system (two people have to be present at all times when working with the virus in CL3, and we swapped between working under the hood and observing in regular intervals) with Michelle Hill and Dr JL Kiappes.

Chapter 4 is based on my first-author paper in *ACS Central Science* "Assessing Antigen Structural Integrity through Glycosylation Analysis of the SARS-CoV-2 Viral Spike".

This work has not been submitted for another degree at this, or any other university.

Table of Contents

Abstract ..... **v**

Acknowledgements ..... **ix**

Statement of Authorship ..... **xi**

Table of Contents ..... **xiii**

List of Figures ..... **xvii**

List of Tables ..... **xx**

Abbreviations ..... **xxii**

Chapter 1 Introduction **29**

1.1 Viral infections **29**

1.1.1 Dengue virus 30

1.1.1.1 Dengue fever burden 30

1.1.1.2 DENV structure and virus life cycle 32

1.1.1.3 DENV glycoproteins 35

1.1.1.4 Dengue virus pathogenesis 38

1.1.1.5 Dengue virus intervention 40

1.1.2 SARS-CoV-2 41

1.1.2.1 COVID-19 burden 41

1.1.2.2 SARS-CoV-2 structure and life cycle 42

1.1.2.3 SARS-CoV-2 pathogenesis 45

1.1.2.4 SARS-CoV-2 intervention 46

1.2 Broad-spectrum antiviral drugs **49**

1.3 Host glycosylation pathway **51**

1.3.1 N-linked glycosylation 53

1.3.1.1 The calnexin cycle and ERAD 55

1.3.1.2 Further N-glycan processing 57

1.3.2 O-linked glycosylation 58

1.3.3 Iminosugars as antivirals 61

1.3.4 Determination of ER alpha-glucosidase inhibition 66

1.3.5 Alpha-glucosidase I as an antiviral target 66

1.4 The unfolded protein response **70**

1.4.1 UPR in DENV infections 75

1.4.2 Unfolded protein response in iminosugar treatment 77

Chapter 2 Research aims **81**

Chapter 3 General Material and Methods **85**

3.1 Cell culture **85**

3.1.1 Mammalian cell lines 85

3.1.2 Insect cell line 87

3.1.3 Human induced pluripotent stem cell derived cells 87

3.1.3.1 Ethics statement for use of stem cell line 87

3.1.3.2 Human induced pluripotent stem cell cultivation 88
3.1.3.3 HiPSCs macrophage differentiation via embryoid body formation 89
3.1.3.4 Terminal differentiation of macrophage precursors to macrophages 90

3.2 Cytotoxicity assay 90

3.3 Gel electrophoresis 91
3.3.1 DNA gel 91
3.3.2 Sodium dodecyl sulphate polyacrylamide gel electrophoresis 91

3.4 Protein detection by western blot 92

3.5 Protein production 93
3.5.1 Bacterial transformation 93
3.5.2 Transfection for protein production 94

3.6 Protein concentration measurements 94
3.6.1 Bradford assay 95
3.6.2 Protein concentration determination at A280 95

Chapter 4 Glycosylation of the viral SARS-CoV-2 spike protein and quality control of a vaccine antigen 97

4.1 Introduction 97

4.2 Material and Methods 100
4.2.1 Propagation and lysis of SARS-CoV-2 100
4.2.2 Protein constructs 101
4.2.2.1 Recombinant SARS-CoV-2 Spike 101
4.2.2.2 SARS-CoV-2 Spike S1 101
4.2.2.3 Vaccine antigen SARS-CoV-2 Spike 102
4.2.2.4 Spike purification from the pellet 102
4.2.3 Protein purification 103
4.2.3.1 Protein A purification of antibodies 103
4.2.3.2 Affinity purification of S_{virus}, $S_{recombinant\ trimer}$, $S1_{recombinant\ monomer}$ and $S_{vaccine\ antigen}$ 103
4.2.4 Detection of spike protein in transfected cells by flow cytometry 105
4.2.5 Glycomics 106
4.2.5.1 Fluorescent labelling of N-linked glycans 106
4.2.5.2 Glycosidase digestion of released glycans 106
4.2.5.3 HILIC-UHPLC to measure PNGase F released glycans 107

4.3 Results 107
4.3.1 Glycosylation of the SARS-CoV-2 spike protein 107
4.3.2 Glycosylation of the antigen of a vaccine candidate 115
4.3.3 Glycosylation of monomeric recombinant S1 121
4.3.4 Identifying the cellular site of $S1_{vaccine\ antigen}$ shedding 123

4.4 Discussion 126

Chapter 5 Antiviral drug screening against SARS-CoV-2 137

5.1 Introduction 137

5.2 Material and Methods 141
5.2.1 Plaque assay 141
5.2.2 Focus forming assay 142

5.3 Results 143
5.3.1 Antiviral drug screening set-up 143
5.3.2 Antiviral assay optimization 146
5.3.3 Antiviral screen 151
5.3.4 Antiviral effect of FDA-approved drugs 151

5.3.5 Antiviral effect of pre-, clinical or experimental compounds 157

5.4 Discussion 164

Chapter 6 Short-term inhibition of ER alpha-glucosidase I as an antiviral strategy 175

6.1 Introduction 175

6.1.1 Aims of this chapter 177

6.2 Material and Methods 178

6.2.1 Dengue virus 178

6.2.1.1 Virus propagation 178

6.2.1.2 In vitro DENV2 infection and drug treatment 178

6.2.1.3 Quantification of viral dengue RNA 179

6.2.1.4 Plaque assay 180

6.2.2 Quantification of intracellular RNA 182

6.2.3 Free oligosaccharide analysis 183

6.2.4 NP-HPLC to measure FOS 183

6.2.5 Immunofluorescence 184

6.2.6 Creation of knockout cell lines in hiPSCs 185

6.2.6.1 Target exon identification and guide RNA design 185

6.2.6.2 NEON transfection of ribonucleoprotein in hiPSCs 187

6.2.6.3 Genomic DNA extraction and PCR screening 188

6.2.6.4 Low density plating of iPSCs for colony picking 188

6.2.6.5 DNA extraction and diagnostic PCR 190

6.2.6.6 Expansion of knockout iPSC lines 191

6.2.6.7 Single nucleotide polymorphism analysis 191

6.2.7 Data analysis and fitting 192

6.3 Results 192

6.3.1 Establishment of a suitable cell culture model 192

6.3.2 Long-lasting antiviral effect of single high-dose iminosugar treatment 204

6.3.3 Mechanism of action of single high-dose treatment 206

6.4 Discussion 214

6.5 Future work 221

6.5.1 Intracellular location of viral proteins in the presence and absence of iminosugar treatment 221

6.5.2 The unfolded protein response in DENV-infected and iminosugar-treated cells 221

6.5.3 Identification of triglucosylated proteins in αGluI inhibited cells 221

6.5.4 Cell death in DENV-virus and iminosugar-treated cells 222

6.5.5 Induced iPSCs knockouts 223

6.5.5.1 Phenotypical description of hiPSCs-derived knockout macrophages 223

6.5.5.2 Dengue virus infection and UPR in hiPSC-derived knockout macrophages 226

Chapter 7 Towards the identification of specific inhibitors of ER alpha-glucosidase I 229

7.1 Introduction 229

7.2 Methods 233

7.2.1 Protein construct Mm αGluI 233

7.2.2 Protein purification 233

7.2.2.1 Sample preparation 233

7.2.2.2 Affinity purification 234

7.2.2.3 Size exclusion chromatography 234

7.2.3 Protein methylation 235

7.2.4 Crystallisation 236

7.2.4.1 Set-up of crystallisation screens 236

7.2.4.2 Data collection....236
7.2.4.3 Data processing, model building and refinement....237
7.2.5 Differential scanning fluorimetry....238
7.2.6 DNA-encoded library....239

7.3 Results....240
7.3.1 Crystal structure of Mm αGluI with NB-DNJ....240
7.3.1.1 Crystallisation and data collection....241
7.3.1.2 Data processing, structure resolution and refinement....242
7.3.1.3 Structure analysis....244
7.3.1.4 Modelling of human alpha-glucosidase I....249
7.3.2 Differential scanning fluorimetry of Mm αGluI with an FDA-approved compound library 251
7.3.3 DNA-encoded chemical library screen to identify new compounds that bind Mm ER αGluI....255

7.4 Discussion....257

Conclusion....261

References....269

Appendix I....309

Appendix II....317

Appendix III....327

Appendix IV....343

List of Figures

Figure 1: The dengue genome possesses a 5' cap and untranslated region (UTR) followed by a 10.2 kb single open reading frame and 3' UTR. 33
Figure 2: Dengue virus infectious life cycle.. 35
Figure 3: SARS-CoV-2 genome annotation. 43
Figure 4: Schematic of the asparagine (N)-linked oligosaccharide precursor $Glc_3Man_9GlcNAc_2$ (glucose, blue circle; mannose, green; N-acetylglucosamine, blue square)..... 54
Figure 5: N-glycosylation and the ERQC checkpoints..... 56
Figure 6: Mammalian N- and mucin-type O-linked glycosylation pathway. by covalently linking a N-acetylgalactosamine (GalNAc) monosaccharide to any serine and threonine. A succession of glycosyltransferases can then ope (366). 59
Figure 7: Iminosugar derivatives of castanospermine, DNJ and DGJ..... 62
Figure 8: Activation of the main UPR pathways in ER stress response..... 72
Figure 9: Purification of SARS-CoV-2 spike glycoprotein..... 110
Figure 10: Purification of $S_{recombinant\ trimer}$. 112
Figure 11: Glycan analysis of the viral and recombinant trimeric SARS-CoV-2 spike glycoprotein.. 114
Figure 12: Western blot analysis of HEK293F cells transfected with $S_{vaccine\ antigen}$. 116
Figure 13: Purification, assembly, and glycosylation of vaccine-derived spike protein with tPA leader sequence..... 118
Figure 14: Purification of $S_{vaccine\ antigen}$ from the cell pellet.. 120
Figure 15: Purification and glycan analysis of $S1_{recombinant\ monomer}$.. 123
Figure 16: Glycan location and macromolecular assembly with N234 and T678 glycan processing..... 125
Figure 17: Cellular location of S protein in $S_{recombinant\ trimer}$ and $S_{vaccine\ antigen}$..... 126
Figure 18: Summary of site-specific glycosylation changes of S1 subunit..... 130
Figure 19: Viruses and vaccine-derived spike glycoproteins have different expression and glycan processing..... 133
Figure 20: Framework of prioritising compounds for drug screening against SARS-CoV-2.. 146
Figure 21: SARS-CoV-2 infection optimization.. 148
Figure 22: Validation of the effect of different DMSO concentrations on cell viability and viral infections on Calu-3 cells.. 150
Figure 23: Schematic of viral infectivity assay.. 151
Figure 24: FDA-approved direct-acting drugs tested against SARS-CoV-2..... 152
Figure 25: FDA-approved host-directed drugs tested against SARS-CoV-2. 155
Figure 26: Direct-acting clinical, pre-clinical and experimental compounds tested against SARS-CoV-2. 158

Figure 27: Clinical, pre-clinical and experimental compounds tested against SARS-CoV-2. 162
Figure 28: Establishment of DENV infection and *N*B-DNJ treatment in Vero E6 cells. 195
Figure 29: Influence of high-dose iminosugar treatment on cytotoxicity and plaque assay....197
Figure 30: FOS analysis of cells treated with *N*B-DNJ or *N*B-DGJ for a continuous low-dose or single high-dose. 200
Figure 31: Antiviral effect of *N*B-DNJ and *N*B-DGJ in DENV2-infected Vero E6 cells in continuous low-dose and single high-dose treatment. 202
Figure 32: Pre-treatment of Vero E6 cells. 203
Figure 33: Treatment regime to recapitulate the long-lasting antiviral effect of continuous low-dose compared to single high-dose treatment. 204
Figure 34: Long-lasting effect of continuous low-dose and single high-dose *N*B-DNJ treatment in DENV2-infected cells. 205
Figure 35: Cytotoxicity of both treatment regimens at different time points. C. 207
Figure 36: Immunofluorescence of E, prM, NS1 and NS4b in DENV2-infected untreated, continuous low-dose, single high-dose treated, and mock-infected cells.. 209
Figure 37: Transcript mRNA level of UPR genes in Vero E6 cells. 211
Figure 38: Transcript mRNA level of the UPR genes *ATF6* and *XBP1s/XBP1t*. 212
Figure 39: Transcript mRNA level of the UPR genes *ATF4* and *DDIT3*....214
Figure 40: Hypothesis of MOA of single high-dose treated DENV2-infected cells. 219
Figure 41: Schematic representation of the CRISPR-Cas9 based knockout strategy in hiPSCs. 224
Figure 42:Genomic structure of *MOGS* and CRISPR/Cas9 targeting. 225
Figure 43: Overall architecture of the ER αGluI. 231
Figure 44: Rod-shaped crystal form of *Mm* ER αGluI co-crystallised with *N*B-DNJ.. 242
Figure 45: Overall structure of *Mm* ER αGluI with *N*B-DNJ in the active site. 245
Figure 46: Superposition of *Mm* ER αGluI complexed with *N*B-DNJ (orange) and *Mm* ER αGluI complexed with M*O*N-DNJ (blue). 246
Figure 47: Active site of *Mm* ER αGluI in complex with *N*B-DNJ. 247
Figure 48: Two-dimensional diagram (LigPlot) showing interactions of *Mm* ER αGluI with (A) *N*B-DNJ (B) M*O*N-DNJ. 248
Figure 49: I-TASSER model of *Hs* ER aGluI.. 250
Figure 50: Vacuum electrostatic potential of human and murine ER αGluI. 251
Figure 51: Differential scanning fluorimetry of *Mm* ER αGluI.. 253
Figure 52: Venn diagram of compounds bound to *Mm* αGluI, *Mm* αGluII, *Hs* UGGT1 and a non-template control (negative control)....256
Figure 53: Sequence coverage of S_{virus} by Mascot.. 312
Figure 54: Sequence coverage of $S_{vaccine\ antigen}$ by Mascot.. 313
Figure 55: MS/MS spectrum of the N74 glycopeptide from $S1_{vaccine\ antigen}$. 314
Figure 56: MS spectrum of N74 containing glycopeptide from $S1_{virus}$. 314
Figure 57: MS/MS spectrum of the T678 glycopeptide from $S1_{vaccine\ antigen}$. 315
Figure 58: Flow cytometry analysis. Representative flow cytometry plots demonstrating the gating technique used to analyse the expression of S1 and S2. ..315

Figure 59: Genomic structure of *GANAB* and CRISPR-Cas9 targeting.. 329
Figure 60: Genomic structure of *ERN1* and CRISPR-Cas9 targeting. 330
Figure 61: Genomic structure of *ATF6* and CRISPR-Cas9 targeting..... 331
Figure 62: Genomic structure of *EIF2AK3* and CRISPR-Cas9 targeting. 332
Figure 63: Genomic structure of *XBP1* and CRISPR-Cas9 targeting. 333
Figure 64: SNP analysis of parental SFC841-03-02 p7+11. 334
Figure 65: SNP analysis of SFC841-03-02 p7+11 ATF6-15B-4A$^{-/-}$. 335
Figure 66: SNP analysis of SFC841-03-02 p7+11 GANAB-19B12A$^{-/-}$..... 336
Figure 67: SNP analysis of SFC841-03-02 p7+11 MOGS-16B-6D $^{-/-}$. 337
Figure 68: SNP analysis of SFC841-03-02_p7+11_ERN1-15B-11C$^{-/-}$..... 338
Figure 69: SNP analysis of SFC841-03-02_p7+11_EIF2AK3-NP-3D$^{-/-}$. 339
Figure 70: SNP analysis of SFC841-03-02_p7+11_XBP1-13B-8E$^{-/-}$. 340
Figure 71: SNP analysis of SFC841-03-02_p7+11_ERNR1-15B-9A$^{+/+}$..... 341
Figure 72: Confirmation of expression and purification of ER *Mm* αGluI.. 343

List of Tables

Table 1: WHO criteria for dengue classification (6). 31
Table 2: Currently approved COVID-19 vaccines. 47
Table 3: List of known patients with mutations in the *MOGS* gene....68
Table 4: List of antibodies used for western blots. 93
Table 5: List of protein constructs used in this thesis....94
Table 6: Molar absorption coefficients of purified proteins. 96
Table 7: Buffer recipes used for CR3022-affinity purification. 104
Table 8: Antibodies used for flow cytometry analysis. 105
Table 9: Mascot analysis of purified S_{virus}. 111
Table 10: Antiviral effect of % DMSO measured by plaque or focus forming assay. 150
Table 11: List of tested FDA-approved direct-acting compounds.. 153
Table 12: List of tested FDA-approved host-targeted compounds....156
Table 13: List of tested experimental direct-acting compounds....159
Table 14: List of tested experimental potential host-targeted compounds.. 163
Table 15: Summary of compounds reaching an IC_{50}, IC_{90} and selectivity index (SI1 = CC_{50}/IC_{50}; SI2 = CC_{10}/IC_{90}). 170
Table 16: Sequence of forward and reverse primer, Taqman probe and DENV2 NS5 standard for DENV2 qRT-PCR. 180
Table 17: Concentration of DENV2 3'UTR qRT-PCR reaction. 180
Table 18: Composition of first and second overlay for plaque assay. 182
Table 19: Taqman primers and probes used for the quantification of cellular mRNA. 182
Table 20: Primary and secondary antibodies used for immunofluorescence. 185
Table 21: FOS analysis of different treatment time and *N*B-DNJ or *N*B-DGJ concentration.. 199
Table 22: Concentration of binding and elution buffer for *Mm* ER αGluI using HisTrap™ excel. 234
Table 23: Concentration of dialysis and gel filtration buffer for *Mm* ER αGluI. 235
Table 24: Data collection parameters of *Mm* ER αGluI *N*B-DNJ....237
Table 25: Data processing statistics of the dataset obtained from the *Mm* ER αGluI *N*B-DNJ crystal in well A2....243
Table 26: Model building and refinement statistics. 244
Table 27: Melting temperature (T_m) and relative melting temperature (ΔT_m) compared to native *Mm* αGluI from DSF.: 253
Table 28: Compounds binding to *Mm* ER αGluI chosen for further investigation. ..256
Table 29: Glycoform abundances observed across $S1_{virus}$. 309
Table 30: Glycoform abundances observed across $S_{recombinant\ trimer}$. 310
Table 31: Glycoform abundances observed across $S1_{vaccine\ antigen}$. 311

Table 32: Glycoform abundances observed across $S1_{recombinant\ monomer}$. 311
Table 33: Gibson assembly and sequencing primers to clone $S_{vaccine\ antigen.}$ 312
Table 34: FDA-approved DAAs used in the drug screening against SARS-CoV-2. 317
Table 35: FDA-approved HTAs used in the drug screening against SARS-CoV-2.318
Table 36: Experimental proposed DAAs used in the drug screening against SARS-CoV-2. 321
Table 37: Experimental proposed HTAs used in the drug screening against SARS-CoV-2. 324
Table 38: List of gRNAs used to create hiPSCs knockouts. 327
Table 39: List of primers for sequencing CRISPR-Cas9 knockouts, or primer to detect DNA between CRISPR cut sites. 328
Table 40: FDA-approved drugs (Pharmakon1600, MicroSource Discovery System screened against soluble ER *Mm* αGluI. 343

Abbreviations

αGluI	ER alpha-glucosidase I
αGluII	ER alpha-glucosidase II
αManI	ER alpha-mannosidase I
2-AA	2-aminoanthranilic acid
2THO-DNJ	N-8′-(2″-tetrahydrofuranyl)-octyl-deoxynojirimycin
3CLpro	3-chymotrypsin like protease, main protease of SARS-CoV-2
4-HPR	N-(4-hydroxyphenyl)retinamide
ACE2	Angiotensin-converting enzyme 2
ADE	Antibody-dependent enhancement
ARDS	Acute respiratory distress syndrome
ARE	antioxidant response element
ASK1	Apoptosis signal-regulating kinase 1
ATF4	Activating transcription factor 4
ATF6	Activating transcription factor 6
ATF6p50	Spliced ATF6
ATF6p90	Full-length ATF6
BCL-2	B-cell lymphoma protein 2
BHK	Baby hamster kidney cells
BID	Twice a day
BiP	Binding immunoglobulin protein, GRP78
bp	Base pair
BSA	Bovine serum albumin
bZIP	Basic Leucine Zipper Domain
C	Capsid protein of DENV
Cas9	CRISPR-associated endonuclease
CAST	Castanospermine
CC_{10}	Cytotoxic concentration of 10%
CD	Cluster of differentiation
CDG-IIb	Congenital disorder of glycosylation IIb

cDNA	Complementary DNA
CH	Central helix
CHOP	C/EBP-Homologous Protein 10
CLEC5A	C-type lectin domain containing 5A
CMC	Critical micelle concentration or carboxymethyl cellulose
CMV	Cytomegalovirus
CNX/CRT	Calnexin/calreticulin cycle
COPII	Coat protein II
COVID-19	Coronavirus disease-19
CPE	Cytopathic effects
CRISPR	Clustered Regularly Interspaced Short Palindromic Repeats
cRNA	Crispr RNA
CV	Column volume
DAA	Direct-acting antiviral
DALYs	Disability-adjusted life years
DAPI	4′,6-diamidino-2-phenylindole
DC-SIGN	Dendritic cell-specific intercellular adhesion molecule-3-grabbing non-integrin
DDIT3	DNA damage-inducible transcript 3
DDM	N-dodecyl-b-D-maltoside
DELopen	DNA-encoded library
DENV	Dengue virus
DGJ	Deoxygalactonojirimycin
DMSO	Dimethyl sulfoxide
DNA	Deoxyribonucleic acid
DNJ	1-deoxynojirimycin
Dol-PP	Dolichol-pyrophosphate
DSB	Double strand break
DSF	Differential Scanning Fluorimetry
dsRNA	Double-stranded RNA
DSS	Dengue shock syndrome
E	Envelope protein of DENV
ε_{280}	Extinction coefficient
EB	Embryoid bodies
EBOV	Ebola virus
EDEM1-3	ER degradation-enhancing alpha-mannosidase-like 1-3
eIF2a	Eukaryotic translation initiation factor 2 subunit-a

ELISA	Enzyme-linked immunosorbent assay
EMA	European Medicines Agency
Endo H	Endoglycosidase H
EnGNase	Endo-b-Nacetylglucosaminidase
ER	Endoplasmic reticulum
ERAD	ER-associated degradation
ERdj4	ER-localized DNAJ4
ERGIC	the ER-Golgi intermediate compartment
ERN1	ER-to-nucleus signaling 1 gene
ERQC	ER quality control
FBS	Foetal bovine serum
FCS	Furin cleavage site
FDA	Food and Drug Administration
FFT	Fast Fourier transform
FFU	Focus Forming unit
FL	Fusion loop
FOS	Free oligosaccharide
FP	Fusion peptide
Fuc	Fucose
G-CSF	Granulocyte colony-stimulating factor
G3BP1/2	Ras GTPase-activating protein-binding protein 1/2
GADD34	Growth Arrest and DNA Damage-Inducible Protein 34
Gal	Galactose
GalNAc	N-acetylgalactosamine
GANAB	Glucosidase II Alpha Subunit
GCN2	General control nonderepressible 2
GE/mL	Genome equivalents/mL
GH63	glycosyl hydrolase 63
GlcNAc	N-acetylglucosamine
Glu	Glucose
GP	General practitioner
gp120	HIV envelope glycoprotein gp120
gp41	Glycoprotein 41 (HIV)
GPI	Glycosylphosphatidylinositol
gRNA	Guide RNA
GRP78	78 kDa Glucose-Regulated Protein, BiP

HBV	Hepatitis B virus
hCoV	Human coronavirus
HCV	Hepatitis C virus
HDR	Homology directed repair
HEK293	Human embryonic kidney cells
hES	Human embryonic stem cell medium
HI FBS	Heat-inactivated foetal bovine serum
HILIC-UHPLC	Hydrophilic interaction liquid chromatography-ultra-high performance liquid chromatography
hiPSCs	Human induced pluripotent stem cells
HIV	Human immunodeficiency viruses
hMPV	Human metapneumovirus
hpi	Hours post infection
HR	Heptad repeat regions
HRP	Horse-radish peroxidase
Hs	Human
hsp	Heat shock protein
HTA	Host-targeted antivirals
I-TASSER	Iterative Threading ASSEmbly Refinement
$IC_{10/50/90}$	Inhibitory concentration for 10, 50 or 90%
IE CMV	Human cytomegalovirus major immediate early enhancer/promoter
IFNɣ	Interferon ɣ
Ig	Immunoglobulin
IL	Interleukin
IP-10	Interferon gamma inducible protein-10
IRE1	Serine/threonine-protein kinase/endoribonuclease inositol-requiring enzyme 1 α
ITC	Isothermal calorimetry
IVA	Influenza A virus
JEV	Japanese encephalitis virus
JNK	c-Jun N-terminal kinases
kb	Kilobase
KEAP1	Kelch-like ECH-associated protein 1
Ki	Inhibitory constant
LLO	Lipid-linked oligosaccharide

LPS	Lipopolysaccharide
M	Membrane protein of dengue virus
M6P	Mannose-6-phosphate
Man	Mannose
MCP-1	Monocyte chemoattractant protein-1
MERS	Middle East respiratory syndrome coronavirus
MIP-1	Macrophage inflammatory protein- 1
miRNAs	Micro RNA
MOA	Mechanism of action
MOGS	Mannosyl-oligosaccharide glucosidase
MOI	Multicipity of infection
M*O*N-DNJ	N-(9′-methoxynonyl)-1-deoxynojirimycin
Mpro	Main protease SARS-CoV-2
MS	Mass spectrometry
MTS	3-(4,5-dimethyl-2-yl)-5-(3-carboxymethoxyphenyl)-2-(4-sulfophenyl)-2H-tetrazolium
MW	Molecular weight
MWCO	Molecular weight cut-off
N	Nucleocapsid
*N*AP-DNJ	*N*-(6'-[4″-azido-2″-nitrophenylamino]hexyl)-1-DNJ
*N*B-DNJ	*N*-butyl-deoxynojirimycin , Miglustat
NCS	Non-crystallographic symmetry
Neu5Ac	N-acetylneuraminic acid
NHEJ	Non-homologous end-joining
*N*N-DGJ	*N*-nonyl-DGJ
*N*N-DNJ	*N*-nonyl-DNJ
NPC1	Niemann-Pick type C1
Nrf2	Nuclear factor erythroid 2-related factor 2
NRP1	Neuropilin-1
NS1-5	Non-structural proteins of DENV
NSP1-16	Non-structural proteins of SARS-CoV-2
NTC	Non-template control
NTD	N-terminal domain
ORF	Open reading frame
OS-9	Osteosarcoma-9 protein
OST	Oligosaccharyltransferase

PAM	Protospacer adjacent motif
PAMPS	Pathogen-associated molecular patterns
PARP	Poly (ADP-ribose) polymerase
PCR	Polymerase chain reaction
PDI	Protein disulfide isomerase
PERK	Kinase R (PKR)-like endoplasmic reticulum kinase
PFA	Paraformaldehyde
PFU	Plaque Forming unit
PKR	Protein kinase R
Plpro	Papain-like protease SARS-CoV-2
PNGase F	Peptide:N-glycosidase F
PP1	Protein phosphatase 1
pp1a, 1ab	Polyprotein 1a, 1ab SARS-CoV-2
PRKCSH	Protein Kinase C Substrate 80K-H
prM	Precursor of the membrane protein of DENV
PVDF	Polyvinylidene difluoride
qRT-PCR	Quantitative reverse transcription polymerase chain reaction
RBD	Receptor binding domain
RdRp	RNA-dependent RNA polymerase
RIDD	Regulated Ire1-dependent decay
RMSD	Root-+A1:B21mean-square deviation
RNA	Ribonucleic acid
RNP	Ribonucleoprotein
Rock	Rho-kinase
ROS	Reactive oxygen species
RSV	Respiratory syncytial virus
S	Full-length SARS-CoV-2 spike protein
S1	Subunit S1 of SARS-CoV-2 spike protein
S2	Subunit S2 of SARS-CoV-2 spike protein
SARS-CoV-1	Severe acute respiratory syndrome coronavirus type 1
SARS-CoV-2	Severe acute respiratory syndrome coronavirus type 2
SB	Selection buffer
SD	Subdomain
SDS-PAGE	Sodium dodecyl sulphate polyacrylamide gel electrophoresis
SEC	Size exclusion chromotography

SERM	Selective oestrogen receptor modulator
SI	Selective index (SI1 = CC50/IC50); (SI2 = CC10/IC9)
SNP	Single nucleotide polymorphism
SP	Signal peptide
SPR	Surface plasmon resonance
TAM	Receptor tyrosine kinase subfamily Tyro3, Axl, Mer
TGN	*trans*-Golgi network
TID	Thrice day
TIM	T-cell immunoglobulin domain and mucin domain
TLS	Translation/Libration/Screw
TM	Transmembrane domain
Tm	Tunicamycin
T_m	Melting temperature
TMPRSS2	Transmembrane serine protease 2
tNCS	Translational non-crystallographic symmetry
TNFα	Tumour necrosis factor alpha
ToP-DNJ	Tocopherol-DNJ
tPA	Tissue plasminogen activator
TSA	Thermal shift assay
UGGT1/2	UDP-glucose:glycoprotein glucosyl transferase 1/2
UPR	Unfolded protein response
UTR	Untranslated region
v/v	Volume per volume
VEGF	Vascular endothelial growth factor
w/v	weight per volume
WB	Washing buffer
WHO	World Health Organization
WNV	West Nile virus
XBP1	X-box binding protein 1
XBP1s	Spliced X-box binding protein 1
XBP1t	Full-length X-box binding protein 1
ZIKAV	Zika virus

Chapter 1 Introduction

1.1 Viral infections

Humans are vulnerable to infection by many different viruses. Although the immune system can manage most viral infections with little harm to the host, some viral infections lead to severe disease or death. The properties of the virus, acute or chronic infections, and variables determined by the host, e.g. genetic predisposition, collectively influence the progression of the infection and patient prognosis (1). Pathogens such as Hepatitis B virus (HBV), Hepatitis C virus (HCV) or herpesviruses can remain in the host and cause chronic or latent infections without, in most cases, causing immediate harm in otherwise-healthy patients. In other cases, acute infections can range from mild or subclinical infections to severe disease or potential death, as is the case of influenza A virus (IVA), dengue virus (DENV) and the severe acute respiratory syndrome coronavirus type 2 (SARS-CoV-2) (1).

Acute viral infections are characterised by a rapid onset of disease, a short duration of symptoms, and a quick recovery time. During the incubation period the viral genome replicates, the host immune response is initiated, and cytokines are produced that lead to typical symptoms like aches, pain, fever, malaise and nausea. With DENV infections, a severe manifestation of the disease can occur after the fever subsides. In some acute viral infections, the inflammatory response leads to an excessive upregulation and release of pro-inflammatory cytokines, commonly referred to as

cytokine storm or cytokine release syndrome (2). This excessive and uncontrolled release of cytokines is difficult to predict and described for several viruses, including DENV and SARS-CoV-2 (2,3).

1.1.1 Dengue virus

1.1.1.1 Dengue fever burden

DENV is an enveloped positive-strand ribonucleic acid (RNA) flavivirus that is the causative agent of dengue. Dengue is a re-emerging arthropod-borne viral infection transmitted by *Aedes* mosquitoes and is the most significant arthropod-borne virus worldwide. Approximately one-third of the world's population is at risk of DENV infection (4); estimates indicate about 390 million people are infected every year, of whom approximately 96 million develop clinically apparent manifestations (5). There are four distinct, but closely related, serotypes of DENV capable of causing disease in humans. The severity of dengue infection can range from asymptomatic or mild disease to severe haemorrhagic fever and death. In 2009, the World Health Organization (WHO) released updated guidelines on dengue identification, classification, and management. The previously used definitions of dengue fever, dengue haemorrhagic fever and dengue shock syndrome (DSS) were updated based on a detailed the prospectively gathered dataset from more than 2000 patients (DENCO study) to dengue with and without warning signs, and severe dengue (**Table 1**) (6). Severe dengue is defined by any combination of a) a systemic vascular leak syndrome resulting in hypovolaemic shock or respiratory distress due to fluid overload, b) severe haemorrhage, and/or c) severe organ dysfunction (7).

Table 1: WHO criteria for dengue classification (6)**.**

Dengue without warning signs	**Dengue with warning signs**	**Severe dengue**
Fever and two of the following: • Nausea, vomiting • Aches and pains • Rash • Positive tourniquet test • Leukopenia	Symptoms as dengue without warning signs with any of the following: • Persistent vomiting • Abdominal pain or tenderness • Clinical fluid accumulation • Lethargy, restlessness • Mucosal bleeding • Liver enlargement >2 cm • Increase in haematocrit concurrent with rapid decrease in platelet count	Dengue with at least one of the following: • Severe plasma leakage leading to: – Shock (DSS) – Fluid accumulation with respiratory distress • Severe bleeding • Severe organ involvement – Liver: Alanine aminotransferase or aspartate aminotransferase ≥ 1000 – Central nervous system: impaired consciousness – Heart/other organ failure

Before 1970, dengue had only been reported from nine countries, but today dengue has become endemic in at least 129 countries. The virus is responsible for significant public health and economic burdens in tropical and sub-tropical regions of the world. Climate change and the rise in uncontrolled urban development in the 20th century, often combined with poor sanitation and inadequate waste disposal services, resulted in expansion of *Aedes* mosquito populations with major disease outbreaks being reported from the 1950's onwards (8). In recent years, dengue virus infection has also reported from southern Europe and the United States (6). Case fatality rates for severe illness can exceed 10% even with medical treatment (9) with up to 20,000 – 25,000 people, predominantly children, dying of dengue every year (5), and therefore the global burden of disease affects countries and age groups disproportionally. While supportive treatment of symptomatic patients can lower case fatality rates to below 1%

(10,11), conservative estimates of morbidity suggest a toll of 264 disability-adjusted life years (DALYs) per million population.

1.1.1.2 DENV structure and virus life cycle

DENV virions have an icosahedral capsid structure of 40 – 60 nm containing a single-strand positive-sense RNA genome of approximately 11 kilobase (kb) enveloped by a lipid bilayer derived from the host endoplasmic reticulum (ER) membrane in which virally encoded envelope glycoproteins are embedded (4). Upon infection, DENV predominantly targets mononuclear phagocytic cells, such as monocytes, macrophages, and dendritic cells (12). The virus is internalised by receptor- and clathrin-mediated endocytosis (13–15).

To date, no specific essential receptor has been identified for DENV. However, several proteins and carbohydrates have been identified important for viral entry as receptors or co-receptors on numerous mammalian cell types, including heparan sulphate (16,17), lipopolysaccharide (LPS) receptor cluster of differentiation 14 (CD14) (18), mannose receptor (MR) (19), heat shock proteins 70 (hsp70) and hsp90 (20), dendritic cell-specific intercellular adhesion molecule-3-grabbing non-integrin (DC-SIGN) (21–23), C-type lectin domain containing 5A (CLEC5A) (24), the T-cell immunoglobulin domain and mucin domain (TIM) and receptor tyrosine kinase subfamily Tyro3, Axl, Mer (TAM) family of receptors (25). Additionally, in secondary infections, after complexing with antibodies DENV can attach to cellular Fcγ-receptors allowing uptake of the virus into the cell via a mechanism known as antibody-dependent enhancement (ADE) (26–28), which is described later in this chapter.

The viral RNA has one open reading frame (ORF), encoding a single polyprotein, which is then cleaved co- and post-translationally in the ER by viral and host proteases into three structural proteins (capsid, C; precursor of the membrane protein (M), prM; and envelope, E) and seven non-structural proteins (NS1, NS2A, NS2B, NS3, NS4A, NS4B, and NS5;

Figure 1) (29,30).

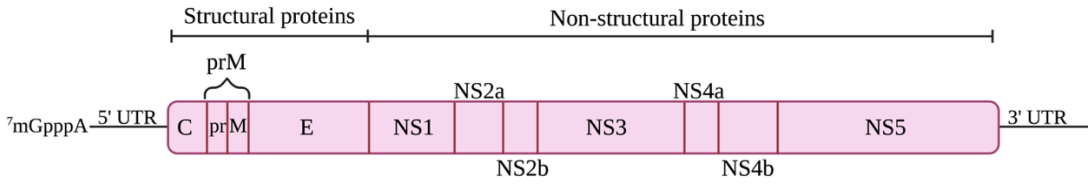

Figure 1: The dengue genome possesses a 5' cap and untranslated region (UTR) followed by a 10.2 kb single open reading frame and 3' UTR. The RNA lacks a polyadenylated tail but is circularised by structural motifs in the 5' and 3' UTRs. The three structural proteins are arrayed in tandem followed by the seven non-structural proteins.

Upon internalization, DENV virions are transported within early endosomes, which develop into acidic late endosomes. The low pH (~5.0) of late endosomes causes conformational changes in the DENV E protein (31,32). This causes the E homodimers to dissociate, exposing the fusion loop (FL) enabling insertion into the cellular membrane. E homotrimers form, and viral and host membranes fuse (32,33). Once fused, the DENV nucleocapsid is ejected into the cytosol, the viral RNA is uncoated and travels to the rough ER where it is translated into the polyprotein (34). Polyprotein processing occurs, giving rise to the three structural and seven non-structural proteins as stated above. Once the protease cleaves the precursor to create active proteins, they

assemble to form a replication complex. These replication factories are virus-induced, organelle-like membrane structures formed by NS1 – NS5 (35).

Once viral RNA is translated to produce sufficient viral proteins to form new virions, the viral RNA is packaged by C protein to form nucleocapsids. Following nucleocapsid budding into the ER, the immature virion consisting of the nucleocapsid core is surrounded by the host ER membrane with 90 dimers of E and 180 copies of prM inserted into the lipid bilayer (36,37). Immature virions are transported through the *trans*-Golgi network (TGN), where the host cell protease furin cleaves prM into M, resulting in mature DENV particles. Progeny DENV virions then exit the cell by exocytosis (30).

Immature virions have a rough appearance, whereas mature virions are smooth. Since furin-mediated cleavage of prM to M in the TGN is incomplete, a mixed population of mature and immature virions is released. This is an important point as the maturation state of the virions is relevant to the type of cell that can be infected due to the diverse expression of receptors on cell surfaces and the binding of specific antibodies to immature or mature DENV particles (38) (**Figure 2**). Immature virions are still able to infect cells by either Fc receptor-mediated uptake of immature virions complexed with anti-prM or anti-E antibodies (39–43), by binding of prM to DC-SIGN (44) or by cleavage of prM by furin during the entry process in the endosomes (39).

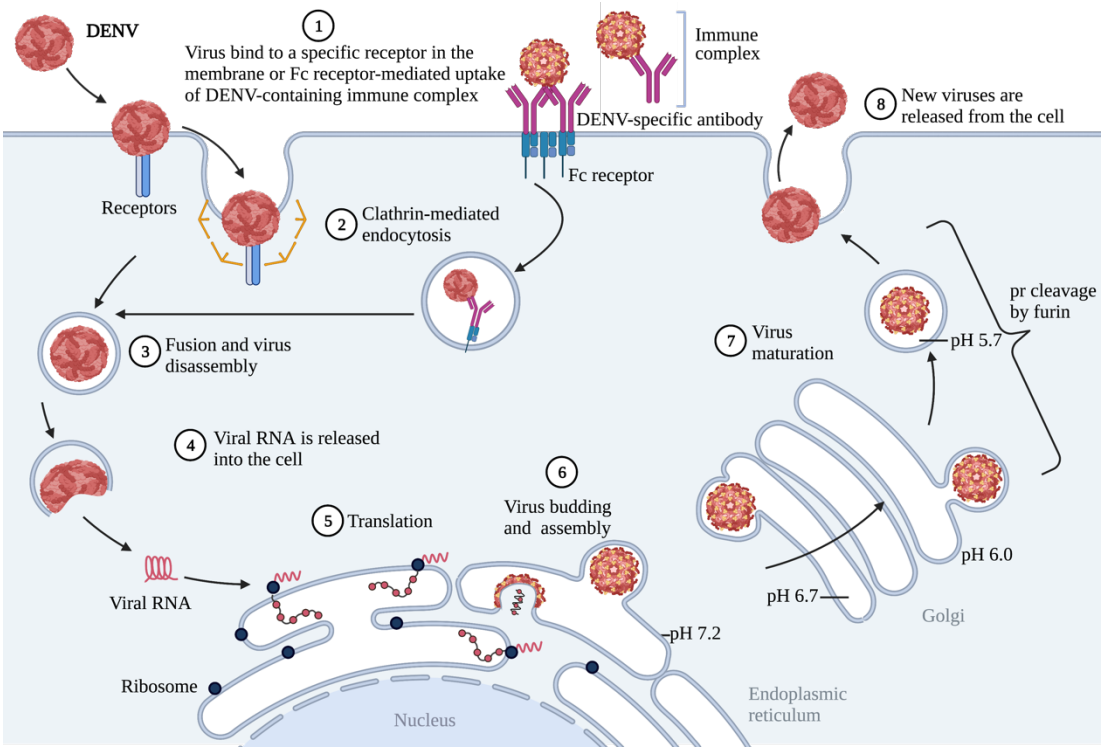

Figure 2: Dengue virus infectious life cycle. (1) DENV binds to appropriate host-receptors and/or co-receptors and is (2) internalized via clathrin-mediated endocytosis or Fc receptor-mediated internalization of fully or nearly immature viral particles into an early endosome, before maturing into a late endosome. (3) The low pH in the late endosome triggers DENV envelope conformational changes, resulting in fusing of the viral and host-cell membranes. (4) Allowing DENV nucleocapsid to be released into the cytoplasm, and viral RNA uncoating. (5) Viral RNA is presented to the rough ER where viral RNA translation, polyprotein processing, RNA synthesis and replication occur. (6) Viral RNA is packed by viral capsid protein, building a nucleocapsid and buds into the ER lumen as an immature DENV particle with prM/E heterodimers. (7) Immature DENV particle travel to the TGN, where furin-cleavage of prM to M occurs (viral maturation). (8) Mature virions are released from the host cell. Adapted from (45) and figured created with BioRender.com ('ZIKV infection Cycle', 2021).

1.1.1.3 DENV glycoproteins

DENV morphogenesis is highly dependent on host-based pathways, particularly the calnexin cycle for N-glycoprotein processing, described later in section 1.3. Four of the ten DENV proteins are N-linked glycoproteins: E (46–48), prM (47), NS1 (47,49) and NS4b (50).

The E protein consists of the receptor-binding domains DI, DII and DIII and a fusion peptide at the tip of DII, sequestered in a hydrophobic pocket created by DI and DIII of the neighbouring E monomer (36). DENV E protein has two N-linked glycosylation sites at N67 and N153 (51). Both glycosylation sites have been assigned functional responsibilities. N67 plays a role in binding to DC-SIGN and is required in some strains for infection of mammalian but not mosquito cells. With the DENV-2 16681 strain, it has been suggested that N67 glycosylation plays a role in virion morphogenesis or release (52–54). The N153 glycan site has been linked to neurovirulence in related flaviviruses like West Nile virus (WNV) (55). However, neurological symptoms are not often associated with DENV infection, though they may be present (56,57). Because DC-SIGN and the MR preferentially interact with high-mannose glycans, the presence of high-mannose glycans on E in virions generated from both mammalian and mosquito cells (58) is critical for receptor binding and is evidently conserved despite their divergent N-glycosylation features. Glycan occupation and glycan structure can be used to differentiate between viral serotypes, strains and different cells of infection (49,58–60).

The single glycosylation site of prM is located in the precursor fragment of the M protein (61). Although little is known about the significance of the precursor protein, it might aid the folding of E protein, as has been shown for other flaviviruses. E.g., the removal the glycan from prM of the Japanese encephalitis virus (JEV) inhibited E protein folding (62). The precursor also covers the FL to prevent premature fusion along the secretory route (19,62–65). The single N-glycosylation site is located at N64 or N69, depending on the serotype (66–68).

DENV NS1 has many roles and properties that have been reviewed in detail (69,70). ER luminal dimeric NS1 is part of the replication complex and is required for negative-strand RNA synthesis (71,72), and involved in ER membrane remodelling to form ER-derived membranous structures to promote replication (73). Dimeric NS1 becomes plasma membrane-associated, or it can hexamerise and be secreted, potentially as a trimer of dimers. It is detectable in patient sera at concentrations of up to 50 μg/mL (74,75) and therefore can be used as a marker for infection. NS1 also can bind to the plasma membrane via interaction with glycosaminoglycans (76). Secreted NS1 can interact with the complement pathways, cross-react with anti-NS1 antibodies, and potentially lead to platelet and endothelial cell damage followed by vascular leakage (70,74,77,78). Additionally, NS1 can stimulate interleukin 10 (IL-10) production from monocytes suppressing protective T-cell response (79,80). NS1 has two N-glycosylation sites and each plays a role in NS1 function and stability. For example removal of the N207 glycan results in reduced monomer and dimer stability and N207 is vital for NS1 secretion (81,82). The second site, N130, has been implicated in virus production (83).

NS4b is also part of the replication complex (84) and exists as glycosylated and non-glycosylated NS4b forms in DENV-infected baby hamster kidney cells (BHK) cells. Deletion of the two N-glycosylation sites at N58 and/or N62 showed a reduction in viral replication indicating they have a functional, yet undefined role (50).

1.1.1.4 Dengue virus pathogenesis

It is still unclear why some individuals develop more severe dengue manifestations than others. Specific DENV serotypes have been linked to severe illness outcomes, for example DENV2 caused more severe illness than any of the other DENV serotypes (85,86). The pathogenesis of the severe disease is due to complex host-virus interactions and modulation of viral replication. The host response seems to play a crucial role in facilitating severe diseases outcome (87).

There are three phases to the clinical course: the febrile, critical, and convalescent phases. The viraemic phase during which patients show fever, myalgia, and other symptoms of a viral disease, usually linked with thrombocytopenia, is known as the febrile phase. The majority of those infected will go into the convalescent phase when their fever has resolved (88). However about 5% develop potentially lethal complications during what is referred to as the critical phase, around day 4-6 of illness. Complications that can occur at this time include a) severe plasma leakage due to increased systemic vascular permeability (potentially resulting in hypovolaemic shock, i.e. DSS), b) bleeding due to thrombocytopenia and coagulopathy, and/or c) severe organ dysfunction. There are no specific treatments for these complications other than good supportive care. The mechanism underlying the altered vascular permeability is thought to relate to the excessive expression of cytokines, i.e. the cytokine storm, mentioned above. Fortunately, the phase of fluid leakage is transient, lasting for around 48 hours before reverting spontaneously to normal. At this point the patient generally recovers (88), or in more rare instances (<1% of cases), results in death (6).

Analysis of secreted cytokines in patients has revealed increases in interferon γ (IFNγ), tumour necrosis factor α (TNFα), and IL-1b, IL-6, IL-10) as reviewed in (89). These inflammatory responses have been linked with dengue severity as they are detected at higher levels in patients with dengue with warning signs compared to patients with dengue without warning signs (90). There is increasing evidence to suggest that the most critical risk factor for severe illness is previous exposure to one of the four serotypes of DENV. Large proportions of DENV antibodies generated after the primary infection are weakly neutralising yet cross-reactive (91–94), resulting in ADE, as mentioned above. In ADE sub-neutralising antibodies may promote the absorption of virions by Fcγ receptor-expressing cells, resulting in increased viral loads, T-cell activation, and pro-inflammatory cytokine release during a heterologous DENV infection, reviewed in (95). The antibody to virus ratio is a predicating factor as well as the affinity of the immunoglobulin G (IgG) antibodies for the Fcγ receptor facilitating viral uptake (96).

Additionally, cross-reactive memory T cells that develop during heterologous secondary infection show a low affinity for the second DENV serotype and are less effective in eliminating the virus than high-affinity naïve T cells (original antigenic sin). The effects of T-cell mediated original antigenic sin are likely to impede the establishment of efficient adaptive immune responses to heterotypic secondary infection (97,98). Following a recurrent dengue infection, $CD4^+$ and $CD8^+$ memory T-cells from a prior infection are thought to proliferate fast and boosting the production of inflammatory mediators (99). However, not all patients develop severe dengue

during a secondary infection (96) and even some primary infections can lead to severe dengue (96).

1.1.1.5 Dengue virus intervention

Currently, there is no widely approved or widely-used vaccine for dengue. Dengvaxia, a tetravalent dengue vaccine, has been approved for use in some endemic countries. However, its efficacy and safety have been questioned. It was originally suggested that the vaccine may increase the incidence of severe disease in children under nine, who are typically the target group for vaccinations (100–103). However, subsequent exploration of the long-term trial data indicated that the increased risk was associated with being dengue-naïve at vaccination rather than with age per se, most likely on the basis of vaccine-induced ADE. The difficulty of eliciting adequate protective immunity against all four antigenically diverse DENV serotypes, without inducing cross-reactivity leading to ADE, is one hurdle in developing an effective vaccine (104).

The Takeda tetravalent dengue vaccine has completed phase II, and also recruitment for phase III in several Latin American and South Asian countries (105–107); initial efficacy results are promising and longer term follow-up data are currently awaited. The National Institutes of Health and the National Institute of Allergy and Infectious Diseases of the United States have completed phases I and II of an attenuated tetravalent lyophilized vaccine, which is presently undergoing phase III trial (104).

No antiviral therapy for dengue has yet been shown to have clinical efficacy. Demonstrating antiviral effectiveness in dengue patients is difficult because administration to a clinic and trial enrolment generally happens after peak viremia,

several days after the onset of fever, at a time when viremia is typically already declining rapidly. Several clinical trials have been conducted using repurposed drugs: Balapiravir, Chloroquine and Prednisolone, but unfortunately no differences in fever clearance, cytokine profile and plasma viral load were observed compared to the control groups (108).

1.1.2 SARS-CoV-2

1.1.2.1 COVID-19 burden

In December 2019, SARS-CoV-2 was first discovered in Wuhan, China (109). It is the causative agent of the coronavirus disease-19 (COVID-19) pandemic, which has a yet-to-be-determined, but unprecedented immense and growing impact on public health and stability globally (110). SARS-CoV-2 has claimed 3,803,592 lives to date worldwide (as of 14/06/2021) (111). However, hundreds of millions have been infected – although most SARS-CoV-2 infected individuals do not require hospitalisation, a small percentage develop severe symptoms and/or long-term health complications, so-called long COVID. Infection with SARS-CoV-2 may lead to life-threatening consequences, such as acute respiratory distress syndrome (ARDS) and systemic multi-organ failure (112). Fortunately, with remarkable speed and international cooperation, scientists around the globe worked together to understand the virus life cycle, its pathology and immune response, producing effective working vaccines in record time, and identifying a number of effective therapeutics for use at different stages of the illness.

SARS-CoV-2 is a single-stranded, enveloped, positive-sense RNA betacoronavirus belonging to the *Coronaviridae* family. Historically, coronaviruses infecting humans have included human coronaviruses (hCoV)-OC43, hCoV-HKU1, and hCoV-229E, which cause the common cold. However, recently coronaviruses have emerged from animal reservoirs and caused new, more severe, human disease (113). Three pathogenic coronavirus strains have arisen in the last two decades. In 2003, SARS-CoV-1 infected about 8000 people with a 10% death rate, while Middle East respiratory syndrome coronavirus (MERS) infected 2500 people in 2012, with a death rate of 36% (114). SARS-CoV-2 has 79% homology to SARS-CoV-1 and 50% with MERS (115). Both virus outbreaks were eventually contained to an end by standard preventive strategies such as travel bans and patient isolation.

Mutations in viruses, especially RNA viruses, are common (116). Most of the observed mutations of circulating SARS-CoV-2 virions were either neutral or mildly detrimental to the virus, leading only to changes in the RNA genome. However, a small number of mutations have impacted the virus phenotype to its advantage, altering features such as viral fitness, pathogenicity, infectivity, transmissibility, antigenicity, and leading to new virus strains (116). Currently, for SARS-CoV-2, the delta strain (B.1.617.2) is a variant of concern, with higher transmissibility and potentially reduced neutralisation in vaccinated individuals (117).

1.1.2.2 SARS-CoV-2 structure and life cycle

SARS-CoV-2 consists of a 30 kb genome, which encodes 14 ORFs (118). In the 5' two-third of the viral genome ORF1a and ORF1b are partially overlapping and encode

the polyproteins, pp1a and pp1ab, that are auto-proteolytically cleaved from the replicase–transcriptase complex, which consists of 16 non-structural proteins (NSP1 – NSP16), including two proteases: the papain-like protease (PLpro, NSP3) and main protease (Mpro, 3CLpro, NSP5). ORF1b results from a programmed −1 ribosomal frameshift (119). The other 13 ORFs encode for the four structural proteins spike (S), envelope (E), membrane (M), and nucleocapsid (N) (120) and nine putative accessory proteins (121) (**Figure 3**).

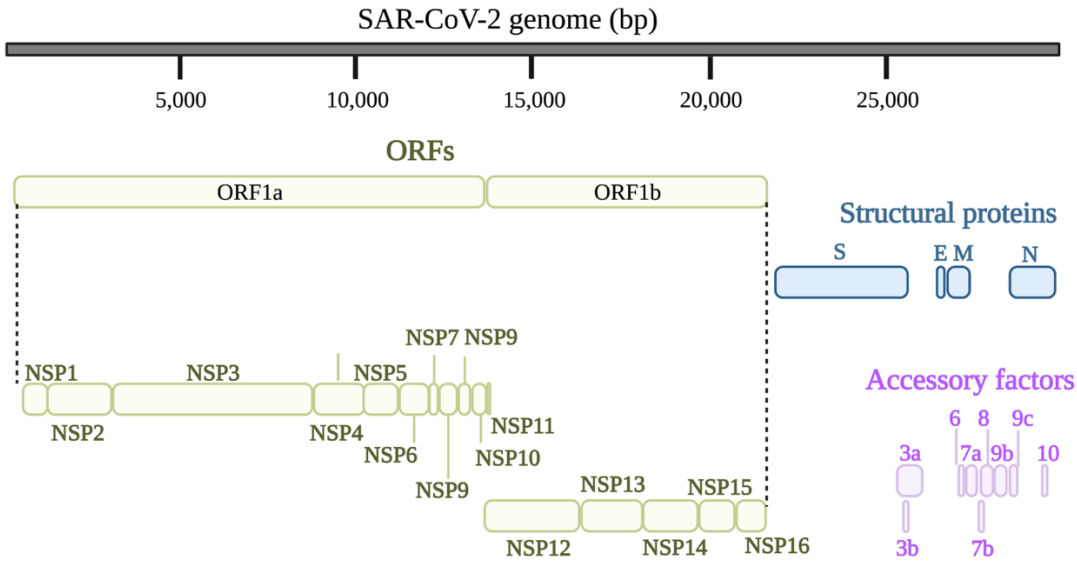

Figure 3: SARS-CoV-2 genome annotation. ORF1a and ORF1b producing polyprotein 1a (pp1a) and pp1ab (NSP1 – 16). The other 13 ORFs encoding for the structural proteins (S, E, M, N) and accessory factors (3a, 3b, 6, 7a, 7b, 8, 9b, 9c,10). Adapted from (118).

The S protein is present as a trimer on mature viruses, with three receptor-binding domains (S1) and a trimeric membrane fusion stalk (S2) containing the heptad repeat regions (HR) and fusion peptides (FP). Viral entry is initiated by binding to the cell surface protein angiotensin-converting enzyme 2 (ACE2) through the receptor-binding domain (RBD) of the S1 subunit of the S protein (122). After binding to the receptor,

the S protein is primed by proteolytic cleavage with the host protease transmembrane serine protease 2 (TMPRSS2) near the junction of its S1/S2 boundary (123). The endosomal cysteine proteases cathepsin B and L can also contribute to viral entry (124–128).

Another host cell mediator, neuropilin-1 (NRP1), present on the cell surface, in particular on olfactory cells, binds to furin-cleaved S1 and increases SARS-CoV-2 infectivity (129,130). The S2 subunit mediates the fusion of viral and cellular membranes upon extensive conformational rearrangements (131,132). This allows viral RNA to be transferred into the host cell cytoplasm, where viral replication takes place, involving RNA synthesis, proofreading by the virus-encoded NSP14, which is unusual for an RNA virus, and capping (133). Newly synthesized viral genomic RNAs, coated with viral N proteins, bud into the lumen of the ER-Golgi intermediate compartment (ERGIC) (134,135). These viral particles contain the viral structural proteins S, M and E embedded into host membranes (136,137). From the ERGIC, virus particles traffic to the Golgi and TGN where further post-translational modifications, including glycosylation, occur (135). Assembled virions were thought to leave an infected cell by bulk secretion (138,139); however, recently, it has been shown that SARS-CoV-2 virions egress infected cells through the lysosomal trafficking pathway (140). During this process, viruses interfered with lysosomal acidification, lysosomal enzyme production, and antigen presentation (140).

SARS-CoV-2 acquired a polybasic cleavage site (PRRAR) at the S1–S2 interface which allows for effective cleavage by furin, a unique property of the SARS-CoV-2 S

protein. Cleavage by furin results in enhanced infectivity (122,131,132,141–143). Furin processing of the SARS-CoV-2 S protein may contribute to increased cell tropism and zoonotic potential and transmissibility (122,141).

1.1.2.3 SARS-CoV-2 pathogenesis

SARS-CoV-2 infects nasal and bronchial epithelial cells, pneumocytes and pulmonary macrophages in the upper respiratory epithelia, tissues where ACE2 expression is high (144–146). Risk factors for developing severe symptoms of COVID-19 are underlying health conditions, age, male sex, obesity and ethnicity (Black and Asian people) (147). SARS-CoV-2, like the other respiratory coronaviruses, is primarily spread by respiratory droplets. After infection, the incubation time is around 4 – 5 days (148–150), and 97.5% of infected individuals who develop symptoms experience symptoms within 11.5 days (150). Viral load peaks at day 5 – 6 after the onset of symptoms. Severe COVID-19 patients who develop ARDS usually do so at approximately day 8 – 9 (112,151).

A local immunological response is triggered by SARS-CoV-2 infection and apoptosis of epithelial lung cells. Macrophages and monocytes are recruited and respond to the infection, by producing cytokines that stimulate the adaptive T- and B-cell immunological responses. In most cases, this process can eradicate the illness. However, in rare circumstances, the immune system malfunctions, resulting in severe lung and even systemic illness. A defective immune response or immune overreaction can trigger a cytokine storm that leads to extensive lung inflammation.

Patients with severe COVID-19 who require hospitalisation exhibit higher levels of IL-2, IL-7, IL-10, granulocyte colony-stimulating factor (G-CSF), interferon gamma inducible protein-10 (IP-10), monocyte chemoattractant protein-1 (MCP-1), macrophage inflammatory protein- 1 (MIP-1) and TNFα in their blood plasma, and IL-6 levels in these patients continue to rise over time (112). Non-survivors have higher levels of these cytokines than survivors (152). Patients with severe COVID-19 had an increase of $CD14^+$ and $CD16^+$ inflammatory monocytes, producing pro-inflammatory cytokines, in their peripheral blood compared to those with moderate disease (153). The mechanism of how SARS-CoV-2 activates and evades the innate immune response is complex and not yet fully understood (reviewed in (154,155)).

1.1.2.4 SARS-CoV-2 intervention

The development of approved vaccines happened at a remarkable speed, made possible by global scientific collaboration. Sixteen vaccines are currently approved in one or more countries, of which six are listed for emergency use by WHO (**Table 2**), with many more currently being assessed in clinical and pre-clinical trials. In April 2020, the WHO established criteria for potential vaccine candidates. These include a minimum of 50% effectiveness against severe illness and a favourable safety profile. Candidates from various platforms have fulfilled these requirements, including vaccines with effectiveness against severe illness estimated to be above 90% (156), with the majority of adverse effects being minor and ephemeral. The length of vaccine-induced protection is an essential scientific question that has yet to be resolved due to the recency of vaccination programs. Predictably, booster vaccinations may be

necessary if the antibody response is similar to that of individuals previously infected with SARS-CoV-1 and MERS, where immunity lasted 2 – 3 years (157).

Table 2: Currently approved COVID-19 vaccines.

	Platform	Name	Manufacturer	Reference
WHO's Emergency Use (stand 10/06/2021) (158)	Inactivated virus vaccine	BBIBP-CorV	Sinopharm and the Wuhan Institute of Biological Products	(159)
		CoronaVac	Sinovac Biotech	(160)
	RNA vaccines	mRNA-1273	Moderna in partnership with the National Institute of Allergies and Infectious Diseases (NIAID)	(161)
		BNT162b2	BioNTech and Pfizer	(162)
	Viral vector vaccine	ChadOx1 nCoV-19	AstraZeneca in partnership with the University of Oxford	(163)
		Ad26.COV2.S	Johnson & Johnson	(164)
Approved in at least one country	Inactivated virus vaccine	Covaxin (BBV152)	Bharat Biotech, ICMR; Ocugen, India	(165)
		WIBP-CorV	Wuhan Institute of Biological Products; China National Pharmaceutical Group (Sinopharm)	(166)
		CoviVac	Chumakov Federal Scientific Center for Research and Development of Immune and Biological Products, Russia	(167)
		QazVac	Research Institute for Biological Safety Problems, Kazakhstan	(168)
		SARS-CoV-2 vaccine (Vero cells)	Minhai Biotechnology Co.; Kangtai Biological Products Co. Ltd., China	(169)
		NVX-CoV-2373	Novavax, USA	(170)
	Protein vaccines	ZF2001	Anhui Zhifei Longcom in partnership with the Chinese Academy of Medical Sciences, China	(171)
	Peptide vaccine	EpiVacCorona	Federal Budgetary Research Institution State Research Center of Virology and Biotechnology, Russia	(172)
	Viral vector vaccine	Sputnik V	Gamaleya Research Institute, Russian	(173)
		Covishield	Serum Institute of India	(174)

Except for inactivated virus vaccines, the S protein, encoded either by deoxyribonucleic acid (DNA) within a viral vector or messenger RNA (mRNA), or synthesised as a recombinant, adjuvanted protein, has been the focus of most

vaccination efforts due to its immunodominance and essential function in cell entry (175). However, most likely, in the future vaccines targeting several antigens of SARS-CoV-2 ('multivalent vaccines'), are most likely to be developed, probably including the viral N protein, which has been shown to have a lower selection pressure than S (176).

While the vaccine roll-out is ongoing, concerns of vaccine-evading SARS-CoV-2 mutants are rising. Moreover, even after vaccination people can still get infected with SARS-CoV-2, but typically with a milder clinical course. Therefore, there is still an urgent need to find novel drugs that are active against SARS-CoV-2, which has been challenging.

So far, two drugs have been found to improve the outcome of severe COVID-19. In the RECOVERY trial, twelve drugs were tested or are currently in clinical trials (aspirin, azithromycin, colchicine, dexamethasone, hydroxychloroquine, tocilizumab and lopinavir-ritonavir, anakinra, dimethyl fumarate, infliximab), as well as convalescent plasma and synthetic neutralising antibodies (177). Only one of these was subsequently recommended for use; the corticosteroid dexamethasone, was approved in June 2020 due to its anti-inflammatory and immunosuppressive properties that resulted in lower 28-day mortality compared to patients receiving either oxygen or mechanical ventilation without dexamethasone (178). The second drug currently in use in early COVID-19 is remdesivir, which acts as a nucleoside analogue inhibiting RNA-dependent RNA polymerase (RdRp). It was approved for treatment of hospitalized patients above the age of 12, shortening the recovery time from 15 to 10

days (179). However, in the SOLIDARITY trial, only a limited effect was measurable in COVID-19 patients (180). Currently, there are 53 drugs in phase IV and 162 in phase III clinical trials (181).

1.2 Broad-spectrum antiviral drugs

The current pandemic caused by SARS-CoV-2 as well as past outbreaks, for example those caused by Ebola virus (EBOV) and Zika virus (ZIKAV) (182–184), have emphasised the urgent need for fast and effective universal anti-viral treatments, which currently do not exist. While vaccines are regarded as the gold standard in preventing viral spread and diseases, even if an effective vaccine can be developed, which is not always the case, this process can take many years. Developing vaccines for some viruses is especially challenging, for example, with dengue virus, the existence of several serotypes with the potential for vaccine-induced ADE makes vaccine development a rather difficult undertaking (185), whereas in the case of SARS-CoV-2, vaccines were created and approved within 12 months since the first patient was hospitalised in December 2019 (12/12/2019) (186). Thus, when a virus of pandemic potential first emerges, the availability of a general broad-spectrum antiviral could significantly limit, if not entirely prevent, viral spread.

Most available antiviral drugs are directed against specific viral proteins (so-called direct-acting antiviral drugs, DAAs), which historically most often target the viral proteases and polymerases, and to a lesser extent other virus encoded proteins. An example is antiviral drugs for the human immunodeficiency virus (HIV), which target the HIV specific reverse transcriptase, integrase, protease and glycoprotein 41 (gp41)

fusion (187); or antivirals against influenza targeting the neuraminidase and endonuclease proteins (188,189). DAAs in some cases can be broad-targeting to some degree, the approved drug favipiravir inhibits the RdRp of influenza and also shows some efficacy against the polymerases of Lassa fever virus and EBOV (190,191).

In contrast to DAAs, some host-targeted antivirals (HTA) offer unique opportunities to treat viral infections. HTAs could target entry receptors important for specific viruses, like maraviroc which targets the HIV co-receptor CCR5 (192). HTAs can also target host cellular processes used by viruses, e.g. glycosylation pathways, cholesterol synthesis pathways, or cyclophilin and other proteins (reviewed in (193)). A third group of drugs are immunomodulatory compounds affecting the response of the host to the virus, as in some cases it is not the virus that leads to the death of the host but the inappropriate and overzealous reaction of the immune system to the virus (as can be the case in severe dengue and severe COVID-19), which such immunomodulators attempt to ameliorate. To date, only a few HTA or immunomodulatory drugs are approved, for example maraviroc (192), ribavirin, a guanosine analogue used against HCV (194), or immunomodulatory drugs like interferons approved for HCV and HBV (195,196), and dexamethasone against SARS-CoV-2.

In order to respond quickly during the emergence of viral outbreaks, especially when detailed knowledge of the virus is limited and there is no time to develop a DAA, targeting a host cellular process that many viruses depend on is arguably the most efficient strategy. Another advantage of HTAs is their much higher barrier for viral escape mutants, compared to DAAs, as seen for viruses like HCV and HIV (197,198).

One common host cell pathway hijacked by many enveloped viruses is the N-glycoprotein folding pathway, which aids in the folding and maturation of viral glycoproteins. Inhibitors of ER alpha-glucosidases I and II (αGluI and αGluII), such as iminosugars, are antiviral against many viruses (199–203). In addition to their effects on viral glycoprotein folding, they were recently shown to also have immunomodulatory effects (204).

This thesis focuses on the N-glycoprotein glycosylation pathway and its potential exploitation for the development of HTAs. This also involves determining the glycan signatures of viral proteins that shed light on their biosynthetic pathway, including intracellular localisation, their overall architecture and stability. In this regard, it is vital to discuss the details of the host glycosylation process.

1.3 Host glycosylation pathway

Glycosylation is the most common co- and post-translational modification of proteins (205). Protein glycosylation, or the addition of carbohydrate moieties to proteins, plays a crucial role in glycoprotein folding, structure, trafficking, localisation and stability (206). Additionally, glycans can interact with proteins and increase protein solubility and bind hydrophobic residues (207). Glycosylation is estimated to occur in more than half of all eukaryotic proteins (208). In eukaryotic cells, three major types of glycosylation are present: N-linked and O-linked glycosylation, and glycosylphosphatidylinositol (GPI)-anchors. GPI is a complex glycolipid that is transferred to the C-terminus of certain proteins, where it acts as a lipid membrane

anchor as reviewed in (209). The two other glycosylation pathways are relevant to this thesis and described further below.

Glycosylation is not just important for eukaryotic host proteins. Many enveloped viruses have evolved to hijack the host cell glycosylation pathway in order to fold their own proteins correctly and coat many of their proteins with glycans that contribute to viral pathogenesis and immune escape. Glycans on pathogens help evade immune detection by shedding fusion proteins and/or by secreting viral glycoproteins that function as decoys (as is the case for EBOV) (210,211). Viral glycan shields function by glycan mimicry, where the glycans effectively shield the virus from the host immune response as the host-derived glycans are immunologically 'self'. Glycans are also used to help the attachment of viruses to cells and increase uptake by immune cells (e.g. alphaviruses) (212).

On the other side of this arms-race with the immune system, glycans can positively influence the host response to viruses. This includes soluble innate immune lectins that act as scavengers capable of recognising under-processed glycans, which are common for viral proteins but unusual for mature host cell glycoproteins (213,214). The innate immune system uses a range of lectins that have varied glycan specificity to collectively recognise pathogenic carbohydrate epitopes as pathogen-associated molecular patterns (PAMPs) that are present among viruses. Additionally, viral glycan shields are commonly incorporated as part of neutralising antibody binding epitopes, as well as underlying viral peptides, as part of the humoral immune response. Some

neutralising antibodies, such as the HIV-targeting 2G12 IgG, target viral glycans entirely (215).

1.3.1 N-linked glycosylation

The folding of nascent glycoproteins is assisted by many enzymes and chaperones, ensuring the secretion of correctly folded and fully functional glycoproteins. Failure of this process can lead to a variety of diseases (e.g. cystic fibrosis). Hence the cell has evolved a series of ER quality control (ERQC) checkpoints that closely monitor the folding of a glycoprotein and, if necessary, direct misfolded proteins toward ER-associated degradation (ERAD) (216).

The first step in N-linked glycoprotein biosynthesis is the co-translational *en bloc* attachment of an N-linked glycan precursor to nascent secretory proteins that emanate from the SEC61 translocon into the ER lumen (29). N-glycan precursor synthesis begins on the cytoplasmic side of the ER membrane, where nascent N-glycans are conjugated to a dolichol-pyrophosphate (Dol-PP) lipid anchor, known as the lipid-linked oligosaccharide (LLO) precursor. The lipid anchored glycan is modified with sequential addition of N-acetylglucosamine (GlcNAc) and mannose (Man) monosaccharides to generate a Dol-PP-$GlcNAc_2Man_5$ structure on the cytoplasmic side of the ER. This structure is then flipped into the luminal side of the ER membrane, where it is further modified step-wise to a final Dol-PP-$GlcNAc_2Man_9Glc_3$ structure (**Figure 4**) (217). This precursor glycan is then transferred by the oligosaccharyltransferase (OST) to an asparagine residue (N) of a polypeptide within

a sequence motif of N-X-S/T (serine / threonine), wherein X can be any amino acid except proline (218).

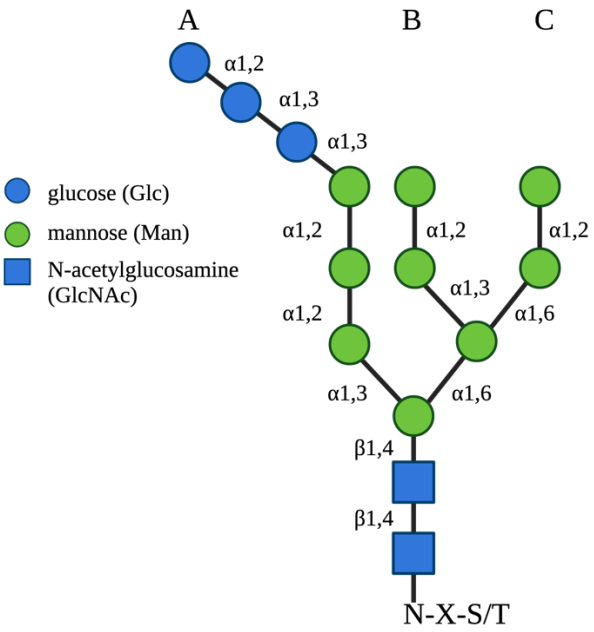

Figure 4: Schematic of the asparagine (N)-linked oligosaccharide precursor $Glc_3Man_9GlcNAc_2$ (glucose, blue circle; mannose, green; N-acetylglucosamine, blue square). A, B, and C are the branches of the N-glycan structure. N, asparagine; S, serine, T; threonine, X ≠ proline.

This is followed by glycan processing enzymes that trim specific monosaccharide residues followed by extensions of N-glycans, resulting in a complex array of glycan structures, which are defined in three structural categories: oligomannose, hybrid, and complex-type (219). In the ER, N-glycans attached to protein mediate their participation in the calnexin/calreticulin cycle (CNX/CRT), which forms part of the ERQC.

1.3.1.1 The calnexin cycle and ERAD

After entering the ER and attachment of the precursor glycan, the first enzyme that acts on an attached N-glycan is the ER αGluI, which removes the terminal α(1,2)-conjugated glucose from the glycan (220) (

Figure 5). This leads to a $Glc_2Man_9GlcNAc_2$ species, which can interact with malectin. Malectin is the latest protein to be discovered in the ERQC pathway, and was found by sequence homology analysis of carbohydrate-binding enzymes (221). It is postulated to be the first misfolding sensor for glycoproteins (222,223), but little is known about a potential so-called malectin cycle. ER αGluII catalyses the cleavage of the middle α(1,3)-linked glucose residue, which gives rise to monoglucosylated substrates for entry into the CNX/CRT cycle (217). CRT is a membrane bound homologue of the soluble CNX (224,225). Both chaperones can bind the monoglucosylated oligosaccharide intermediate $Glc_1Man_9GlcNAc_2$ and coordinate the glycoprotein's interaction with various protein disulfide isomerase (PDIs) and foldases to sample the protein folding landscape. Eventually, αGluII removes the last α(1,3)-linked glucose residue irrespective of whether the protein is folded correctly or not (224). If the protein has achieved its native form, it travels to the Golgi apparatus where the glycans are processed further (described in 1.3.1.2). However, if the protein is misfolded, it will be recognised and reglucosylated by UDP-glucose:glycoprotein glucosyl transferase 1 (UGGT1), making it a substrate for another cycle with CNX/CRT (226).

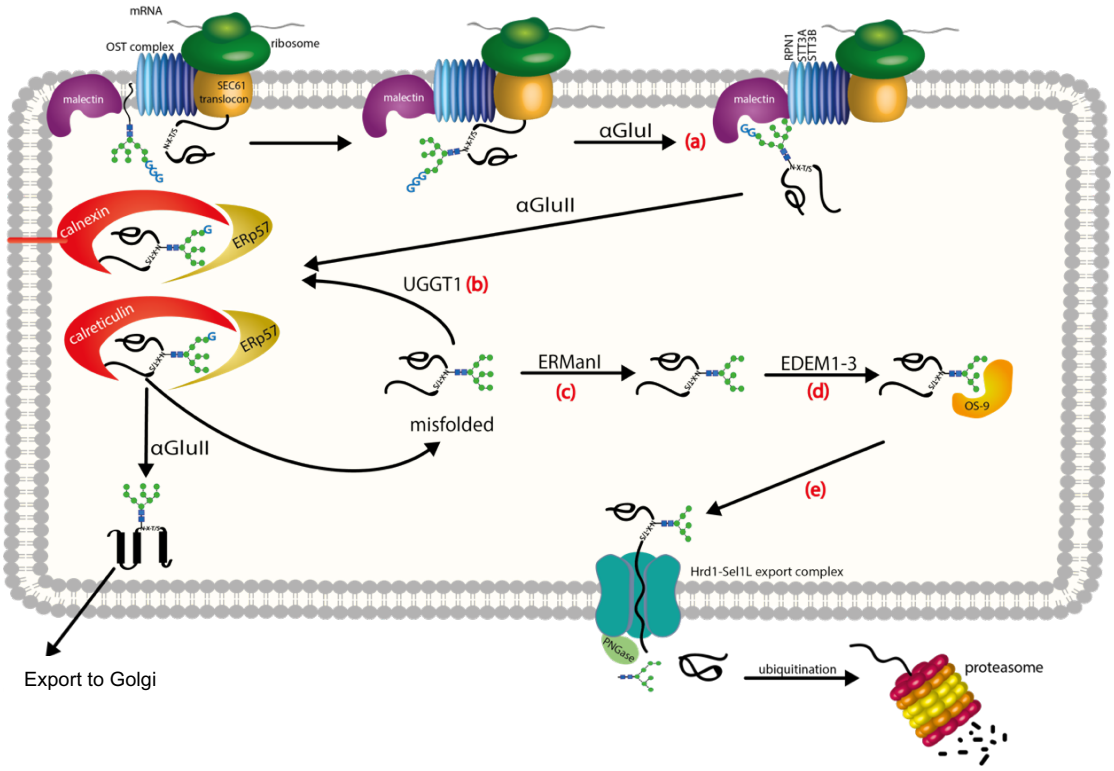

Figure 5: N-glycosylation and the ERQC checkpoints. The nascent polypeptide enters the ER through the SEC61 pore. Simultaneously, a $Glc_3Man_9GlcNAc_2$-glycan is added to an asparagine residue on the nascent polypeptide, catalysed by the oligosaccharyltransferase (OST) complex. Cleavage of the first terminal glucose residue by ER α-glucosidase I (αGluI) leads to a diglucosylated form which can bind to malectin (a), a purported ERQC checkpoint, before the N-glycan is further trimmed by α-glucosidase II (αGluII) to interact with calnexin/calreticulin and the co-chaperone ERp57. Repeated cycling can occur before correctly folded proteins are exported to the Golgi for further processing. Misfolded proteins are either (b) reglucosylated by (UDP)-glucose:glycoprotein-glucosyltransferase 1 (UGGT1) or (c) persistently misfolded glycoproteins are degraded via the ER associated degradation (ERAD) pathway by ER α-mannosidase I (αManI), followed by ER degradation enhancing alpha-mannosidase like protein 1-3 (EDEM 1-3) (d) and osteosarcoma-9 protein (OS-9)/XTP3-B (e) mediated transfer to the HRD1 ubiquitination complex. Peptide:N-glycosidase (PNGase) cleaves the glycan from the protein and the protein gets degraded via the proteasome.

Terminally misfolded proteins will eventually have mannose residues removed, first from the B arm, followed by the C and then A-arm of the N-glycan, which tags them for degradation via the ERAD pathway (227). ER α-mannosidase I (αManI) removes the first mannose on the B branch of the glycan (228). For degradation, the protein

needs to remove further mannose residues using ER-degradation-enhancing mannosidase-like proteins (EDEM1, 2 and 3) to expose an α(1,6)-mannose which is recognised by osteosarcoma-9 protein (OS-9) which delivers the misfolded protein to the Sel1L-Hrd1 ERAD complex in preparation for transport to the cytosol (229). Several rounds of demannosylation by αManI (230), or mannosidases of the Golgi apparatus during ER to Golgi cycling remove the remaining mannoses (231). Removing the outer mannose on the A branch excludes the substrate from UGGT1-mediated reglucosylation and re-entry into the calnexin/calreticulin cycle, ending any further attempts at protein folding (224).

1.3.1.2 Further N-glycan processing

Glycan processing occurs in the *cis*-, *medial*- and *trans*-Golgi compartments. In these compartments, glycosyltransferases and glycosidases assemble various glycan structures in a series of steps influenced by substrate availability, enzyme activity, gene transcription levels, enzyme position within the organelles as well as the structure of the nascent glycoprotein. This leads to proteins with hybrid and complex glycans, with various compositions of galactose, fucose, mannose, N-acetylglucosamine or sialic acid among others(232).

The glycosylation processes in viral infections are not always linear, some viral particles bud off early during the glycosylation pathway, into the ER lumen, including DENV and HCV (73,233), whereas others bud into the ERGIC such as SARS-CoV-2, or into the late endosomal multivesicular bodies such as HBV (234), and still others bud from the plasma membrane, including HIV and IVA (235,236). Additionally,

many viral glycoproteins do not follow the classical secretion pathway, as SARS-CoV-2 get secreted via the lysosomes (237), and this is reflected in their attached N-glycans. A summary of the N-linked glycan processing is presented in **Figure 6A, B**.

1.3.2 O-linked glycosylation

O-linked glycans can be added to amino acids that have functional hydroxyl groups, commonly serine and threonine. The most prevalent O-linked glycans in mammals are GlcNAc and N-acetylgalactosamine (GalNAc) (238). The latter are known as mucin-type O-glycans and are briefly described here. Mucin-type O-glycan synthesis is initiated by over 20 polypeptide GalNAc transferases (238). Although they are generally promiscuous, the GalNAc transferases differ in their selectivity for amino acid motifs, which provides a level of control to how and where O-glycans are attached. Unlike N-glycans, O-glycans do not have a lipid-linked precursor. Rather their structures are derived by sequential action of various glycosyltransferase enzymes as a given protein travels through the *cis*-, *medial*-, and *trans*-Golgi compartments (238). Following the addition of GalNAc residues, the glycopeptide O-glycan chain is modified by specific glycosyltransferases that can add galactose (Gal), GlcNAc, sialic acid and fucose. **Figure 6A, C** summarises O-linked glycan structures and biosynthesis.

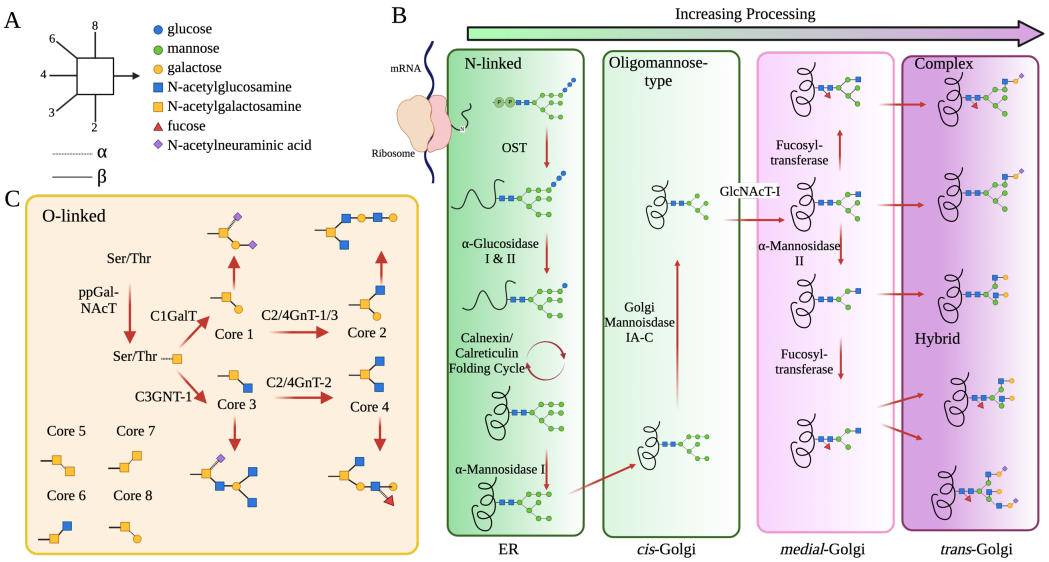

Figure 6: Mammalian N- and mucin-type O-linked glycosylation pathway. (A) Key to glycan nomenclature. (B) The OST co-translationally transfers the mature precursor glycan ($GlcNAc_2Man_9Glc_3$)-Dol-PP-glycan, to a polypeptide chain to the asparagine residue in an asparagine – X - serine/threonine sequon, where X cannot be proline. Glucosidases sequentially remove the three glucose residues and the protein folds with the aid of the CNX/CRT cycle. Several ER and Golgi mannosidases cleave mannose residues to provide $GlcNAc_2Man_5$ glycans. The GlcNAc transferase-I (GlcNAcT-1) initiates the first branch of the N-glycan. Once α-mannosidase II removes two more mannose residues, other glycan processing enzymes such as galactosyl-, fucosyl-, and sialyltransfersases can act on the glycan and build complex-type glycans. (C) A class of ppGalNAc transferases initiates mucin-type O-linked glycosylation pathways by covalently linking a N-acetylgalactosamine (GalNAc) monosaccharide to any serine and threonine. A succession of glycosyltransferases can then operate on the main GalNAc residue to form the eight typical O-linked glycan cores. Each of these eight cores may be expanded and processed further to produce a large number of O-linked glycans of the mucin type. C1GalT, core 1 glycoprotein-N-acetylgalactosamine 3-beta-galactosyltransferase 1; C3GNT-1, core 3 beta1,3-N-acetylglucosaminyltransferase; C2/4GnT, core2/4 beta1,6- N-acetylglucosaminyltransferase Image adapted from (366).

In general, secretory protein glycosylation occurs in two cellular locations: the ER and Golgi. Each site contributes differently to glycoconjugate biosynthesis and stages of glycoprotein production, maturation, localization, and secretion. N-glycosylation involves four key steps: formation of LLO precursor glycans ($Glc_3Man_9GlcNAc_2$) at the ER, transfer to nascent polypeptides in the ER lumen, trimming in the ERGIC and *cis*-Golgi by mannosidases, and extension in the *medial*- and *trans*-Golgi by glycosyltransferases. Three N-glycan structures exist (oligomannose, complex, and hybrid), defined by monosaccharide composition and glycan structure (217–219, 224–227, 232). Physical constraints of processing enzymes in the ER and Golgi primarily determine the N-glycan type found on proteins.

By contrast, protein O-glycosylation occurs entirely post-translationally on serine and threonine residues and does not entail a precursor oligosaccharide donor. The first step in O-glycan biosynthesis relies on the action of O-GalNAc transferases that add a single GalNAc residue. This monosaccharide can then be extended by various glycosyltransferases to produce one of eight possible O-glycan cores, four of which are commonly found in human cells (as described in 1.3.2). Like the steric hinderance described for N-glycan processing, O-glycosylation occupancy and extensions are driven by the tertiary and quaternary structure of a glycoprotein assembly. Additionally, glycoprotein dynamics and flexibility contribute to glycan processing, which is particularly relevant for viral spike glycoproteins as they are intrinsically metastable. This is confounded by an additional component, furin cleavage, that not only functions for normal protein processing but is also required for proteolytic cleavage and activation of several viral spike glycoproteins. Furin is a host protease

located in the *trans*-Golgi and cleaves spikes (e.g. of HIV, filoviruses and SARS-CoV-2) into two functional units. Furin can also be further transported to the cell surface and back via the endosomal pathway (239). Any changes to a protein structure or flexibility as a result of furin cleavage would be subject to N- and O-glycan processing that takes place in the *trans*-Golgi (240).

1.3.3 Iminosugars as antivirals

Iminosugars are monosaccharide mimetics in which the cyclic oxygen is replaced by a nitrogen atom (**Figure 7**) (241). Initially, iminosugars were isolated from natural sources like plants (242), and were shown to display antibacterial effects (243,244). The lead natural occurring iminosugars are the monocyclic 1-deoxynojirimycin (DNJ) and the bicyclic iminosugar castanospermine (CAST) (245). As monosaccharide mimetics, iminosugars can competitively inhibit numerous hydrolytic enzymes, such as glycosidases and glycosyltransferases (246,247), with potential therapeutic applications against various diseases (248).

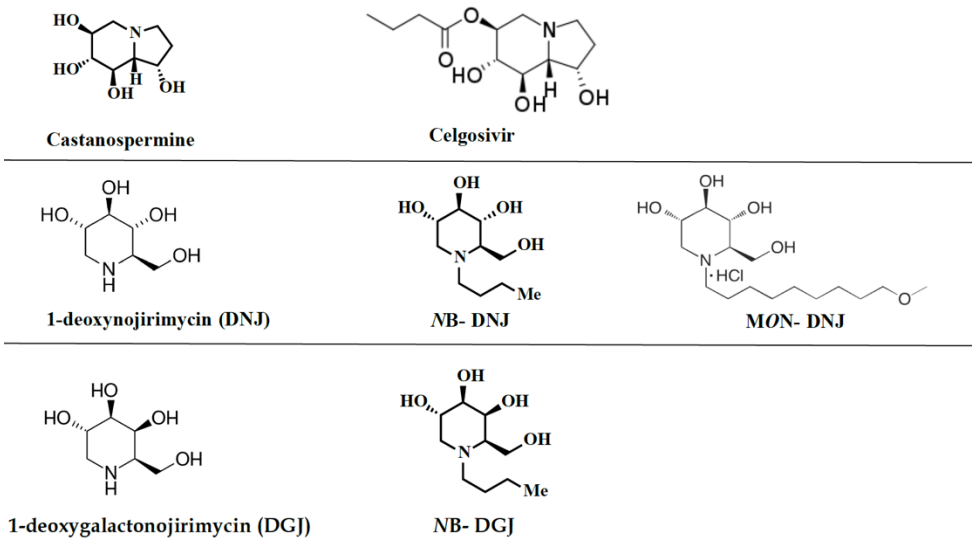

Figure 7: Iminosugar derivatives of castanospermine, DNJ and DGJ. This figure show celgosivir derived from castanospermine, *N*B-DNJ and M*O*N-DNJ derived from DNJ and the iminosugars with a galactose stereochemistry *N*B-DGJ (derived from deoxygalactonojirimycin, DGJ).

To date, two iminosugars have been approved as therapeutic agents: *N*-hydroxyethyl-DNJ (miglitol) for the treatment of Type 2 *diabetes mellitus* (249) and *N*-butyl-deoxynojirimycin (*N*B-DNJ, miglustat) for treatment of Gauchers' disease and Niemann-Pick C disease (250). In these diseases, the intended targets of the iminosugars are the intestinal alpha-glucosidases and ceramide-specific glucosyltransferases (247), respectively. However, due to their mimicry of monosaccharides, the selectivity of iminosugars is generally low, and when the intended targets are ER α-glucosidases, the on-target enzymes for the above diseases become unintended off-target enzymes when developing these iminosugars into antiviral drugs. This can lead to side effects such as osmotic diarrhoea (251). Another iminosugar group, one that mimic galactose (for example *N*B-DGJ), inhibits predominantly galactosidases and affects glycolipid metabolic processes (252).

As mentioned above, iminosugars can competitively inhibit ER αGluI and αGluII, impede the host glycoprotein folding machinery that is also used by many invading viruses. These effects can translate into broad-spectrum antiviral effects, as has been demonstrated *in vitro* and in small animal models. Antiviral effects are reported against a range of viruses including the flaviviruses DENV (253–255), JEV (253), WNV (255–257), Kunjin virus (258), Yellow fever virus (256,259), ZIKAV (259), HCV (260,261), the filoviruses EBOV (202,259,262,263) and Marburg virus (202), and also against HBV (264,265) and IVA (266). Proof of principle experiments with ER α-glucosidase knockout cells have shown that they do not support viral infection, measured by expression of viral proteins (267). Although these enzymes are also involved in the processing of host glycoproteins, there appears to be a more substantial reliance by particular viruses on these host processes compared to host proteins, resulting in a useful selectivity window for viral morphogenesis inhibition over host protein folding inhibition. Because the formation of infectious virion particles is thought to rely on the highly coordinated interaction of numerous copies of envelope glycoproteins, misfolding of a tiny proportion of viral glycoproteins might result in significant impairment in virion assembly and infectivity (268).

In general, derivates of primarily DNJ have been generated to minimise toxicity at submicromolar dose ranges required for antiviral efficacy (254,255,257,269,270). The extension of the four carbon alkyl chain of *N*B-DNJ led to N-(9'-methoxynonyl)-1-deoxynojirimycin (M*O*N-DNJ, also known as UV4B), which is a more potent binder of αGluII (271). M*O*N-DNJ is also antiviral against various other viruses *in vitro* and *in vivo,* including DENV, where treatment resulted in an increase in the survival of

DENV-infected mice (200,203,254,272). Through inhibition of the ER alpha-glucosidases, iminosugar treatment can diminish virion production and secretion while also reducing the specific infectivity of secreted virions for certain viruses. A decrease in specific infectivity has been shown for HIV-1 (273,274), cytomegalovirus (CMV) (275), and Kunjin virus (258), HBV (276). However, for IVA (266), DENV (199), as well as for HBV (276,277), the antiviral effect is predominantly due to inhibition of viral secretion.

Another mechanism of action for certain long alkyl chain iminosugars is known and involves the inhibition of the formation of pore complexes. The HCV viral protein p7 forms cation-conducting ion channels (278) that are required for viral infection (279,280). *N*-nonyl-DNJ (*N*N-DNJ), *N*-nonyl-DGJ (*N*N-DGJ), and *N*-7-oxanonyl-6-deoxy-DGJ reduce the activity of p7 ion channels, either by blocking the channel pore and/or by interrupting channel formation (261,281,282).

To date, clinical studies against various viruses have been performed using the iminosugar *N*B-DNJ against HIV (283), celgosivir (a prodrug of CAST) against HCV (284,285) and M*O*N-DNJ and celgosivir against DENV (286,287). In the clinical study against HIV, *N*B-DNJ had an antiviral effect apparently with minimal cytotoxicity (288) with side effects as gastrointestinal distress, elevated liver functions and leukopenia and neutropenia. However, safety concerns related to cataracts in rat toxicology studies (later shown to be transient and animal-specific), led to the termination of phase II clinical trial (289,290). In clinical trials against DENV celgosivir was safe and well-tolerated in phase 1b. However, there was no significant

difference in viraemia or fever compared to the placebo group (287). A close examination of the trial finds several shortcomings. The endpoints studied were related to viraemia and symptoms that occur in the febrile period. However, a characteristic of severe DENV is fluid leakage, which occurs after the febrile phase. The multiple ascending dose phase 1b clinical of M*O*N-DNJ to determine the safety profile and pharmacokinetics was initiated with five cohorts of healthy subjects, receiving drug doses from 30 mg, three times a day (TID) onwards (286). The study was terminated because it was determined that it was not commercially viable. The main adverse effect reported were haemorrhoids that occurred in a single patient (Dr Kelly Warfield, Emergent BioSolutions, personal communication).

Antiviral effects of iminosugars are not limited to the misfolding of viral proteins. Immune responses to viral infection can lead to pro-inflammatory cytokine release, including production of IFNα and IFNβ. For some viruses, like DENV, release of cytokines is correlated with the severity of the disease outcome (discussed in section 1.1.1.4). DNJ-derivates and celgosivir have been shown to dampen the cytokine and chemokine response *in vitro* and *in vivo*, an effect not detected in DGJ-derivate treatments (204,287,291). A reduction of cytokine release was measured with M*O*N-DNJ treatment not only in viral infections but in LPS-treated primary macrophages modelling bacterial sepsis (204), indicating a much broader clinical potential of iminosugars.

In clinical studies and *in vivo* work described so far, iminosugars were administered several times daily with the aim of maintaining drug serum concentrations above the

IC_{50} that had been determined previously in *in vitro* experiments. In such studies with this treatment approach, only αGluII and not αGluI was inhibited *in vivo*, as determined by analysing the levels of free oligosaccharides (FOS), discussed below.

1.3.4 Determination of ER alpha-glucosidase inhibition

Accumulation of triglucosylated N-glycans reflects αGluI inhibition; di- and monoglucosylated N-glycans accumulate due to αGluII inhibition. When proteins undergo ERAD, the cytosolic peptide:N-glycanase (PNGase) F releases the glycan from the protein by cleaving between the innermost GlcNAc residue and the protein's asparagine. The resulting FOS are rapidly further processed from $GlcNAc_2$ to $GlcNAc_1$ containing species by the cytosolic endo-β-Nacetylglucosaminidase (EnGNase), i.e. $GlcNAc_1$ containing species are derived from the cytosol (292). $GlcNAc_2$ containing species originate from the ER lumen as they have not been cleaved in the cytosol by EnGNAse; the glucosyl cap which remains as a result of glucosidase inhibition prevents them from leaving the ER lumen via the FOS transporter (293). The origin of these $GlcNAc_2$ containing FOS is proposed to be in the ER lumen by a mechanism involving another peptide:N-glycanase-like activity (294). Therefore, because of this biology, the FOS described can be used as biomarkers of αGluI/αGluII inhibition in cells or in organisms.

1.3.5 Alpha-glucosidase I as an antiviral target

Inherent mutations in the ER alpha-glucosidase enzymes can result in diverse clinical presentations. For example, mutation in the gene mannosyl-oligosaccharide

glucosidase (*MOGS*, the gene for αGluI) leads to a congenital disorder of glycosylation type IIb (CDG-IIb), which often leads to premature death (**Table 3).** Mutations in the glucosidase II alpha subunit (*GANAB*) or beta subunit Protein Kinase C Substrate 80K-H (*PRKCSH*, gene names for the αGluII alpha- and beta-subunit, respectively) can cause polycystic kidney disease (295). The ER alpha-glucosidases seem to be more important in early development compared to in adult life, which has also been shown in mice. Hence, despite the impact that mutations in these genes have on especially in developing organisms, targeting these enzymes in adult organisms for short-term therapy of acute illness offers therapeutic potential.

In 2014, Sadat *et al.* reported two siblings, 6 and 11 years old, with mutations in the *MOGS* gene, who, unlike previously described CDG-IIb patients, were alive but had significant neurological problems; however, no further information is available post 2014. The siblings had severe hypogammaglobulinemia, due to a change in the processing of N-linked glycans attached to Ig, which resulted in a shorter half-life of Ig molecules in circulation. Despite the hypogammaglobulinemia, there was no clinical indication of recurring infections in these patients. Patient-derived cells displayed a decreased susceptibility to infections with enveloped viruses, such as HIV and IAV H1N1, which heavily depend on the glycoprotein folding machinery, indicating that ER αGluI is important for the viral life cycle. Infecting these patient cells with non-enveloped viruses such as adenovirus, poliovirus 1, or vaccinia virus, which do not depend on N-glycosylation for entry or egress (296), was not affected by the *MOGS* mutation. Interestingly, even though the patient-derived cells of the two CDG-IIb patients are resistant to enveloped viral infection, the ERAD and unfolded

protein response (UPR, described in section 1.4) appear to occur at normal levels in their cells when stressed with tunicamycin, a potent inhibitor of LLO assembly and an UPR inducer, or when treated with MG-132, an ERAD inducer (296).

Table 3: List of known patients with mutations in the *MOGS* gene.

Patient	*MOGS* mutation	Immunology	Outcome	Reference
1	p.[Arg486Thr]; [Phe652Leu]; P[Thr802ILe]; [Arg535*]	IgA deficiency	Died (74 days)	(297)
2	p.[Gln124*]; [Ala22Glu]; [Arg100His]	IgG, IgA, IgM deficiency - decreases susceptibility to HIV and IAV H1N1	Alive (11 years)	(296)
3	p.[Gln124*]; [Ala22Glu]; [Arg100His]	IgG, IgA, IgM deficiency - decreases susceptibility to HIV and IAV H1N1	Alive (6 years)	(296)
4	P[Thr802Ile]; [Arg535*]	IgA, IgM deficiency	Died (4 months)	(298)
5	p.[Asp414Leufs*17]; p.[Gly182Arg]	ND	Died (9 months)	(299)
6	p.[Asp566Glu]	ND	Died (10 months)	(299)
7	p.[Arg495Ter]; p.[Gly752Asp]	IgA deficiency	Died (1 year)	(300)
8	p.[Arg4504His]	IgA, IgG, IgM deficiency	Alive (2 years)	(301)
9	p.[Gln50del]; p.[Arg495Ter]	IgA, IgG deficiency	Alive (13 years)	(302)
10	ND	IgA, IgG deficiency	Died	(302)
11	p.[Gln50del]; p.[Arg535Ter]	IgA, IgG deficiency	Died	(302)

The *MOGS* phenotype resembles that of iminosugar treated virally infected cells. In the more common low-dose iminosugar treatment regime, αGluII is usually reported

to be inhibited and not αGluI. It is known that although the *in vitro* efficacy of iminosugars is very similar against both isolated ER alpha-glucosidase enzymes, for unknown reasons a higher iminosugar concentration is required to affect αGluI *in vivo* compared to αGluII (303). However, αGluI inhibition can be achieved by using a higher iminosugar concentration. More commonly DENV- or IVA-infected mice were treated in a 'low-dose regimen' with 50 – 100 mg/kg M*O*N-DNJ twice per day (BID) or TID for 5 or 7 days, from 1 hour before infection up to 24 hours post infection (hpi), depending on the study, showing a life-saving effect up to of 90% with reduction in viral secretion and cytokine response (200,202,203,272). Remarkably, in an unusual 'high-dose regime', for IVA-infected mice (with IVA H1N1 and IVA H3N2) treated 8 – 24 hpi with a single and/or double dose of 250 – 1000 mg/kg M*O*N-DNJ an equivalent survival rate was observed compared to previous 'low-dose' treatment regimens (203). Similar results were observed in DENV-infected mice, when a double high dose of drug was administered at 48 and 64 hpi. In both, continuous low- and high-dose treatment regimens, reduction of pro-inflammatory cytokines, such as IFNγ, IL-6, IL-12, TNFα, IL-1b, IL-10, IL-17, and vascular endothelial growth factor (VEGF), was observed. Quantification of FOS levels showed that in the mock-infected mice treated with the single high M*O*N-DNJ dose, αGluI was inhibited in addition to αGluII, something that is not usually observed for the low-dose thrice daily treatment regime. Interestingly, the life-saving effect of the single high-dose administration outlasts the half-life of the compound in mice, ~5 hours (200); the presence of triglucosylated glycans was observed for at least 16 hours, when drug levels would have dropped below αGluI inhibitory levels.

Furthermore, the antiviral impact of inhibiting ER αGluI with a single high-dose, even when given days after infection, suggests that employing ER αGluI inhibitors as a strategy of managing viral infections, particularly those that represent a threat of fast worldwide spread, is beneficial (304). M*O*N-DNJ is safe in humans at doses up to at least 1 g (highest dose tested to date), which is in the predicted antiviral efficacy range (being only 2 – 5 times lower), based on a combination of animal efficacy data in lethal virus models, and exposure data from nonclinical safety analyses (200,202). Of note, this treatment regime was also tried for another flavivirus infection, ZIKV, but no life-saving effects with a single and/or double high-dose were achieved (Dr Kelly Warfield, Emergent BioSolutions, personal communication). In contrast to IVA and DENV infection, ZIKV infection does not initiate a cytokine storm (305), suggesting that the life-saving effect observed for DENV and IVA might be due to a combination of misfolding of viral glycoproteins and dampening of pro-inflammatory cytokines.

1.4 The unfolded protein response

Viruses use the host cellular machinery to produce their proteins (306). Infections can lead to changes in calcium homeostasis, cellular redox status, and nutrient starvation, all of which cause the accumulation of unfolded and/or misfolded proteins (307,308). When levels of proteins exceed the ER folding and clearing capacity and disturb the ER homeostasis, a cellular stress response known as ‘ER stress’ is triggered, which activates the UPR aimed to restore the ER homeostasis (309). This signal cascade is vital in viral and bacterial infections as well as in non-pathogenic disadvantageous circumstances (e.g. cancer). For viral infections it balances cell survival by virus

elimination (307) with inducing autophagy, apoptosis and activation of the innate immune system and pro-inflammatory responses (307,308).

The UPR consists of three arms: the double-stranded RNA (dsRNA)-activated protein kinase R (PKR)-like ER kinase (PERK; gene name: eukaryotic translation initiation factor 2-alpha kinase 3, *EIF2AK3*), inositol-requiring enzyme 1 (IRE1, gene name: ER-to-nucleus signaling 1, *ERN1*), and the activating transcription factor 6 (ATF6, gene name: *ATF6*) (**Figure 8**). All three proteins are located in the ER membrane. When the cell is not stressed, the proteins are inactive and bound to the folding chaperone immunoglobulin heavy chain binding protein (BiP or GRP78; gene name: *HSP5*). BiP belongs to the HSP70 chaperone family and is competitively sequestered by misfolded proteins in the ER and released from the UPR initiation proteins when ER stress occurs. IRE1 and PERK first homodimerize and then phosphorylate, resulting in downstream signalling cascade activation (307). Other possible activation mechanisms include IRE1 directly detecting misfolded proteins (310). For ATF6, it is hypothesised that BiP masks its Golgi-localisation signal. After BiP release, ATF6 interacts with coat protein II (COPII) and is transported to the Golgi (311).

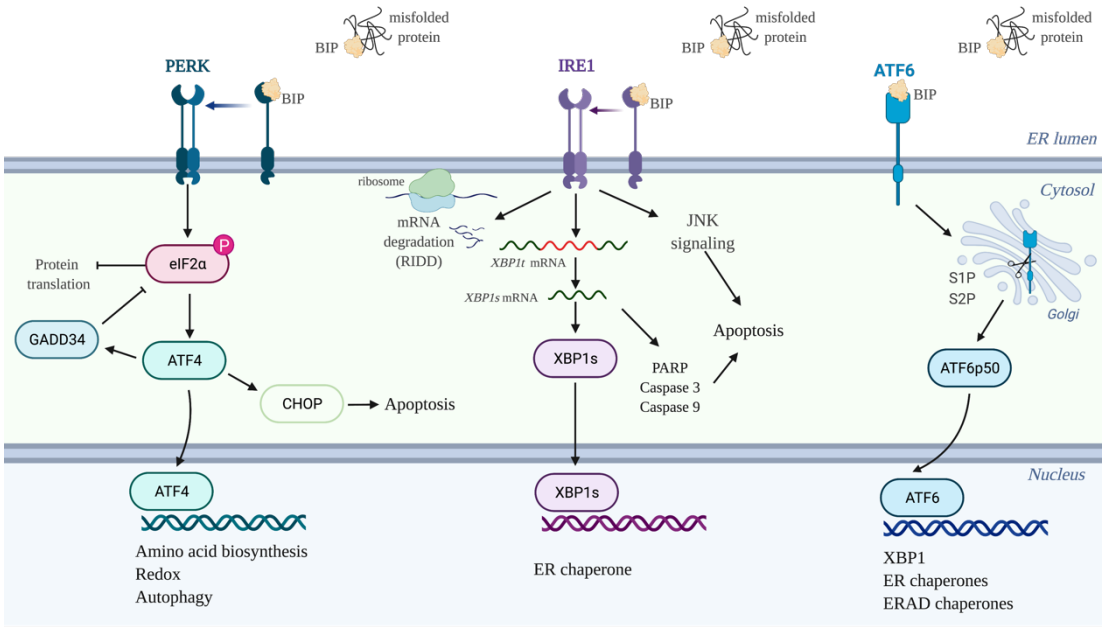

Figure 8: Activation of the main UPR pathways in ER stress response. PERK is maintained in an inactive state by binding to BiP. Once BiP dissociates, PERK dimerises and autophosphorylates to activate its kinase activity. Activated PERK catalyses phosphorylation of the eukaryotic translation initiation factor 2α (eIF2α) which stalls protein translation. The eIF2α induces activating transcription factor 4 (ATF4), which then induces activation of C/EBP homologous protein (CHOP) which mediates apoptosis. ATF4 also induces DNA damage inducible 34 (GADD34). GADD34 dephosphorylates eIF2α to maintain negative feedback. IRE1 is kept in an inactive state by BiP. Dissociation of BiP results in dimerization and trans-autophosphorylation (by the kinase domain) of IRE1, which activates the RNase domain. The IRE1 RNase segment cleaves X-box binding protein 1 (XBP1t) mRNA transcript of the multifunctional transcriptional factor, XBP1s. XBP1s activates ERAD associated genes to degrade misfolded proteins and genes promoting protein folding. IRE1 activates regulated Ire1-dependent decay (RIDD), the RNAse domain causes degradation of several mRNA and microRNA (e.g. mir17). IRE1 recruits TNF receptor associated factor 2 (TRAF2) and apoptosis signal-regulating kinase-1(ASK1) which activates c-Jun N-terminal kinases (JNK) to induce apoptosis. XBP1s activates caspase 3, 9 and poly(ADP-ribose) polymerase PARP to promote apoptosis if ER stress persists. ATF6 is maintained in an inactive state by BiP. Dissociation of BiP from ATF6 uncovers the Golgi localization signal, leading to cleavage of the N-terminus of ATF6 in the Golgi. ATF6 is there cleaved by site 1 and site 2 proteases (S1P and S2P). Cleaved and activated transcription factor ATF6p50 translocates to the nucleus to induce genes associated with ERAD and ER chaperones and XBP1.

PERK is the first UPR arm reacting to ER stress. After BiP dissociates, PERK homodimerizes and autophosphorylates. Then PERK phosphorylates the eukaryotic translation initiation factor 2 subunit-α (eIF2α). This results in a transient attenuation of global protein translation (312), a mechanism designed to decrease the misfolded protein load in the ER by preventing the synthesis of new proteins. At the same time, phosphorylated eIF2α initiates translation of the activated transcription factor 4 (ATF4) (312), a stress-inducible transcription factor that regulates redox homeostasis, amino acid metabolism, protein synthesis, apoptosis, and autophagy. ATF4 engages in a feedback loop to dephosphorylate eIF2α to restore protein synthesis by upregulation of the protein phosphatase 1 (PP1) regulatory component growth arrest and DNA damage-inducible protein GADD34 (313). ATF4 also activates the C/EBP homologous protein (CHOP, gene name: DNA Damage Inducible Transcript 3, *DDIT3*), which initiates apoptosis. The nuclear factor (erythroid-derived 2 factors)-related factor (Nrf2) is also phosphorylated by PERK, which allows it to translocate into the nucleus by dissociating it from the cytoskeletal anchor Kelch-like ECH-associated protein (KEAP1). To maintain redox homeostasis, Nrf2 activates genes that contain an antioxidant response element (ARE). Alternative routes of eIF2α activation include phosphorylation and activation by PKR, general control nonderepressible-2-kinase (GCN2), and heme-regulated eIF2 kinase (314).

Activation of IRE1, a type 1 ER transmembrane protein kinase/endoribonuclease, causes the X-box binding protein 1 (XBP1; gene name: *XBP1*) mRNA to be spliced (312,314,315), the regulated IRE1 dependent-decay pathway (RIDD) to be activated, and the ER membrane to expand (314). The RIDD can cleave a small set of mRNAs or precursor microRNA (miRNAs) targets, which leads to their degradation. RIDD

might reduce mRNA quantity and, as a result, protein folding burden in the ER (314). The cleaved XBP1 protein (XBP1s) is a transcription factor, which activates ERAD associated genes to degrade misfolded proteins and genes promoting protein folding (314). Apoptosis signal-regulating kinase-1 (ASK1) is recruited by IRE1, which phosphorylates the c-Jun N-terminal kinase (JNK) inducing apoptosis. XBP1s can also activate caspase 3, 9 and the poly(ADP-ribose) polymerase PARP to induce apoptosis (307,316–318).

During ER stress, full-length ATF6 (ATF6p90) travels from the ER to the Golgi apparatus, where it is cleaved by site-1 protease (S1P) and site-2 protease (S2P) to release the transcription factor ATF6p50 containing a basic leucine zipper domain (bZIP), which translocates to the nucleus and induces gene expression. ATF6p50 and XBP1s, independently and in an overlapping manner control transcription of genes encoding ER chaperones to relieve ER stress by enhancing expression of ERAD proteins (319). Furthermore, XBP1s and ATF6p50 stimulate ER and Golgi apparatus biogenesis to increase the secretory cell capacity during ER stress. Low levels of ER stress are thought to be addressed by the ATF6 cascade, while ATF6 and IRE1-XBP1 respond to medium to high levels of ER stress. Prolonged ER stress, on the other hand, activates cell death pathways (320).

The UPR is activated by various viruses, including DNA viruses such as adenovirus (321), CMV (322), herpes simplex virus (323), human papillomavirus (324), but also RNA viruses such as IVA (325), WNV (326), JEV (327) HCV (328), ZIKAV (329,330), and SARS-CoV-1 (331).

In this thesis, I focus on the activation of the UPR in DENV infection, and especially in the context of iminosugar treatment.

1.4.1 UPR in DENV infections

DENV infection is known to trigger the UPR. The virus takes advantage of this response as shown for immune cells like monocytes and macrophages (332,333) and various non-immune cell lines such as monocytic cell lines U937 and THP1 (332,334), human fibrosarcoma cell lines (318), HepG2 human hepatocyte cell line (335) and A549 human alveolar epithelial cell line (84).

While some studies indicate that DENV activates all three arms of the UPR pathway (84), others suggest that only the PERK and IRE1-XBP1 pathways are activated (316,336), or only activation of IRE1-XBP1 occurs (333). It seems the different UPR arms are activated in a time-dependent manner depending on how far along infection has progressed and is differently activated by specific DENV serotypes (84). Early in DENV infection, the PERK arm is activated, followed by IRE1-XBP1, and ATF6 activation at the late stage of infection (316).

In mouse embryonic fibroblast PERK knockout cells, increased DENV secretion was detected, indicating an antiviral role of this pathway (316). The activation of the PERK arm at 6 hpi in human fibrosarcoma cells results in eIF2α phosphorylation, which inhibits mRNA translation in an attempt to lower the ER protein load but was later reversed in order to keep viral protein synthesis ongoing (316). Pharmacological activation of the PERK pathway with *N*-(4-hydroxyphenyl) retinamide (4-HPR), a

nuclear transport inhibitor, was protective in a lethal DENV mice model (337), or inhibited GADD34-mediated dephosphorylation of eIF2α with the drug Salubrinal resulted in inhibition of DENV viral replication in A549 cells (84). Inhibition of the kinase activity of PERK in primary macrophages (with the inhibitor GSK2606414) did not change the secretion of infectious virions, suggesting no activation of the PERK pathway in DENV infection. However, inhibiting this pathway led to a decreased secretion of the cytokine TNFα (333). This also suggests the possibility of the PERK-Nrf2 activation leading to CLEC5α mediated TNFα secretion (338). DENV seems to control the PERK pathway to survive translation attenuation, and pharmacological stimulation of this mechanism leads to increased antiviral action.

DENV infection helps to reduce ER stress by activating the IRE1-XBP1 pathway and a subset of XBP1-activated genes (EDEM1, ER-localized DNAJ4 (ERdj4)) involved in ERAD (333,339). The IRE1-XBP1 pathway is induced by DENV ER anchored proteins (NS2A, NS2B, NS4B) and its glycoproteins prM, E and NS1. Furthermore, DENV inhibits apoptotic mediators downstream of IRE1-XBP1, resulting in improved cell survival and viral replication (316). In combination with DENV infection, small interfering RNA (siRNA) knockdown of XBP1 resulted in decreased ER growth, enhanced viral cytopathic effects, and elevated levels of the apoptotic marker pro-caspase 3 (339). Inhibition of IRE1 endonuclease activity with an inhibitor resulted in an antiviral effect, suggesting a pro-viral function for this pathway (333).

As discussed above, during DENV infection pro-inflammatory cytokines are released and can result in a cytokine storm. This overreaction correlates with the severity of the disease outcome (340,341). The UPR has a critical role in virus-induced inflammatory

signalling (308). The involvement of the UPR in DENV-mediated inflammation is as yet under-investigated, and general statements are difficult to make due the use of various cell systems and pathways investigated (reviewed in (342)). In DENV infection, the UPR interacts with the anti-inflammatory and pro-inflammatory pathways. Manipulation of the UPR pathways in DENV infection reveals that the UPR constituents can influence viral replication and immunopathology by suppressing and inducing innate immunological and inflammatory pathways. Further research into these interactions might aid the discovery of antiviral treatment targets and a better understanding of DENV pathogenesis.

1.4.2 Unfolded protein response in iminosugar treatment

Iminosugars that inhibit the ER αGluI and αGluII enzymes, which are important for glycoprotein folding, induce unfolded and misfolded proteins. It is no surprise that this leads to activation of the UPR (204,333,343). Celgosivir is antiviral in THP-1 cells against DENV and it modulates the UPR by increasing the expression of ERAD genes, however, protein levels were not evaluated in this study (343). Similarly, transcriptomic analysis of primary macrophages infected with DENV and treated with M*O*N-DNJ identified up-regulated host UPR genes (*XBP1, ATF4, ERN1, NFE2L2, ATF6*) after 6 and 24 hours of treatment (204). This is supported by *in vivo* data, in which peripheral blood mononuclear cells and liver tissue of DENV-infected M*O*N-DNJ treated mice showed a decrease in the full-length XBP1 transcripts (XBP1t) (204). However, this decrease was not detected with celgosivir-treated mice, suggesting a drug-dependent role (204). Also, treatment of naïve primary macrophages

with another iminosugar, N-8′-(2″-tetrahydrofuranyl)-octyl-deoxynojirimycin (2THO-DNJ), showed no activation of the PERK and IRE1-XBP1 pathway in non-infected primary macrophages. This suggests that 2THO-DNJ does not induce ER stress in basal state resting primary cells (333). These different findings of UPR activation in DENV infection and iminosugar treatments could have arisen from the use of different cell culture models, highlighting the necessity of employing appropriate cell lines to better understand and interpret the UPR. Furthermore, the neoplastic nature of cell lines increases the protein turnover and disrupts cell signalling pathways, thus masking virally generated effects.

The importance of the UPR and hence the in-depth discussion presented herein is based on my DPhil research aims and suggestion I put forward that the UPR is likely to play a crucial role in explaining results from my exploratory experiments. Based on literature and experiences in the laboratory, I concluded it was central to use a primary cell line to study the UPR effects. Furthermore, in order to disentangle the various arms of the UPR it was necessary to use specific inhibitory drugs. However, we have seen that these drugs are not sufficiently inhibitory, especially not against PERK or IRE1. Moreover, only limited work has been published about ATF6 in DENV infection. Therefore, I started to create clustered regularly interspaced short palindromic repeats and CRISPR-associated protein 9 (CRISPR Cas9) knockouts in human induced pluripotent stem cells (hiPSCs) of four UPR genes (*ATF6, EIF2AK3, ERN1, XBP1*).

Before COVID-19 forced us to stop laboratory work, I started to differentiate the hiPSC knockouts into macrophages to establish these cells for DENV infection and to perform experiments on DENV-infected knockout stem cell to evaluate the importance of each UPR arm. Nonetheless, the generation of these hiPSCs is significant in and of itself and will lay the foundation for extensive research with notable potential in the continued development of antivirals that target the UPR. Also, having to stop all non-COVID-19 related research did not halt my research activities as I pivoted my work towards characterisation of the glycan shield of SARS-CoV-2, which not only led to a comprehensive understanding of spike glycosylation but insights into novel DNA/RNA-based vaccine designs.

Chapter 2 Research aims

My research activities did not stop due to the mandated shut down of non-COVID-19 related research, as I adapted my work to focus on SARS-CoV-2 with several research objectives listed here:

1. Vaccine development against SARS-CoV-2 is focused on the trimeric S fusion protein, which contains 66 N-glycosylation sites. How is the S protein glycosylated? The presence or absence of glycans and their site-specific structures is incredibly important as it can affect important viral characteristics, including the ability to evade immune detection or even recognition. Understanding the glycosylation signature of virus derived wildtype S protein could aid in vaccine design that is aimed at mimicking the glycosylation of the viral wildtype S protein. Therefore, I sought to characterise the glycosylation signatures of virus-derived spike expressed in human lung epithelial cells and compare it to a stabilised prefusion trimeric S, a monomeric S1 and to an antigen of a non-stabilised vaccine candidate. Such a comparative study was the first of its kind and has implications for vaccine design in general, beyond its importance for SARS-CoV-2 (Chapter 4).

2. The Zitzmann laboratory helped to set up the COVID-19 core facility at the Sir William Dunn School of Pathology, Oxford University in the beginning of the pandemic. Initially we set up and optimised a medium-throughput antiviral cellular screening assay for SARS-CoV-2 inhibitors with the objective to help

in prioritising and deprioritising Food and Drug Administration (FDA)-approved compounds for clinicians, contribute to the global anti-COVID-19 effort called the "Moonshot project" which works towards a SARS-CoV-2 Mpro inhibitor, and thirdly screen compounds with credible mechanism of actions (MOAs) against SARS-CoV-2 (Chapter 5).

The COVID-19 pandemic emphasises the urgent need for broad-spectrum antivirals – drugs that are readily available early in a pandemic and before basic information of the emerging pathogen becomes available. The development of such host targeting broad-spectrum antivirals is at the core of many projects in our laboratory, which specialises in targeting the N-glycosylation and folding pathway of secreted glycoproteins. Before COVID-19 required me to suspend my original DPhil research projects, I endeavoured to explain a recent observation made in the group, namely that single high-doses of an iminosugar have surprisingly long-lasting antiviral and life-saving effects in IVA- or DENV-infected mice. If explained and found safe, such single high-dose treatment would be a paradigm shift for the treatment or postexposure prophylaxis of IVA and DENV infections in humans. I worked towards understanding the MOA of this treatment regime and pursued the following questions:

1. What is the MOA of short-term inhibition of αGluI and drug administration up to 48 hpi for DENV causing a long-lasting antiviral effect in lethal challenge mouse models? Can a similar antiviral effect by a single high-dose treatment be recapitulated in an *in vitro* cellular infection model, which would lend itself to mechanistic studies? For this, I first had to establish an *in vitro* cellular infection model (Chapter 6).

2. Can I unravel the potential MOA behind how the UPR contributes to the original observation? From previous work in the Zitzmann laboratory I knew that the UPR signature differs between cancerous cell lines (e.g. THP1-monocytic cells) and primary monocyte-derived macrophages, and work with primary cells would be preferred, as they are more physiologically relevant. However, in such cells any of the three UPR arms can only be partially inhibited using chemical inhibitors at non-toxic doses. Therefore, I started to develop CRISPR-Cas9 knockout cell lines in hiPSCs of the genes *EIF2AK3, XBP1, ATF6, ERN1* which can be differentiated into macrophages. To complete the set of different knockout cell lines, I worked to knockout the genes encoding for αGluI and αGluII (*MOGS, GANAB*), which should activate a constant UPR. All six genes were successfully knocked out before COVID-19 forced me to stop further experiments with these cells (Chapter 6).

3. As αGluI inhibition plays a crucial role in the observed antiviral effect, can we develop a specific inhibitor for αGluI? As glucose mimicking iminosugars have undesired off-targets and side effects, finding an αGluI specific inhibitor (not necessarily an active site inhibitor and ideally not a sugar mimic) is advantageous. Towards this goal, I initiated an X-ray crystallography study and further biophysical methods to screen drug libraries to identify additional molecules binding αGluI (Chapter 7).

Chapter 3 General Material and Methods

All buffer solutions were made up using ultrapure reagent-grade type 1 water from a MilliQ Academic apparatus (Millipore), unless for RNA or DNA purification, for which nuclease-free H_2O was used (Ambion). All 0.22 μm filtering of solutions was performed with Millipore Express PLUS 0.22 μm PES membranes (Millipore). All drugs for cellular assays were dissolved in suitable solvents, either ultrapure reagent-grade type 1 water (MilliQ) or dimethyl sulfoxide (DMSO, Merck), and sterilised using 0.22 μM centrifuge tube filters (Corning). All cells used were maintained mycoplasma negative and regularly tested with the EZ-PCR™ Mycoplasma Detection Kit (Biological Industries). Unless specified otherwise, all graphs were produced in Prism version 9 (GraphPad).

3.1 Cell culture

3.1.1 Mammalian cell lines

Mammalian cell lines used in this thesis include African green monkey (*Chlorocebus sabaeus*) Vero E6 cells (ATCC CRL-1586), Rhesus macaque (*Macaca mulatta*) kidney cells (Lilly Laboratories Cell-Monkey Kidney 2, LLC-MK2; a gift from Armed Forces Research Institute of Medical Sciences, Thailand [AFRIMS]), human lung cancer cell line Calu-3 (a gift from Dr Anderson Ryan, Department of Oncology, University of Oxford, as part of an ongoing collaboration), and human embryonic kidney suspension cells FreeStyle™ 293-F (HEK293F, Thermo Fisher Scientific).

Vero E6 cells were cultured in Dulbecco's Modified Eagle Medium (DMEM, Gibco) containing 4.5 g/L glucose and 2 mM L-glutamine supplemented with 10% heat inactivated fetal bovine serum (HI FBS, Gibco), 100 U/mL penicillin and 0.1 mg/mL streptomycin (MilliporeSigma) at 37°C and 5% CO_2. LLC-MK2 cells were maintained in Medium 199 (Gibco) supplemented with 10% HI FBS, 100 U/mL penicillin and 0.1 mg/mL streptomycin (MilliporeSigma) at 37°C and 5% CO_2. Calu-3 cells were grown in a 1:1 mixture of DMEM and Ham's F12-medium (Gibco) supplemented with 10% HI FBS, 1% non-essential amino acids (NEAA, Gibco), 1% sodium pyruvate (Gibco), 100 U/mL penicillin and 0.1 mg/mL streptomycin (MilliporeSigma) at 37°C and 5% CO_2. The HEK293F cell line was maintained in Freestyle expression media (Thermo Fisher Scientific) and incubated at 37°C, 8% CO_2 and 130 rpm.

To passage adherent cell lines (Vero E6, LLCMK$_2$ and Calu-3), media was aspirated, cells washed once with phosphate-buffer saline (PBS) and incubated with trypsin-ethylenediaminetetraacetic acid (EDTA, Gibco) at 37°C until cells were lifted. Trypsin-EDTA was diluted with corresponding medium and cells were spun down at 400 x *g*, 5 minutes, counted and freshly seeded. Cell lines were frozen by resuspending the cell pellet in freezing media (expansion media supplemented with 1% HI FBS and 1% DMSO) aliquoted in cryo vials and frozen in Nalgene® cryo 1°C freezing container (Thermo Fisher Scientific) at −80°C for 24 hours, for subsequent storage in liquid nitrogen.

3.1.2 Insect cell line

To grow DENV stocks the mosquito cell line *Aedes albopictus* C6/36 (a gift from US Armed Forces Research Institute of Medical Sciences, Thailand [AFRIMS]) was used. The cells were maintained in Leibnitz L15 medium (Gibco) supplemented with 10% HI FBS, 1% NEAA, 1 mM 4-(2-hydroxyethyl)-1-piperazineethanesulfonic acid (HEPES, Gibco), 100 U/mL penicillin and 0.1 mg/mL streptomycin at 28°C without CO_2. Cells were passaged by carefully scraping to dislodge cells and dispensing these into new flasks. Frozen cell stocks were prepared as described in section 3.1.1.

3.1.3 Human induced pluripotent stem cell derived cells

3.1.3.1 Ethics statement for use of stem cell line

The SFC841-03-02 iPSC line used in this thesis for creating CRISPR-Cas9 knockouts has been published previously (344). It was derived from dermal fibroblasts by using non-integrating Sendai reprogramming vectors (Cytotune, Life Technologies), from a healthy adult donor recruited through StemBANCC (345) / Oxford Parkinson's Disease Center: participants were recruited to this study having given signed informed consent, which included derivation of hiPSC lines from skin biopsies (Ethics Committee: National Health Service, Health Research Authority, NRES Committee South Central, Berkshire, UK [REC 10/H0505/71]). It is deposited in the European Bank for Induced Pluripotent Stem Cells, EBiSC (https://cells.ebisc.org/) and listed in hPSCreg (https://hpscreg.eu/) as STBCi044-B.

3.1.3.2 Human induced pluripotent stem cell cultivation

The hiPSC line SFC841-03-02 was cultured in feeder-free conditions. Culture dishes were coated with 1% Geltrex (Life Technologies) for 20 minutes at 37°C replaced with expansion media consisting of either mTeSR™1 supplemented with 1x supplement (Stem Cell Technologies) or OXE8 medium (346) advanced DMEM/F12 (Gibco) supplemented with 2mM GlutaMAX (Gibco), 100 ng/mL heparin solution (Gibco), 220 µM ascorbic acid-2 phosphate magnesium salt (Sigma-Aldrich), 100 ng/mL FGF-2 basic 145 aa (Bio-Techne) resuspended in 30% human serum albumin (Sigma-Aldrich) and 2 ng/mL TGF-beta (Peprotech) containing 10 µmol/L Rho-kinase inhibitor Y-27632 (Rock inhibitor, Abcam). Cells were thawed, diluted in PBS and centrifuged at 400 x *g* for 5 minutes. Cell pellet was resuspended in expansion media containing 10 µmol/L Rock inhibitor. Cells were incubated at 37°C, 5% CO_2. Media was exchanged every 24 hours using expansion media without Rock inhibitor.

Human iPSCs were passaged at a confluency of 80 – 90% using TrypLE Express (Gibco) for single-cell solution or in patches with 0.5 mM EDTA-PBS. Cells were washed with PBS and incubated with TrypLE Express or 0.5 mM EDTA-PBS for 5 minutes at 37°C and resuspended in expansion media with Rock inhibitor. Cells were kept at low passage number to reduce the likelihood of genetic change and frozen in single nucleotide polymorphism (SNP) quality-controlled batches from which the CRISPR-Cas9 knockouts were created.

The cells were frozen in freeze medium (Advanced DMEM/F12 supplemented with 10% DMSO, 30% embryonic stem cell FBS (Life Technologies)) at $2x10^6$ cells per

cryovial in Nalgene® cryo 1°C freezing container (Thermo Fisher Scientific) at –80°C and subsequently stored in liquid nitrogen.

3.1.3.3 HiPSCs macrophage differentiation via embryoid body formation

Differentiation of hiPSCs into macrophages was achieved by forming embryoid bodies (EB) using AggreWell™ 800 24-well plates (Stemcell Technologies) as described in Wilgenburg *et al.* (347). Briefly, hiPSCs were lifted with TrypLE as described in 3.1.3.2. AggreWell™ 800 wells were washed with 0.5 mL rinsing solution (Stemcell Technologies) by spinning the plate at 300 x *g* for 3 minutes. The rinsing solution was aspirated and replaced with 2 mL EB medium containing Rock inhibitor (OXE8 medium supplemented with 50 ng/mL human BMP4 recombinant protein (Gibco), 50 ng/µL human VEGF recombinant protein (Gibco) and 50 ng/mL human SCF (Miltenyi Biotec)) and $4x10^6$ hiPSCs were added per AggreWell™ 800. The plate was centrifuged at 300 x *g* for 3 minutes without brake. One well of a AggreWell™ 800 produces around 300 EBs. For three days the EBs were daily fed with EB medium. On day 4, EBs were transferred into two 175 cm^2 cell culture flask (Corning) with factory medium (XVIVO15 (Lonza) supplemented with 2mM GlutaMAX (Gibco), 0.5 mL 2-mercaptoethanol (1000x, Gibco), 100 ng/mL human M-CSF recombinant protein (Gibco) and 25 ng/mL human IL-3 recombinant protein (Gibco)). Factories were fed once a week by adding 10 – 15 mL factory medium. Around week 4 – 6 EBs started to produce macrophage precursors.

3.1.3.4 Terminal differentiation of macrophage precursors to macrophages

Harvested macrophage precursors as described in 3.1.3.3 were passed through a 40 µm cell strainer and subsequently spun at 400 x *g* for 5 minutes and resuspended in macrophage media (XVIVO15 (Lonza) supplemented with 2 mM GlutaMAX (Gibco), 0.5 mL 2-mercaptoethanol (1000x, Gibco), 100 ng/mL human M-CSF recombinant protein (Gibco)). Cells were seeded at $0.2x10^6$ cells per well in a 24-well plate in 0.5 mL medium with additionally 0.5 mL media added on day 4 until differentiation was achieved on day 7. For continuous experiments media changes were performed every 3 – 4 days.

3.2 Cytotoxicity assay

Cytotoxicity of compounds was assessed by measuring the mitochondrial metabolic activity using the CellTiter 96® AQueous One Solution Cell Proliferation Assay (Promega) as per the manufacturer's instructions. Briefly, 20 µL of the solution containing the tetrazolium compound (3-(4,5-dimethyl-2-yl)-5-(3-carboxymethoxyphenyl)-2-(4-sulfophenyl)-2H-tetrazolium; MTS) and the electron coupling reagent (phenazine ethosulfate) was added to seeded cells in a 96-well plate in 100 µL medium. Samples were incubated between 1 – 4 hours at 37°C, 5% CO_2 and absorbance were measured at 490 nm on the SpectraMax M5 microplate reader (Molecular Devices) or for measurements in the CL3 laboratory with the CLARIOstar microplate reader (BMG Labtech). Absorbance of blank readings was subtracted, and samples were normalised to untreated controls.

3.3 Gel electrophoresis

3.3.1 DNA gel

DNA agarose gels were prepared with 0.7 – 2% weight per volume (w/v) agarose (Sigma-Aldrich) in Tris acetate EDTA buffer (TAE; 0.4 M tris acetate pH 8.3, 0.01 M EDTA). GelRed nucleic acid gel stain (Biotium) was added to molten agar and poured into gel casts. PCR product samples were prepared with the addition of 6x loading dye (New England Biolabs) and loaded into the gel. Separation of samples was achieved using 150 V for 45 – 90 minutes. Gels were visualised under UV excitation. Product size was estimated using reference ladders, ranging from 50 bp to 1 kilobase (kb; New England Biolabs).

3.3.2 Sodium dodecyl sulphate polyacrylamide gel electrophoresis

Sodium dodecyl sulphate polyacrylamide gel electrophoresis (SDS-PAGE) was performed using NuPAGE (Life Technologies) 4 – 12% Bis-Tris gels in NuPage MOPS or MES buffer according to the manufacturer's protocol. Briefly, secreted proteins were directly mixed with 4x loading dye with or without NuPAGE reducing agent. Cell lysate samples were either lysed in 1% n-dodecyl-β-D-maltoside (DDM, Sigma-Aldrich) in PBS. Gels were run at 200 V for 35 – 50 minutes with Color Prestained Protein Standard (New England Biolabs) or for western blotting the Novex MagicMark XP (Thermo Fisher Scientific) was used to estimate protein size in samples. Gels were either stained directly in Instant Blue protein stain (Expedeon), SimplyBlue SafeStain (Thermo Fisher Scientific) or further processed for western blotting.

3.4 Protein detection by western blot

SDS-PAGE gels were transferred onto polyvinylidene difluoride (PVDF) membranes using the iBlot 2 Dry Blotting System (Thermo Fisher Scientific) following the manufacturer's protocol. The membrane was blocked in 5% w/v milk powder (Sigma-Aldrich) dissolved in Tris-buffered saline with 0.1% Tween 20 (TBS-T) for 1 hour at room temperature. Subsequently the membrane was washed with TBS-T and incubated with different antibodies (**Table 4**) diluted in 5% w/v bovine serum albumin (BSA, Sigma-Aldrich) for a further 1 hour at room temperature or at 4°C overnight. This was followed by washing the membrane with TBS-T three times for 10 minutes and incubation with the corresponding horse radish peroxidase (HRP)-conjugated secondary antibody diluted in TBS conjugated for 1 hour at room temperature. After the final washing of the membranes in TBS-T, Amersham ECL Prime Western Blotting Reagent (GE Life Sciences) was used to visualise the detected proteins by chemiluminescence using a Fuji LAS 1000 camera.

Table 4: List of antibodies used for western blots.

Target	Clone	Reactivity	Final concentration	Company
anti-S2 spike SARS-CoV-2	HL237	Rabbit	10 µg/mL	Genetex (#GTX635693)
anti-S1 spike SARS-CoV-2	CR3022	Human	20 µg/mL	In-house produced (gift Krammer Laboratory, Department of Microbiology, Icahn School of Medicine at Mount Sinai, New York)
anti-S2 spike SARS-CoV-2	1A9	Mouse	10 µg/mL	Genetex (#GTX632604)
anti-αGluI	C-11	Mouse	2 µg/mL	Insight Biotechnology Ltd (#sc-374006)
anti-6xHIS HRP	3D5	Mouse	1:2000	Thermo Fisher Scientific (#R93125)
anti-Human IgG, HRP-conjugated			1:5000	GE Healthcare (#NA933)
anti-Rabbit IgG, HRP-conjugated			1:5000	Promega (#W4011)
anti-Mouse IgG, HRP-conjugated			1:5000	Sigma Aldrich (#71045)

3.5 Protein production

3.5.1 Bacterial transformation

Competent cells (*E. coli* DH5α, produced in-house or Stellar™ Competent Cells (TaKaRa)) were incubated with the recombinant DNA for 30 minutes on ice, cells were heat-shocked at 42°C for 40 seconds followed by cooling on ice for 2 minutes. Super Optimal broth with catabolite repression (SOC; New England BioLabs) was added to the cells and left to incubate at 37°C for 1 hour with agitation. The cells were plated on agarose plates and incubated for 16 hours at 37°C under antibiotic selection (25 µg/mL carbenicillin; Sigma-Aldrich), and single colonies were picked for DNA sequencing (Source Biosciences). Competent cells carrying the correct protein constructs of interest were used to produce DNA for transfection with the Plasmid Maxi Kit (Qiagen) according to manufacturer's instructions. Purified DNA was used to transfect HEK293F cells.

3.5.2 Transfection for protein production

Transfection of all protein constructs (listed in **Table 5**) was carried out in HEK293F cells (Thermo Fisher Scientific) at a cell density of 1 – 1.2x10^6 cells/mL with the Freestyle™ MAX reagent (Thermo Fisher Scientific) and OptiPRO™ SFM (Gibco) according to the manufacturer's protocol. A total of 1 µg/mL plasmid DNA was used for transfection. For co-transfection of heavy- and light-chain for antibody expression (CR3022 and EY-2A) a molar ratio of 1:2, respectively, was used. Cells were incubated in polycarbonate vented Erlenmeyer flasks (Corning) with agitation at 130 rpm, 37°C, 5% CO2.

Table 5: List of protein constructs used in this thesis.

Construct	Vector	Source
Mm ER αGluI	popinGS	Alessandro T Caputo, Zitzmann laboratory
CR3022 heavy chain	pFUSEss-CHiGg-hG1	Florian Krammer, Department of Microbiology, Icahn School of Medicine at Mount Sinai, New York
CR3022 light chain	pFUSEss2-CLig-hK	
EY2A heavy chain	N/A	Arthur Huang (Taiwan) via Alain Townsed and Jack Tan (Weatherall Institute of Molecular Medicine, University of Oxford)
EY2A heavy chain	N/A	
Soluble SARS-CoV-2 $S_{recombinant\ trimer}$	pCAGGS	Florian Krammer, Department of Microbiology, Icahn School of Medicine at Mount Sinai, New York
Soluble SARS-CoV-2 $S1_{recombinant\ monomer}$	pHLsec	Mario Hensen, Zitzmann laboratory
$S_{vaccine\ antigen}$	pENTR4-LPTOS	Vector: Simon Draper, Jenner Institute, University of Oxford; full-length spike construct: Addgene #141382

3.6 Protein concentration measurements

Protein concentrations of samples for free oligosaccharide analyses were measured using the Bradford assay. To determine protein concentration for biophysical methods

the absorbance at 280 nm (A_{280}) on a NanoDrop 1000 (Thermo Fisher Scientific) was used.

3.6.1 Bradford assay

Quantification of protein concentration in cell lysates for FOS analyses was conducted by an adapted Bradford assay as described previously (348). Briefly, cell lysates were lysed in 1% Triton X-100 and diluted to 0.02% Triton X-100 in MilliQ water and mixed 1:50 with Quick Start™ Bradford Protein Assay (Bio-Rad) and incubated for 5 minutes at room temperature. Absorbances were measured at 595 nm over 450 nm to increase sensitivity and protein concentration was calculated against a serially diluted standard of BSA.

3.6.2 Protein concentration determination at A280

To measure protein concentrations of purified proteins, the absorbance at 280 nm (A_{280}) was measured using a NanoDrop® 1000 (Thermo Fisher Scientific). To determine the protein concentration in mg/mL the extinction coefficient (ε_{280}) and molecular weight (MW) of the protein, without consideration of additional glycans, was used (**Table 6**). Both parameters were calculated using ProtParam ExPASy (349).

Table 6: Molar absorption coefficients of purified proteins.

Protein construct	MW (g/mol)	ε (1/Mcm)
Mm αGluI	88011	167850
Antibody	150000	210000
$S_{recombinant\ trimer}$	142352	155450
$S1_{virus}$	77555	91900
$S1_{vaccine\ antigen}$ (monomer)	141000	147470
$S1_{recombinant\ monomer}$	81995	106005

Chapter 4 Glycosylation of the viral SARS-CoV-2 spike protein and quality control of a vaccine antigen

4.1 Introduction

Vaccines are urgently needed to contain the ongoing COVID-19 pandemic. According to the WHO, there are 96 vaccines in clinical development and 322 in pre-clinical development (as of 10th June 2021) (350). This effort is significant considering the short period of time between the discovery of SARS-CoV-2 and its pandemic status. Several vaccines based on new technologies have already been approved by the FDA and European Medicine Agency (EMA) and global vaccination efforts started in December 2020. These include the mRNA vaccines Pfizer BNT162b2 and Moderna mRNA-1273. Additionally, the AstraZeneca AZD1222 (ChAdOx1 nCoV-19) and Janssen JNJ-78436735 (Ad26.COV2.S) viral vector vaccines have been approved for widespread use. Other vaccines have been approved by organisations outside of the United State of America and European Union such as the Sputnik V and Convidicea, which are non-replicating viral vectors, the BBIBP-CorV and Covaxin as inactivated viruses, and the EpiVacCorona, which is a spike protein subunit vaccine. The main goal of these vaccines is to induce neutralising antibodies and T-cell responses against the spike protein, which protrudes from the viral surface. The S protein is a trimeric

class I fusion protein that undergoes major structural rearrangement from its metastable profusion conformation to its fusion-competent state upon interaction with the host cell receptor (351).

The S protein consists of an extracellular N-terminal domain (NTD), a transmembrane domain (TM) anchored in the viral outer-membrane lipid bilayer and a short intracellular C-terminal domain (352,353). The N-terminus consists of a signal peptide (SP), the S1 and S2 subunit that are separated by a furin-cleavage site. Furin cleavage is an important distinguishing factor between SARS-CoV-1 and SARS-CoV-2 (141). The RBD is located in the S1 subunit, whereas the FP, HR1, HR2, TM domain and cytoplasm domain comprise the S2 subunit (354). Viral entry depends on the S1 subunit. Specifically, the RBD within S1 binds the host cell surface receptor ACE2, which is abundant in lung, kidney, and intestinal tissues among others. The prefusion spike trimer is destabilised upon receptor binding, which results in shedding of the S1 subunit, and the S2 subunit transitioning to a stable post-fusion conformation (355). The RBD of S1 is dynamic and undergoes hinge-like conformational motions to target ACE2, temporarily hiding or exposing the determinants of receptor binding. These two states are known as the ‘down’ and the ‘up’ conformation. The ‘down’ conformation corresponds to the receptor-inaccessible state and ‘up’ refers to the more stable receptor-accessible state (356–358). The receptor binding sites are only accessible while one of the three RBDs adopt an ‘up’ conformation and therefore the spike structure can be present in the ‘RBD down’, ‘one-RBD up’ and ‘two-RBD up’ states at any given time (122,352,359). The RBD alternates between a ‘standing-up’ and a ‘lying-down’ posture for receptor binding and immune evasion (360,361).

Viruses use two major techniques to shield their conserved receptor binding domains or immunogenic protein backbone from host adaptive immune responses (362). The first strategy is conformational masking, in which viruses hide their RBDs in unusual places such as canyons (as in picornaviruses) (363) or hidden pockets (as in HIV) (364). The second method is glycan shielding, which occurs when viruses mask vital parts of their spike proteins behind host-derived 'self' glycan clusters that hide underlying immunogenic protein epitopes from antibody neutralisation (as in HIV, EBOV , HCV and other coronaviruses) (365,366).

Host-derived virus glycosylation plays a number of functions in viral pathobiology. In addition to immune evasion, it affects viral tropism and mediates viral protein folding and stabilisation (366). The S protein of SARS-CoV-2 displays 66 N-linked glycans on each trimeric spike surface and an undefined number of O-linked glycans (367). As membrane anchored trimers, S proteins migrate to the ERGIC, where they are incorporated into the membranes of viruses budding into the ERGIC lumen (138,139).

As viruses pass through the secretory pathway, their N-glycans are processed and modified by ER- and Golgi-resident glycosylation enzymes, and O-glycans are added to nascent glycoproteins in the Golgi, resulting in S trimers protruding from the viral surface. S trimers come into contact with the host protease furin inside the Golgi, which cleaves between S1 and S2 (141,368), leaving the subunits non-covalently assembled before the virus is secreted into the extracellular environment (140). Changes in the glycosylation pattern of secreted spike proteins can indicate changes in accessibility to the various enzymes of cellular glycosylation machinery (369,370).

These glycan signatures provide crucial information, such as the secreted protein's conformational and oligomerization condition. Understanding how SARS-CoV-2 takes advantage of glycosylation on native S proteins will assist in vaccine production (371). Glycans also serve as functional epitopes in immune recognition (372), which emphasises the importance of molecular mimicry between viruses and vaccines for priming of the immune system.

In this chapter, we performed quantitative and site-specific glycan analysis of the SARS-CoV-2 spike glycoprotein. We compared these data to recombinant forms of the trimeric spike, where the furin-cleavage site was abolished and a stabilising proline mutation in the S2 subunit was introduced (373), in order to keep the trimer in the prefusion state (352,356). Moreover, a mimicry of a viral vector-based vaccine was produced (ChAdOx1 nCoV-19, AZD1222) and the glycan content was compared.

4.2 Material and Methods

4.2.1 Propagation and lysis of SARS-CoV-2

The SARS-CoV-2 England/02/2020 strain (GISAID: EPI_ISL_407073) was provided at passage one from Public Health England, Collindale. SARS-CoV-2 was propagated by infecting Vero E6 cells at a multiplicity of infection (MOI) of 0.01 in DMEM (Gibco) with 2% HI FBS (Gibco) and harvested 72 hpi. Culture media was centrifuged at 3200 x *g* for 5 minutes, aliquoted and stored at –80˚C until further use. To obtain SARS-CoV-2 virions for endogenous spike glycoprotein purification, Calu-3 cells

were infected with SARS-CoV-2 in Calu-3 media containing 2% HI FBS at a MOI of 0.1. Cell culture supernatant was harvested 72 hpi and centrifuged at 3200 x *g* for 5 minutes. Virus-containing supernatant was concentrated one-log by using a 100 kilodalton (kDa) cut-off centrifugal filter (Amicon, Merck) with subsequent inactivation of virions with a final concentration of 1% Triton X-100 (Sigma-Aldrich) by incubation for 30 minutes at 4 ˚C.

4.2.2 Protein constructs

4.2.2.1 Recombinant SARS-CoV-2 Spike

The vector pCAGGS encoding for the SARS-CoV-2 spike glycoprotein construct ($S_{recombinant\ trimer}$) (374), missing the transmembrane domain (residues 1-1213, transmembrane domain residues 1214-1273; a gift from Florian Krammer, Department of Microbiology, Icahn School of Medicine at Mount Sinai, New York) was codon-optimised for mammalian cell expression. The polybasic furin-cleavage site (RRAR to A, residues 682-685) was mutated to alanine and the prefusion conformation stabilisation mutations K986P and V987P were introduced. The construct consists of an ampicillin resistance gene, an additional C-terminal thrombin cleavage site, a T4 fibritin trimerization domain and a hexahistidine tag. The construct was heat-shock transferred into *E. coli* DH5*α* competent cells (described in 3.5.1).

4.2.2.2 SARS-CoV-2 Spike S1

The $S1_{recombinant\ monomer}$ construct was prepared by Mario Hensen (Zitzmann laboratory). The vector pHLsec (AgeI/KpnI linearised; Addgene) encoding for SARS-CoV-2 spike glycoprotein residue 1-682 (GenBank isolate: MN908947) with an

additional hexahistidine tag was optimised for mammalian cell expression and subcloned using Gibson Assembly® Master Mix (New England BioLabs) according to the manufacturer's instructions. Recombinant product was used to heat-shock transform *E. coli* DH5α competent cells (described in 3.5.1).

4.2.2.3 Vaccine antigen SARS-CoV-2 Spike

The full-length SARS-CoV-2 spike glycoprotein from amino acid residues 2-1723 (Addgene #141382) was cloned into the pENTR4-LPTOS vector (a gift from Prof Simon Draper, Jenner Institute, University of Oxford), in frame with an N-terminal tissue plasminogen activator (tPA) secretion leader peptide using InFusion cloning (TaKaRa), cloning primers listed in **Appendix I, Table 33**.The plasmid also encodes a modified human cytomegalovirus major immediate early enhancer/promoter (IE CMV). The assembled product was heat-shock transformed into Stellar^{TM} Competent Cells (TaKaRa).

4.2.2.4 Spike purification from the pellet

Transfected cells (as described in section 3.5.2) were spun down at 1500 x *g* for 5 minutes. Pelleted cells were lysed in 20 mM HEPES pH 8.0, 500 mM NaCl, 10% glycerol, 10 mM imidazole and protease inhibitors (cOmplete^{TM} Mini EDTA-free Protease Inhibitor Cocktail, Sigma-Aldrich) and sonicated (5 seconds on / 10 seconds off; 60% amplitude for 5 minutes).

Lysed cells were ultracentrifuged at 45,000 rpm for 2 hours, supernatant discarded, and cell membranes lysed in lysis buffer containing 1% DDM. Samples were

homogenised using a Dounce homogeniser (Kimble Chase) and incubated for 1 hour with agitation at 4°C, followed by centrifugation at 40,000 rpm for 1 hour at 4°C. Supernatant was run through the CR3022 column (described in section 4.2.3.2).

4.2.3 Protein purification

4.2.3.1 Protein A purification of antibodies

The recombinant monoclonal antibodies CR3022 and EY2A (anti-Spike and anti-N, respectively) were transiently expressed in HEK293F cells (described in section 3.5.2). Seven days post transfection, cells were spun at 3000 x *g* for 20 minutes. Supernatants were harvested, sodium phosphate was added to a final concentration of 20 mM, pH 7.2 and the supernatants sterile filtered. Antibody supernatants were applied to a protein A-Sepharose Fast Flow column (GE Healthcare) equilibrated in 20 mM sodium phosphate, pH 7.2. Antibody was eluted with 100 mM citric acid (pH 3.5) and the pH of the eluate was adjusted immediately to 7.2 using 1M Tris-NaOH pH 10. Antibody was concentrated (100 kDa molecular weight cut-off (MWCO) centrifugal filter, GE Healthcare) and applied to a Superdex™ 200 pg 16/600 column (GE Healthcare) equilibrated in 1x PBS.

4.2.3.2 Affinity purification of S_{virus}, $S_{recombinant\ trimer}$, $S1_{recombinant\ monomer}$ and $S_{vaccine\ antigen}$

The CR3022 antibody was immobilised on cyanogen bromide activated Sepharose 4B resin (CNBr Activated Sepharose 4B, Cytvia) following the manufacturer's instructions (instructions: 71-7086-00 AF). The culture supernatant of SARS-CoV-2 infected Calu-3 cells was collected, spun at 3200 x *g* for 10 minutes and inactivated

with 0.5% Triton X-100 for 30 minutes at 4°C. The sample was step-diluted (1:1, 1:5, 1:10) with dilution buffer (**Table 7**) to reduce the Triton X-100 concentration to a critical micelle concentration (CMC) of ~0.02% and incubated for 30 minutes at 4°C between each step. Supernatant was loaded onto the CR3022-affinity column (~1 – 4 mL/ minute) and washed with 10 column volume (CV) of dilution buffer. Subsequently bound protein was eluted with 2 CV elution buffer and immediately buffer exchanged into protein buffer. Eluate was further concentrated using a 30 kDa MWCO centrifugal filter (GE Healthcare). The recombinant proteins ($S_{\text{recombinant trimer}}$, $S1_{\text{recombinant monomer}}$ and $S_{\text{vaccine antigen}}$) were purified in the same manner, though omitting the detergents throughout the purification process. Protein recovery yields and purity were calculated by densitometry measurements using Fuji ImageJ software. To calculate protein recovery yields western blots were performed before and after purification and densitometry of S1 or full-length S values were used to calculate the percentage of recovery. To determine protein purity, the entire gel lane and the specific visible bands were subjected to densitometry, and background values from an empty lane were subtracted and the percentage calculated.

Table 7: Buffer recipes used for CR3022-affinity purification.

Buffer	Recipe
Dilution buffer	20 mM Tris HCl, 500 mM NaCl, 0.03% DDM, pH 8
Elution buffer	3 M $MgCl_2$, 20 mM Tris HCl, 500 mM NaCl, 0.03% DDM, pH 8
Protein buffer	10 mM Tris HCl, 75 mM NaCl, pH 7.2

4.2.4 Detection of spike protein in transfected cells by flow cytometry

HEK293F cells were transfected with the protein constructs for $S_{recombinant\ trimer}$ and $S_{vaccine\ antigen}$ as described in section 3.5.2. Cells were harvested 48 hours post transfection (centrifugation at 400 x *g*, 5 minutes), cell pellets were washed with PBS and cells were stained using the LIVE-DEAD fixable near-IR dead cell stain kit (Life Technologies) for 20 minutes, followed by fixation of the cells in 2% paraformaldehyde (PFA; Electron Microscopy Sciences) for 10 minutes. Cells were blocked in blocking buffer (PBS with 0.5% w/v BSA, 5 mM EDTA, 5% HI goat serum and 5% HI normal human plasma) for 20 minutes and treated with 0.5% saponin (Sigma-Aldrich) for 30 minutes prior to staining with primary antibodies for 1 hour. Cells were washed thrice in washing buffer (PBS with 0.5% w/v BSA, 5 mM EDTA) and stained with the appropriate secondary antibody for 1 hour (**Table 8**). Flow cytometry acquisition was performed using an Attune NxT Flow Cytometer (Thermo Fisher Scientific) and gated on live cells. A minimum of 10,000 gated events were identified and results were analysed using the software tool FlowJo V10.

Table 8: Antibodies used for flow cytometry analysis.

Target	Clone	Reactivity	Final concentration	Company
anti-S1 spike SARS-CoV-2	CR3022	Human	20 µg/mL	In-house produced (Florian Krammer, Department of Microbiology, Icahn School of Medicine at Mount Sinai, New York)
anti-S2 spike SARS-CoV-2	1A9	Mouse	10 µg/mL	Genetex (#GTX632604)
anti-Human IgG, Alexa Fluor™ 488-conjugated			10 µg/mL	Thermo Fisher Scientific (#A-11013)
anti-Rabbit IgG, Alexa Fluor™ 488-conjugated			10 µg/mL	Thermo Fisher Scientific (#A-11008)

4.2.5 Glycomics

4.2.5.1 Fluorescent labelling of N-linked glycans

Glycans were enzymatically released from peptides from the in-gel trypsin digests using PNGase F (New England Biolabs). Released glycans were labelled with 2-aminoanthranilic acid (2-AA; Sigma-Aldrich as described previously (375). Briefly, samples were resuspended in 30 µL of water followed by addition of 80 µL of labelling mixture (30 mg/mL 2-AA and 45 mg/mL sodium cyanoborohydride (Sigma-Aldrich) in a solution of sodium acetate trihydrate [4% w/v] and boric acid [2% w/v] in methanol). Samples were then incubated at 80°C for 1 hour. Unconjugated 2-AA label was removed using Spe-ed Amide-2 cartridges (Applied Separation).

4.2.5.2 Glycosidase digestion of released glycans

Endoglycosidase H (Endo H, New England BioLabs) digestion was used for quantitation of oligomannose structures. Digestions were performed at 37°C for 16 hours, according to manufacturer's instructions. The digested glycans were purified using a PVDF protein-binding membrane plate (LudgerClean 96-well Post-Exolycosidase Clean-up plate) prior to hydrophilic interaction liquid chromatography-ultra performance liquid chromatography (HILIC-UHPLC) analysis. Data processing was performed using Empower 3 software. The percentage abundance of oligomannose-type glycans was calculated by integration of the relevant peak areas before and after Endo H digestion, following normalisation to PNGase F released glycans.

4.2.5.3 HILIC-UHPLC to measure PNGase F released glycans

Fluorescently labelled glycans were resolved by HILIC-UHPLC using a 2.1 mm × 10 mm Acquity BEH Amide Column (1.7 µm particle size, Waters, Elstree, UK). The mobile phase used was solvent A: 50 mM ammonium formate, pH 4.4, and solvent B: acetonitrile. The gradient used to separate fluorescently labelled glycans on the analytical column was: time = 0 minute (t = 0): 22.0% A, 78.0% B (flow rate of 0.5 mL/minute); t = 38.5: 44.1% A, 55.9% B (0.5 mL/minute); t = 39.5: 100% A, 0% B (0.25 mL/minute); t = 44.5: 100% A, 0% B (0.25 mL/minute); t = 46.5: 22.0% A, 78.0% B (0.5 mL/minute), t = 48: 22.0% A, 78.0% B (0.5 mL/minute). Fluorescence was measured using an Ex_{λ} = 360 nm and a Em_{λ} = 425 nm.

4.3 Results

4.3.1 Glycosylation of the SARS-CoV-2 spike protein

Glycosylation of a glycoprotein antigen can play a major role in vaccine design, as seen for other viruses such as HIV (372). Therefore, it is important to understand the glycosylation profiles of spike proteins produced by different vaccine candidates and compare these to the glycosylation of endogenous viral spike. Beginning with the SARS-CoV-2 virus (England/02/2020 strain), Calu-3 cells, which are a lung epithelial cell line, were infected and the virus-containing supernatant was harvested, concentrated via spin-concentrator, lysed and inactivated in 1% Triton X-100. The viral supernatant concentration did not affect the infectivity of the virus; a 10x concentration of the volume led to an increase of one-log in the viral concentration, whereas no virus was detected in the flow-through of the concentrator. Inactivated and

lysed samples were analysed via western blot probed with anti-S1 antibody (CR3022) and anti-S2 antibody that is specific to the C-terminal region to identify the abundance of spike protein in the harvested supernatant (**Figure 9**).

Moreover, shedding of S1 was observed (**Figure 9A**), which is a known decoy mechanism of viruses (210,372,376,377). Since there was no loss of viral infectivity when the viral supernatant was concentrated, the shedding of S1 was not based on the virus concentration. Detergent-solubilised spike was immune-purified using a CR3022 antibody column prepared in-house (**Figure 9B**). Purified spike protein was analysed on an SDS-PAGE, presenting three distinct bands (**Figure 9C**). Bottom-up mass spectrometry analysis confirmed that S1 ($S1_{virus}$) was purified with a recovery yield of ~83% (mass spectrometry (MS) coverage **Appendix I, Figure 53**), together with a small amount of S2 and BSA as a contaminant, most likely derived from the cell medium (calculated protein purity ~51% $S1_{virus}$, ~11% $S2_{virus}$ and ~29% BSA). Interestingly, the SARS-CoV-2 nucleoprotein and membrane protein was detected with low coverage (**Table 9**) in the mass spectrometry proteomics analysis. Western blot analysis of purified spike in denaturing non-reduced gels confirmed that S1 was purified, with a smaller band below of unknown identification. Additionally, S and S2 were detected, even though full-length S was not detected well with the CR3022 but with the C-terminal antibody. Since S1 and S2 are non-covalently associated (378) the full-length S is furin-uncleaved spike protein. However, the protein band intensities for full-length S and S2 were too low for identification by MS (**Figure 9D**).

There is a possibility that already shed S1 in the viral supernatant could have been co-purified in the concentrate as the MW of S1 with glycans is 105 kDa and a MWCO of 100 kDa was used for concentration. In this case, more S1 would be purified than full-length S. S1 and full-length S were able to bind to the CR3022-column. However, S2 was also detected in both unpurified and purified samples. It is plausible that by solubilising the virions S1 and S2 could be both incorporated into the detergent micelles which were then subsequently immunopurified for S1. Or if cleaved full-length S is bound to CR3022 high sheer forces due to high flow rate could break weak interactions between S1 and S2. To detect if shedding occurs post immunoprecipitation by binding to CR3022, flow-through and wash of the purification would need to be analysed by western blot analysis. However, at the time this work was performed we did not have access to any anti-S2 antibodies and therefore could not perform western blot analysis on these samples with an appropriate anti-S2 antibody at the time of its purification. Regrettably the flow-through and wash samples were not stored, and so if a suitable S2 antibody became available, this experiment would need to be repeated to perform this analysis. Though, purification of viral S with a CR3022 antibody column was achieved and identified via western blot and MS.

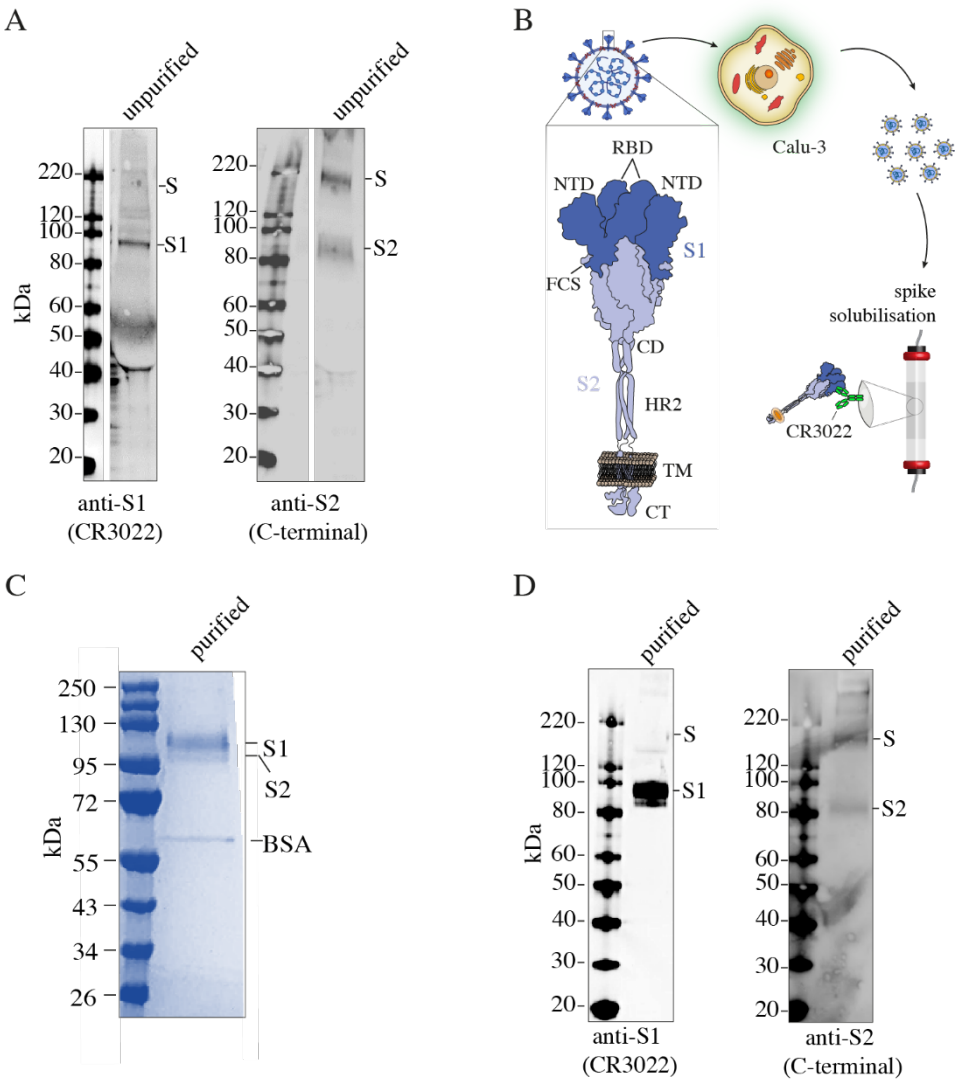

Figure 9: Purification of SARS-CoV-2 spike glycoprotein. (A) Western blot analysis of unpurified SARS-CoV-2 spike probed with anti-S1 (CR3022) and anti-S (C-terminal) antibodies, showing full-length S protein, S1 and S2 subunit. (B) Schematic representation of spike purification from SARS-CoV-2 infected Calu-3 cells by immunoaffinity purification using S1 targeting CR3022 antibodies. (C) SDS-PAGE of CR3022-purified spike protein showing the presence of S1 and S2 subunits of virus-derived spike and a contamination of BSA. (D) Western blot analysis of immunoaffinity-purified SARS-CoV-2 spike. Gels were run under denaturing non-reducing conditions.

Table 9: Mascot analysis of purified S_{virus}. Identification of SARS-CoV-2 spike, nucleoprotein and membrane protein in prepared sample from alpha lytic protease in-solution digestion.

Protein identified	Accession number	Mascot score	Mass	Sequence coverage
Spike glycoprotein SARS-CoV-2	P0DTC2	1206	141088	49%
Nucleoprotein SARS-CoV-2	P0DTC9	105	45598	31%
Membrane protein SARS-CoV-2	P0DTC5	48	25130	26%

To compare the glycosylation of endogenous spike to soluble stabilised spike trimers, which have been extensively studied through structural and biophysical approaches, we expressed and purified a recombinant soluble spike protein that carries mutations to abolish the furin-cleavage site plus two trimer-stabilising proline mutations (K986P, V987P) (356).

This recombinant soluble trimeric full-length form of S, $S_{recombinant\ trimer}$, was produced by transfection of HEK293F cells and purified with a CR3022 antibody column similar to the virion material (**Figure 10A**). Analysis of the protein by western blot confirmed the purification of full-length S with the anti-S1 (CR3022, **Figure 10B**) and the anti-S2 (C-terminal, **Figure 10C**) antibody. A protein recovery yields of ~91% in western blot with anti-S1 (CR3022) and protein purity of ~90% was calculated. Moreover, analysis of unreduced $S_{recombinant\ trimer}$ revealed polymerisation as detected with anti-S1 antibody.

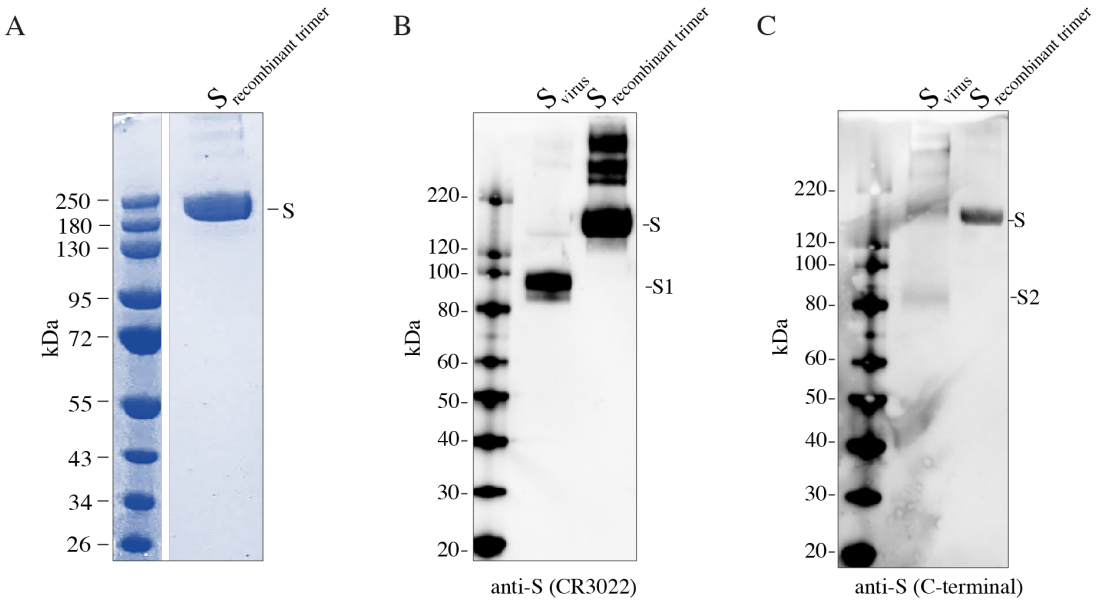

Figure 10: Purification of $S_{recombinant\ trimer}$. HEK293F cells were transfected to express $S_{recombinant\ trimer}$ for 4 days and purified by applying the supernatant to the immunoaffinity CR3022 column. (A) SDS-PAGE of $S_{recombinant\ trimer}$ after S1-immunity affinity purification. (B and C) Western blot analysis of purified S_{virus} and $S_{recombinant\ trimer}$ probed with anti-S1 (CR3022) anti-S (C-terminal), showing full-length S protein S, S1 subunit and S2 subunit. Gels were run under denaturing non-reducing conditions.

Quantitative N-glycan analysis was performed using UHPLC between the $S1_{virus}$ and $S_{recombinant\ trimer}$ glycoproteins (**Figure 11A, B**). Released N-glycans were further treated with Endo H to differentiate between oligomannose and complex glycans due to resistance of Endo H on complex glycans. UHPLC analysis of $S1_{virus}$ revealed a predominant population of complex-type N-glycans (79%) with 21% oligomannose and/or hybrid structures. Comparing these values to $S_{recombinant\ trimer}$, which also contains S2 N-glycans, due to the inactive furin-cleavage site, carries only 11% oligomannose/hybrid and 89% complex N-glycans. This difference points to variations in glycan biosynthesis, a mechanism that depends on high glycan density and local protein architecture, both of which can sterically inhibit glycan maturation. Changes in glycan maturation, namely an abundance of under-processed

oligomannose type N-glycans, can be a responsive reporter of native-like protein architecture (379), as well as an effective predictor for quality management and immunogen efficacy.

To identify where, and to what extent, the differences in glycan processing occur, we performed a quantitative site-specific N- and O-glycosylation analysis of $S1_{virus}$ and $S_{recombinant\ trimer}$ by glycoproteomics MS (**Figure 11C, D; Appendix I, Table 29-30**). The glycosylation profile of $S1_{virus}$ and the S1 domain of $S_{recombinant\ trimer}$ were comparable, with N61, N234 and N604 as predominantly occupied by oligomannose structures. The remaining sites on $S1_{virus}$ were either occupied almost entirely by tri-antennary complex-type N-glycans (N149 and N165) or by a mixture of tri-antennary complex plus oligomannose (namely $Man_5GlcNAc_2$, i.e. M5) structures. In comparison to a separate N-glycan study on virus-derived S, N61 contained mainly complex-type (with some oligomannose) glycans, N234 contained a mixture of oligomannose, hybrid, and complex structures, and N603 contained mostly complex-type glycans (380). No O-glycosylation was detected on T323/S325 for $S1_{virus}$ and $S_{recombinant\ trimer}$, an observation that is variably reported among recombinant S or S1 material (371,380–382). However, we found T678 to be unoccupied for $S_{recombinant\ trimer}$ but O-glycans were detected on $S1_{virus}$. This supports that S1 is more available to GalNAc transferases in the Golgi, and the viral spike could be present in a more open/flexible trimeric state than the recombinant one. The S2 domain of $S_{recombinant\ trimer}$ consisted of oligomannose/hybrid glycans on N709 with increasingly complex glycans to N1194.

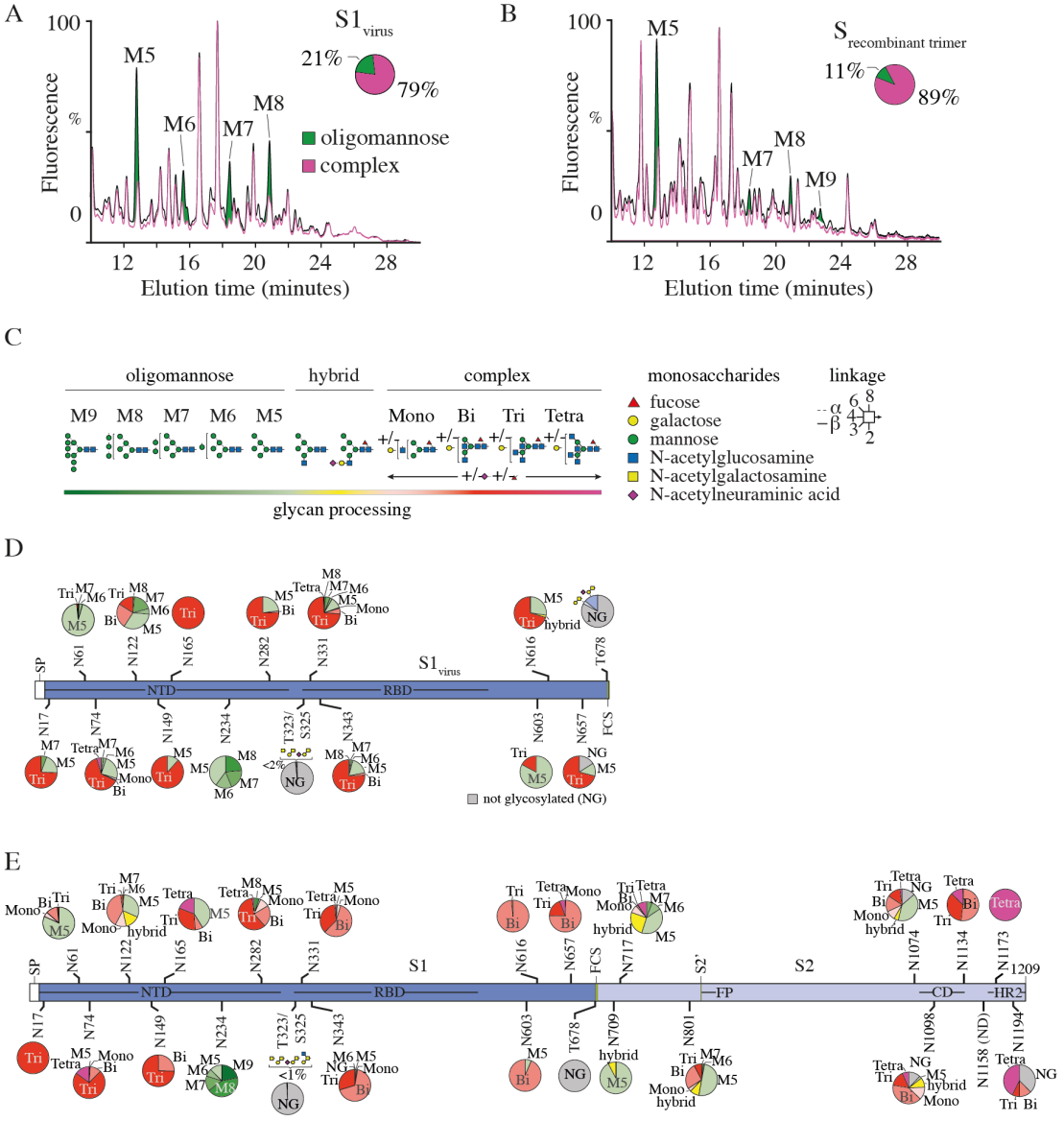

Figure 11: Glycan analysis of the viral and recombinant trimeric SARS-CoV-2 spike glycoprotein. (A and B) Quantitative UHPLC N-glycan analysis of purified viral and recombinant trimeric S showing the distribution of oligomannose and complex type-glycans on $S1_{virus}$ (A) and $S_{recombinant\ trimer}$ (B). (C) N-glycan maturation showing colour coding for degree of glycan processing from oligomannose in green to hybrid glycans in yellow to complex coloured in purple. (D and E) Quantitative site-specific N- and O-glycosylation by bottom-up glycoproteomics of $S1_{virus}$ (D) and $S_{recombinant\ trimer}$ (E), displaying pie charts summarising the quantification of the glycan content present at each glycan site. CD, connector domain, FCS, furin cleavage site; FP, fusion peptide; HR2, heptad repeat 2, NG, not glycosylated; RBD, receptor binding domain.

4.3.2 Glycosylation of the antigen of a vaccine candidate

To compare the site-specific S glycosylation in the context of vaccine design and antigen structure, an expression construct mimicking the ChAdOX1 nCoV-19 shuttle vector that produces the viral vector vaccine candidate was assembled in-house. This construct contains SARS-CoV-2 amino acids 2-1273, preceded by an N-terminal leader peptide of tPA and a modified human cytomegalovirus major immediate early promoter and was used for the recombinant expression for S protein containing the transmembrane domain ($S_{vaccine\ antigen}$). Glycan biosynthesis, a mechanism that depends on high glycan density and local protein architecture, can differ between membrane-bound ($S_{vaccine\ antigen}$) and soluble proteins ($S_{recombinant\ trimer}$), and both of which can sterically inhibit glycan maturation. Another factor that may contribute to the glycosylation difference is transit times through the organelles and the time the glycoprotein spends in the Golgi (383–385). Changes in glycan maturation, namely an abundance of under-processed oligomannose type N-glycans, can be a responsive reporter of native-like protein architecture (379), as well as an effective predictor for quality management and immunogen efficacy.

The difference between our construct, designed to mimic the ChadOx1 nCoV-19 vaccine, and the actual vaccine, is the use of the shuttle vector, with which the ChadOx1 nCoV-19 is produced, for transfection of HEK293F cells. Four days post transfection, the HEK293F cells were spun down, the supernatant was harvested and the pellet was lysed. Equal volumes of supernatant and lysed cells were loaded onto an SDS-PAGE and analysed by western blot probed against S1 and S2 with the same antibodies as those above (**Figure 12).**

In the supernatant, full-length S and S1 ($S_{vaccine\ antigen}$ and $S1_{vaccine\ antigen}$) were detected, indicating secretion of soluble S1, without S2. Detection of S, S1, or S2 in the cell pellet was not clearly possible due to unspecific binding of the probed antibodies to cellular proteins, but anti-S2 (HL237) detected S and S2, suggesting that S2 remained embedded in the cell membrane.

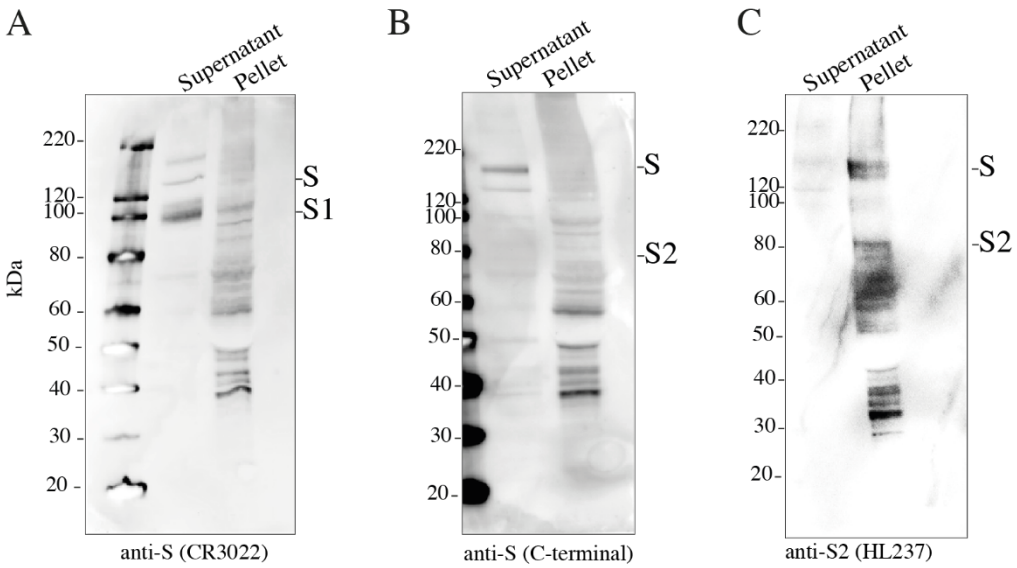

Figure 12: Western blot analysis of HEK293F cells transfected with $S_{vaccine\ antigen}$. HEK293F were transfected and grown for 4 days. Cells were spun down, and the cell pellet was lysed in 1% DDM. Equal volumes of supernatant and lysed cell pellet were applied to the SDS-PAGE and western blots were probed with (A) anti-S (CR3022), (B) anti-S (C-terminal) and (C) anti-S2 (HL237) showing full-length S, S1 and S2 subunits. Gels were run under denaturing, non-reducing conditions.

Using the same purification strategy as for the $S_{recombinant\ trimer}$, except for the use of detergent, it was observed that the majority of over-expressed protein was secreted into the supernatant as soluble S1 ($S1_{vaccine\ antigen}$) as detected by SDS-PAGE and western blot (**Figure 13A, B, C**). For $S1_{vaccine\ antigen}$ a protein recovery yield of ~88% in western blot probed with anti-S1 and protein purity of ~96% was calculated. MS was used to confirm the presence of S1 in the supernatant (MS sequence coverage

Appendix I, **Figure 54**). The secreted S1 (hereafter referred to as $S1_{vaccine\ antigen}$) was assessed by mass photometry, a single-molecule mass imaging technique, which confirmed that S1 was monomeric and not present as an aggregate. We benchmarked the analysis of $S1_{vaccine\ antigen}$ with mass photometry of the stabilised $S_{recombinant\ trimer}$ (**Figure 13D**).

Next, UHPLC, which is proficient in quantifying N-glycosylation, was used. Analysis of $S1_{vaccine\ antigen}$ glycans showed that 96% were complex-type glycan compared to 4% oligomannose-type (**Figure 13E**). Quantitative site-specific N- and O-glycosylation analysis by glycoproteomics confirmed that the overall N-glycan occupancy of $S1_{vaccine\ antigen}$ is comparable to $S1_{virus}$, except for N17, which was 46.6% non-glycosylated and N657, which had N-glycan populations that were more processed, suggested by the increase of complex glycosylation at N74, N122, N343, and N616. The oligomannose content at N61 and N603 was reduced from 98% and 83% on $S1_{virus}$ to 12% and 18% on $S1_{vaccine\ antigen}$, respectively (**Figure 13F; Appendix I, Table 31**).

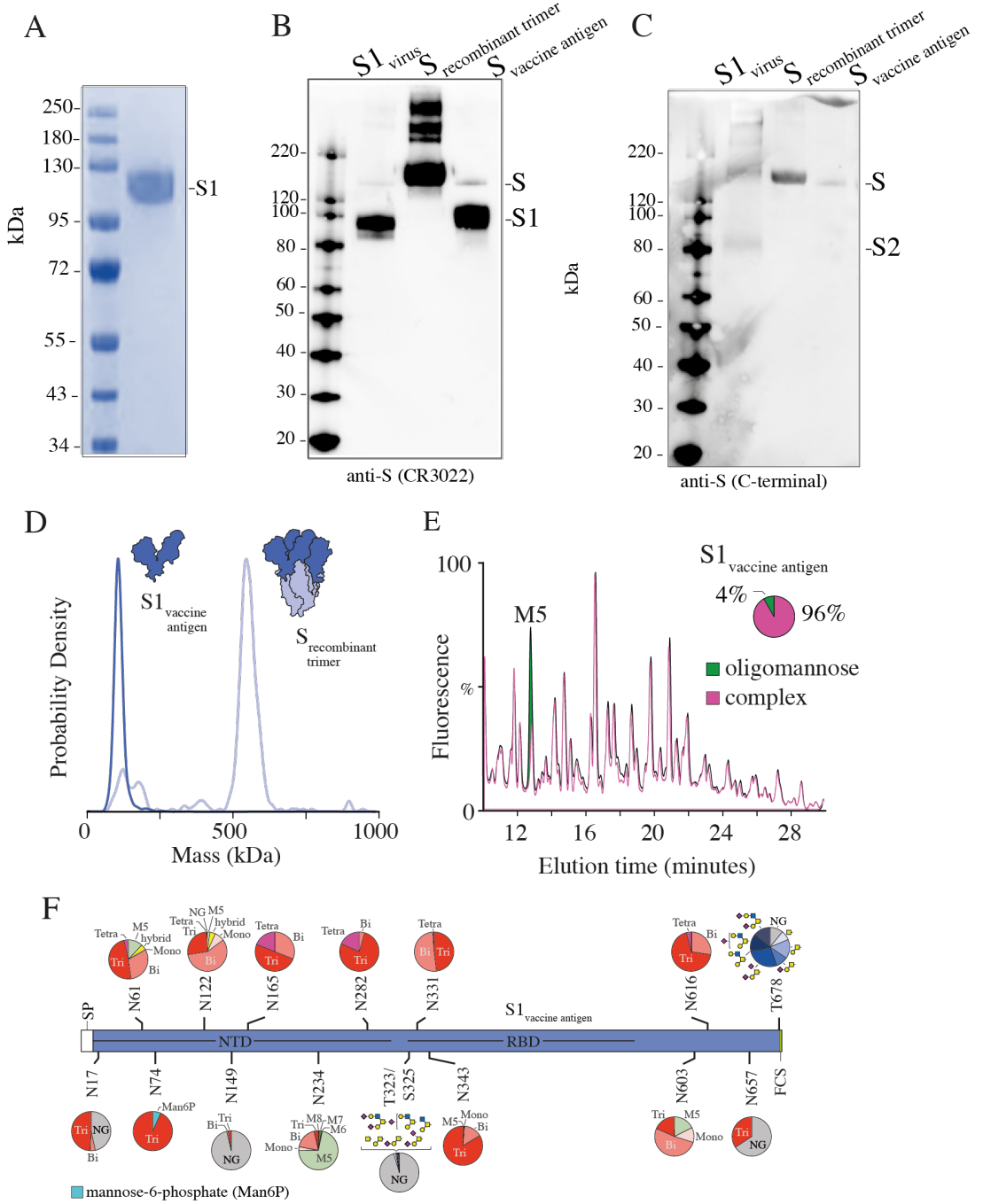

Figure 13: Purification, assembly, and glycosylation of vaccine-derived spike protein with tPA leader sequence. (A) SDS-PAGE of affinity-purified S of transfected HEK293F 4 days post transfection. (B and C) Western blot analysis of purified S_{virus}, $S_{recombinant\ trimer}$ and $S_{vaccine\ antigen}$ probed with (B) anti-S (CR3022) and (C) anti-S (C-terminal). (D) Mass photometry of purified $S1_{vaccine\ antigen}$, ~120 kDa, and $S_{recombinant\ trimer}$, ~550 kDa, showing $S1_{vaccine\ antigen}$ in monomeric form compared to trimeric form of the recombinant S protein. (E) Quantitative UHPLC N-glycan analysis of $S1_{vaccine\ antigen}$ represents the degree of glycan processing of oligomannose to complex-type glycans. (F) Purified $S1_{vaccine}$ sample was used for site-specific N- and O-glycosylation by bottom-up glycoproteomics. Pie charts depict the degree of N-glycan processing and reference shown in Figure 11C. Gels were run under denaturing, non-reducing conditions.

On the two O-glycosylation sites, T325/S325 and T678, an increase in O-glycan extension was detected (i.e. presence of core-2 structures), as well as a 50% increase in sialylation at T678. O-glycosylation is largely governed by steric hindrance and the ability of GalNAc transferases to access serine, threonine, or tyrosine amino acids and/or add monosaccharides to the core GlcNAc by a range of O-glycan processing enzymes in the Golgi. Therefore, differences in O-glycosylation point to changes in protein structure, assembly, or dynamics during trimer biosynthesis.

The glycan site N234 on $S1_{virus}$ maintained under-processed glycans (60% $GlcNAc_2Man_{6\text{-}8}$ (M6, M7, M8)), whereas N234 on $S1_{vaccine\ antigen}$ carried the more processed M5 N-glycans. The remaining structures did not progress to more complex types of glycosylation. The N234 site is a useful metric for understanding spike assembly or dynamics as changes at this position can only be explained by alterations in the architecture of the S trimer. This is because N234 is located in a pocket formed by neighbouring RBDs and one NTD, so when this pocket is absent (i.e. not a fully folded trimer), an overall increase in N-glycan processing would be predicted. Importantly, the N234 glycosylation site varied significantly between the $S1_{virus}$, $S_{recombinant\ trimer}$ and $S_{vaccine\ antigen}$. For example, with the $S1_{vaccine\ antigen}$ changing from 100% to 74.8% oligomannose. In theory, this processing would increase in the absence of trimer assembly (discussed further below). Additionally, mannose-6-phosphate (M6P) was detected on $S1_{vaccine\ antigen}$ on MS (**Appendix I, Figure 55**). M6P is a sugar tag that is added in the *cis*-Golgi in the form of Glc-NAc-M6P and is decapped in the *trans*-Golgi. It is recognised by the M6P receptor, which then directs the tagged protein from the *trans*-Golgi to the late endosome/lysosome (386). This has been described

for SARS-CoV-2 (237); however, the amount of M6P was below the level of detection in our virus samples but was indicated by MS (**Appendix I, Figure 56**).

Purification of the S protein directly from the cell membrane was attempted to identify the glycosylation profile of cell-membrane-associated S (**Figure 14**). The cell pellet was lysed, ultracentrifuged, and CR3022 immuno-purified as described above. Samples were analysed on an SDS-PAGE, but the purification was not clean, and there was insufficient material to perform MS. Western blot analysis with anti-S1 (CR3022) confirmed the presence of full-length S and S1 in cellular samples.

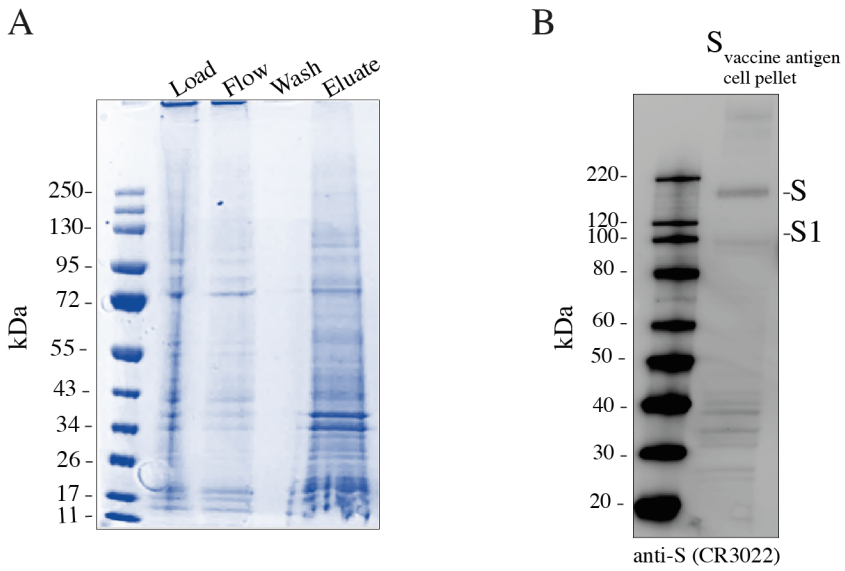

Figure 14: Purification of $S_{vaccine\ antigen}$ from the cell pellet. HEK293F transfected cells were harvested 4 days post transfection, cells were spun down, cell pellet was lysed in 1% DDM and sonicated. Sample was centrifuged for 2 hours at 45,000 rpm at 4°C, and final pellet was resuspended in lysis buffer. (A) SDS-PAGE of the load, flow-through, wash, and eluate of the membrane-bound isolated $S_{vaccine\ antigen}$ sample. (B) Western blot analysis of the affinity-purified membrane-bound $S_{vaccine\ antigen}$ probed with anti-S (CR3022), showing bands at the size of full-length and S and S1. Gels were run under denaturing, non-reducing conditions.

Comparison of $S1_{virus}$ (21% oligomannose/79% complex), $S_{recombinant\ trimer}$ (11% oligomannose/89% complex) and $S1_{vaccine\ antigen}$ (4% oligomannose/96% complex) showed an increase in complex glycans. Although the $S_{recombinant\ trimer}$ consists of the S1 and S2 domain, major differences on the glycosylation site N61, N122, N149, N234, T323, N603, N657 and T678 were detected between the three samples. Glycan maturation increased from $S1_{virus}$ to $S_{recombinant\ trimer}$ and was most processed (i.e., complex-type) in $S1_{vaccine\ antigen}$. This glycan difference can be an indication of biosynthesis or a reflection of where the shedding of the $S1_{vaccine\ antigen}$ subunit occurs.

Therefore, to test this hypothesis of where shedding occurs, a fourth SARS-CoV-2 glycoprotein was produced to compare the glycosylation of the $S_{recombinant\ trimer}$ and $S1_{vaccine\ antigen}$ to the monomeric recombinant S1 ($S1_{recombinant\ monomer}$) containing the transmembrane domain.

4.3.3 Glycosylation of monomeric recombinant S1

Specifically, the $S1_{recombinant\ monomer}$, maintaining the transmembrane domain as the $S_{vaccine\ antigen}$, was produced to identify the organelle (ER, Golgi, or cell membrane) from which $S1_{vaccine\ antigen}$ is shed from full-length $S_{vaccine\ antigen}$. Similar to the production of $S_{recombinant\ trimer}$, HEK293F cells were transfected and $S1_{recombinant\ monomer}$ was purified via the CR3022 affinity column followed by analysis using SDS-PAGE analysis and MS (**Figure 15A, Appendix I, Table 32).** Even though the protein recovery yield could not be calculated due to the lack of a western blot of unpurified sample, the purity $S1_{recombinant\ monomer}$ reached ~35%. Potentially, $S1_{recombinant\ monomer}$

could interact with proteins from the cells or medium; however, this has not been further investigated. N-glycan UHPLC analysis showed that 99% were complex-type structure and only 1% oligomannose, which indicated significant glycan processing compared to the other S samples (**Figure 15B**). This is contrasting to findings made by Shajahan *et al.*, where S1 and S2 were expressed separately and $Man_5GlcNAc_2$ was the major structure on S1. However, N17 and N603 were unoccupied in their study, highlighting differences in overall N-glycosylation (382). Here, site-specific N- and O-glycan analysis supported an increase of complex glycans compared to the $S_{recombinant\ trimer}$, especially on N61, N122, N165, N234, N282, and N616. In contrast, N149 and N657 were mostly non-glycosylated in comparison to the $S_{recombinant\ trimer}$, where they were predominantly complex-type glycans. For the $S1_{virus}$, glycan were predominantly tri-complex and oligomannose-type (**Figure 15C; Appendix I, Table 32).**

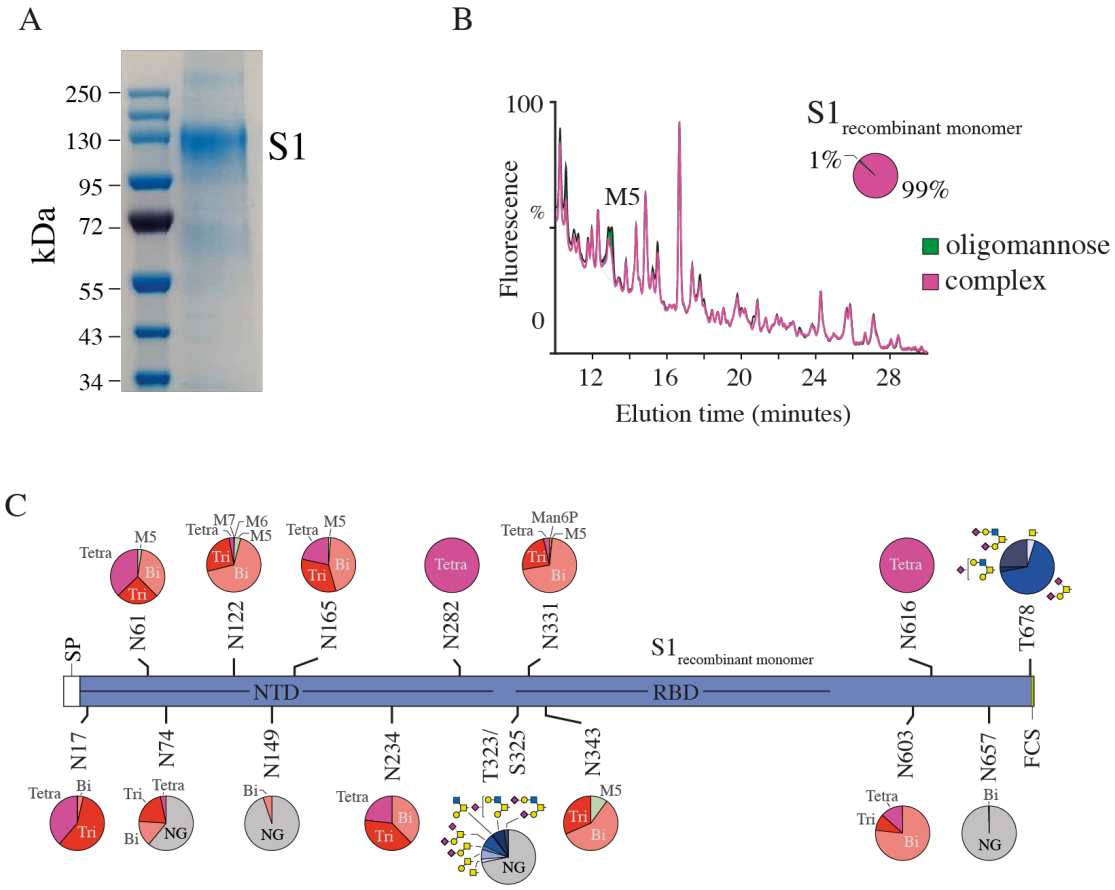

Figure 15: Purification and glycan analysis of S1$_{\text{recombinant monomer}}$. HEK293F cells were transfected with the S1$_{\text{recombinant monomer}}$ construct and harvested 4 days post transfection. Cells were spun down, and supernatant was applied to the CR3022 column to purify S1$_{\text{recombinant monomer}}$. (A) SDS-PAGE of purified S1$_{\text{recombinant monomer}}$. (B) Quantitative UHPLC N-glycan analysis of S1$_{\text{recombinant monomer}}$ distribution of oligomannose and complex glycans. Glycans were released with PNGase F and prior Endo H treatment labelled with 2-AA. Only oligomannose glycans are released by Endo H, making a comparison of oligomannose to complex glycans possible. (C) Site-specific N- and O-glycosylation of purified S1$_{\text{recominant monomer}}$ sample was used for bottom-up glycoproteomics. Pie charts depict the degree of N-glycan processing, a reference map is shown in Figure 11C. Gels were run under denaturing non-reducing conditions.

4.3.4 Identifying the cellular site of S1$_{\text{vaccine antigen}}$ shedding

Analysis of S1$_{\text{recombinant monomer}}$ supported the view that certain N- and O-glycan sites are indicators for trimer assembly and biosynthesis. Therefore, a more detailed view

was warranted, specifically for the two glycosylation sites N234 and T678. 100% of $S_{recombinant\ trimer}$ and $S1_{virus}$ had $GlcNAc_2Man_{5-8}$ (M5, M6, M7 and M8) structures on N234, whereas $S1_{vaccine\ antigen}$ derived only carried 74.8% oligomannose, and $S1_{recombinant\ monomer}$ had only complex glycans at these sites (**Figure 16A, B**).

The 74.8% under-processed glycans on $S1_{vaccine\ antigen}$ indicate that this protein, derived from a spike, which was initially trimerised in the ER. Because these sites are less accessible in the assembled form and consequently the glycans are less processed. The $S1_{vaccine\ antigen}$ would therefore be a less closed trimer and more accessible to mannose-trimming ER enzymes compared to its SARS-CoV-2 full virus expressing counterpart. More extensive glycan processing of the N-glycan at N234 is ruled out because of the unusual and temporal assembly of S proteins in the ER and Golgi. When S trimerization in the ER prevents early N-glycan trimming at this site, N234 glycans are protected in a pocket formed partly by the RBD and the NTD on the same protomer, and partly by a neighbouring RBD, resulting in largely unprocessed oligomannose N-glycans (**Figure 16A**). Additionally, $S_{vaccine\ antigen}$ contains the active furin-cleavage site and is therefore cleaved by furin in the *trans*-Golgi. However, unlike endogenous viral spikes, where we postulate that additional stabilising viral factors are present, some S1 dissociates from S2 upon furin cleavage of the vaccine-derived antigen and becomes secreted. The degree of processing for the O-glycosylation site T678 was reversed compared to N234 between all four proteins on their occupied level. Specifically, $S_{recombinant\ trimer}$ is 100% unoccupied, compared to 77% for $S1_{virus}$, 10% for $S1_{vaccine\ antigen}$, and 0% for $S1_{recombinant\ monomer}$ (**Figure 16C, D;** MS/MS spectrum **Appendix I, Figure 57**).

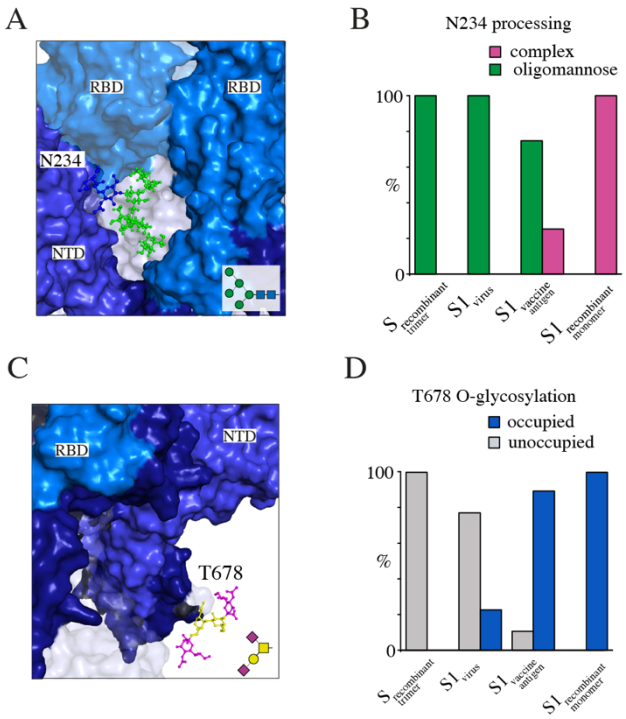

Figure 16: Glycan location and macromolecular assembly with N234 and T678 glycan processing. (A) Structural location and orientation of the S1 N-glycan N234 (shown as $Man_5GlcNAc_2$) in a pocket formed by the RBD (shaded light blue) and NTD of the same protomer, and the neighbouring RBD (light blue). GLYCAM web server (http://glycam.org) was used to model the glycan on to the PDB 6VXX and rendered using PyMOL. (B) Comparison of percentage of complex versus oligomannose distribution between $S_{recombinant\ trimer}$, $S1_{virus}$, $S1_{vaccine\ antigen}$ and $S1_{recombinant\ monomer}$. (C) Structural position of the S1 O-glycan T678 (displayed as disialylated core-1 structure) positioned in the subdomain near the furin-cleavage site between S1 and S2 (modelled on PDB 6VXX using GLYCAM webserver) and rendered using PyMOL. (D) Percentage change in oligomannose to complex glycan between all samples tested.

Furin cleavage of $S_{vaccine\ antigen}$ is not complete, as approximately 10% is not O-glycosylated (**Figure 16D)** and appears on the cell surface, as observed by flow cytometry (**Figure 17**, gating strategy shown in **Appendix I**, **Figure 58**). This was confirmed using staining with the CR3022 antibody of either unpermeabilised cells, where only surface S1 protein will be detected, or detergent-permeabilised cells to detect both surface and internalised S1 (**Figure 17A**), or staining for S2, respectively (**Figure 17B**). It is possible that the S1 detected on the cell membrane is trimerized

giving the antibody responses seen in the ChAdOx1 nCoV-19 clinical trials (163,387,388).

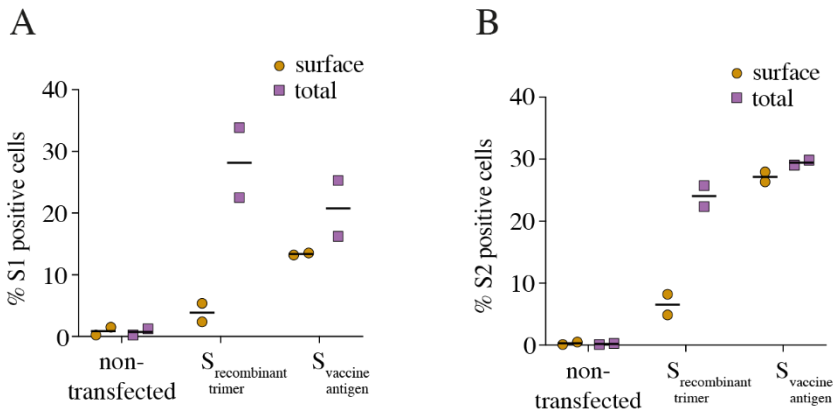

Figure 17: Cellular location of S protein in $S_{recombinant\ trimer}$ and $S_{vaccine\ antigen}$. Flow cytometry analysis was performed on non-transfected, $S_{recombinant\ trimer}$ and $S_{vaccine\ antigen}$ transfected HEK293F cells. Cells were harvested 2 days post transfection, spun down, and fixed with 2% PFA and either solely stained for S1 on the cell surface or subjected to intracellular staining after permeabilization with 0.5% saponin. In both conditions, cells were stained for S1 (CR3022) or S2 (1A9). Flow cytometry was performed to determine the percentage of S1 or S2 positive cells positive cells relative to total cells. Data are from two independent experiments and are shown as mean ± standard error of mean (n = 2).

4.4 Discussion

Vaccination with AstraZeneca AZD1222 (ChAdOx nCoV-19) elicits neutralizing antibody and spike-specific T-cell responses (389–391). However, it is not known if, and to what extent, the spike immunogen design of ChAdOx nCoV-19 compared to stabilised versions (i.e., Pfizer BNT162b2 and Moderna mRNA-1273) may have influenced vaccine efficacy. Shedding of viral subunits is a known phenomenon *in vitro* and *in vivo* (392,393). Trimer stabilisation by introducing prolines to the central stalk of the spike proteins may help explain some of the differences in B-cell responses

between vaccines with and without such stabilisation strategy. The additional step of removing the furin-cleavage site, as performed, for example, in the adenovirus serotype 26 vector-based vaccine by Johnson & Johnson (reviewed in (176)), could equally benefit vaccine responses. Both are supported by findings during early HIV vaccine development, where immunogens were suboptimal due to the inability of monomeric gp120 to elicit a broadly neutralizing antibody response needed for virus neutralization (377). Shedding of S1 subunits from viruses occurs during native infection (355,356) and the Chadox nCoV-19 antigen was designed using the intact Wuhan spike sequence without any change to the furin cleavage site or introduction of stabilising prolines (387). Therefore, shedding of S1 from ChAdOx nCoV-19-encoded spike is very likely to occur in the physiological context. It may favour production of non-neutralising antibodies that target the trimer interface exposed on soluble S1. Normally, in the context of a trimer on an infectious virus, this interface would not be accessible. Hence, the presence of shed S1 may influence the repertoire, quality, and breadth of neutralising antibodies. Although the shedding seen here could be more pronounced due to overexpression in HEK cells compared to a physiological context, protein antigen production is nevertheless also high during a viral infection and post-vaccination. To detect if shedding is more pronounced in HEK cells, a comparison to other cell lines or measurements of vaccinee sera (e.g., by enzyme-linked immunosorbent assay (ELISA)-based detection against S1 and conformational full-length S antibodies) would need to be performed, which was not done here due to patient or vaccinee serum samples not being made accessible early in the pandemic.

The consequence of S1 shedding in the viral infection/disease pathology of SARS-CoV-2 is unclear. It has been shown that in male mice intravenously injected with S1, the antigen can cross the blood-brain barrier, whereas intranasally administered S1 enters the brain at a rate ten times lower (394). Moreover, in a study published as a preprint, platelet-poor plasma of healthy donors incubated with S1 can result in hypercoagulation, promoting potential thrombosis (395). Another hypothesis centres on natural S1 shedding, stating that shed S1 may bind to ACE2 and downregulate its cell surface expression. Based on continuous or elevated ACE2 activity in the lungs, a decrease in ACE2 activity could contribute to a higher prevalence of angiotensin II effects over angiotensin, thereby promoting thrombosis, inflammation, and pulmonary injury. This theory also indicates a link between the lack of increased severity of the COVID-19 infection caused by the mutant (D614G) SARS-CoV-2 variant, considering its higher infectivity and *in vivo* viral load, and less pronounced shedding of S1 particles identified for the S protein carrying the D614G mutation (versus the wild type D614 protein) (396).

Shedding of monomeric and non-physiologically glycosylated $S1_{\text{vaccine antigen}}$ from immunogen generating cells is also reminiscent of early HIV vaccine production. Specifically, finding a viable vaccine candidate was slowed by the inability of monomeric gp120 to evoke the broadly neutralizing antibody response necessary for virus neutralization (377). Consistent with this, immunogens that do not imitate infectious virion trimeric S glycoproteins may effectively serve as a decoy, eliciting more of the unwanted suboptimal or non-neutralizing antibodies that are incapable of binding and neutralizing the trimeric spikes (210,376,377,397). Since some of the

vaccine antigen lacks the native protein architecture, antibodies that neutralise by binding to the trimer apex will not be elicited by shed $S1_{vaccine\ antigen}$. The antibody S2M11 (398) and C144 (399) bind to a quaternary epitope formed at the trimer apex by two adjacent RBDs. Non-neutralising epitopes buried on assembled trimers can be exposed by soluble monomeric S1. Furthermore, glycosylation at N234 impacts the RBD's up/down orientation and ACE2 binding (400). Increased glycan processing on shed $S1_{vaccine\ antigen}$ could theoretically have a detrimental effect on antibody recognition due to a difference in glycan charge and size (i.e. increased sialic acid content and heightened branching), which might obstruct peptide epitope recognition. However, ACE2 binding in HeLa S3 cells infected with ChAdOX1 nCoV-19 was measured by flow cytometry, which confirmed correct folding of S on the cell surface, as well as antibody binding of Ab45, Ab71 and Ab11 which recognise the RBD, trimeric spike and the NTD, respectively. Interestingly, binding of antibody Ab44 to S2 was also detected, which suggests that shedding of some S1 does occur (401).

The comparison of the glycans on $S_{recombinant\ trimer}$, endogenous viral shed $S1_{virus}$, shed $S1_{vaccine\ antigen}$ and monomeric $S1_{recombinant\ monomer}$ revealed an increase in processed structures (**Figure 18**), from the least processed on $S_{recombinant\ trimer}$ to $S1_{virus}$ and $S1_{vaccine\ antigen}$ to the most processed on $S1_{recombinant\ monomer}$. These data indicate increased accessibility of Golgi-resident enzymes to process glycans from oligomannose to complex-type depending on the protein architecture of trimeric or monomeric S assemblies. However, others have found slightly different glycosylation profiles, in which another recombinant trimeric S (371) and viral S (380) had higher oligomannose content than our data. In a different study, recombinant S1 and S2 subunits were

produced separately and analysed, identifying $Man_5GlcNAc_2$ as the predominant structure across all S1 sites (382), which resembles the N-glycosylation profile of full-length $S_{recombinant\ trimer}$ described here. Our data of shed $S1_{vaccine\ antigen}$ in the Golgi is supported by the increase of complex-type N-glycans in $S1_{recombinant\ monomer}$ to $S_{recombinant\ trimer}$ and increase of occupation of O-glycosylation (for T678) in $S1_{recombinant\ monomer}$ that were not present on the trimeric prefusion spike protein.

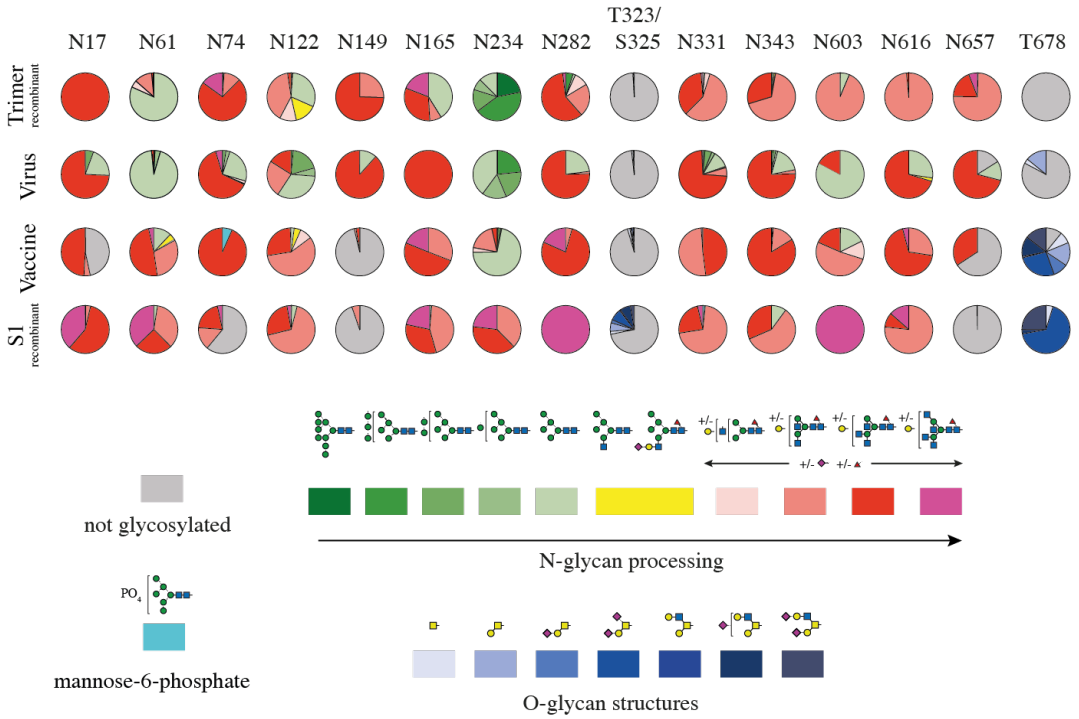

Figure 18: Summary of site-specific glycosylation changes of S1 subunit. Cumulative site-specific glycosylation changes across S1 subunit from $S_{recombinant\ trimer}$, $S1_{virus}$, $S_{vaccine\ antigen}$, and $S1_{recombinant\ monomer}$.

Compared to our study, in which 30% of HEK293F transfected with $S_{vaccine\ antigen}$ were positive for S1 on the cell surface, 60 – 70% of HeLa S3 cells infected with the ChAdOx nCoV-19 were expressing S (401). This discrepancy might be due to transfection efficiency of the expression construct compared to infection with ChAdOx nCoV-19. For glycan analysis by Watanabe *et al.*, HEK293F cells were

infected with ChAdOx nCoV-19, and the cell pellets were lysed, revealing the presence of S, S1 and S2 by western blotting. To visualise the S glycoprotein subunit by SDS-PAGE, 90 gel bands were combined and used for glycan analysis. Intracellular uncleaved S had predominantly under-processed oligomannose/hybrid type glycans (85%/15%), whereas the S1/S2 cleaved sample dropped to 56%/44% oligomannose/hybrid to complex glycans (401). However, the authors did not perform SDS-PAGE in this study. Shedding of S1 was mentioned as a possibility, but not further investigated. It would be advantageous to know what the structural architecture of S on the cell surface is, conceivable methods on this end are microscopy or tomography, which was not performed during this DPhil. Cryo-electron tomography on human osteosarcoma epithelial cells (U2OS) infected with ChAdOx nCoV-19 shows that these infected cells express prefusion S proteins on the cell surface. However, due to the lack of a specific anti-S2 antibody, cryo-immunolabelling of post-fusion spikes on the cell surface was not possible. At the same time, few post-fusion spikes were detected by cross-correlation of tomographic volume (401).

A strong B-cell response of a vaccine is dependent on an invading pathogen's immunogen mimicry. As a result, we assume that a stabilised trimeric prefusion spike protein with the furin-cleavage site removed would elicit neutralising antibodies with the necessary substantial breadth and potency for the most successful SARS-CoV-2 vaccine. Viral vector-based vaccines, such as the ChAdOx1 nCoV-19 vaccine, and nucleic acid-based vaccines, such as the Pfizer BNT162b2 and Moderna mRNA-1273 vaccines, rely on the antigen-encoding DNA or RNA sequence. Once inside a cell, these sequences produce spike proteins that faithfully resemble viral S proteins in both

glycosylation and assembly, eliciting a robust immune response. However, the cellular secretion process followed by DNA/RNA-derived vaccine antigens varies fundamentally from that followed by antigens present during viral infection, where factors other than a single protein-coding sequence may play a key role in immunogen presentation (**Figure 19**). Both involve potential differential splicing (402), the intracellular site of viral morphogenesis (the organelle from which a virus buds), and the general macromolecular assembly of an immunogen as it interacts with the host glycosylation machinery during a natural infection. The Pfizer BNT162b2 and Moderna mRNA-1273 vaccine antigens aim to address some of these important factors by using a strategy used for MERS and SARS-CoV-1 spike vaccine design (356,403). Specifically, the two proline mutations introduced close to the first HR of each protomer, stabilising the spike in its prefusion cohesion (404). Stabilising viral proteins by introducing proline substitutions in specific positions that sustain the protein in the prefusion form is routinely used in structure-guided vaccines design for various viruses as HIV, Respiratory syncytial virus (RSV), EBOV, MERS, Lassa virus and human metapneumovirus (hMPV) (405).

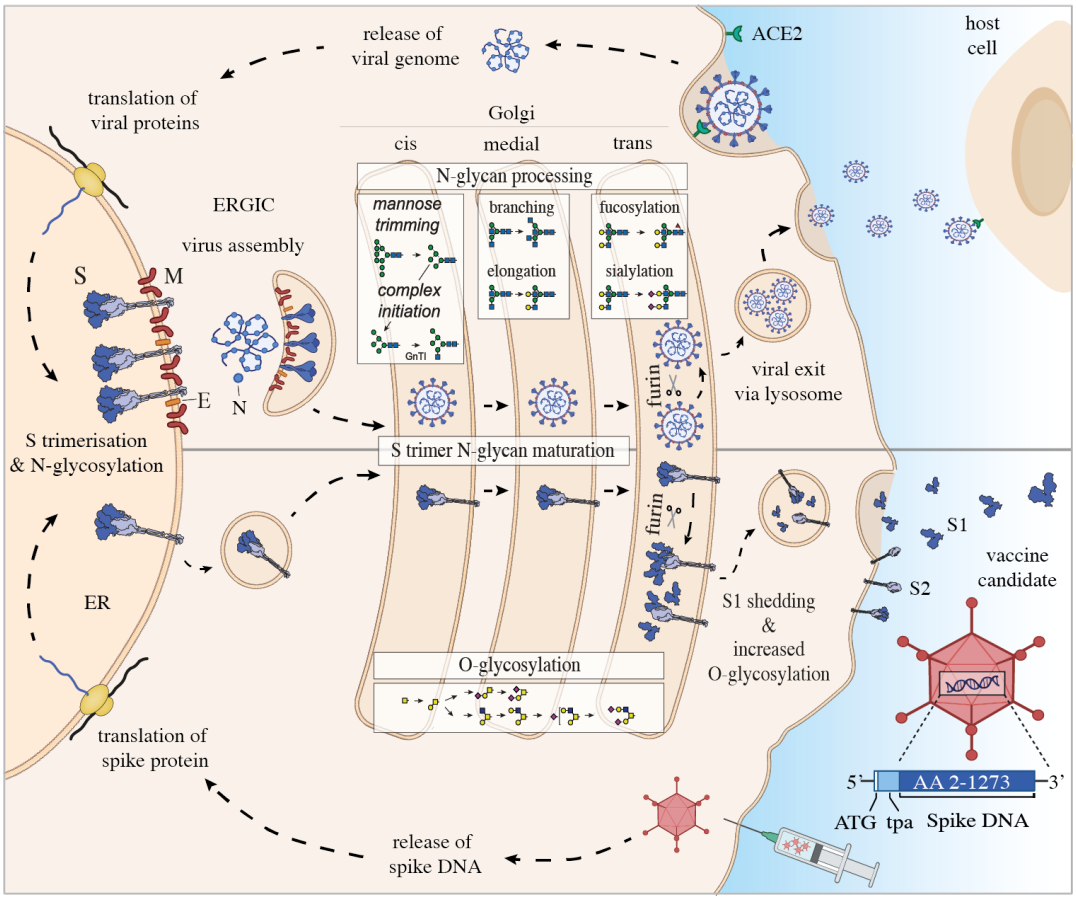

Figure 19: Viruses and vaccine-derived spike glycoproteins have different expression and glycan processing. SARS-CoV-2 infects cells by binding to its receptor ACE2, allowing the viral genome to be released and viral proteins to be translated. Spike protein is N-glycosylated during co-translation and forms trimers in the ER, which then travel to the ERGIC and are inserted into budding virions. Individual virions proceed to the *trans*-Golgi through the secretory pathway before exiting via lysosomal egress. The vaccine candidate receives spike DNA from an adenovirus vector system, and S protein is synthesised in the ER, where it is N-glycosylated and trimerizes as before. However, since it is not incorporated into a budding virion in the ERGIC, it proceeds to the plasma membrane through the secretory pathway and lysosomes. The spike glycoproteins have access to the N- and O-linked host glycosylation machinery in both cases. S1 and S2 of the virus remain non-covalently linked after furin cleavage in the *trans*-Golgi, while furin cleavage of the vaccine antigen results in monomeric shedding of $S1_{\text{vaccine antigen}}$. The N-linked glycosylation occupancy levels calculated in the ER for $S1_{\text{virus}}$ and $S1_{\text{vaccine antigen}}$ are comparable, according to a glycomic signature study of these two proteins. The attached glycoforms, on the other hand, vary due to their different accessibility to glycan processing enzymes. $S1_{\text{vaccine antigen}}$ contains more complex N-glycans than other vaccine antigens. However, after furin cleavage in the *trans*-Golgi, as most $S1_{\text{vaccine antigen}}$ is shed and secreted in a soluble monomeric form, it is extensively O-glycosylated. On the cell surface, certain $S1_{\text{vaccine antigen}}$ and $S2_{\text{vaccine antigen}}$ are visible, possibly as trimers. Adapted from (406).

As mentioned above, a more potent antibody responses are likely to be elicited by removing the furin cleavage site, avoiding S1 shedding, and adding mutations that trap spike immunogens in a prefusion conformation. Some vaccine candidates combine the methods of furin site abolition and stabilisation mutation (407,408). One study compared the effects of furin cleavage, stabilisation, and the involvement of the tPA signal sequence on vaccine efficacy. The construct that lacked the trimer stabilisation mutations but kept the furin cleavage site and tPA leader sequence was the least successful of the seven platforms evaluated in non-human primates (408), supporting our results. Moreover, cells transduced with a construct expressing a tPA leader sequence and no stabilisation mutations in the spike proteins demonstrated binding of antibodies of non-neutralising S2 antibodies (CR3046 and CR3015) in cell-based ELISA assay and flow cytometry (409).

The unprocessed S protein precursor contains an ER signal peptide (SP), which targets the protein to the rough ER membrane and is then removed by a cellular signal peptidase in the ER lumen. To obtain natively folded proteins, correct N-terminal signal peptidase processing is required (410). A conserved cysteine (Cys15) is present downstream of the SP, which forms a disulfide bond with Cys136 and could be necessary for proper folding of the NTD (378,409). Cleavage of the SP was identified by liquid chromatography (LC-MS)/MS in CR3022 and ACE2 purified recombinant membrane-bound protein of 1) S with wildtype SP and two proline mutation and 2) S with wildtype SP and an additional tPA on the N-termini (as in ChAdOx nCoV-19). SARS-CoV-2 wildtype SP on S with the two-proline mutation was cleaved after position 13 in the NTD. The addition of tPA to the wildtype SP led to a lower number

of correct N-termini. Moreover, tPA addition to wildtype SP of S cleaved in the wildtype SP sequence predominantly after position 13 rather than at the correct wildtype cleavage site of the spike protein (409). Due to the low LC-MS/MS signals, soluble prefusion trimeric spike protein constructs with either the wildtype SP or the tPA SP was expressed, demonstrating that the wildtype SP resulted in a higher percentage of correctly cleaved N-termini (99.5% compared to 11.0%) (409), which might have implications for the folding of S.

The proteins $S_{\text{recombinant trimer}}$, $S_{\text{vaccine antigen}}$ and $S1_{\text{recombinant monomer}}$ were purified from transfected in HEK293F cells, whereas the viral SARS-COV-2 S protein was purified from infected Calu-3 cells. Calu-3 cells express ACE2 (411,412) and TMPRSS2 (412) and often chosen as a model to study respiratory viruses. To compare potentially differences between the glycosylation of S_{virus} and $S_{\text{recomibinant trimer}}$, SARS-CoV-2 infection in HEK293T cells (a variant of HEK293 cells carrying SV40 origin of replication, whereas HEK293F are adapted for suspension culture (413)) was tested. Low viral titre was detected and purification of S after CR3022 purification was insufficient. The replication-deficient adenovirus vectored vaccines are administered intramuscularly, causing antigen expression mainly in skeletal muscle cells, which express robust levels of ACE2 and TMPRSS2 (414). Intramuscular administration of ChadOx1 nCoV-19 in rhesus macaques challenged with SARS-CoV-2 presented a reduced viral load in the bronchoalveolar lavage fluid and lower respiratory tract, but no difference on nasal shedding between vaccinated and control animals was detected (387). Some studies assessed the difference of intramuscular to intranasal vaccination in mice, with replication-defective human type 5 adenovirus encoding spike protein

with a tPA leader sequence or adenovirus type 5 vectored-vaccine encoding the RBD, showing a stronger B-cell and T-cell immune response if vaccinated intranasally (415,416). This implies intranasal administration can improve the immune response, however, the potential problem of shed S1 was not addressed. Examining the vaccine-derived antigen in primary cells, or iPSCS-derived skeletal muscle cells might be useful in understanding virus-associated glycosylation in cells similar to those that would produce the vaccine antigen in vaccinated individuals.

In vaccine development, each vaccine candidate's glycan signatures should be compared to the wild-type virus. In this and future pandemics, understanding and characterising the viruses' proper glycosylation, as we have done here, will guide vaccine design strategies and allow for the creation of a high-quality immune response. aimed at achieving the correct immunogen presentation.

Chapter 5 Antiviral drug screening against SARS-CoV-2

5.1 Introduction

Vaccines are the best way of comprehensively keeping viral disease under control. Various types of vaccines have been developed and novel technologies are emerging at a fast pace. Specifically, vaccine strategies include vectored vaccines (409,417), mRNA/DNA vaccines (161,418), vaccines with the RBD as a target (419), protein/protein subunit-based vaccines (420), as well as live, attenuated and inactivated virus-based vaccines (421). Other tools to fight unknown viruses include the use of convalescent sera (422) and recombinant antibodies (423).

However, in combatting a newly emerging virus with pandemic potential, there would ideally be a potent drug that can be produced quickly, inexpensively, and capable of being administered rapidly, which in principle is a small molecule with broad antiviral capacity. Nevertheless, *de novo* antiviral drug discovery is challenging during viral pandemics, with the timeframe from drug discovery to pre-clinical, clinical trials and eventually approval by regulatory bodies and large scale manufacturing typically taking 10 – 13 years (424). Moreover, the attrition rate is high with one approved drug for every 5,000 – 10,000 starting compounds on average (425). This protracted process means a novel drug is unlikely to be developed and available in time for an emerging

virus. Therefore, the more attractive option tends to be re-screening drugs already approved for other applications, in the hope that any approved drug with activity may be repurposed within a short and useful timeframe. There are currently over 20,000 FDA-approved drugs on the market (426), the screening of which exceeds the capacity of all laboratories. Moreover, any high-throughput screens invariably employ easy-to-handle and, more often than not, less physiologically relevant host cells (e.g., Vero E6) as well as quick readouts of infection (e.g., observation of cytopathic effects (CPE), immunofluorescence (IF) of infected cells, or quantitative reverse transcription polymerase chain reaction (qRT-PCR) of secreted virions).

When the COVID-19 pandemic forced our laboratory to stop all non-COVID-19 related work, we decided to apply our expertise in growing viruses and drug screening knowledge towards the common goal of identifying drugs to fight SARS-CoV-2. In collaboration with other research groups, we opened the COVID-19 core facility at the Sir William Dunn School of Pathology, Oxford University, where the Zitzmann laboratory was responsible for setting up and optimising a medium-throughput antiviral cellular screening assay. Initially, only already approved drugs were screened that could be immediately repurposed if shown to be active against SARS-CoV-2. Compounds were ranked according to their likelihood of having a potentially credible MOA against this virus as well as their availability for widespread distribution. After the initial phase of screening drugs, we included compounds currently in clinical phases III, II and I as well as pre-clinical compounds. The latter are mostly direct acting drug-like lead compounds being developed specifically for SARS-CoV-2. These compounds mainly target the Mpro and are mostly derived from a large international

collaborative initiative aimed at contributing to the global anti-COVID-19 effort, namely the “COVID-19 Moonshot”, of which the Zitzmann laboratory was a part (427). These efforts are still ongoing, and in this chapter, I describe the work conducted and my contribution to this effort up to and including January 2021.

Both repurposed drugs as well as novel COVID-19 specific drugs can be generally divided into three categories:

1) DAA that specifically target the virus. The first ones to be developed are often protease and polymerase inhibitors, but in principle any virally encoded protein can be a target.

2) HTA that inhibit human proteins or host cell processes that the virus uses.

3) Immunomodulatory drugs capable of modifying negative effects of an overreactive immune system (as described in section 1.2).

Immunomodulatory drugs are often of particular importance in more severe cases of viral infections, such as dengue haemorrhagic fever or severe COVID-19, where it is not the virus itself that causes the patient to succumb to the disease but rather an excessively activated immune system reacting to the invading virus. Importantly, the virus can be absent when the disease is at its most severe stages (2,3,112). Immunomodulatory drugs generally cannot be screened in simple cellular antiviral screens such as the one we deployed during the early phase of the pandemic; instead, they need to be tested directly in infected human patients. An example would be the steroid dexamethasone. Dexamethasone was identified in the Oxford-led Randomised Evaluation of COVID-19 Therapy (RECOVERY) (428), a large clinical trial of

potential interventions for people admitted to hospital with severe COVID-19. So far ten treatments have been tested on adults, including eight repurposed drugs, convalescent plasma and one newly developed drug (177). HTA have the potential for broad-spectrum antiviral activity if they target a pathway that is commonly used by multiple viruses, and have a much higher genetic barrier to the development of drug-resistant viral escape mutants (245). Host-targeting compounds can either target a cellular process which is critical for a virus to survive, or they can be immune system modulators, that may influence the reaction of the immune system. Unfortunately, the efficacy of repurposable DAA drugs is likely suboptimal as these are less specific in their mode of action or binding affinities compared to their original development designed directly against a specific virus.

After the most promising repurposable drugs were screened in our cellular assay, our attention turned to compounds in the earlier stages of drug development, namely via our participation in the COVID-19 Moonshot project. This project was created to build on early results and advance the development of Mpro inhibitors. Mpro, is the viral main protease and is required for cleaving precursor polyproteins into functional viral proteins. This essential function makes it a promising drug target. After the structure of Mpro was determined (429), researchers rapidly conducted with crystallographic and high-throughput fragment-screening of the structure (430). The fragments were designed based on computational docking-based approaches, structure-based designs, machine learning techniques, and literature research on SARS-CoV-1 and MERS compounds. The results are published live at https://postera.ai/covid. Before testing

these drugs in an antiviral assay, the enzymatic activity of the compounds was first measured by biophysical methods (427).

This chapter describes the establishment of a medium-throughput antiviral screen against SARS-CoV-2.

5.2 Material and Methods

The SARS-CoV-2 England/02/2020 strain (GISAID: EPI_ISL_407073) was propagated as described in section 4.2.1.

5.2.1 Plaque assay

Virus titres of SARS-CoV-2 and antiviral effects of drugs on viral titres were measured by plaquing the virus as previously described (431). Virus dilutions (Log_{10} dilutions) were prepared in virus propagation medium (1:1 mixture of DMEM and Ham's F12-medium (Gibco) supplemented with 2% HI FBS, 1% NEAA (Gibco), 1% sodium pyruvate (Gibco), 100 U/mL penicillin and 0.1 mg/mL streptomycin (MilliporeSigma) at 37°C and 5% CO_2). Hundred µL of each virus containing dilution was used for inoculation in triplicate wells of a 24-well plate (Greiner Bio-one) containing 0.5 mL of Vero E6 cells at 0.5 x 10^6 cells/mL in virus propagation media. The plates were incubated for 2 hours before the addition of 0.5 mL 2% carboxymethyl cellulose (CMC, Merck) overlay (1:1 mix of 4% CMC in H_2O and virus propagation medium). The plates were incubated for further 4 days before staining with naphthol blue black (Merck). Plaques were counted by eye.

5.2.2 Focus forming assay

To increase the throughput of tested drugs, the focus forming assay was adapted, as previously described (432). Briefly, half log dilutions of the viral supernatant to be analyzed were prepared in virus propagation medium (4.2.1). Twenty µL of each virus-containing dilution, in quadruplicate, was used for inoculation in a 96-well plate (Greiner Bio-one), containing 100 µL Vero E6 cells at 0.45 x 10^6 cells/mL in virus propagation medium. The plates were incubated for 2 hours prior to the addition of 100 µL 2% CMC overlay (for composition see 5.2.1). Plates were incubated for an additional 24 hours at 37°C, 5% CO_2. Subsequently, the overlay was carefully removed, and the cells were washed once with PBS (Gibco), fixed with 4% PFA (Alfa Aesar) for 30 minutes. The samples were quenched with 1% ethanolamine in PBS (Merck). Cells were permeabilized with 2% Triton X-100 in PBS (Merck) at 37°C for 30 minutes. The plates were washed thrice with wash buffer (0.1% Tween-20 in PBS (Merck) before the addition of EY2A anti-N human monoclonal antibody (mAb; gift from Arthur Huang (Taiwan), Alain Townsend and Jack Tan (Weatherall Institute of Molecular Medicine, University of Oxford)) at 10 pmol in wash buffer. The plates were incubated at room temperature for 1 hour and subsequently washed thrice with wash buffer. Secondary goat anti-Human IgG (Fc-specific)-peroxidase-conjugated antibody (Merck) was diluted at 1:5000 in wash buffer and added to the samples. The plates were incubated at room temperature for one further hour. The plates were thrice washed with wash buffer and TrueBlue peroxidase substrate (Insight Biotechnology Ltd) was added. The samples were incubated at room temperature for 10 minutes, the substrate was removed, and the plates were washed with ddH_2O for 10 minutes. Plates

were air-dried before the foci were counted using an ELISPOT classic reader system (AID GmbH).

5.3 Results

5.3.1 Antiviral drug screening set-up

Most screening efforts at the beginning of the pandemic used the African Green Monkey kidney cell line Vero E6, or similar established cell lines, because of their ease of use (433). However, cellular antiviral screening data show large variations across different screening laboratories (434). A major determinant of antiviral activity is related to the cell type used for antiviral screens. For example, strong antiviral activity (IC_{50} = 13.3 µM) was measured for hydroxychloroquine in the Vero E6 that is widely used for antiviral screening, whereas significantly reduced activity (IC_{50} = 119 µM) was detected in the lung cell line Calu-3 (127). This variance across cell types may be due to differences in viral entry. Specifically, SARS-CoV-2 entry in Vero cells requires a low pH and is triggered by acid-dependent endosomal proteases, whereas in Calu-3 cells, it is pH-independent and requires TMPRSS2 (435). Therefore, we selected the cell line that would produce the most robust and relevant results, even though this slowed down the process. The human lung adenocarcinoma Calu-3 cell line demonstrates characteristics of bronchial epithelium, and can be infected by SARS-CoV-2 (436), retaining these properties over repeated passages (437). Calu-3 cells were already established as a cell model for other respiratory viral infections such as rhinovirus (438), IVA (439), RSV (440) and SARS-CoV-1 (441). The screen was designed by infecting naïve Calu-3 cells with SARS-CoV-2, treating the infected cells

with potential antiviral compounds, and harvesting the cell supernatant containing the secreted virions. The supernatant was then used to reinfect naïve Vero E6 cells to determine the quantity of infectious secreted virions. This method, compared to those above, can inform on antiviral activity regardless of whether the compounds inhibit viral entry, expression, secretion, or infectivity. In other words, it is possible that an antiviral agent can reduce the infectivity of secreted virus with or without effecting either virus expression in the infected cell (as measured by CPE or IF) or secretion (as measured by qRT-PCR) (442,443).

Although we initially sought to focus only on approved drugs, there are more than 20,000 of these drugs, and therefore prioritisation was needed. To prioritise the order in which drugs would be screened, the Zitzmann laboratory, in collaboration with Annette von Delft (Centre of Medicines Discovery, Oxford) developed a framework for drug testing (**Figure 20**). The first drugs to be screened would ideally be available as generics that are approved by regulatory bodies, followed by compounds in clinical trials with proven antiviral activity against SARS-CoV-2 or potent activity against its proteins *in vitro*. Finally, we then prioritised compounds with a credible MOA to potentially cause an antiviral effect against SARS-CoV-2.

In an initial screen, selected compounds were first tested for their cytotoxicity in uninfected Calu-3 cells, using three different concentrations chosen based on available cellular or organism-based data. The closest concentration that caused a maximum of 10% cell death (cytotoxic concentration of 10%; CC_{10}) was used to perform antiviral assays in duplicates. If a reduction in the secretion of infectious virions was detected

larger than 40%, a full screen with seven half-log diluted concentrations (in triplicates) was conducted. Additionally, for each compound, the drug concentrations required to elicit effective reduction of infectious virus with those concentrations required to observe cytotoxic effects, the selectivity of each compound was assessed, if possible. Whereas the first selectivity index (SI1, CC_{50}/IC_{50}) predominates in the literature for drug discovery, however, a more stringent selectivity index (SI2; CC_{10}/IC_{90}) might better reflects the potential of a drug to be used in a clinical setting (204).

In a fast-moving global pandemic with very scarce worldwide resources for antiviral drug screening, immediate exchange of information is important. Therefore, the results of the screened compounds were published as soon as possible after obtaining the data, on a 'live' SARS-CoV-2 Cellular Tracker website built by JL Kiappes, Michelle Hill (Zitzmann laboratory), Annette von Delft, Carina Gileadi, Viktor Rangel (Structural Genomics Consortium, Oxford) and Nicholas Devito (Centre for Evidence Based Medicine Oxford) (http://sarscov2.assaytracker.net/).

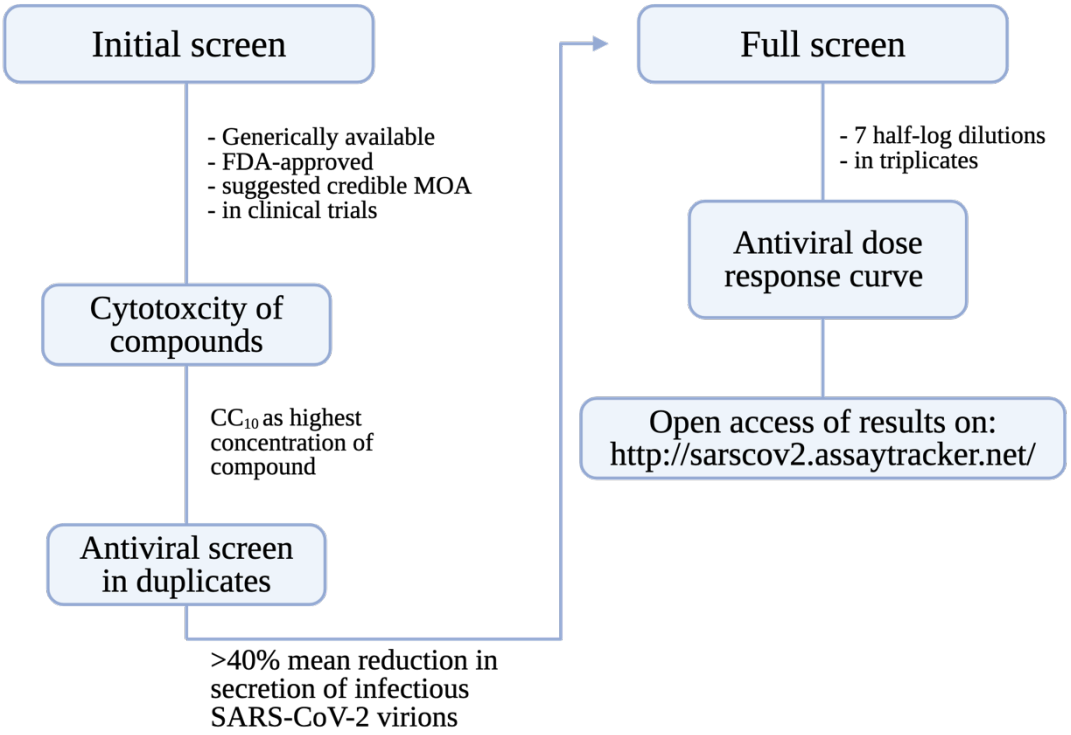

Figure 20: Framework of prioritising compounds for drug screening against SARS-CoV-2. Compounds were ranked according to several rationales, such as the availability of the compound, whether the compound was already FDA-approved or in a clinical trial, whether the compound showed an antiviral effect in a different assay and finally whether a credible MOA of the compound against SARS-CoV-2 was suggested. All compounds were screened for cytotoxicity in Calu-3 cells by MTS assay and the concentration closest to but below the CC_{10} was used for initial antiviral testing in technical duplicates. A reduction of 40% in the secretion of infectious virions was set as the minimum to pursue a full antiviral screen to calculate a dose response (in technical triplicates). All results were published on an open access website (http://sarscov2.assaytracker.net/).

5.3.2 Antiviral assay optimization

To maximise the throughput of the assay, it was optimised for 96-well plates. Initially, three different cell seeding densities (20, 40 and $80x10^3$ cells/well) and two MOI (0.5 and 1) were tested for 72 and 96 hpi. After initial seeding testing, we noticed that Calu-3 cells needed more than 24 hours to adhere to the plates if they were not treated with poly-lysine or collagen. Therefore, cells were seeded 36 hours prior to infection. Cells

were infected with the SARS-CoV-2 England/02/2020 strain. After 72 and 96 hpi the supernatant was harvested, and the viral titre was determined by plaque assay (**Figure 21**). By the end of a 4-day assay, the viral titre dropped to between $1.02x10^3$ to $1.47x10^4$ plaque forming unit (PFU)/mL for MOI 0.5 and MOI 1 infections, which is more than one order of magnitude lower compared to 72 hpi in which the highest titre was achieved with a cell density of $80x10^3$ cells/well and MOI 0.5, resulting in a titre of $1.05x10^5$ PFU/mL. For both MOIs, viral secretion at 72 hpi was highest with a seeding density of $80x10^3$ cells/well, $1.05x10^5$ PFU/mL and $7.83x10^4$ PFU/mL (for MOI 0.5 and 1, respectively). Therefore, experiments were proceeded with seeded $80x10^3$ cells/well, MOI 0.5 for 72 hours.

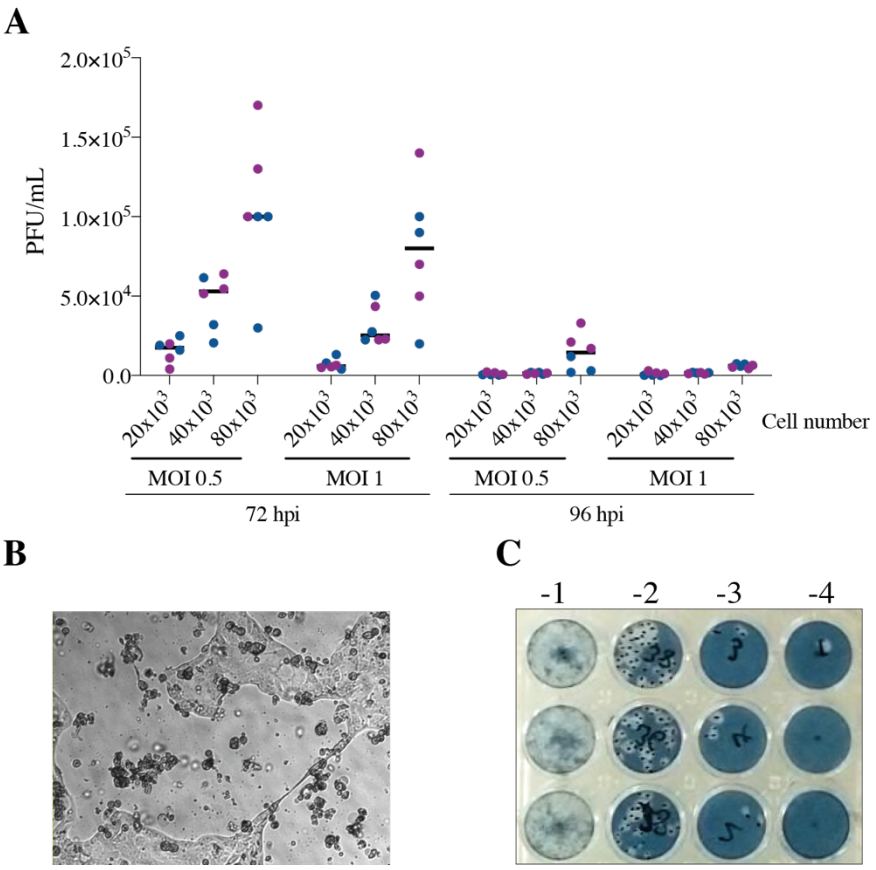

Figure 21: SARS-CoV-2 infection optimization. (A) Cells at three different seeding densities were infected in duplicates (blue and purple) at MOI 0.5 and 1 for 72 or 96 hours. Supernatant was used to detect secretion of infectious SARS-CoV-2 virions in triplicate by plaque assay. The line represents the mean value of the indicated points. (B) Representative microscopy image of Calu-3 cells infected with SARS-CoV-2 at MOI 1 at 72 hpi. (C) Representative picture of a plaque assay.

After identifying an optimal cell density and MOI for the infection assay, the effect of DMSO at various concentrations on cell viability and infection was tested, since it was the most common solvent used for the compounds tested (**Figure 22A**). The CC_{10} of DMSO was 2.6% (by volume), however 1% DMSO had no influence on cell viability and was therefore chosen as the maximum concentration for further assays. We also tested whether DMSO itself was antiviral against SARS-CoV-2, for which titres were measured by both plaque and focus forming assay, since the latter increased the throughput of the experiment (**Figure 22B**). An antiviral effect was observed for

DMSO, which showed differences between the two assays (**Table 10**). At 1% DMSO, the concentration chosen for further screening, a decrease of ~70% (72% for PFU/mL and 70% for focus forming unit (FFU)/mL) in the secretion of infectious virions was measured. Even though the read-out for 1% DMSO was similar between the two assays and showed no statistical significance calculated by a nonparametric t-test, the values for the IC_{10} and IC_{50} displayed a bigger discrepancy but were within the standard deviation of each other and no statistically significant difference could be calculated.

As we needed to increase the throughput of the antiviral screen, focus forming assay (**Figure 22C**). assay was chosen, and based on the antiviral effect of DMSO itself, a corresponding DMSO concentration to each concentration of the compound was used as the reference.

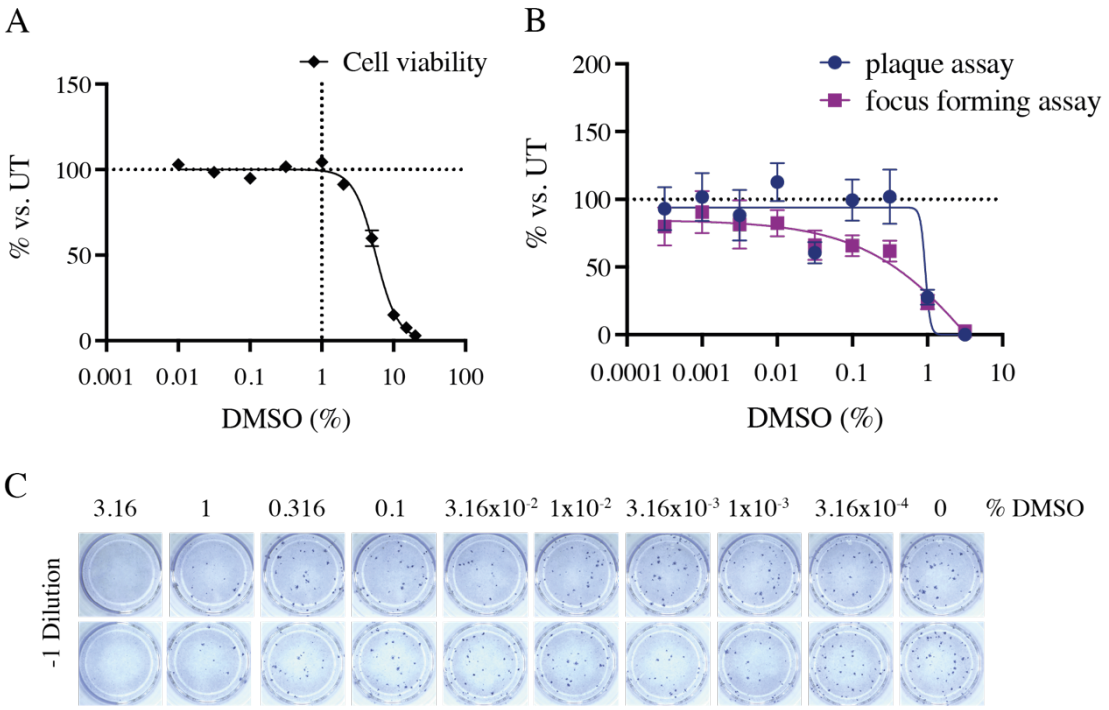

Figure 22: Validation of the effect of different DMSO concentrations on cell viability and viral infections on Calu-3 cells. (A) Calu-3 cells were seeded at $80x10^3$ cells/well 36 hours prior incubation with DMSO for 72 hours. Cell viability was measured by MTS which measures the metabolic mitochondrial activity. Values are shown as the mean of technical quadruplicates and error bars representing the standard error of the mean. (B) Detection of secreted infectious SARS-CoV-2 virions (72 hpi, MOI 0.5) treated with DMSO and comparison between plaque and focus forming assay. Values are shown as the mean of two independent experiments with standard errors. (C) Representative picture of focus forming assay in Vero E6 cells when infected for 24 hours with supernatant containing secreted infectious virions from Calu-3 cells, stained against SARS-CoV-2 nucleoprotein. Focus forming units were detected using the ELISPOT system.

Table 10: Antiviral effect of % DMSO measured by plaque or focus forming assay.

	Plaque assay	Focus forming assay
IC_{10}	0.74%	N/A
IC_{50}	0.93%	0.36%
IC_{90}	1.10%	2.29%

5.3.3 Antiviral screen

With the assay parameters determined (**Figure 23**), I was involved in screening 152 compound (the compounds are listed in **Appendix II, Table 34-36**). On each plate, controls containing the exact DMSO concentrations corresponding to those of each test compound were used to control for the DMSO effect, since DMSO alone was antiviral at certain concentrations. Infected, untreated cells were used as infection control. Additionally, supernatant of mock-infected cells was used in FFU staining to subtract background in the staining protocol.

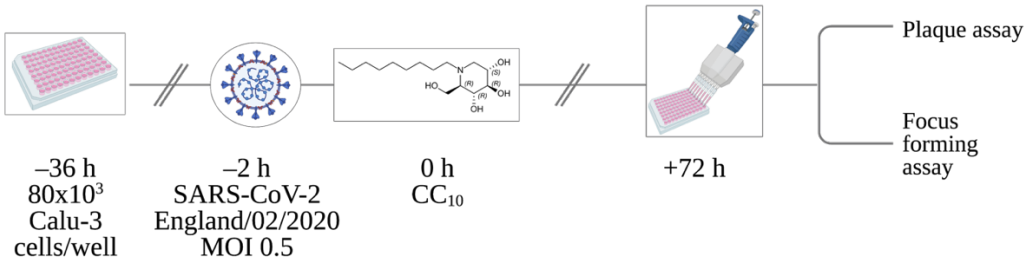

Figure 23: Schematic of viral infectivity assay. After determining the CC_{10} concentrations of drugs by MTS assay, Calu-3 cells were infected with SARS-CoV-2 for 2 hours. The medium was then removed and replaced with potential antiviral compounds at the respective CC_{10} concentration and incubated for a further 72 hours. We used plaque assays, or to increase the throughput of testing compounds, focus forming assays, in order to measure the antiviral activity of compounds. On each plate, a corresponding concentration of DMSO was used as a control for each drug concentration; staining of mock-infected cells was used as background in focus forming assay staining.

5.3.4 Antiviral effect of FDA-approved drugs

Out of the 152 compounds tested, 55 compounds were FDA-approved and used to treat various conditions. Eleven compounds were DAAs, of which only Boceprevir achieved a reduction of 44% in viral secretion in the initial screen and was therefore

tested in a full antiviral screen (**Figure 24A**; **Table 11**; full information of compounds in **Appendix II, Table 34**). Boceprevir is a protease inhibitor, acting on the NS3/4a protease of HCV, inhibiting its viral replication (444). In the full SARS-CoV-2 antiviral screen, Boceprevir achieved an IC_{50} of 89.1 µM, which was below the CC_{10} concentration of >100 µM (CC_{10} above tested concentration; SI1 = >1.12).

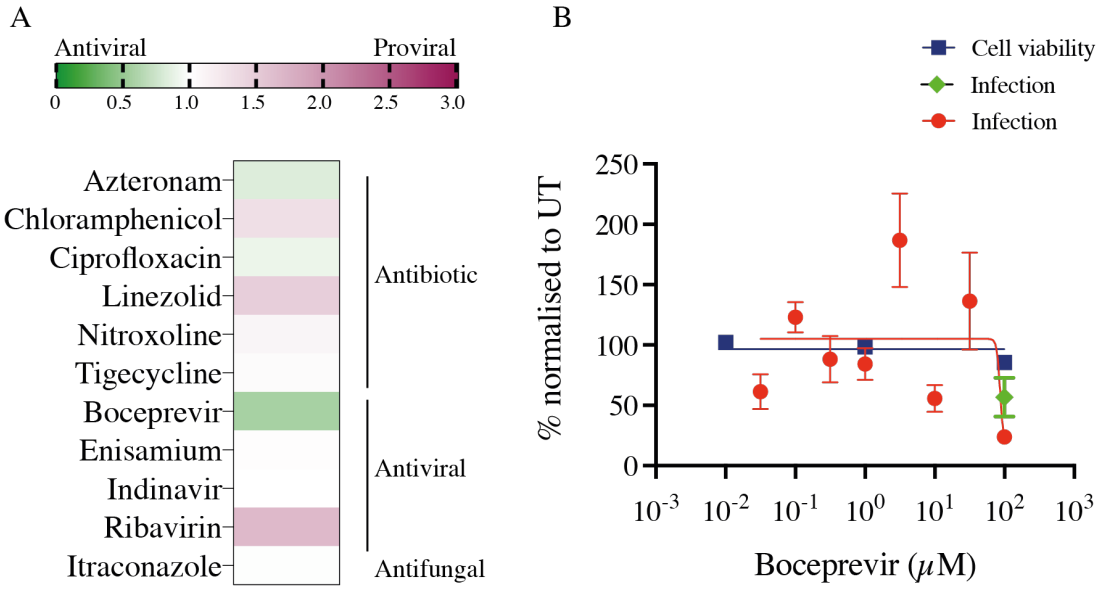

Figure 24: FDA-approved direct-acting drugs tested against SARS-CoV-2. (A) 11 compounds were tested against SARS-CoV-2 infected (MOI 0.5) Calu-3 cells for 72 hours. The supernatant was removed and analysed by plaque or focus forming assay as indicated in Appendix II, Table 36. (B) For Boceprevir the IC_{50} (89.1 µM) was below the highest concentration measured for toxicity (100 µM). In green, preliminary screen n = 2 (with technical triplicates), in red full antiviral screen n = 1 (with technical triplicates), in blue cell viability n =1 (with technical quadruplicates). Error bars are shown as standard error of the mean of three or four technical replicates. Data were fitted using Prism, with a comparison of fits between a horizontal line and a four-parameter dose-response curve (with a 95% confidence interval) with limitation that the bottom of the curve be < 0, using the extra sum-of-squares F test to determine the better fit, with $p < 0.05$ required to reject the horizontal line.

Table 11: List of tested FDA-approved direct-acting compounds. Displaying the drug concentration, percentage of infection normalised to untreated, and IC_{50}, IC_{90} and selectivity index (SI1 = CC_{50}/IC_{50}; SI2 = CC_{10}/IC_{90}). SEM, standard error of the mean.

Compound name	µM used	% infection vs. UT	SEM	CC_{50} (µM)	CC_{10} (µM)	Full antiviral	IC_{50} (µM)	IC_{90} (µM)	SI1	SI2
Aztreonam	50	82.0	2.5							
Chloramphenicol	1000	130.8	34.4							
Ciprofloxacin	66.7	90.0	4.0	217.2	90.5					
Linezolid	1000	147.8	20.0							
Nitroxoline	1	109.8	13.1	82.3	33.9					
Tigecycline hydrate	10	105.5	6.3	83.6	8.1					
Boceprevir	100	56.9	19.6	>100		yes	89.1		>1.1	
Indinavir	10	99.4	8.0	144.1	80.9					
Enisamium	10	102.8	11.2		396.0					
Ribavirin	10	167.5	58.9	222.9	17.3					
Itraconazole	1.325	98.6	7.2		4.4					

Next, we tested 44 FDA-approved host-targeting compounds, some of which are approved for use in cancer or as anti-inflammatory agents (**Figure 25**, **Table 12**, full information in **Appendix II, Table 35**). Among these, seven compounds achieved a viral reduction of at least 40% (Raloxifene, Nafamostat, 5-Thioguanine, Cisplatin, Silmitasertib, Miglustat, and Amiloride). A full antiviral dose-curve was performed for six of these compounds; however, due to compound in availability issues, a full antiviral dose-curve for Raloxifene was not performed.

Raloxifene is a selective oestrogen receptor modulator (SERM) (445). This compound decreased infectious virion secretion by 82.4% at a concentration of 81.2 µM and would have been screened for a full antiviral dose-response curve if the compound was available. Nafamostat is a synthetic serine protease inhibitor that has been approved by the EMA to treat cystic fibrosis (446). The use of Nafamostat as an anticoagulant treatment for patients undergoing continuous renal replacement therapy has been approved in Asian countries (447). This drug displayed an IC_{50} of 2.6 µM and an IC_{90} of 5.0 µM with a high SI (SI1 = 75.0; SI2 = 6.9, **Figure 25B**). Several anti-cancer

drugs were tested, including 5-Thioguanin, a purine analogue which blocks the use and synthesis of purine nucleotides and is widely used as an anti-cancer and immunosuppressive drug (448). However, 5-Thioguanin did not achieve an IC_{50} below its CC_{10} concentration. The SI could not be calculated, because no measurements at CC_{50} were performed (**Figure 25C)**. Cisplatin is an alkylating compound that binds to DNA, inducing single-stranded DNA breaks, which trigger blockage in cell division and the induction of apoptosis (449). It is used in chemotherapy against various cancers (450). In the SARS-CoV-2 antiviral assay, cisplatin achieved an IC_{50} of 96.2 µM, but a CC_{10} could not be calculated at the highest dose tested of 100 µM, leading to a SI >1.0 (**Figure 25D)**. The kinase inhibitor Silmitasertib (451) showed a strong antiviral effect at low micromolar concentration (IC_{50} of 0.24 µM), however it did not reach an IC_{90} (SI1 = 93.4) (**Figure 25E)**. Amiloride inhibits sodium reabsorption and is therefore used as an antikaliuretic-diuretic agent. In the initial screen, a decrease of secreted infectious virions by 88.5% was measured. However, in the full antiviral screen these results could not be reproduced and therefore no IC_{50} or IC_{90} are reported (**Figure 25F**). The glycoside hydrolase inhibitor Miglustat is an iminosugar approved for the treatment of Gaucher disease. Miglustat showed an IC_{50} of 169.5 µM but did not achieve an IC_{90} even at the maximum concentration tested of 2 mM with no cytotoxicity (**Figure 25G**).

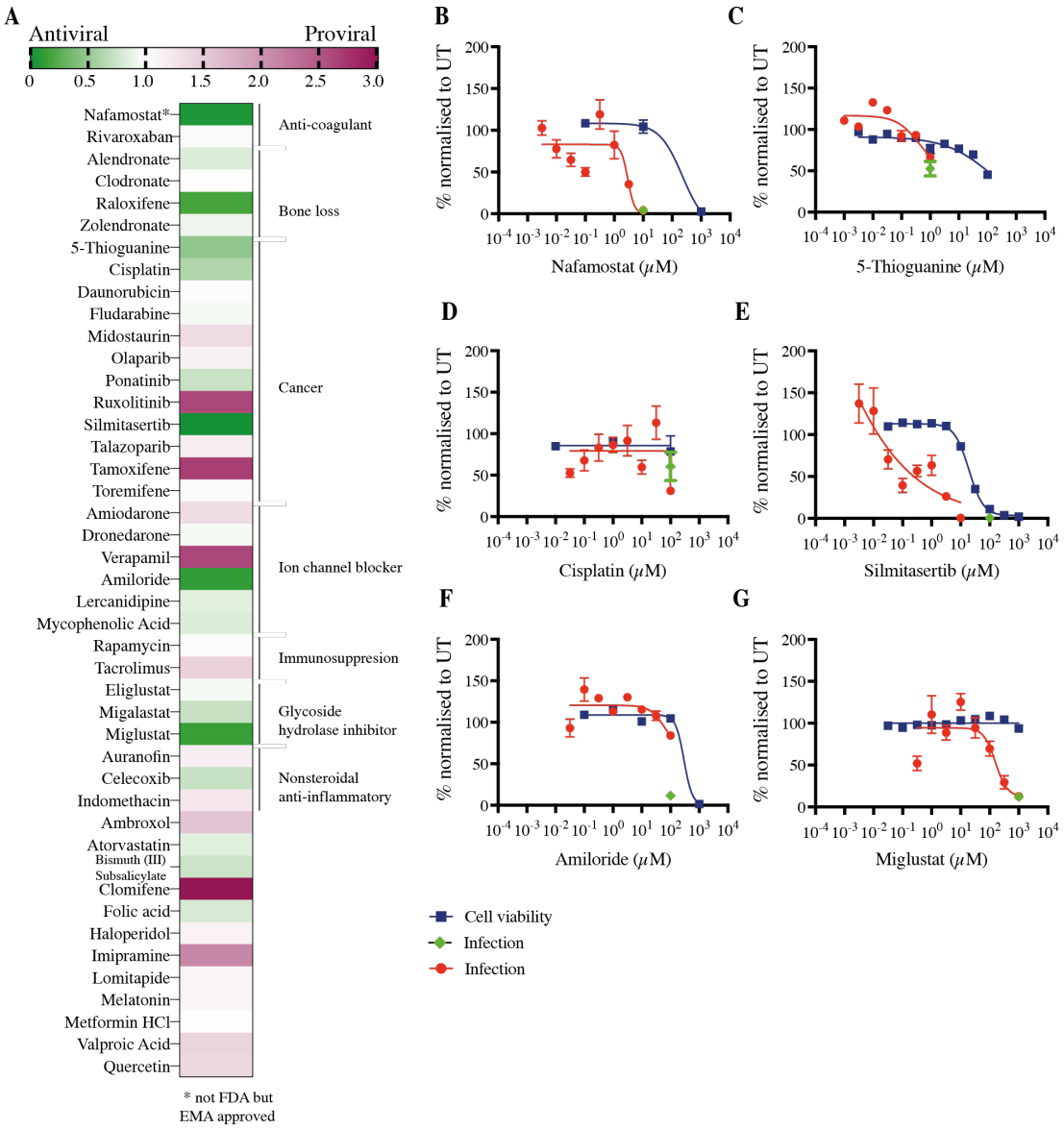

Figure 25: FDA-approved host-directed drugs tested against SARS-CoV-2. (A) 44 compounds were tested in Calu-3 cells infected with SARS-CoV-2 for 72 hours at MOI 0.5. Virus-containing supernatant was harvested and analysed by either plaque assay or focus forming assay, as indicated in Appendix II, Table 36. (B) Nafamostat (C) 5-Thioguanine (D) Cisplatin (E) Silmitasertib (F) Amiloride (G) Miglustat. Raloxifene could not be further investigated due to lack of compound availability. In green, preliminary screen n=2 (with technical triplicates), in red full antiviral screen n=1 (with technical triplicates), in blue cell viability n=1 (with technical quadruplicates). Error bars are shown as standard error of the mean of three or four technical replicates. Data were fitted using Prism, with a comparison of fits between a horizontal line and a four-parameter dose-response curve (with a 95% confidence interval) with limitation that the bottom of the curve be < 0, using the extra sum-of-squares F test to determine the better fit, with $p < 0.05$ required to reject the horizontal line.

Table 12: List of tested FDA-approved host-targeted compounds. This table describes the drug concentration, percentage of infection normalised to untreated, IC_{50}, IC_{90} and selectivity index (SI1 = CC_{50}/IC_{50}; SI2 = CC_{10}/IC_{90}). SEM, standard error of the mean. *not FDA- but EMA-approved.

Compound name	µM used	% infection vs. UT	SEM	CC_{50} (µM)	CC_{10} (µM)	Full antiviral	IC_{50} (µM)	IC_{90} (µM)	SI1	SI2
Nafamostat*	10	4.2	1.9	196.6	44.8	yes	2.6	5.0	75.0	6.9
Rivaroxaban	1	106.9	4.3		5.8					
Alendronate	1	81.5	5.2		11.1					
Clodronate	10	98.8	3.9		10.1					
Raloxifene	81.2	17.6	3.7	82.8	70.1					
Zoledronate	1	90.7	4.2	29.2	2.8					
5-Thioguanine	1	46.8	10.2	96.6	0.04	yes				
Cisplatin	100	60.7	21.1	>100		yes	96.2		>1.0	
Daunorubicin	0.1	104.7	25.8	0.227	0.014					
Fludarabine	1	94.9	5.6	51.48	6.36					
Midostaurin	1	134.8	12.9	61.9	6.8					
Olaparib	1	113.0	6.8							
Ponatinib	10	72.3	25.8	90.3	89.1					
Ruxolitinib	10	262.5	10.0	531.4	439.0					
Silmitasertib	10	0.50	0.14	22.8	9.0	yes	0.24		93.4	
Talazoparib	0.05	116.7	6.8							
Tamoxifene	1	269.1	7.7	10.05	4.5					
Toremifene	12.7	106.3	10.5	26.6	14.4					
Amiodarone	24.5	133.4	8.6	27.74	24.3					
Dronedarone	1	95.0	12.4	46.8	31.5					
Verapamil	86.7	264.7	39.4	97.4	88.7					
Amiloride	100	11.5	1.5	310.7	174.7	yes				
Lercanidipine	1	85.3	7.2	19.75	2.4					
Mycophenolic Acid	0.1	82.0	14.0	1.78	0.16					
Rapamycin	0.001	97.9	17.7		0.002					
Tacrolimus	1	143.8	19.1	12.22	4.5					
Eliglustat	10	93.8	14.5	432.4	499.0					
Migalastat	1000	70.6	9.6							
Miglustat	1000	12.5	1.7	>1000	>1000	yes	169.5		>5.9	
Auranofin	1	116.0	9.2	71.8	52.9					
Celecoxib	10	71.2	5.6	92.01	63.6					
Indomethacin	100	124.9	5.3	593	353.2					
Ambroxol	121	156.5	8.4	305.3	121.2					
Atorvastatin	10	84.4	9.1	33.49	30.5					
Bismuth (III) Subsalicylate	10	73.2	26.2							
Clomifene	3.23	301.8	12.7	5.76	3.2					
Folic acid	51.5	79.1	8.5		343.7					
Haloperidol	100	111.9	10.3	265.8	210.7					
Imipramine	11.4	212.0	8.3	85.3	16.0					
Lomitapide	1	110.0	10.2	9.42	8.0					
Melatonin	100	110.2	27.2	958.2	506.9					
Metformin HCl	100	102.3	19.8		875.2					
Valproic Acid	100	141.9	16.9		950.1					
Quercetin	100	140.6	12.7							

5.3.5 Antiviral effect of pre-, clinical or experimental compounds

In total, we tested 97 different compounds for their ability to counter SARS-CoV-2. These compounds were either in clinical phases I-III or had evidence, based on literature, of providing an antiviral effect against SARS-CoV-2. Of these, 64 were considered as direct-acting and were analogues of antibiotics or antivirals. Out of these compounds, eight COVID-19 Moonshot compounds and Antipain achieved a sufficient antiviral effect to undergo full screening (**Figure 26**, **Table 13,** full information in **Appendix II**, **Table 36**). Even though these nine compounds showed an antiviral effect in the initial screening, an IC_{50} could only be determined for seven of these compounds (**Figure 26B-H**).

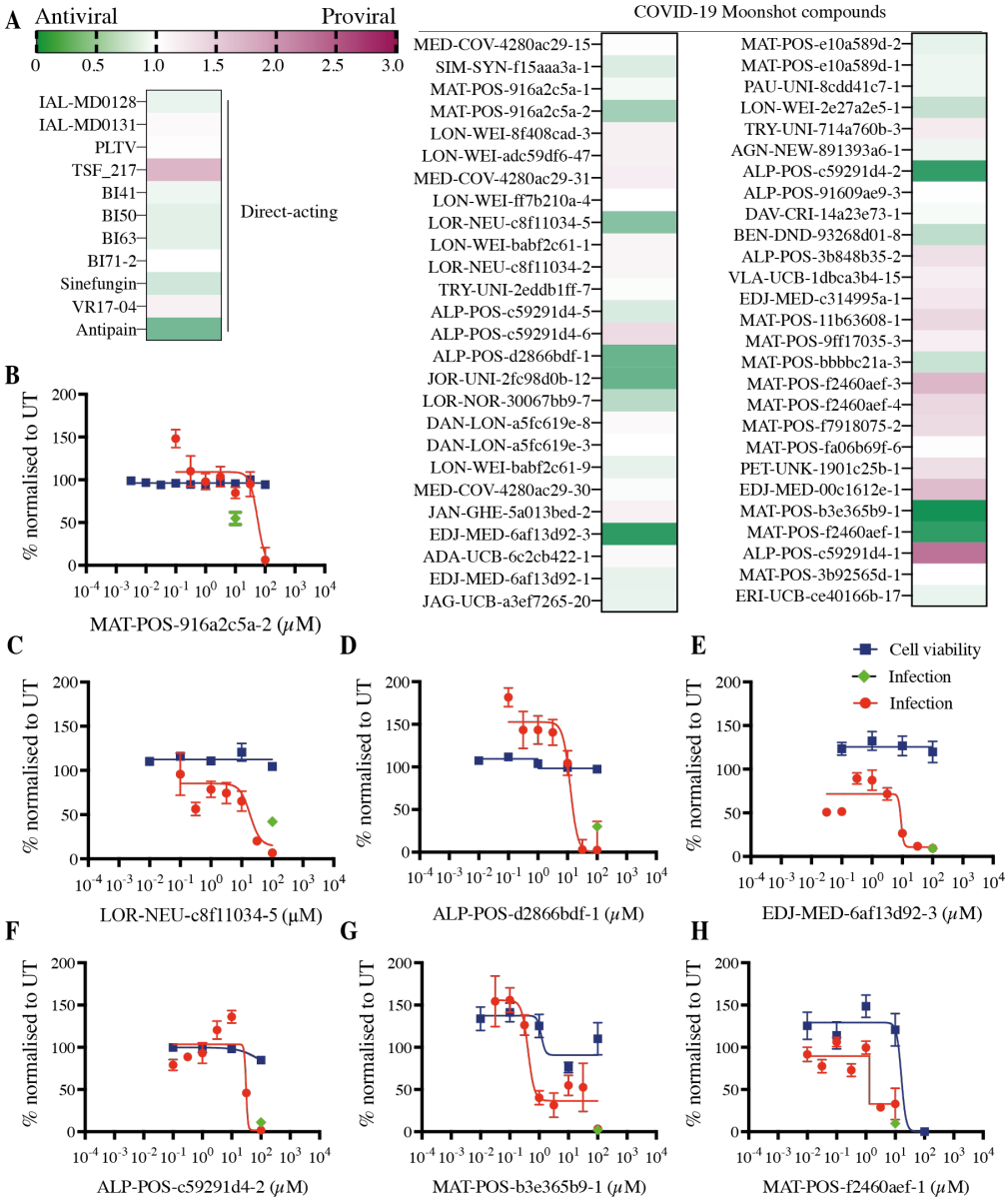

Figure 26: Direct-acting clinical, pre-clinical and experimental compounds tested against SARS-CoV-2. (A) 64 compounds were tested in Calu-3 cells infected with SARS-CoV-2 for 72 hours at MOI 0.5. Virus-containing supernatant was harvested and either analysed by plaque or focus forming assay, as indicated in Appendix II, Table 36, to determine a reduction in secretion of infectious virions. (B) MAT-POS-916a2c5a-2 (C) LOR-NEU-c8f11034-5 (D) ALP-POS-d2866bdf-1 (E) EDJ-MED-6af13d92-3 (F) ALP-POS-c59291d4-2 (G) MAT-POS-b3e365b9-1 (H) MAT-POS-f2460aef-1. In green, preliminary screen n=2 (with technical triplicates), in red full antiviral screen n=1 (with technical triplicates), in blue cell viability n=1 (with technical quadruplicates). Error bars are shown as standard error of the mean of three or four technical replicates. Data were fitted using Prism, with a comparison of fits between a horizontal line and a four-parameter dose-response curve (with a 95% confidence interval) with limitation that the bottom of the curve be < 0, using the extra sum-of-squares F test to determine the better fit, with $p < 0.05$ required to reject the horizontal line.

Table 13: List of tested experimental direct-acting compounds. This table displays the drug concentration, percentage of infection normalised to untreated, IC_{50}, IC_{90} and selectivity index (SI1 = CC_{50}/IC_{50}; SI2 = CC_{10}/IC_{90}) of these drugs. SEM, standard error of the mean.

Compound name	Drug (µM)	% infection vs. UT	SEM	CC_{50} (µM)	CC_{10} (µM)	Full antiviral	IC_{50} (µM)	IC_{90} (µM)	SI1	SI2
IAL-MD0128	10	89.7	34.1	112.3	39.0					
IAL-MD0131	50	91.1	20.8	405.0	401.4					
PLTV	100	88.5	15.9							
TSF_217	100	150.2	28.0							
BI41	100	82.2	15.2							
BI50	100	73.6	13.8							
BI63	100	76.3	13.9							
BI71-2	100	87.4	16.5							
Sinefungin	500	73.2	12.7							
VR17-04	10	102.8	22.1		91.1					
Antipain	100	28.7	5.3			yes				
MED-COV-4280ac29-15	1	103.1	7.3							
SIM-SYN-f15aaa3a-1	1	81.4	13.1	46.7	26.8					
MAT-POS-916a2c5a-1	1	93.4	8.3	47.4	19.1					
MAT-POS-916a2c5a-2	1	55.0	8.9	>100	>100	yes	58.2	110.4	>1.7	>0.91
LON-WEI-8f408cad-3	1	115.3	18.0	29.9	3.71					
LON-WEI-adc59df6-47	1	115.5	8.8	45.03	28.62					
MED-COV-4280ac29-31	1	116.6	12.5	7.012	0.41					
LON-WEI-ff7b210a-4	10	101.3	6.8	87.9	73.5					
LOR-NEU-c8f11034-5	100	39.5	6.0	>100	>100	yes	15.5	54.2	>6.5	>1.9
LON-WEI-babf2c61-1	10	111.6	5.1		88					
LOR-NEU-c8f11034-2	10	110.3	6.0		80.4					
TRY-UNI-2eddb1ff-7	10	99.6	5.6		72.3					
ALP-POS-c59291d4-5	100	79.7	8.5							
ALP-POS-c59291d4-6	100	137.5	8.7							
ALP-POS-d2866bdf-1	100	31.8	5.5	>100	>100	yes	15.3	26.8	>6.5	>3.7
JOR-UNI-2fc98d0b-12	100	31.4	6.8	17.1	11.6	yes				
LOR-NOR-30067bb9-7	10	65.2	0.9		20.4					
DAN-LON-a5fc619e-8	10	106.2	3.6	76.1	61.7					
DAN-LON-a5fc619e-3	10	100.5	3.2	71.7	55.7					
LON-WEI-babf2c61-9	10	86.6	2.8	77.3	60.9					
MED-COV-4280ac29-30	10	96.6	4.4	87.1	76.6					
JAN-GHE-5a013bed-2	10	113.2	2.9	104	73.6					
EDJ-MED-6af13d92-3	100	9.4	2.3	>100		yes	15.3		>6.5	
ADA-UCB-6c2cb422-1	10	107.8	3.4		59					
EDJ-MED-6af13d92-1	10	86.8	3.3							
JAG-UCB-a3ef7265-20	100	88.0	4.9							

TAT-ENA-80bfd3e5-1, MAT-POS-e10a589d-2	100	86.9	9.3							
MAT-POS-e10a589d-1	1	91.0	3.3							
PAU-UNI-8cdd41c7-1	10	90.8	3.4	32.2	30.9					
LON-WEI-2e27a2e5-1	10	69.9	3.2	81.7	58.5					
TRY-UNI-714a760b-3	10	119.3	5.2							
AGN-NEW-891393a6-1	10	91.9	2.3							
ALP-POS-c59291d4-2	100	11.1	2.9	>100	52.2	yes	31.2	36.8	>3.2	1.4
ALP-POS-91609ae9-3	10	98.7	3.8	86.1	20.0					
DAV-CRI-14a23e73-1	10	94.9	1.9	81.8	71.5					
BEN-DND-93268d01-8	10	67.4	5.3							
ALP-POS-3b848b35-2	10	130.7	21.2							
VLA-UCB-1dbca3b4-15	10	116.6	20.0							
EDJ-MED-c314995a-1	10	124.7	5.6	12.9	9.52					
MAT-POS-11b63608-1	10	139.7	11.4	26.0	17.6					
MAT-POS-9ff17035-3	1	115.8	3.7	2.1	1.2					
MAT-POS-bbbbc21a-3	100	71.8	4.6							
MAT-POS-f2460aef-3	10	169.5	13.6	79.3	59.2					
MAT-POS-f2460aef-4	1	139.5	5.7	9.8	7.9					
MAT-POS-f7918075-2	1	135.0	7.4		1.1					
MAT-POS-fa06b69f-6	100	101.7	11.5							
PET-UNK-1901c25b-1	1	131.7	5.0	24.5	8.2					
EDJ-MED-00c1612e-1	1	164.7	8.2	4.9	1.1					
MAT-POS-b3e365b9-1	100	0.7	1.2	>100		yes	0.70		>142.9	
MAT-POS-f2460aef-1	10	9.7	2.1	17.7	14.0	yes	1.32		13.4	
ALP-POS-c59291d4-1	100	228.0	12.2							
MAT-POS-3b92565d-1	10	99.8	3.0	13.7	10.5					
ERI-UCB-ce40166b-17	100	88.4	7.3		80.6					

The remaining 44 compounds are host-targeting drugs against various conditions such as cancer or viral infections (**Figure 27**, **Table 14**, full information in **Appendix II, Table 37**). The latter group of compounds includes various glycosyl hydrolases and synthase inhibitors, of which Lucerastat (*N*B-DGJ, **Figure 27C**), an inhibitor of glucosylceramide synthase, might soon be FDA-approved for Fabry disease (452). (D)-

PDMP and *N*N-DGJ (glycolipid inhibitors, **Figure 27F**), and the iminosugars M*O*N-DNJ, *N*-(6'-[4″-azido-2″-nitrophenylamino]hexyl)-1-DNJ (*N*AP-DNJ), *N*N-DNJ (which inhibit various glucose-binding enzymes, **Figure 27D, E, G**) also decreased secretion of infectious virions by 40%. For *N*N-DGJ (**Figure 27F**), a cell viability test was not performed and therefore the extent of the antiviral effect cannot be stated with certainty. However, for (D)-PDMP a four-parameter dose-response curve could be fitted to the data points.

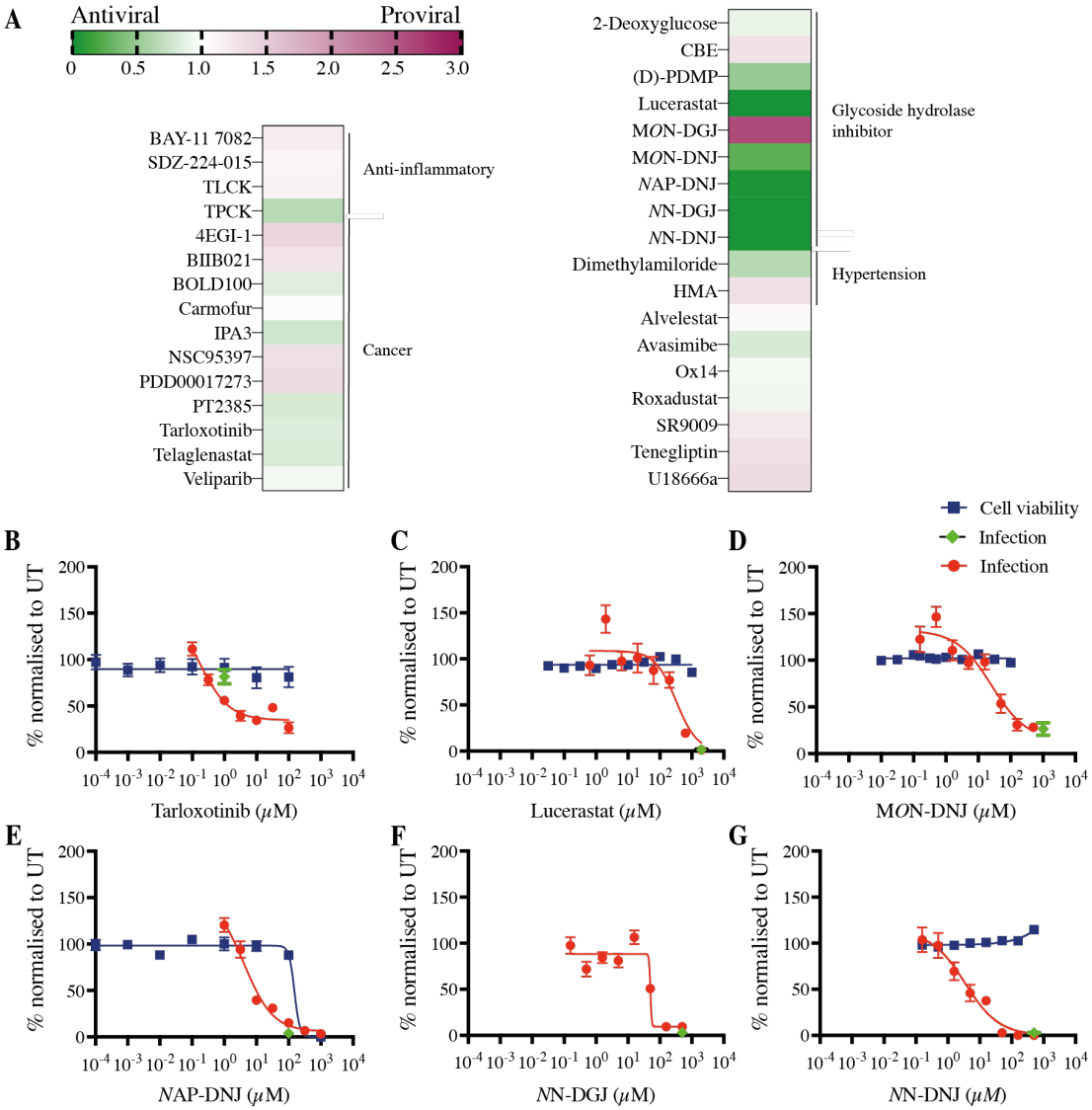

Figure 27: Clinical, pre-clinical and experimental compounds tested against SARS-CoV-2. (A) 44 compounds were tested in Calu-3 cells infected with SARS-CoV-2 for 72 hours at MOI 0.5. Virus-containing supernatant was harvested and either analysed by plaque or focus forming assay, as indicated in Appendix II, Table 36, to determine either a reduction in secretion of virions and/or in the infectivity of secreted virions. (B) Tarloxotinib (C) Lucerestat (D) M*O*N-DNJ (E) *N*AP-DNJ (F) *N*N-DGJ (G) *N*N-DNJ. In green, preliminary screen n=2 (with technical triplicates), in red full antiviral screen n=1 (with technical triplicates), in blue cell viability n=1 (with technical quadruplicates). Error bars are shown as standard error of the mean of three or four technical replicates. Data were fitted using Prism, with a comparison of fits between a horizontal line and a four-parameter dose-response curve (with a 95% confidence interval) with limitation that the bottom of the curve be < 0, using the extra sum-of-squares F test to determine the better fit, with $p < 0.05$ required to reject the horizontal line.

Table 14: List of tested experimental potential host-targeted compounds. The drug concentration, percentage of infection normalised to untreated, and IC_{50}, IC_{90} and selectivity index (SI1 = CC_{50}/IC_{50}; SI2 = CC_{10}/IC_{90}) are shown. SEM, standard error of mean.

Compound name	Drug (µM)	% infection vs. UT	SEM	CC_{50} (µM)	CC_{10} (µM)	Full antiviral	IC_{50} (µM)	IC_{90} (µM)	SI1	SI2
BAY-11 7082	1	99.4	21.3	9.5	2.5					
SDZ-224-015	0.1	110.9	13.9	2.0	0.06					
TLCK	100	112.6	12.0							
TPCK	1	64.1	15.5	25.3	4.5					
4EGI-1	1	141.0	18.3	16.8	8.6					
BIIB021	0.01	126.7	23.8	0.59	0.005					
BOLD100	10	83.2	8.7							
Carmofur	0.1	104.5	27.3	92.1	6.9					
IPA3	100	76.0	33.9							
NSC95397	1	129.8	16.1	8.8	2.5					
PDD00017273	5	134.1	8.0							
PT2385	200	79.1	10.4							
Tarloxotinib	100	81.9	11.9	>100	1.1	yes	1.4		>74.1	
Telaglenastat	1	80.0	13.8		4.7					
Veliparib	5	93.6	3.5							
2-Deoxyglucose	100	88.8	25.3	360.9	109.2					
CBE	200	128.4	21.6							
(D)-PDMP	10	50.6	13.7		0.012	yes				
Lucerastat	2000	1.4	0.28	>2000		yes	364.1		>5.5	
MON-DGJ	250	258.4	14.7		2.7					
M*O*N-DNJ	100	26.4	3.3	>100	>100	yes	71.9		>1.4	
*N*AP-DNJ	100	3.5	0.86	150.4	95.8	yes	9.8	160.6	15.4	0.60
*N*N-DGJ	500	3.0	0.70			yes	50.0	62.8		
*N*N-DNJ	500	2.8	0.20	>500	>500	yes	4.6	60.2	>21.6	>1.7
Dimethyl amiloride	10	63.8	8.3	94.1	30.0					
HMA	1	130.8	16.5	9.4	8.5					
Alvelestat	1	107.3	7.6		3.9					
Avasimibe	1	79.7	9.4	9.5	1.0					
Ox14	1	93.6	3.5	16.0	9.8					
Roxadustat	100	91.5	10.1							
SR9009	1	122.6	16.3							
Teneligliptin	47.7	130.8	13.4	69.3	477.0					
U18666a	0.202	134.7	16.9	7.9	0.31					

5.4 Discussion

The emergence of SARS-CoV-2 has resulted in widespread morbidity and mortality, necessitating the development of new therapeutics and vaccines. Approved drugs may be repurposed to allow the accelerated implementation of therapeutics that have been tested in humans. So far, the corticosteroid dexamethasone has been shown to significantly improve the outcome of COVID-19. This drug has saved one out of eight lives of critically ill SARS-CoV-2 infected patients (428) and was approved in June 2020 in the United Kingdom (453). In addition, remdesivir was approved to treat hospitalized patients above the age of 12, shortening the recovery time from 15 to 10 days (179).

In this chapter, antiviral cellular screens against SARS-CoV-2 were conducted to identify compounds that could be re-purposed to aid the battle against this virus. Specifically, 152 compounds were evaluated, of which 55 were already FDA-approved. The remaining compounds are either in clinical trials, in preclinical studies and have displayed *in vitro* activity against SARS-CoV-2 or related viruses, or have been shown to bind specific SARS-CoV-2 proteins. We chose the human lung adenocarcinoma Calu-3 cell line to represent a more physiologically relevant host cell for SARS-CoV-2 infection. It has been shown that the antiviral activity of compounds against SARS-CoV-2 can be cell type specific. In Dittmar *et al.*, out of 33 drugs that were antiviral in Huh7.5 cells, only nine showed antiviral activity in Calu-3 cells (435). In lung epithelial Calu-3 cells, SARS-CoV-2 entry is pH independent and requires TMPRSS2, while in mammalian cell lines such as African Green Monkey kidney Vero

cells and human hepatoma Huh7.5 cells, viral entry requires a low pH and is triggered by acid-dependent endosomal proteases (435). However, it is not known if there is horizontal spreading in Calu-3 cells at MOI 0.5, and we have not evaluated this. If a drug affects the structure of the receptor or induces metabolic changes that take longer to manifest than the timescale of our assay, we would not detect any potentially induced antiviral activity. For example, if the receptor is misfolded under drug treatment but its half-life is 72 hours, then we would not detect this with this assay and a longer drug pre-treatment of cells would be necessary.

Of the 152 compounds tested, 23 (of which eight were FDA-approved) decreased the PFU/mL or FFU/mL by 40% compared to untreated cells in the initial screen. Eighteen of these compounds had IC_{50}s lower than their CC_{10} (or a CC_{10} was not reached at the highest concentration tested), six had IC_{90}s lower than their CC_{10} (or a CC_{10} was not reached at the highest concentration tested), summary in **Table 15**. Amongst these six compounds were inhibitors of the Niemann-Pick type C1 (NPC1) receptor, kinases, oxidative stress inducer, protease inhibitor, and inhibitors for glycan processing enzymes.

SARS-CoV-2 uses ACE2 for cellular entry and employs the serine protease TMPRSS2 for S protein priming (123). The serine protease inhibitor nafamostat inhibits the catalytic activity of TMPRSS2 (454) and was previously shown to be antiviral against MERS (455) and SARS-CoV-1 (456,457). Nafamostat is currently in phase II/III clinical trials, and has been approved in Japan as an anti-coagulant in renal replacement therapy (458). Moreover, prophylactic anticoagulation treatment with heparin showed

a decreased risk of mortality in COVID-19 (459). A case report of a patient administered heparin in combination with Nafamostat showed improvement in severe hypoxemia induced by COVID-19 (460).

A recent study identified that the nucleoprotein of SARS-CoV-2 interacts with the NPC1 receptor by co-immunoprecipitation (461). Nieman-Pick type C disease is a hereditary disorder, which impairs cholesterol egress from the late endosome/lysosome compartment, resulting in intracellular cholesterol accumulation (462). The endosomal NPC1 receptor membrane protein controls intracellular cholesterol trafficking, and acts as a host receptor for EBOV (463,464). NPC1 knockout A549 cells showed a reduction in SARS-CoV-2 entry (465,466). We tested several compounds known to have an effect on the NPC1 receptor, namely Amiodarone, Clomifene, Imipramine, Itraconazole, Raloxifene, Toremifene and U18666A. Apart from U18666A, these compounds are FDA-approved for various diseases (467–473). Raloxifene, Tamoxifen and Clomiphene can inhibit EBOV infection (474). U18666A treatment has an antiviral effect in HCoV 299E infected Huh7 cells (461), while Clomifene has an antiviral effect against SARS-CoV-2 in Vero cells (475) and Amiodarone and Imipramine have an antiviral effect in Calu-3 cells (476). Amiodarone is in a phase II clinical trial against SARS-CoV-2, and a Tamoxifen clinical trial is in preparation. However, our results show that only Raloxifene has an antiviral effect by decreasing secretion of infectious virions by 82.4% compared to untreated. On the other hand, Clomifene and Imipramine appeared to be pro-viral by 301.75% and 212.00%, respectively.

Viruses in the *Coronaviridae* family are known for manipulating stress granules and associated RNA biology (477,478). Stress granule formation is thought to be mainly an antiviral reaction. SARS-CoV-2 N proteins bind to stress granule proteins Ras GTPase-activating protein-binding protein 1 (G3BP1) and G3BP2 (118). The casein kinase 2 (CK2) promotes assembly of stress granules, by phosphorylation of G3BP1 (479). Silmitasertib, an inhibitor of the CK2 kinase, displayed an antiviral effect with an IC_{50} of 0.24 µM, which is similar to its antiviral activity against SARS-CoV-2 in Vero E6 cells (IC_{50} = 2.34 µM) (480). Silmitasertib is currently in phase II clinical trials against COVID-19.

The SARS-CoV-2 main protease Mpro cleaves the polyprotein of pp1a and pp1b. Its functional relevance in the viral life cycle, along with the lack of closely associated homologues in humans, makes it an appealing target for antiviral drug development. Several compounds capable of binding Mpro identified by MS: 5-Thioguanine, Auranofin and Cisplatin (FDA-approved host-targeting compounds), Bismuth (III) Subsalicylate, TPCK, BAY-11, TLCK, IPA3, NSC95397, and Antipain (experimental host-targeting compounds), Boceprevir (an approved anti-HCV drug), Nitroxoline (an approved antibiotic) and TSF_217, PLTV, BI41, BI50, BI71-2 and BI63 (penicillin derivatives) (481). 5-Thioguanine and Boceprevir showed an antiviral effect, however these compounds did not reach an IC_{50} at CC_{10} concentrations and were therefore regarded as toxic to cells. 5-Thioguanine inhibited the PLpro catalytic domain of MERS, SARS-CoV-1 and SARS-CoV-2 (482–484) and was found antiviral in our cellular screen, but no IC_{50} could be reached. Auranofin inhibits SARS-CoV-2 replication, by inhibition of redox enzymes leading ultimately to intrinsic apoptosis

(485), and is anti-inflammatory in Huh7 cells (486). Bismuth (III) Subsalicylate was antiviral in a Syrian hamster model (487), whereas NSC95397 showed antiviral activity against IVA in human bronchial epithelial cells (488). Cisplatin never featured as an antiviral in the literature before, but here we found an IC_{50} of 96.2 μM in SARS-CoV-2 infected Calu-3 cells. Cisplatin is an alkylating agent used to treat a number of cancers by causing DNA damage in cancerous cells; it also can induce reactive oxygen species (ROS) that trigger cell death independent of DNA damage in oxidative stressed cells (489). However, because of its associated cytotoxicity, cisplatin is an unlikely candidate for development into an antiviral.

COVID-19 Moonshot compounds are structurally designed to bind to Mpro of SARS-CoV-2. For seven of 53 compounds an IC_{50} could be determined with values ranging from 0.70 – 58.2 μM. The work on these compounds is ongoing and better analogues are being synthesised to improve specificity, toxicity and antiviral activity. The Moonshot initiative has developed several distinct chemical series, including three non-covalent series of Isoquinolines, Quinolones and Benzotriazoles. These current lead scaffolds show good antiviral activity also against other SARS-CoV-2 variants (tested in other laboratories in the COVID-19 Moonshot initiative) in various cell types (IC_{50} <200 nM), and moderate activity against other coronaviruses (IC_{50} ~3 μM). These compounds have progressed further with the goal of performing pre-clinical studies in animals.

Glycosyl hydrolase inhibitors such as iminosugars with glucose stereochemistry have antiviral effects against a number of viruses. As compounds targeting host cell

glycosylation they have been developed as potential broad-spectrum antivirals for decades. Iminosugars inhibit enzymes such as the ER αGluI and αGluII, which are involved in the early stages of N-linked glycoprotein folding in the ER (490), leading to misfolding of viral glycoproteins and subsequently to antiviral effects against e.g. HIV-1, HVC, DENV, ZIKV, IVA and EBOV (199,201–203,246,261,290,442,491). Some iminosugars with either glucose or galactose stereochemistry, provided they have a sufficiently long alkyl sidechain, can also inhibit the ceramide glucosyltransferase which catalyses the first step in glycosphingolipid biosynthesis. Galactose-based iminosugars inhibit the ceramide glucosyltransferase but not the α-glucosidases (492). We showed that iminosugars are also antiviral against SARS-CoV-2 in infected Calu-3 cells. Miglustat, M*O*N-DNJ, and *N*N-DNJ were also shown to be antiviral against SARS-CoV-2 by others (493–496).

Table 15: Summary of compounds reaching an IC_{50}, IC_{90} and selectivity index (SI1 = CC_{50}/IC_{50}; SI2 = CC_{10}/IC_{90}).

Compound name	FDA-approved	Used for	Mechanism of action	CC_{50} (µM)	CC_{10} (µM)	IC_{50} (µM)	IC_{90} (µM)	SI1	SI2
Boceprevir	yes	Antiviral	HCV NS3/4 protease inhibitor	>100	>100	89.1		>1.12	
Nafamostat*	yes	Anticoa-gulant	Serine protease inhibitor	196.6	44.8	2.62	4.96	75.0	6.90
Cisplatin	yes	Cancer	Alkylating agent	>100	>100	96.2		>1.04	
Silmitasertib	yes	Cancer	Casein kinase 2 inhibitor	22.8	8.96	0.24		93.44	
Miglustat	yes	Gaucher disease	Glucosylceramide inhibitor	>1000	>1000	169.5		>5.89	
MAT-POS-916a2c5a-2	no	Antiviral	Mpro inhibitor	>100	>100	58.2		>1.72	
LOR-NEU-c8f11034-5	no	Antiviral	Mpro inhibitor	>100	>100	15.5	54.2	>6.45	>1.85
ALP-POS-d2866bdf-1	no	Antiviral	Mpro inhibitor	>100	>100	15.3	26.8	>6.54	>3.73
EDJ-MED-6af13d92-3	no	Antiviral	Mpro inhibitor	>100	>100	15.3		>6.54	
ALP-POS-c59291d4-2	no	Antiviral	Mpro inhibitor	>100	52.2	31.2	36.8	>3.21	1.42
MAT-POS-b3e365b9-1	no	Antiviral	Mpro inhibitor	>100	>100	0.70		>142.90	
MAT-POS-f2460aef-1	no	Antiviral	Mpro inhibitor	14.5	12.5	1.32		13.4	
Tarloxotinib	no	Cancer	Pan-HER tyrosine kinase inhibitor	>100	1.14	1.35		>74.1	
Lucerastat	no	Gaucher disease	Glucosylceramide inhibitor	>1000	>1000	364.1		>2.75	
M*O*N-DNJ	no	Antiviral	ER glycosidases inhibitor	>100	>100	71.9		>1.39	
*N*AP-DNJ	no	Antiviral	ER glycosidases inhibitor	150.4	95.8	9.76	160.6	15.41	0.60
*N*N-DGJ	no		Glycolipid inhibitor			158	215		
*N*N-DNJ	no	Antiviral	ER glycosidases inhibitor	>500	>500	4.62	60.2	>21.6	>1.66

*not FDA- but EMA-approved.

Some compounds tested did not show sufficient antiviral effects in the initial screening but are currently in clinical trials against SARS-CoV-2. Some of these have anti-inflammatory activity (Ruxolitinib, Rapamycin, Tacrolimus, Indomethacin, Melatonin, and Metformin) and could potentially dampen excessive cytokine release, which might have a positive effect in severe COVID-19 patients. Such effects, however, cannot not be detected in our cell culture assay (118,497–499), or they may be cell-type specific (435,500). Additionally, in our assay, the drugs were incubated at 37°C and if the compounds have a short half-life (e.g. Quercetin (501)), the cells could be considered 'untreated' for a substantial portion of the assay. Likewise, if the drug tested (e.g., inhibitor of glycolipid pathways) affect molecules with long half-lives,

any antiviral effects might not be seen during the duration of the assay in our screening set-up. One possibility would be to pre-treat the cells with such drugs so that any antiviral effect would be more pronounced and easier to detect by the readout described in this chapter. Additionally, testing drugs in combination, e.g., the DAA Nafamostat with a HTA iminosugar, was discussed and will be performed in the future. However, toxicity testing of the combination of both drugs also need to be performed for such drug combination tests.

In interactions with general practitioner and clinical committees, concerns were raised about commonly used antibiotics or other commonly prescribed drugs being potentially proviral. Therefore, we tested a range of antibiotics (Aztreonam, Chloramphenicol, Ciprofloxacin, Linezolid, Nitroxoline, Tigecycline hydrate) of which only Chloramphenicol and Linezolid showed strong effects with an increase in secretion of infectious virions by 30.80% and 47.83%, respectively, at 1 mM. However, for both antibiotics the standard deviation was that high, that we cannot be certain about a proviral role of these drugs for SARS-CoV-2. Although most compounds tested either had no effect on the virus or were antiviral, a few notable exceptions emerged and were considered proviral based on our data. The FDA-approved compounds Clomifene, Tamoxifene, Verpamil, Ruxolitinib, Imipramine, and Ribavirin led to an increase of secretion of infectious virions by a minimum of 50%. These results were also immediately communicated to clinical committees, so that general practitioners (GP) may interrogate their databases and monitor any potentially adverse effects.

Of the drugs that we showed to have some antiviral activity in our cellular assay, Silmitasertib and Nafamostat are currently in clinical trials against SARS-CoV-2. All iminosugars tested showed antiviral activity. For *N*B-DNJ (Miglustat) an antiviral effect was observed in the millimolar range. With known pharmacokinetics and pharmacodynamics data in humans for this compound (502), the concentrations needed to achieve an antiviral effect are likely too high to be useful for the treatment of patients. However, at the highest *N*B-DNJ concentrations previously administered to patients (48 mg/kg/day for 1 month (290)) the effect may be beneficial and Miglustat is currently being considered for a 'baseline' study in uncomplicated COVID-19 (personal communication). M*O*N-DNJ, which had previously completed a clinical phase I trial against DENV where it was given at 150 mg TID, reached an IC_{90} concentration of 75.1 µM against SARS-CoV-2 in our results. This concentration is still too high for a therapeutic treatment regimen of low drug concentrations given TID. M*O*N-DNJ was recently shown to save IVA- and DENV-infected mice from virally induced death when given in one or two consecutive single high-doses (203). Such an approach may prove feasible for SARS-CoV-2 treatment and awaits confirmation in an animal infection model.

In this chapter, a medium through-put screening platform to screen drugs against SARS-CoV-2 was established. We chose to use Calu-3 cells, which demonstrate characteristics of bronchial epithelium, and can be infected by SARS-CoV-2, to work with a more physiologically relevant cell line compared to other cell lines (e.g., macaque kidney cell line Vero E6 or the human hepatocyte Huh7 cell line). To increase our screening capacity, screening was performed in a 96-well format. Compounds

were initially tested at a single concentration close to their established CC_{10} concentration (deemed tolerable as the highest concentration) to identify if the compound had any effect at all before performing a more time-consuming dose-response experiment.

As it had been observed that compounds which are antiviral in some cell lines (e.g., in Vero E6 cells) can have less or no activity in SARS-CoV-2 infected Calu-3 cells (435), and vice versa, it was imperative to choose the more physiologically relevant Calu-3 cells, despite their slower growth rate and increased difficulty in infection compared to other cell lines, which consequently slowed down the screening process. Our two-step screening approach – I) infect and treat Calu-3 cells and then II) use virus-containing supernatant to reinfect naïve Vero E6 cells and perform plaque forming or focus forming assays – is more time consuming than direct measurements via CPE detection or IF staining. However, it is more accurate and informative and can inform on antiviral activity regardless of whether it is viral entry, expression, secretion, or infectivity that is affected by the compound screened. Although this approach is therefore superior to some of the faster readouts and capable of detecting several antiviral MOA, some mechanisms still cannot be evaluated by this approach, e.g., lipid metabolism or misfolding of the entry receptor, which would require longer pre-treatment of the cells with the compounds under investigation, and/or different time points to collect samples for analysis.

Initially, we only had one negative control (untreated cells) and did not include a positive control in our experiments, for several reasons: no such positive control was

known in the very early days and when that changed it was not immediately available. Not only did we work under enormous time pressure but also every test slot was precious and re-screening a known drug seemed like wasting precious resources at that early stage. However, we included Remdesivir routinely later on for well-controlled, publishable experiments.

The method protocol we have developed in the early days of the COVID-19 pandemic can be applied in any future pandemic caused by a respiratory virus if no vaccine or host-targeting broad-spectrum antiviral is available. There are faster ways of screening, but in that case aspects of physiological relevance of the test system often need to be sacrificed. A combination of faster and more relevant testing systems is advisable, as we have also done in the context of the COVID-19 Moonshot project (427), where our screen was used last in the triage, as the most time-consuming and effort-intensive, but nevertheless as the one used as the strongest indicator for relevant hits. In a pandemic, clinicians are forced to triage the numerous repurposable drugs, deciding which should advance to clinical trials for the novel disease. Preliminary results from cellular studies are critical in making these decisions. The work reported here is instrumental in prioritising and selecting, but also deprioritising several candidate drugs for COVID-19 clinical trials. We were in contact with clinical decision-making committees throughout the pandemic and based on our screening, many drugs were deselected or deprioritised. This is very important information to provide, as it results in resources being used more effectively and patients being administered medication with a higher likelihood of success.

Chapter 6 Short-term inhibition of ER alpha-glucosidase I as an antiviral strategy

6.1 Introduction

Influenza A- and dengue virus have been a growing global threat to public health long before the arrival of SARS-CoV-2. They are well-studied viruses and as such we know much more of their biology than other emerging viruses, including SARS-CoV-2. Accordingly, we have extensively studied their dependence on the ER glycoprotein folding pathway. One important study in this context is the Sadat *et al.* report, which describes two siblings with a rare genetic defect in *MOGS* (encodes ER αGluI) who showed resistance to viral infections, thereby identifying ER αGluI as a key antiviral target (296). Subsequently, Warfield and Alonzi *et al.* showed that this resembled the observation made with iminosugar-treated cells, where a single dose of UV4B (the hydrochloride salt form of M*O*N-DNJ) was capable of inhibiting ER αGluI *in vivo* and was sufficient to prevent death in mice infected with lethal viral doses, even when treatment is started as late as 48 hpi (203). This is the basis for targeting ER αGluI with either a single or two separate high doses of an iminosugar like M*O*N-DNJ, or, as discussed in this following chapter, the already FDA-approved drug *N*B-DNJ, to alter treatment paradigms for acute viral disease through the development of a therapeutic regime consisting of one or two high doses. While this work was begun before and was interrupted by the COVID-19 pandemic, it could not be more relevant to the current situation. If such a single 'post-infection prophylactic' dose could be

tested in a COVID-19 setting, as it is planned now and was found to work, it could provide a much-needed stop gap in an early pandemic situation where not much is known about an emerging virus and a vaccine is not yet available or not yet rolled out worldwide.

It had been observed that the single high-dose approach worked *in vivo* in mice, and that the antiviral effect appeared to correlate with ER αGluI inhibition, as demonstrated by the appearance and presence of triglucosylated FOS for up to 16 hours. However, the mechanism was not known how exactly this short-lived inhibition of ER αGluI resulted in the long-lasting presence of triglucosylated FOS and how the antiviral effect originated, so it was sought to recreate the *in vivo* observation in mice in an *in vitro* setting that was more amenable to manipulation and interrogation. The primary aim was to find out what (if any) protein could be attributed to the long-lived triglycosylated N-glycans may cause the prolonged antiviral effect that outlasted actual enzyme inhibition. DENV was used as our test virus, due to its relevance for global health and our existing research interests in this particular virus. As mentioned in section 1.1.1, in the case of severe dengue which may lead to death it is not the virus but the excessive overstimulation of the immune system which can be lethal. Indeed, the virus is usually entirely gone by the time the immune response becomes dysregulated. This is difficult to recreate in a cellular system, and here I tried to see how much, if any, of the *in vivo* observations, could be recapitulated in a cellular setting. I succeeded insofar as I observed a long-lasting antiviral effect and noted IF staining patterns indicating accumulation of viral glycoproteins. This observation, combined with mRNA levels of relevant UPR players, led to the hypothesis that

overloading of the ER may cause the UPR to initiate apoptosis. As UPR is known to be highly cell type-specific and specific inhibitors of the various UPR arms are not sufficiently potent at non-toxic levels to distinguish between the extent of the involvement of individual UPR arms, I then decided to create hiPSC knockouts of the main UPR constituents.

However, due to the COVID-19 pandemic interrupting this work at the time, I did not have the chance to properly phenotypically describe any of the results from stem cell knockouts I generated, nor did I have the opportunity to explore downstream effects following infection with DENV.

6.1.1 Aims of this chapter

- Establish an amenable and easy-to-manipulate *in vitro* cellular system that could recapitulate single high-dose iminosugar effects as observed in dengue infected mice.
- Understand the underlying MOA of the observed long-lasting antiviral effect.
- Create stem cell knockouts that could help evaluate the contribution of the various UPR arms towards the effects observed.

6.2 Material and Methods

All dengue virus work was carried out in a biosafety 3, schedule 5 laboratory.

6.2.1 Dengue virus

6.2.1.1 Virus propagation

Viral stocks of DENV serotype 2 (DENV2), strain 16681 (a gift from E. Gould, Centre for Ecology and Hydrology, Oxford, UK) were obtained by infecting C6/36 cells at a MOI of 0.15 in Leibnitz L15 media containing 1.5% HI FBS, 1% NEAA, 1 mM HEPES, 100 U/mL penicillin and 0.1 mg/mL streptomycin at 28°C without CO_2. Supernatant containing virus was harvested and media replaced on day 3, 7 and 10 (depending on the CPE). Virus containing supernatant was cleared from cell debris by centrifugation at 400 x *g* for 15 minutes at 4°C. The virus was concentrated by precipitation with 10% w/v polyethylene glycol M_n 6000 (Sigma-Aldrich) and 0.6% sodium chloride (Sigma-Aldrich) at pH 7.2 overnight at 4°C. Subsequently, the concentrated virus was collected by centrifugation at 2830 x *g* for 45 minutes at 4°C. The resulting pellet was resuspended in C6/36 infection media and stored at −80°C until further use.

6.2.1.2 *In vitro* DENV2 infection and drug treatment

Infection of Vero E6 cells was carried out as follows: The virus was diluted in Minimal Essential Medium Eagle (MEM, Sigma-Aldrich) without any supplements to determine virus PFU at a specific MOI. Before virus infection, cells were washed once with Hanks' Balanced Salt Solution (HBSS, Gibco), and virus was added and left to attach on cells for 90 minutes (20°C, with rocking). Upon removal of virus inoculum,

cells were washed with PBS and fresh growth media with or without drugs was placed on cells for further incubation at 37°C and 5% CO_2 for various lengths of times, depending on the experiment. The supernatant was harvested and centrifuged for 5 minutes (400 x *g,* 4°C) to pellet any cell debris and stored at −80°C for plaque assays or DENV2 NS5 qRT-PCR. The cells were harvested, pelleted by centrifugation (5 minutes, 2000 x *g*, 4°C) and stored at −80°C or subsequently lysed and inactivated in RNAeasy (Qiagen) lysis buffer or 1% Triton X-100 for FOS analysis.

6.2.1.3 Quantification of viral dengue RNA

Viral RNA in the cell supernatant was extracted using the QiaAmp Viral RNA mini kit (Qiagen) according to the manufacturer's protocol and analysed by a one-step qRT-PCR for DENV2 NS5 using the Luna Universal one-step RT qPCR kit (New England BioLabs) on the Applied Biosystems 7500 FAST real-time PCR system (Thermo Fisher Scientific). Genome copies of the 3'UTR of DENV2 were quantified by a Thermo-Start DNA Taq polymerase enabling the release of fluorescently labelled dyes from a DENV2 3'UTR-specific probe as described previously (probe and primer sequences are listed in **Table 16**) (503). The reaction mix (for concentrations see **Table 17**) was prepared according to the manufacturer's protocol in MicroAmp Fast 96-well reaction plates (Thermo Fisher Scientific) and sealed with MicroAmp optical adhesive film (Thermo Fisher Scientific). The thermal cycles were programmed as follows: Synthesis of complementary DNA (cDNA) was achieved for 30 minutes at 48°C, followed by thermocycling with fluorescence detection of the TAMRA-probe by 40 cycles of 1) activation of the Thermo-Start Taq polymerase for 15 minutes at 95°C; 2) denaturing double-stranded DNA for 15 seconds at 95°C; 3) annealing of primers for

1 minute at 60°C; and 4) primer extension for 1 minute at 55°C and a final fluorescence read step for 25 seconds at 60°C. All samples were run in technical duplicates and compared to a standard curve. PCR thermocycling with fluorescence detection was performed for 40 cycles.

Table 16: Sequence of forward and reverse primer, Taqman probe and DENV2 NS5 standard for DENV2 qRT-PCR.

Name	Detection	Sequence (5' – 3')	Company
Forward primer	DENV2 3'UTR	GAAAGACCAGAGATCCTGCTGTCT	Thermo Fisher Scientific
Reverse primer	DENV2 3'UTR	ACCATTCCATTTTCTGGCGTT	Thermo Fisher Scientific
Probe	FAM-TAMRA	(6FAM)-AGCATCATTCAAGGCAC-(TAM)	Applied Biosystems UK
Standard	DENV2 3'UTR	GAAAGACCAGAGAUCCUGCUGUCUCCU CAGCAUCAUUCCAGGCACAGAACGCCA GAAAAUGGAAUGGU	IDT

Table 17: Concentration of DENV2 3'UTR qRT-PCR reaction.

Component	Final concentration
Luna 2x Onestep reaction mix	1:2
Forward primer NS5 5'	0.4 µM
Reverse primer NS5 5'	0.4 µM
FAM-TAMRA probe	0.2 µM
Luna enzyme	1:100

6.2.1.4 Plaque assay

To quantify infectious DENV2 titre, virus containing supernatant was plaqued on naïve LLC-MK_2 cells. To ensure single cells were in solution prior to seeding LLC-MK_2 cells were resuspended with a 19-gauge needle (Terumo) and seeded at a concentration of $0.35x10^6$ cells per well of a 12-well dish (Greiner) and allowed to

adhere overnight to form a monolayer. On the day of the assay, the media was aspirated, and cells were washed once with HBSS, then 100 µL of MEM media with 100 µL of the serial dilutions of virus in MEM were added to each well. The virus dilutions were incubated for 90 minutes at 20°C with rocking, before the viral supernatant was removed and the first overlay (composition see **Table 18**) mixed 1:1 with low-melting point tissue grade agarose (Sigma-Aldrich) was added and allowed to solidify at 20°C, adapted from (504). Cells were cultured for a further five days at 37°C, 5% CO_2, until the second overlay containing 1.8% low-melting agarose (1:1 mix, composition shown in **Table 18**) supplemented with neutral red staining live cells was added, and allowed to solidify at 20°C. Cells were cultured for a further 16-24 hours at 37°C, 5% CO_2 and plaques were counted by eye. Plaque counts were converted to PFU/mL as below:

$$PFU/mL = n\ x\ dilution\ factor\ x\ 10$$

n = number of plaques

Table 18: Composition of first and second overlay for plaque assay. Hank's balanced salt solution A consisted of 2.47 M NaCl, 107.3 mM KCl, 16.6 mM $MgSO_4$, 25.3 mM $CaCl_2$ in deionized water. Hank's balanced salt solution B consisted of 8.5 mM Na_2HPO_4, 8.8 mM KH_2PO_4, 111.0 mM $C_6H_{12}O_6$ in deionized water. Both solutions were filter-sterilised before use.

1st overlay	2nd overlay	
10%	10%	Hank's balanced salt solution A
10%	10%	Hank's balanced salt solution A
2%	2%	100x MEM vitamin solution (Thermo Fisher Scientific)
2%	2%	50x MEM amino acid solution (Thermo Fisher Scientific)
10%	-	HI FBS (Gibco)
1.2%	1.2%	L-glutamine (Gibco)
4%	-	7.5% sodium bicarbonate; pH 8.2 (Gibco)
2%	2%	100 U/mL penicillin and 0.1 mg/mL streptomycin (Sigma-Aldrich)
Fill up to 100%		Deionized water
pH 8.2	pH 6.3	Adjust pH to

6.2.2 Quantification of intracellular RNA

Cellular RNA was isolated from cells using Qiagen RNeasy mini kit (Qiagen) according to the provided protocol. Quantitative RT-PCR was performed using Taqman primer (Thermo Fisher Scientific) for the gene of interest (**Table 19**), following the same protocol as described in 6.2.1.3 Gene expression levels were expressed as a percentage change by the $\Delta\Delta C_t$ method compared to housekeeping gene RPLP2.

Table 19: Taqman primers and probes used for the quantification of cellular mRNA.

Gene of interest	Gene ID
XBP1g	Hs 03929085_g1 (FAM)
XBP1m	Hs 00231936_m1 (FAM)
HSPA5	Hs 00607129_gH (FAM)
ATF4	Hs 00909569 (FAM)
RPLP2	Hs 01115128_gH (VIC)

6.2.3 Free oligosaccharide analysis

To determine the amount and type of free oligosaccharides accumulating inside cells, Vero E6 were seeded in a 6-well plate and either DENV2 or mock-infected and treated with or without iminosugars. After specific time points, the supernatants were removed, cells washed thrice with PBS, and treated with Trypsin-EDTA solution (Sigma-Aldrich) for 5 minutes at 37°C, 5% CO_2. The trypsin-cell mix was diluted with MEM, samples centrifuged at 400 x *g* for 5 minutes, supernatant was removed, and the cell pellet washed once with PBS. After a final centrifugation step at 400 x *g* for 5 minutes, the cell pellet was lysed in 1% Triton-X100 and after 1 hour 50x diluted with ddH_2O and the protein concentration was determined by Bradford assay (described in section 3.6.1. Free oligosaccharides were prepared as previously described in (375) and in section 4.2.5.1. After removal of excess 2-AA label, labelled oligosaccharides were purified using a Concanavalin A-Sepharose 4B column (Sigma-Aldrich). Glycans were separated by normal phase high performance liquid chromatography (NP-HPLC; described below) and peak areas were used to assess molar quantity in comparison to those of standards of known identity, a panel of synthetic oligosaccharide. FOS generation was normalised to total protein concentration in the sample.

6.2.4 NP-HPLC to measure FOS

NP-HPLC was used to separate the purified 2-AA labelled FOS according to (375). A 4.6×250 mm TSK Gel Amide-80 column (Sigma-Aldrich) was installed in a Waters Alliance 2695 separations module. An in-line Waters 474 fluorescence detector set at Ex_λ = 360 nm and Em_λ = 425 nm was used. Data were processed using Empower

software. Glucose unit (GU) values were determined by interpolation from a standard curve obtained by analysing a 2-AA labelled glucose oligomer standard (partial hydrolates of dextran). Under peak area was used to assess molar quantity and normalised to measured protein concentration described in section 3.6.1.

6.2.5 Immunofluorescence

Vero E6 cells were seeded in 8-well slides (Ibidi GmbH). Following infection and iminosugar treatment (as described in 6.2.1.2), supernatant was aspirated, and cells were washed with PBS. Fixation of the cells and inactivation of DENV was achieved by the addition of 4% PFA (Alfa Aesar) in PBS for 15 minutes at 4°C. Fixed cells were washed twice in PBS, followed by permeabilization with 0.5% (volume per volume; v/v) Triton X-100 in PBS for 15 minutes at room temperature. Primary antibody (**Table 20**) was added and incubated for 1 hour at room temperature. Cells were washed three times with PBS and incubated for 1 hour with the corresponding secondary antibody. Cells were washed twice with PBS, followed by counterstaining the DNA with 300 nM 4',6-Diaminidino-2-Phenylindole (DAPI; Thermo Fisher Scientific) for 5 minutes and final two washing steps with PBS. Ibidi-slides were mounted with Vectashield mounting medium (Vector Laboratories Inc), dried at room temperature, and imaged on a Nikon Eclipse TE200-U fluorescent microscope.

Table 20: Primary and secondary antibodies used for immunofluorescence.

Target	Clone	Reactivity	Final concentration	Company
anti-DENV2 E	3H5	mouse IgG1	10 µg/mL	In-house produced, purified from ATCC hybridoma HB-46
anti-DENV prM	2H2	mouse IgG2a	10 µg/mL	In-house produced, purified from ATCC hybridoma HB-114
anti-DENV NS1	DN2	mouse IgG1	1:50	abcam #ab41623
anti-DENV NS4b	polyclonal	rabbit	1:100	Thermo Fisher Scientific #PA5-32198
Donkey anti-Mouse Alexa Fluor™ 488 IgG (H+L)			1 µg/mL	Thermo Fisher Scientific #A32723
Goat anti-Rabbit Alexa Fluor™ 594 IgG (H+L)			1 µg/mL	Thermo Fisher Scientific Invitrogen #PIA32740

6.2.6 Creation of knockout cell lines in hiPSCs

The methods designing guide RNAs, CRISPR transfection and screening were established by Sally A. Cowley in the Sir William Dunn School.

6.2.6.1 Target exon identification and guide RNA design

Homozygous knockouts of the genes *MOGS*, *GANAB*, *EIF2AK3*, *XBP1*, *ERN1*, *ATF6* in hiPSCs were attempted. The method for designing a pair of crispr RNA (crRNA; one part of a guide RNA (gRNA) with a tracrRNA which serves as binding scaffold for the Cas9 nuclease) involved flanking a splice acceptor site, i.e. the first crRNA is targeted against an intron and the second crRNA against the following exon to induce nonsense mediated decay. Several points need to be considered when designing the gRNA: 1) The targeted exon has to be a coding exon; 2) An early exon needs to be targeted, in case nonsense mediated decay is not completely efficient and a truncated protein may still be functional; 3) The first coding exon should be avoided, as this

could result in the usage of an alternative start site and a truncated protein that may exert a phenotype; 4) The last two exons should not be targeted, to ensure nonsense mediated decay; 5) A conserved exon between splice variants of the protein should be chosen; 6) The exons preceding and following the target exon must be out of frame with respect to each other, to ensure a frame shift mutation resulting in an early stop codon and nonsense mediated decay; 7) One should target to delete 100 – 200 b).

If it was not possible to follow these rules when designing crRNA, then an attempt was made to design crRNA of a splice donor site or on either side of an exon. The exon structure of the gene of interest was found on the Ensembl genome browser (https://www.ensembl.org/index.html) and analysed, to identify which exons are conserved among various splice variants, and the protein was checked on UniProtKB/Swiss-Prot reference (https://www.uniprot.org/statistics/Swiss-Prot) to look at the protein domain structure and possibly identify specific functions of the various protein domains.

Once the exon to target was identified, CCtop (https://cctop.cos.uni-heidelberg.de:8043/) CRISPR/Cas9 target online predictor tool was used to select for optimal guides, to choose 20 bp gRNAs with high efficiency and no off-targets. Chosen gRNAs were re-checked with WGE off-target finder tool (https://wge.stemcell.sanger.ac.uk/find_crisprs) and NCBI BLAST (https://blast.ncbi.nlm.nih.gov/Blast.cgi). If the 20 bp crRNA matched with three or more nucleotides in the genome, crRNA constructs were rejected. Designed gRNA were finally checked with the Alt-R HDR design tool for high efficiency and no off-

targets and ordered at IDT. The designed gRNAs must not include the protospacer adjacent motif (PAM) sequence 'NGG'.

6.2.6.2 NEON transfection of ribonucleoprotein in hiPSCs

This method is based on protocols and methods described by Moore *et al.* (505). Briefly, one hour before transfection of the hiPSCs, cells were pre-treated with Rock inhibitor at 10 µM in mTeSR complete. The needed wells of a 24-well plate were coated with Geltrex (Life Technologies) for at least 20 minutes. Transfection was performed using the Neon transfection system (Thermo Fisher Scientific) using the program 'HiTrans' 1400 V, 20 ms width and 1 pulse.

Alt-R CRISPR electroporation enhancer was resuspended in 100 mM Duplex buffer (IDT) and the Alt-CRISPR electroporation enhancer was diluted to 10.8 µM in buffer R (IDT). The gRNAs were resuspended to 100 µM in Duplex buffer. For each transfection 4.4 µL of gRNA, 4.4 µL tracrRNA (IDT) and 1.2 µL Duplex buffer were mixed and incubated for 5 minutes at 95°C. Subsequently, 0.3 µL Cas9 (IDT) with 0.2 µL buffer R, were mixed with 0.5 µL gRNA complex (mix of both gRNAs per knockout) and incubated for 20 minutes at room temperature. The medium of the hiPSCs was aspirated, cells were washed with 0.5 mM EDTA in PBS, and incubated for 5 minutes with EDTA-PBS mix at 37°C. Simultaneously, Geltrex was removed from wells and replaced with 0.5 mL mTeSR with Rock inhibitor. Cells were lifted and diluted to $2.2x10^6$ cells/mL in buffer R. The transfection was prepared by mixing 1 µL ribonucleoprotein (RNP), 9 µL cells and 2 µL transfection enhancer. With a Neon Pipette (Thermo Fisher Scientific) 10 µL of the cell-RNA suspension was drawn and

the Neon Pipette was inserted into the Neon Pipette station (in a Neon tube filled up with 3 mL buffer E). After completion of the Neon transfection, transfected cells were transferred to prewarmed mTeRS with Rock inhibitor and incubated at 37°C, 5% CO_2.

Cells were fed daily with mTeSR medium until they reached a confluency of 80%. Cells were then washed with PBS, lifted with TrypLE (Thermo Fisher Scientific), split into half, and spun for 5 minutes at 400 x *g*. One cell pellet was frozen to extract genomic DNA and the other one was resuspended in 1 mL freeze medium and stored as described in section 3.1.3.2.

6.2.6.3 Genomic DNA extraction and PCR screening

Genomic DNA was extracted from the transfected iPSC pellet using DNAeasy Blood & Tissue kit (Qiagen) according to the manufacturer's protocol. Polymerase chain reaction (PCR) was performed using the Q5 High-Fidelity DNA Polymerase protocol (New England Biolabs). The reaction was run in a Veriti PCR machine (ABI Biosystems). Primers flanking the deletion were used, listed in **Appendix** III**, Table 39**. The agarose gel was run (described in section 3.3.1), the appropriate bands were cut from the gel, and cleaned up using a QIAquick PCR Purification kit (Qiagen) according to manufacturer's protocol. The purified PCR products were sequenced using Source Bioscience using PCR primers.

6.2.6.4 Low density plating of iPSCs for colony picking

Colonies of hiPSCs were picked from mitotically inactivated EmbryoMax® Primary Mouse Embryonic Fibroblast (PMEF, Strain CF1; Sigma-Aldrich) to increase cell

survival of hiPSCs compared to feeder-free culture. PMEF were mitotically inactivated in the James Martin Stem Cell Facility (Sir William Dunn School of Pathology, University of Oxford, UK). Wells of a 6-well plate were coated with 0.1% gelatin (Sigma-Aldrich) for 20 minutes. PMEF cells were thawed and plated at $0.5x10^6$ cells/well in Advanced DMEM (Gibco), 10% HI FCS, 1% GlutaMAX (Gibco) and 0.1% 2-mercaptoethanol (Gibco), and incubated overnight at 37°C, 5% CO_2. On the next day, medium was aspirated, and cells were rinsed with KnockOut™ DMEM (Gibco) to remove any residual FBS. Human embryonic stem cell medium (hES medium, consisting of KnockOut™ DMEM, 20% KnockOut™ Serum Replacement (Gibco), 1% NEAA, 2 mM GlutMAX, 0.1% 2-mercaptoethanol, 100 U/mL penicillin and 0.1 mg/mL streptomycin and 5 µg/mL recombinant human FGF (R&D system)) with 10 µM Rock inhibitor was added to PMEF cells. Transfected iPSCs were thawed, spun and the cell pellet resuspended in hES medium with Rock inhibitor and cells counted. Cells were passed through a cell strainer (40 µm, Falcon®) and various cell numbers ($8x10^3$, $4x10^3$ and $2x10^3$) were plated on the PMEFs and iPSCs-PMEFs mix were incubated at 37°C, 5% CO_2. Remaining cells were plated on Geltrex coated plates, amplified and frozen down as a back-up. Daily 50% hES medium change was performed until hiPSCs colonies were ready for manual picking.

After approximately 7 days colonies were visible. To pick single iPSCs colonies, wells of a 96-well plate were coated with Geltrex for 20 minutes, followed by exchanging the Geltrex with mTeSR with Rock inhibitor. Subsequently, the media was exchanged on the hiPSCs-PMEFs cells with mTeSR with Rock inhibitor and incubated for one hour. For iPSCs clone picking an EVOS core microscope inside a tissue culture hood

was used. A 200 µL pipette (set to 50 µL) was used to pick colonies by scraping the colony off and transferring the cells to a well in a prepared 96-well plate. Each colony was broken into smaller pieces by pipetting up and down.

After several days, depending on the density of cells in each well, two further 96-well plates were coated with Geltrex and replaced with 50 µL/well mTeSR with Rock inhibitor. Media was aspirated from the cells, they were then washed with 0.5 mM EDTA in PBS, lifted with EDTA-PBS and split between the two additional 96-well plates. Wells of the initial plate were filled with 100 µL mTeSR with Rock inhibitor and all three plates were incubated at 37°C, 5% CO_2, and the cells fed daily with mTeSR until the majority of them reached a confluency of 80%. For the initial 96-well plate, media was aspirated, cells washed with PBS and the plate frozen at −20°C for subsequent genomic DNA isolation and diagnostic PCR to identify if homozygous knockout had been successful. Cells from the other two 96-well plates were frozen down by removing the media, washing the cells with PBS and lifting them with 0.5 mM EDTA in PBS for 5 minutes at 37°C, 5% CO_2. The EDTA containing solution was removed and cells frozen in the 96-well plate in 100 µL cool freezing medium (described in section 3.1.3.2). Plates were sealed with adherent foil and cells frozen in a CoolCell™ freezing container (Corning) at −80°C. Plates were transferred into liquid nitrogen storage on the following day.

6.2.6.5 DNA extraction and diagnostic PCR

DNA was isolated from cells in the frozen 96-well plate from 6.2.6.4. Cells were lysed in 50 µL lysis buffer (10 mM Tris pH 7.5, 10 mM EDTA, 10 mM NaCl, 0.25% v/v

Triton X-100, freshly added 1 mg/mL proteinase K (Sigma-Aldrich)) and incubated overnight at 55°C in a humidified box. Subsequently, 100 µL of ice-cold precipitation solution (75 mM NaCl, 100% v/v ethanol) was added to the wells without mixing and DNA left for precipitation for 2 hours at room temperature. Plates were inverted and liquid discarded, DNA was stuck to the plate and washed twice with 70% v/v ethanol, extracted gDNA was airdried and resuspended in 50 µL H_2O and incubated overnight at 4°C. Diagnostic PCR was performed as described in section 6.2.6.3.

6.2.6.6 Expansion of knockout iPSC lines

Wells of a 24-well plate were coated with Geltrex for at least 20 minutes, which was then replaced with mTeSR complete with Rock inhibitor. The thawed cells were transferred into a 96-well V-bottom plate and spun at 400 x *g* for 3 minutes. The media was aspirated, and the cell pellets resuspended in mTeRS with Rock inhibitor and transferred to the prepared 24-well plate. Media was exchanged daily with mTeRS complete until cells reached 80% confluency and were split into wells of a 6-well plate. At this stage the media was changed to OXE8 and cells grown to reach six confluent wells of a 6-well plate. At this stage cells were frozen down at $2x10^6$ cells/ cryovial as described in section 3.1.3.2.

6.2.6.7 Single nucleotide polymorphism analysis

For single nucleotide polymorphism analysis, $2x10^6$ hiPSCs were pelleted and their DNA was extracted using the DNeasy Blood & Tissue Kit (Qiagen) according to the manufacturers protocol, including the RNase A incubation to obtain RNA-free DNA.

SNP analysis was performed with 10 µL of 100 ng/µL DNA using Illumina BeadChip, which detects copy number-variation and copy-neutral variants of 654,027 markers. The SNP data were analysed using the Genome Studio software (Illumina) by Jane Vowles and Sally Cowley (James Martin Stem Cell facility, Sir William Dunn School of Pathology, University of Oxford).

6.2.7 Data analysis and fitting

Details of statistical methods for comparisons can be found in the figure legends. All data analysis was performed using Prism 9. Different multiple comparison tests were deployed, 1) Tukey test was used to compare every mean to every other mean 2) the Dunnett's multiple comparison test to compare every mean to a control mean and 3) Šidâk test to compare a set of means to each other.

6.3 Results

6.3.1 Establishment of a suitable cell culture model

Many iminosugars are antiviral in cell lines and primary cells *in vitro* (199,200,202,272). In these published studies, cells were usually treated with comparably low doses of iminosugar, usually enough to achieve inhibitory concentrations for ER αGluII, with administration starting immediately after infection, and continuing over several days, as iminosugars do not get metabolized in cells neither do they degrade in medium/serum (290). In these experiments only αGluII and not αGluI inhibition was observed as measured by FOS levels; however, FOS analysis was only carried out in mock-infected cells.

To understand the mechanism of the long-lasting antiviral effect after a single high-dose iminosugar administration in mice which appeared to correlated with ER αGluI inhibition, a suitable *in vitro* model was needed in which ER αGluII and αGluI inhibition can be achieved. Vero E6 cells were used for these experiments, because they are easy to handle and susceptible to DENV2 infection (506). I compared the infection levels of DENV2 16681 in Vero E6 cells at different days after infection (at MOI 1) by measuring the expression of the DENV2 envelope protein (as detected with the monoclonal antibody 3H5) and by measuring the secretion of virions as detected by qRT-PCR (**Figure 28A, B**). The infection level was rising from ~28 % on day 1 to ~91 % on day 6 by immunofluorescence, and secreted virions could be detected by qRT-PCR from day 1, albeit at very low levels, with the highest concentration on day 5 with $5.85x10^9$ genome equivalents (GE)/mL, with a standard error of $3.97x10^8$, followed by a slight drop on day 6 ($5.77x10^9$ GE/mL, with a standard error of $1.25x10^9$). Levels were deemed high enough at day 4 to see an antiviral effect. In an attempt to mimic the animal data, in which the mice were treated up to 48 hpi, here I chose day 4 (when ~66 % cells were 3H5-positive) to trial a high-dose iminosugar treatment, and to be able to still detect a potential antiviral effect.

Even though M*O*N-DNJ was used in the animal work, *N*B-DNJ was chosen in the *in vitro* experiments, because of availability of this compound and its FDA approval status, so it could have been repurposed immediately if found effective in this novel treatment regime. To be able to compare a treatment regime of single high-dose iminosugar treatment to the more conventional continuous low-dose treatment, I also needed to evaluate this for *N*B-DNJ in Vero E6 cells. I first determined the toxicity after 96 hours as well as the IC_{50} of *N*B-DNJ against DENV2 in Vero E6 cells in the

continuous low-dose treatment regime. Up to 3.16 mM of *N*B-DNJ was tested and no cytotoxicity was observed (**Figure 28C**).

The infectious virus released from DENV2-infected Vero E6 cells was quantified by plaque assay and the total secreted viral genome copies measured by qRT-PCR. Treatment with *N*B-DNJ resulted in reduction of both total genome copies and infectious virus levels, suggesting that *N*B-DNJ reduces virus output as seen for other cell lines and primary cells (199,333,507). An IC_{50} of infectious virus was measured at 27.4 µM with a confidence interval (CI) of 95% 11.3 – 63.9 µM. The IC_{50} of total virus secreted was slightly lower with 19.5 µM (CI 9.3 – 36.0 µM) (**Figure 28D**). However, calculating the specific infectivity (infectious virus in PFU divided by total viral genome copies) no significant difference was detected, meaning the secreted virions do not differ in their infectivity compared to those being secreted from untreated DENV2-infected cells. For further experiments a concentration of 60 µM *N*B-DNJ was chosen to achieve a minimum of 50% reduction in the viral infectivity, hereafter referred to as the continuous low-dose treatment. As a control, the galactose-derivative *N*B-DGJ was used, which is known to show no antiviral effect against DENV2 (199,333). No toxicity or antiviral effects were observed when DENV2 infected cells were treated with up to 3.16 mM *N*B-DGJ.

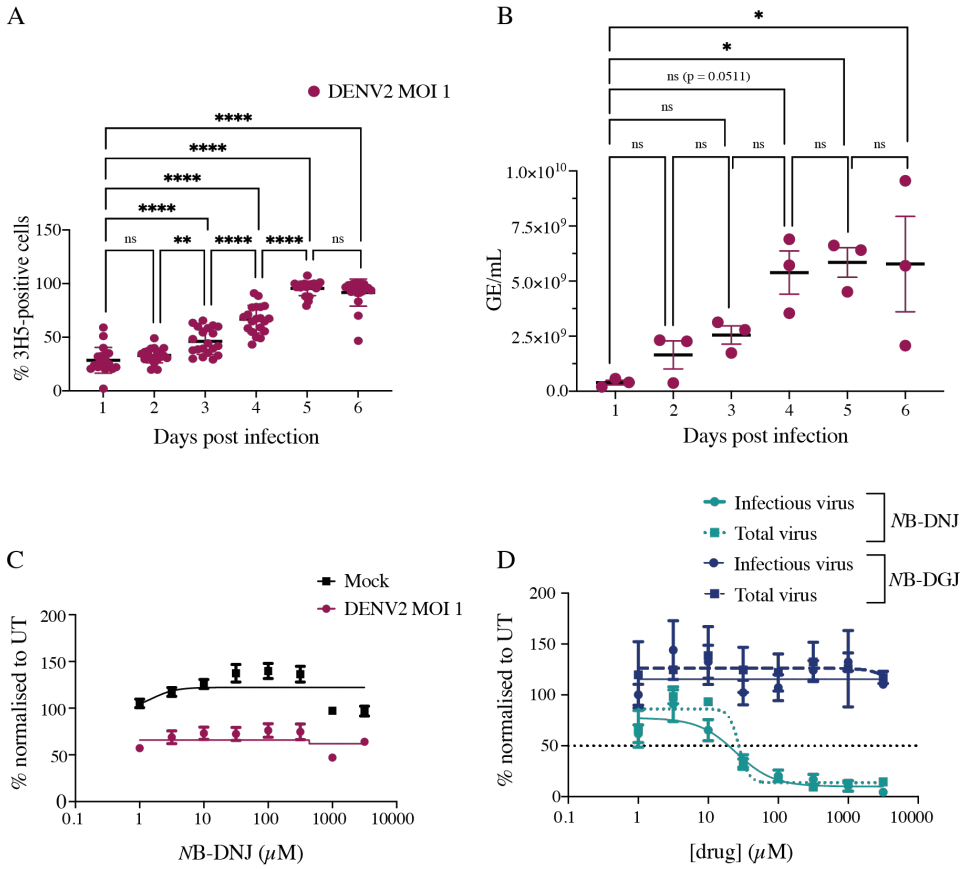

Figure 28: Establishment of DENV infection and *N*B-DNJ treatment in Vero E6 cells. (A) Vero E6 were susceptible to DENV2 infection as identified by antibody staining (3H5) against the envelope protein by immunofluorescence. The percentage of infected cells were calculated by total cell nuclei stained with DAPI – a total of 500 to 750 cells were counted. Statistical significance was calculated by one-way ANOVA test with Tukey's multiples comparison test using Prism 9. *, $p \leq 0.05$; ** $p \leq 0.01$; ***, $p \leq 0.001$; ****, $p \leq 0.00001$. (B) Vero E6 cells were infected with DENV2 MOI 1 for one to six days. Supernatant was harvested daily, and total virus secretion determined by DENV2 NS5 qRT-PCR. Statistical significance was calculated by one-way ANOVA test with Tukey's multiples comparison test. *, $p \leq 0.05$. (C) Vero E6 cells were inoculated with DENV2 MOI 1 and subsequently treated with various concentrations of *N*B-DNJ for 96 hours prior to cell viability assessment by MTS assay. Data were normalised to untreated and represented as mean of three biological independent experiments with propagated error presented as standard error of the mean. (D) Secreted (total virus) and infectious virus from DENV2 MOI 1 infected and *N*B-DNJ- or *N*B-DGJ-treated cells was quantified by qRT-PCR and plaque assay, respectively, after 96 hpi. The average titre with each treatment was determined and converted to a percentage of the average untreated titre. Data were normalised to untreated and represented as mean of three biological independent experiments with propagated error presented as standard error of the mean. Data were fitted using Prism 9, with a comparison of fits between a horizontal line and a four-parameter dose-response curve (with a 95% confidence interval) with limitation that the bottom of the curve be < 0, using the extra sum-of-squares F test to determine the better fit, with $p < 0.05$ required to reject the horizontal line

To mimic a single high-dose treatment with a compound such as *N*B-DNJ, which does not get metabolised, a short-term treatment up to eight hours was tested followed by replacing the media without any added drugs. High doses of iminosugars can inhibit both ER αGluI as well as αGluII *in cellulo* (333), therefore first the toxicity of this short-term high-dose iminosugar treatment was tested. When Vero E6 cells were mock- or DENV2-infected, and the iminosugar was added 88 hpi for 8 hours, there was no significant cytotoxicity measured for *N*B-DNJ or *N*B-DGJ up to 8 mM (**Figure 29A**).

The method for DENV plaque assay used in this thesis uses supernatant of infected cells to re-infect Vero E6 with agarose as an overlay for six days to prevent viral spread. Therefore, it was important to establish whether the high dose of iminosugar would interfere with the plaque assay readout to determine if the single high-dose can achieve ER αGluII and αGluI inhibition. Therefore, a plaque assay with a known PFU of DENV2 with various concentration of *N*B-DNJ was performed (**Figure 29B**). A significant decrease in plaque read-out was detectable in *N*B-DNJ concentration higher than 0.5 mM. Therefore, when using concentrations higher than 1mM in experiments, I used a serial dilution starting from 10^{-1} to dilute the inhibitor remaining down to concentrations that would not interfere with the plaque count and did not exceed concentrations of 5 mM in experiments.

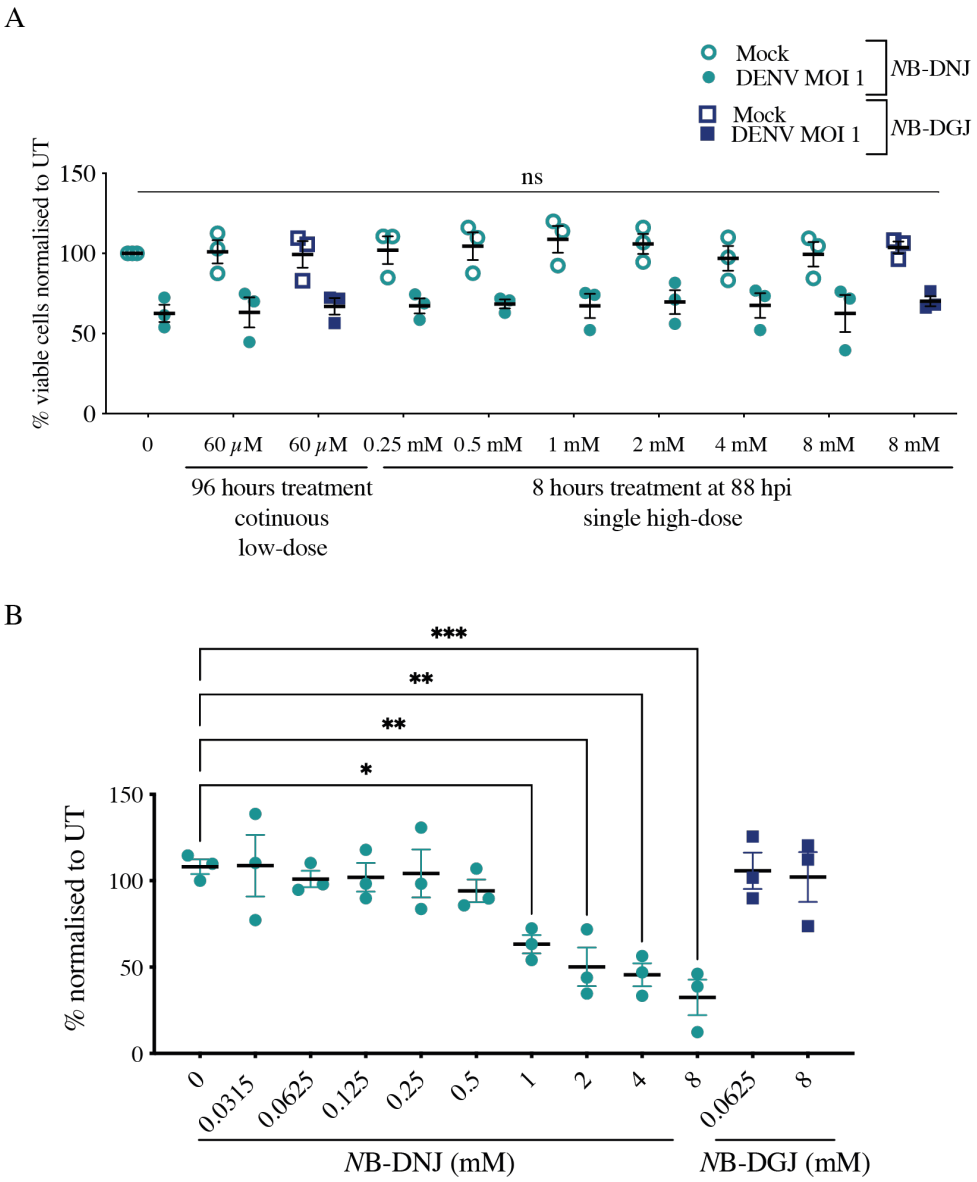

Figure 29: Influence of high-dose iminosugar treatment on cytotoxicity and plaque assay. (A) Vero E6 cells were infected with DENV2 MOI 1 and subsequently treated with a low dose or at 88 hpi with various high concentrations of iminosugars for 8 hours, followed by cell viability assessment by MTS assay. Data were normalised to untreated and represented as mean of three biological independent experiments with propagated error presented as standard error of the mean. Data were analysed by two-way ANOVA comparing drug treatment to untreated sample with Dunnett's multiple comparison test using Prism 9. (B) Interference of iminosugars in plaque assay tested. DENV2 was mixed with different concentrations of iminosugars and plaque assay was performed. Data were normalised to untreated and represented as mean of three biological independent experiments with propagated error presented as standard error of the mean. Data were analysed by one-way ANOVA with Dunnett's multiples comparison test using Prism 9. In both panels, each point indicates an individual replicate. * $p < 0.05$, ** $p < 0.01$, *** $p < 0.005$.

Various concentrations of *N*B-DNJ ranging from 0.25 mM to 4 mM over a period of 1 to 8 hours were tested for inhibition of the ER αGluII and αGluI enzymes via FOS analysis. The highest increase in total FOS (pmol/mg) was detected in treatment with 4 mM *N*B-DNJ for 8 hours (**Table 21**) and therefore used for further experiments. *N*B-DNJ treatment at low micromolar concentrations over 96 hours in mock- and DENV2-infected Vero E6 cells resulted in accumulation of monoglucosylated glycans (**Figure 30A**), while lower levels of Glc_1-species were detected in single high-dose treatment. Continuous low-dose treatment in DENV2-infected cells also resulted in accumulation of triglucosylated species contrary to FOS seen in mock infected cells (**Figure 30B**). Triglucosylated glycan species were detected in single high-dose treatment for mock- and DENV2-infected cells, with a significant increase in DENV2-infected cells at 4 mM *N*B-DNJ and continuous low-dose treatment. Levels of all FOS-species in *N*B-DGJ treated cells were similar to untreated cells. Only a small amount of diglucosylated FOS was detected, which has been previously shown in other studies (303). This low amount indicates that iminosugars are poor at preventing removal of the first α1,2-linked glucose. The kinetics of αGluI and αGluII leads to fast hydrolysis of tri- and diglucosylated glycans to monoglycosylated glycans, allowing interaction with the CNX/CRT chaperones. Due to the slower hydrolysis rate of the proximal glucose residue by αGluII monoglycosylated glycans display a longer half-life than tri- and diglucosylated glycans (508–510).

Table 21: FOS analysis of different treatment time and *N*B-DNJ or *N*B-DGJ concentration. Vero E6 cells were infected and treated with indicated concentration with *N*B-DNJ or *N*B-DGJ for 2, 4, or 8 hours (single high-dose treatment). Or cells were continuously treated at a low dose iminosugar for 96 hours. n = 3.

			Mock-infected				DENV-infected			
			Glc_1-species		Glc_3-species		Glc_1-species		Glc_3-species	
Hours treatment	Drug	Concen-tration	mean (pmol/mg)	SEM	mean (pmol/mg)	SEM	mean (pmol/mg)	SEM	mean (pmol/mg)	SEM
2	*N*B-DNJ	0	6.48	1.10	0.32	0.00	14.32	2.32	0.41	0.24
		0.25 mM	4.50	1.20	0.00	0.00	19.44	4.07	15.02	1.56
		0.5 mM	4.10	1.30	0.54	0.36	14.70	7.80	28.51	4.89
		1 mM	3.70	0.98	5.65	1.34	16.74	9.91	61.69	12.37
		2 mM	4.33	2.60	6.66	0.65	17.45	6.32	86.52	15.43
		4 mM	7.65	5.60	12.41	1.28	31.65	18.22	140.95	10.30
	*N*B-DGJ	4 mM	9.32	4.32	0.00	0.00	12.32	2.32	10.67	3.13
4	*N*B-DNJ	0	4.23	0.32	0.54	0.36	11.22	7.65	11.67	3.68
		0.25 mM	9.60	2.47	1.67	0.14	21.84	3.02	76.24	14.93
		0.5 mM	5.00	1.12	5.69	1.36	26.96	10.78	106.67	24.79
		1 mM	7.23	2.65	7.89	2.55	33.63	10.18	132.76	27.64
		2 mM	6.32	3.32	18.45	3.12	31.32	8.72	126.06	26.12
		4 mM	19.65	6.32	20.44	2.36	36.29	18.54	166.22	31.49
	*N*B-DGJ	4 mM	19.65	3.20	1.38	0.30	21.32	11.32	25.82	4.12
8	*N*B-DNJ	0	8.81	1.16	1.48	0.43	17.18	2.70	10.71	2.49
		0.25 mM	8.54	1.91	31.85	0.67	27.16	7.11	103.31	11.39
		0.5 mM	8.93	2.25	50.23	2.58	34.55	5.53	136.77	10.80
		1 mM	6.98	1.42	75.94	6.54	26.93	7.36	173.36	6.67
		2 mM	16.13	2.11	82.36	4.47	25.03	5.25	156.60	13.60
		4 mM	16.60	2.16	82.16	7.19	32.18	5.21	228.67	39.74
	*N*B-DGJ	4 mM	4.78	0.51	0.72	0.25	7.94	0.25	29.71	4.15
96	*N*B-DNJ	60 µM	68.44	11.33	12.57	0.43	124.44	14.32	156.50	9.40
	*N*B-DGJ	60 µM	18.45	5.53	2.90	1.05	15.24	2.85	21.80	2.99

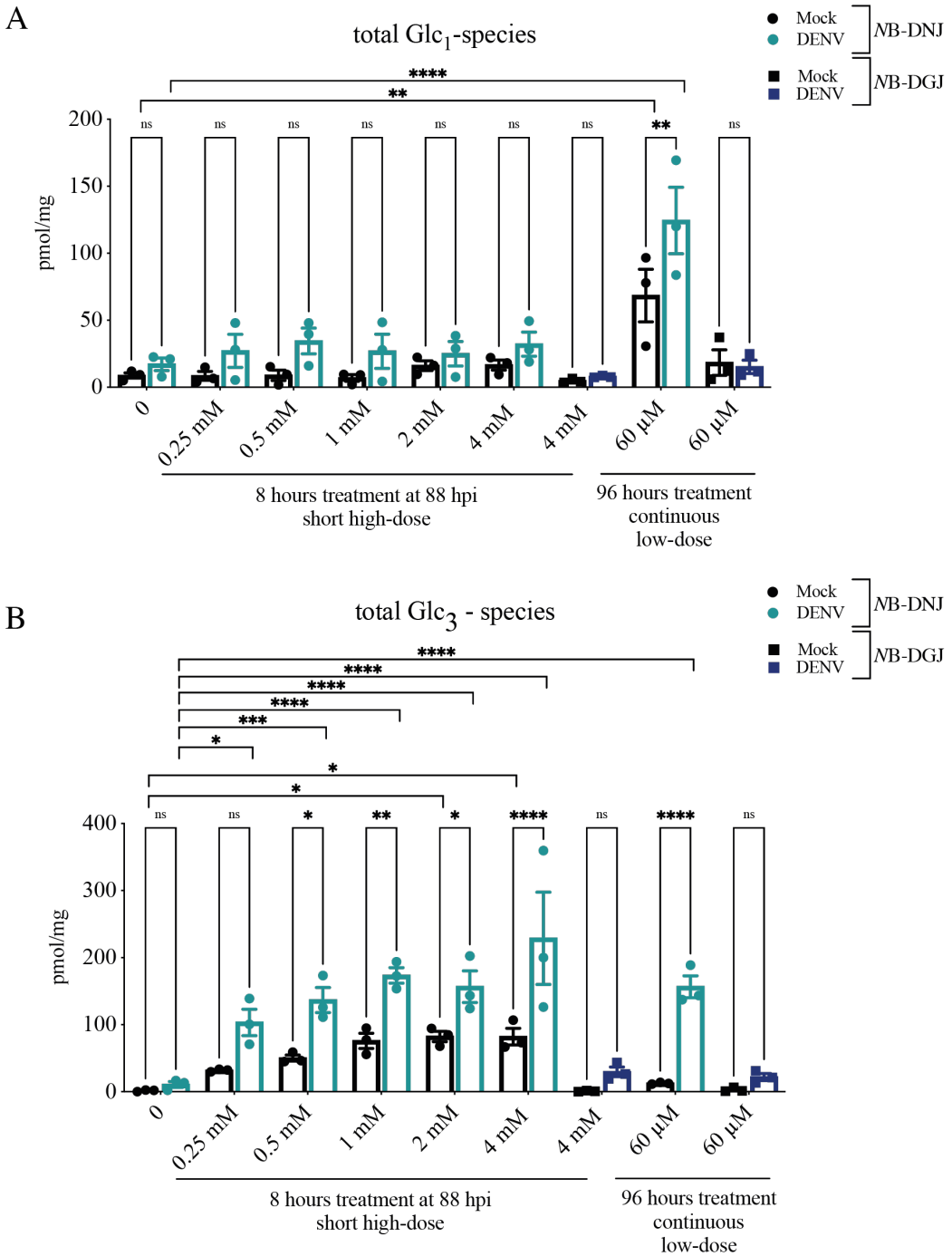

Figure 30: FOS analysis of cells treated with *N*B-DNJ or *N*B-DGJ for a continuous low-dose or single high-dose. (A) Continuous low-dose treatment leads to accumulation of monoglucosylated glycans in mock-infected cells, (B) whereas continuous low-dose treatment in DENV2-infected and single high-dose treatment in mock- and DENV2-infected cells leads to accumulation of triglucosylated glycans. In both panels, each point represents an individual replicate value of three biological independent experiment with error bars representing the standard error of the mean. Statistical significance was calculated by two-way ANOVA with Šídák's multiple comparison using Prism 9. *, $p \leq 0.05$; ** $p \leq 0.01$; ***, $p \leq 0.001$; ****, $p \leq 0.00001$.

An increase of total FOS levels in DENV2-infected Vero E6 cells was measured, which may be a result from the higher protein turnover during infection, where even a low concentration of *N*B-DNJ might be sufficient to give an observable αGluI inhibition if the amount of viral glycoproteins overwhelms the folding machinery. Potentially, αGluI inhibition becomes only measurable in infected cells, perhaps either by the enzyme being upregulated in response to unfolded proteins or by αGluI being overwhelmed by the amount of additional viral glycoproteins attempting to fold. Even though continuous low-dose treatment also led to αGluI inhibition albeit only in DENV2-infected, in this case and unlike in the single high-dose treatment, Glc_1-species were also still observed, suggesting that inhibition of αGluI was not complete. In the single high-dose treatment almost no Glc_1-species were detected, and high levels of the Glc_3-species were present, showing successful inhibition of αGluI and αGluII. However, we do not know whether the same would happen *in vivo*, as cells derived from virus-infected mice could not be made available for FOS analysis. However, in primary immature dendritic cells, αGluI inhibition could not be achieved with continuous low-dose treatment (333).

Next, total secreted viral genome copies were measured by qRT-PCR (**Figure 31A**) and the infectious virus released from DENV2-infected and iminosugar-treated cells was quantified by plaque assay (**Figure 31B**). Treatment with *N*B-DNJ resulted in reduction of both total genome copies and infectious virus levels suggesting that these drugs reduced virus output. The specific infectivity showed no significant increase or decrease (**Figure 31C**). In contrast, treatment with *N*B-DGJ did not result in any antiviral effect (**Figure 31A, B**).

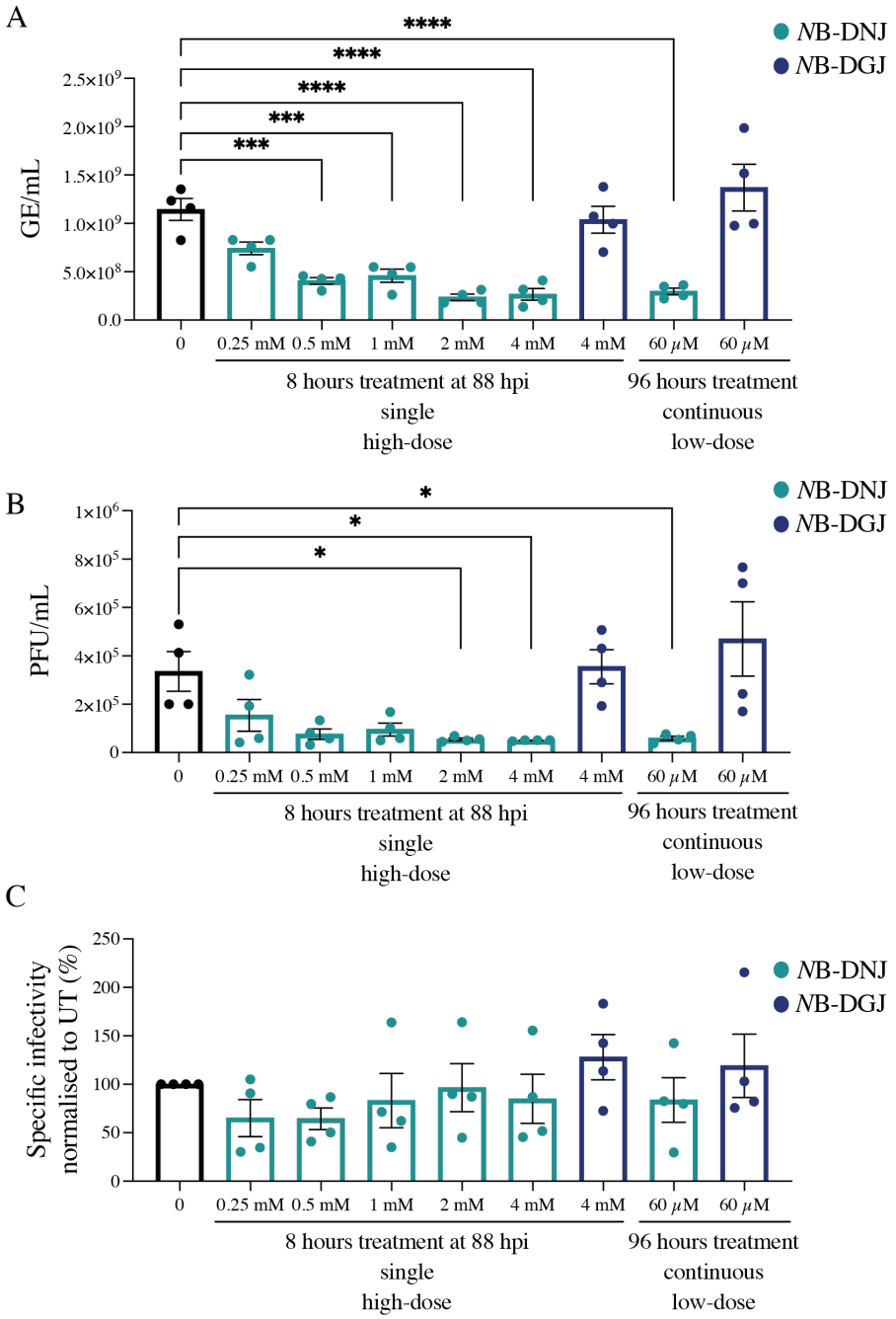

Figure 31: Antiviral effect of *N*B-DNJ and *N*B-DGJ in DENV2-infected Vero E6 cells in continuous low-dose and single high-dose treatment. (A) Secretion of total virions (B) and infectious virus secretion from DENV2-infected and iminosugar-treated Vero E6 cells quantified by qRT-PCR or plaque assay, respectively. (C) Specific infectivity of the secreted virus was calculated by division of infectious virus to total virus for each concentration. Data were normalised to untreated and represented as mean of three biological independent experiments with propagated error presented as standard error of the mean. Data were analysed by one-way ANOVA with Dunnett's multiples comparison test using Prism 9. *, $p \leq 0.05$; ** $p \leq 0.01$; ***, $p \leq 0.001$; ****, $p \leq 0.00001$.

To determine whether a host protein might be responsible for the antiviral effect, cells were pre-treated with 4 mM *N*B-DNJ and *N*B-DGJ for 8 hours, washed with PBS and media (without iminosugar) was added for a further 24 hours. Virion secretion and infectivity was measured (**Figure 32A, B**). No significant effect was detected when cells were pre-treated with a high dose of iminosugar, suggesting after eight hours treatment no host protein which may be crucial for viral infection is affected.

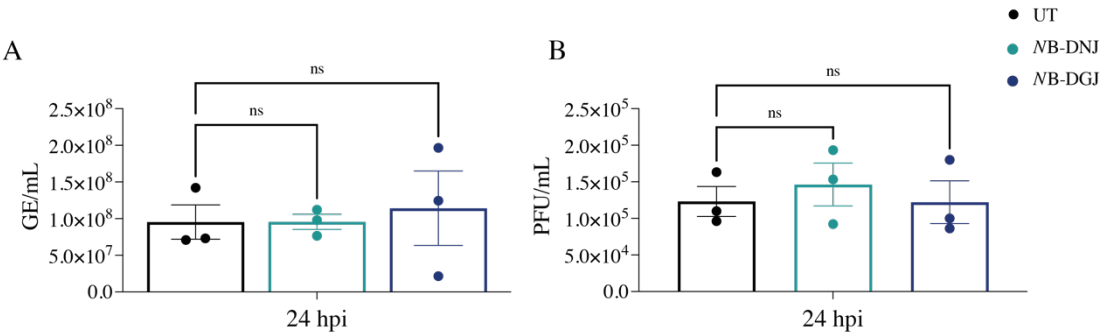

Figure 32: Pre-treatment of Vero E6 cells. Cells were treated with 4 mM *N*B-DNJ or *N*B-DGJ for 8 hours, washed with PBS four times for 5 minutes each and media replaced without iminosugar. (A) (A) Secretion of total virions and (B) infectious virions were measured. Values are shown as the mean of three biological independent experiments with propagated error presented as standard error of the mean. Statistical significance was calculated by one-way ANOVA with Dunnett's multiples comparison test. UT, untreated.

Taken together these data showed that a single high-dose treatment at non-toxic concentrations could achieve ER αGluI inhibition and lead to an antiviral effect. Therefore, I adopted the following approach: Cells were infected with DENV2 (MOI 1) and infection was allowed to proceed for 88 hours, followed by treatment with a high dose of 4 mM *N*B-DNJ for eight hours. Drug containing media got replaced with fresh media containing no iminosugar, after washing cells with PBS four times for 5 minutes, the assay was continued up to 168 hpi. To prevent cells becoming overconfluent during the long duration of this experiment, an initial confluency of cells

of 50% was chosen which resulted in a confluency of around 70% at time of immunofluorescence analysis (**Figure 33**).

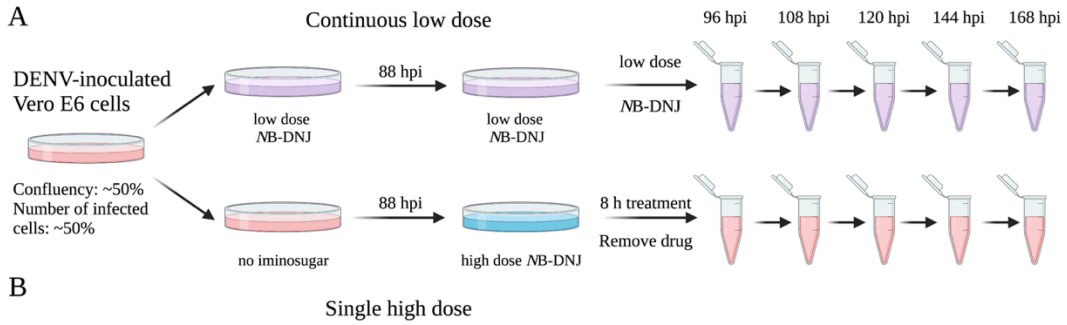

Figure 33: Treatment regime to recapitulate the long-lasting antiviral effect of continuous low-dose compared to single high-dose treatment. (A) Cells were inoculated with DENV2 MOI 1 for 90 minutes, and treated continuously with 60 µM *N*B-DNJ, at 88 hpi media was replaced with 60 µM *N*B-DNJ for further 8 hours and again replaced at 96 hpi for further timepoints. (B) Cells were infected for 90 minutes, incubated for 88 hours, followed by treatment with fresh media containing 4 mM *N*B-DNJ for 8 hours. Media was again replaced with media without iminosugar. (A-B) Media at 96, 108, 120, 144 and 168 hpi was harvested and used for detection of total virion secretion and infectivity measurements.

6.3.2 Long-lasting antiviral effect of single high-dose iminosugar treatment

After establishing the single high-dose treatment, the next step was to identify if a long-lasting antiviral effect remains after removing the media containing 4 mM *N*B-DNJ. Secretion of virions and their infectivity was measured 12 hours (108 hpi), 24 hours (120 hpi), 48 hours (144 hpi) and 72 hours (168 hpi) after the eight hour iminosugar treatment by qRT-PCR and plaque assay. Simultaneously, for the continuous low-dose treatment, the media was replaced with fresh media containing 60 µM *N*B-DNJ. A significant reduction of secretion of virions was detected in the continuous low-dose treatment up to 120 hpi, with no effect on their specific infectivity (**Figure 34A, B**). Similarly, for the single high-dose treatment the total amount of secreted virions was reduced (**Figure 34C**). However, looking at the specific

infectivity, the secreted virions showed a reduced infectivity from 120 hpi onwards (**Figure 34D**). A decrease in specific infectivity at higher concentrations of iminosugar, capable of achieving αGluII and αGluI inhibition, was also observed with *N*B-DNJ, M*O*N-DNJ and 2THO-DNJ treatment of DENV2-infected monocyte-derived dendritic cells and monocyte-derived macrophages (333,511), even though a continuous low-dose treatment regime was used in these studies. Here, in Vero E6 cell a 60 µM *N*B-DNJ continuous low-dose treatment I observed ER αGluI inhibition, however this had no influence on the specific infectivity.

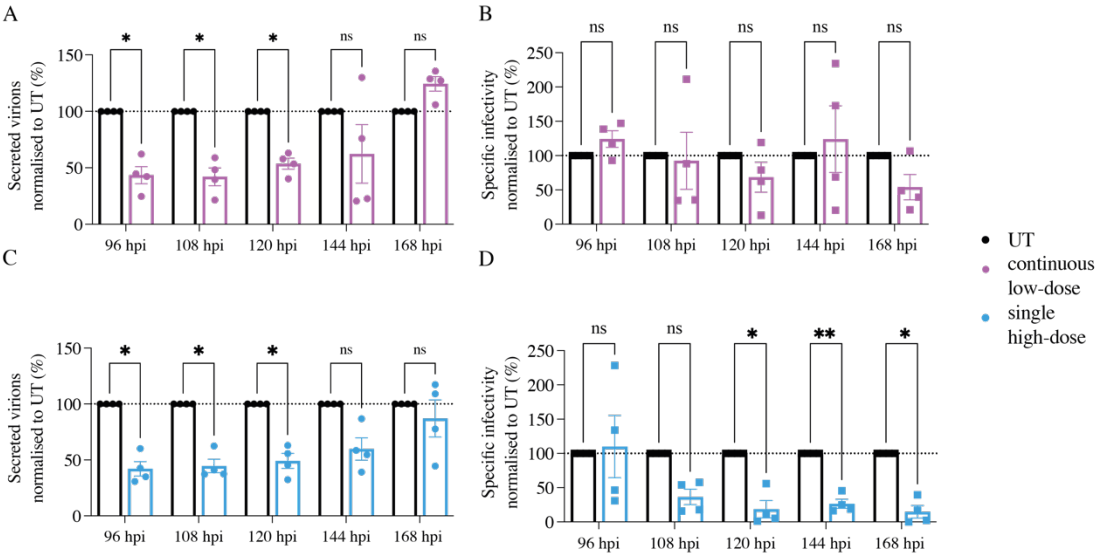

Figure 34: Long-lasting effect of continuous low-dose and single high-dose *N*B-DNJ treatment in DENV2-infected cells. Cells were treated as explained in Figure 33. Secreted virions normalised to untreated (UT) cells in (A) continuous low-dose (C) or single high dose treatment quantified by qRT-PCR. (B, D) specific infectivity for each treatment regime. Values are shown as the mean of four biological independent experiments with propagated error presented as standard error of the mean. Data were analysed by two-way ANOVA with Šidák's multiples comparison test. *, p≤ 0.05; ** p≤ 0.01.

6.3.3 Mechanism of action of single high-dose treatment

After establishing that there was an antiviral effect of a single high dose treatment regime up to 168 hpi, the next step was to identify the mechanism of action of this dosing regimen. The cytotoxicity can be measured by the mitochondrial metabolic activity, interpreting the cell viability. Measurements of the cell viability directly after the eight hours treatment showed that cell viability was not affected (**Figure 29A**). However, after removing *N*B-DNJ, cells 12 hours post-treatment (108 hpi) in mock- and DENV2-infected cells showed a significant decrease in health (**Figure 35A, B**). Mock-infected cells seemed to recover 24 hours post-treatment (120 hpi, **Figure 35A**), whereas DENV2-infected cells a significant decrease in health was detected up to 144 hpi (48 hours post-treatment, **Figure 35B**). This suggested that in DENV2-infected cells a single high-dose treatment had a stronger influence on the metabolic activity when compared to mock-infected single high-dose treated cells. At 168 hpi no significant difference between untreated and single high-dose treated DENV2-infected cells was detected, indicating that either the single high-dose treated cells had recovered to the state of untreated infected cells, or untreated DENV2-infected cells decreased their metabolic activity to the same level of single high-dose treated cells (**Figure 35B**).

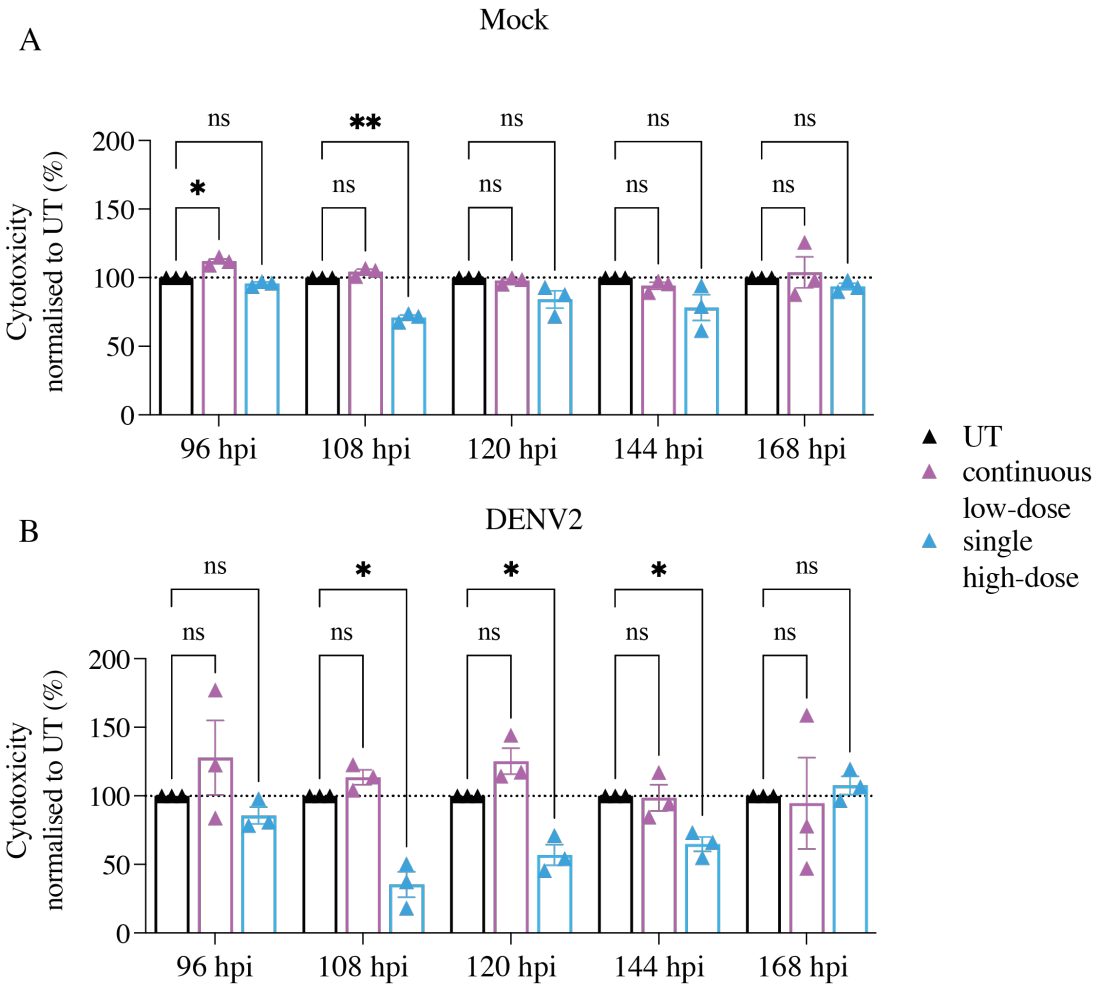

Figure 35: Cytotoxicity of both treatment regimens at different time points. Cells were treated as described in Figure 33 and cytotoxicity measured by MTS for (A) mock-infected or (B) DENV2-infected cells. The average of each titre with each treatment was determined and converted to a percentage of the average untreated titre. Values are shown as the mean of three biological independent experiments with propagated error presented as standard error of the mean. Statistical significance was calculated by two-way ANOVA with Dunnett's multiples comparison test. *, $p \leq 0.05$; ** $p \leq 0.01$.

Reduction of secreted virions was measured in both treatment regimens. IF staining was performed on mock- and DENV-infected cells treated with and without iminosugar to see if the morphology of cells changed in the two treatment regimens (**Figure 36**). Interestingly, based on viral envelope expression (3H5 antibody staining) at 96 hpi ~60% of cells were DENV2-positive, however, staining for prM, NS1 or NS4b suggest that ~100% of cells are infected at 96 hpi (**Figure 36I, J, K, M, N, O**).

Cells were seeded at the same density, however, fewer cells were visible for high-dose treated cells, possible due to cytotoxicity of DENV infection and single high-dose treatment, as shown in **Figure 35**. The intensity of the immunofluorescence signal in continuous low-dose treated cells seems to be higher compared to untreated cells for the E, prM, NS1 and NS4b proteins. However, it is difficult to differentiate the quantity of specific proteins inside cells by immunofluorescences, therefore, this observation needs to be confirmed by alternative methods with quantification options, like flow cytometry. Additionally, the antibody against the E protein is a known confirmational antibody (512) (no information for the antibodies against prM, NS1 and NS4b was available), which can influence the staining if proteins are misfolded due to iminosugar staining. In single high-dose treatment, there seems to be a different phenotype of the E, prM and NS1 protein, with punctate staining patterns (**Figure 36C, G, K**). This was not the case for NS4b, a cytoplasmic non-structural protein important in the ER membrane-associated replication complex (**Figure 36O**) (513), which, unlike NS1 or E and prM, is not secreted during infections. These punctate patterns could be due to misfolded protein aggregates, which would suggest a stalling of the aggregates inside the ER before degradation. However, to this time point no co-staining with ER, or other organelle markers was performed and therefore, this hypothesis cannot be proven yet. But when proteins accumulate in the ER, the UPR is induced to balance protein expression of ER chaperones and ERAD proteins, and induction of apoptosis. Moreover, previous data showed that the UPR is activated in DENV infection (204,316,333,339,343) and iminosugar treatment in cells (204,333,343).

Therefore, I decided to identify if any and which arms of the UPR may be differentially regulated upon high-dose iminosugar treatment; and whether the long-lasting effect observed may involve the UPR. Initially, I measured the mRNA levels of various UPR players, with the plan to quantify protein levels later, which was however prevented by the pandemic.

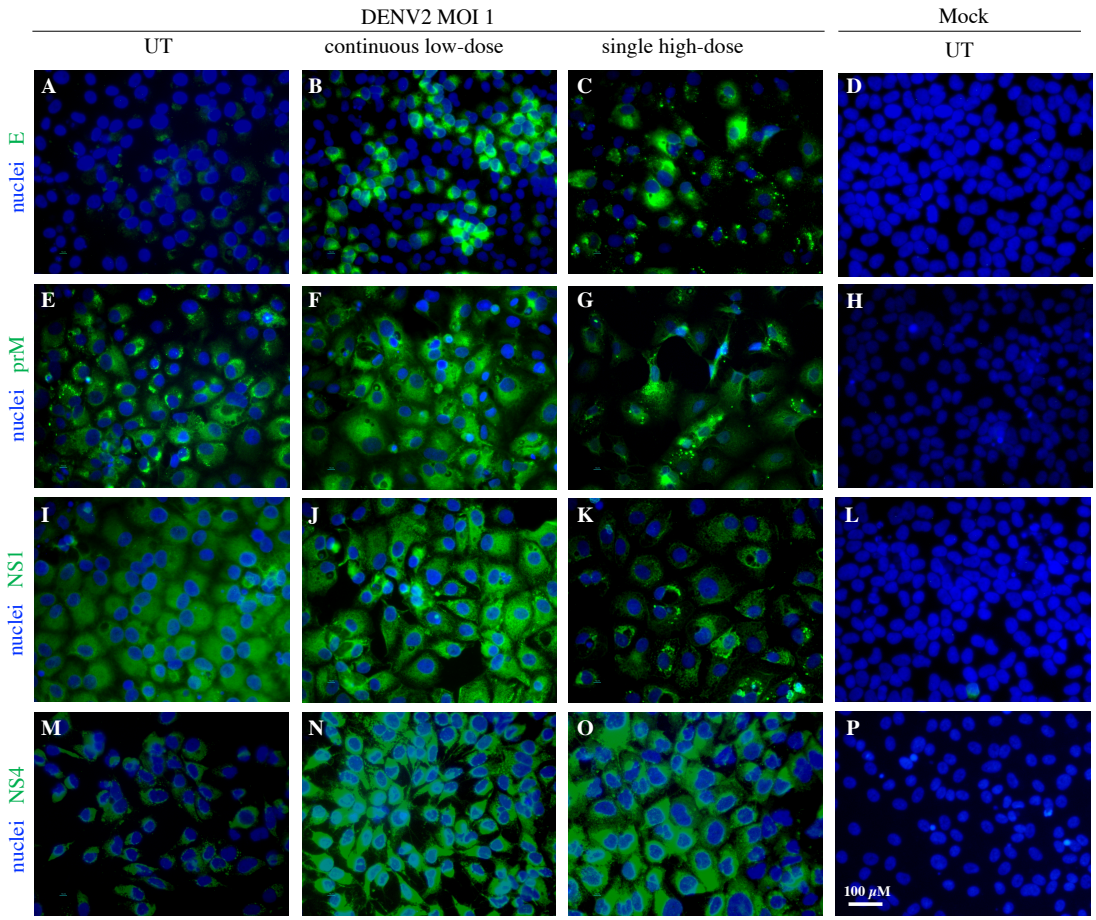

Figure 36: Immunofluorescence of E, prM, NS1 and NS4b in DENV2-infected untreated, continuous low-dose, single high-dose treated, and mock-infected cells. Cells were infected with DENV2 and treated with *N*B-DNJ as described in Figure 33 or mock-infected. At 96 hpi, cells were fixed and stained with antibodies against the glycoproteins E (A-D), prM (E-H), NS1 (I-L) and NS4b (M-P).

As mentioned above, DENV infection itself, as well as iminosugars by themselves, can activate the UPR, which acts to counteract the ER stress induced by viruses and

drugs to evade cell death, or if these adaptive mechanisms fail, to induce cell death (204,333). The high dose iminosugar treatment could potentially induce ER stress by inhibiting the ER α-glucosidases, overwhelming the degradation machinery and leading to the accumulation of proteins in the ER. Therefore, the mRNA levels of the ER stress marker BiP (*HSP5*) and the downstream UPR genes *ATF6*, *XBP1*, *ATF4* and *DDIT3* (encodes for CHOP) were measured by qRT-PCR. Tunicamycin (Tm) was used as a positive control as it inhibits the N-linked glycosylation pathway, leads to ER stress and UPR activation. After eight hours Tm treatment, the only significant activation measured was that of IRE1-XBP1 transcript, as measured by an increase of splicing of *XBP1*, and *DDIT3*, a gene downstream of the PERK-ATF4 and IRE1-XBP1 arm (**Figure 37A**). The effect of Tm in Vero E6 cells is similar to that reported in primary macrophages (333). However, quantifications of the mRNA levels might be misleading since protein levels have been not measured, e.g. the active form of ATF6 (ATF6p50) is cleaved in the Golgi before it induces genes associated with the ERAD pathways and ER chaperones. DENV2 infection with and without *N*B-DNJ treatment or single high-dose treatment revealed increased levels of *HSP5* transcript (**Figure 37B**), suggesting that the UPR might be activated in DENV2 infected cells but also specifically in the single high-dose treatment regimen at 96 hpi (directly after treatment). Interestingly, in mock-infected cells single high-dose treated cell levels of *HSP5* significantly decreases compared to untreated cells from 108 hpi, also a reduction in *HSP5* levels in DENV2-infected single high-dose treated cells at 120 hpi was measurable, suggesting a decrease of the ER stress in DENV2-infected single high-dose treated cells over time (**Figure 37B**).

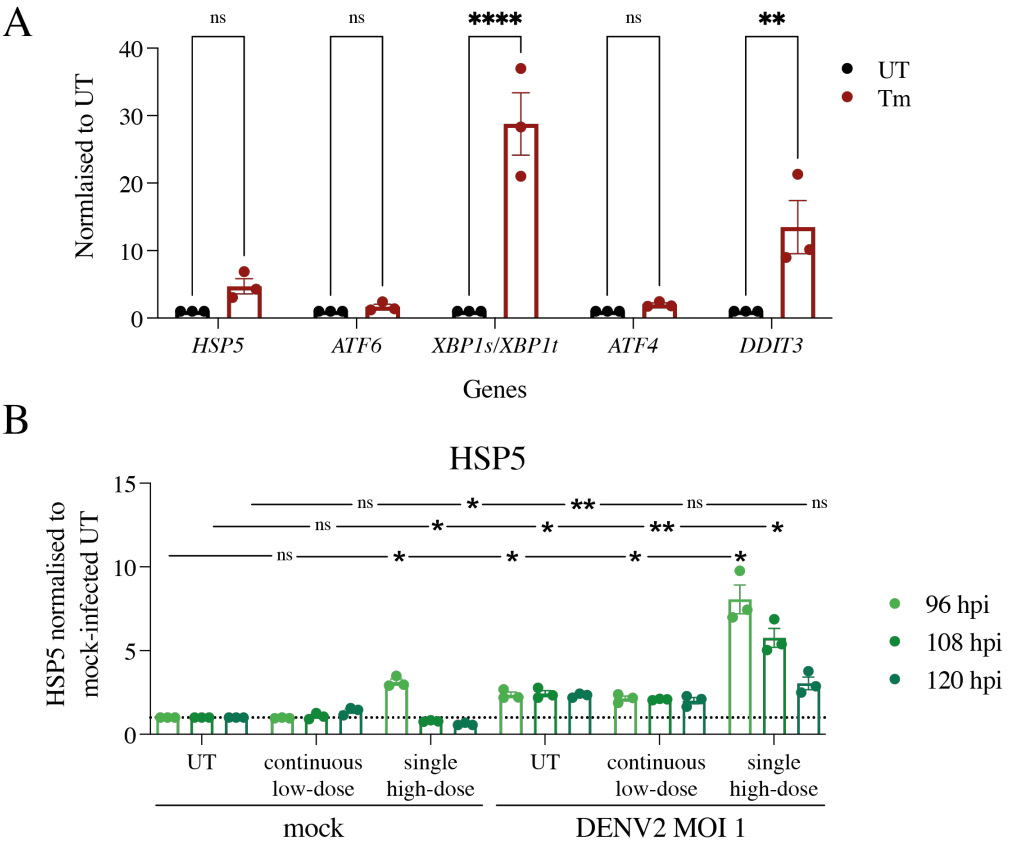

Figure 37: Transcript mRNA level of UPR genes in Vero E6 cells. (A) Vero E6 cells were treated with Tm 1 µg/mL for 8 hours. qRT-PCR was performed for *HSP5*, *ATF6*, *XBP1s* and *XBP1t*, *ATF4* and *DDIT*3. Values are shown as the mean of three biological independent experiments with propagated error presented as standard error of the mean. Statistical significance was calculated by two-way ANOVA with Šidák's multiples comparison test. **, p≤ 0.01; ****, p≤ 0.0001. (B) mRNA level of *HSP5* of different treatment regimen in mock- and DENV2-infected cells were quantified. Values are shown as the mean of three biological independent experiments with propagated error presented as standard error of the mean. Statistical significance was calculated by two-way ANOVA with Dunnett's multiples comparison test. *, p≤ 0.05; ** p≤ 0.01. UT, untreated; Tm, Tunicamycin-treated.

The mRNA levels of the specific UPR arms were analysed to identify if one specific UPR arm is involved in the mechanism of action of the long-lasting antiviral effect in single high-dose treated cells. As for Tm-treated Vero E6 cells, no change in *ATF6* transcript levels were detected (**Figure 38A**). To exclude the role of this UPR pathway in DENV2-infection and iminosugar treatment different methods would need to be applied, as mentioned above. In addition, a greater increase in splicing of the *XBP1*

mRNA was detected in DENV2-infected untreated cells (by a ratio above one of *XBP1s/XBP1t*), and in both *N*B-DNJ treatment regimens (**Figure 38B**). Increase of the *XBP1s* variant in DENV2-infected and continuous low-dose treatment was not seen in primary macrophages treated with 2THO-DNJ (333).

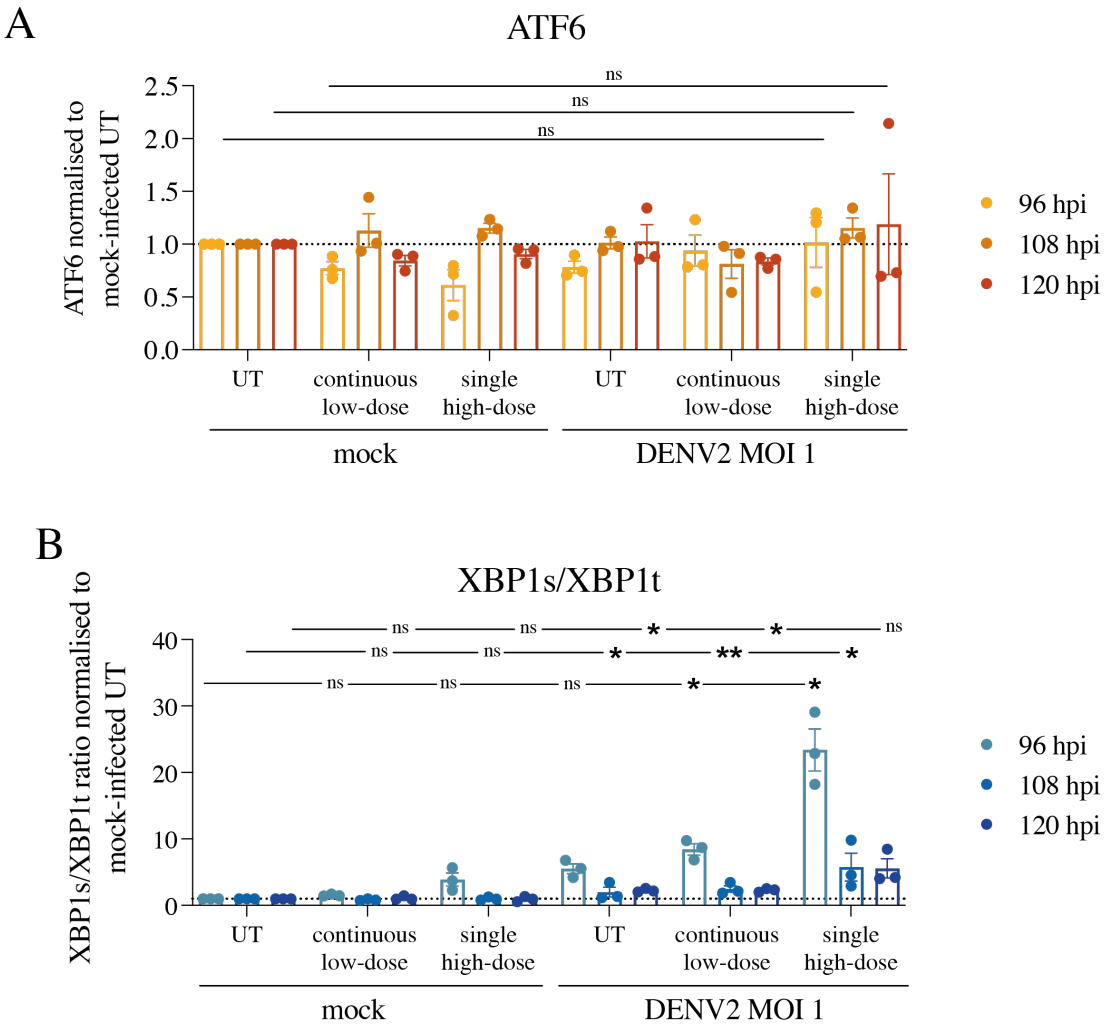

Figure 38: Transcript mRNA level of the UPR genes *ATF6* and *XBP1s/XBP1t*. Vero E6 cells were mock- or DENV2-infected and treated with described dosing regimen. (A) mRNA level of *ATF6* and (B) ratio of the mRNA levels of *XBP1s* and *XBP1t*. Values are shown as the mean of three biological independent experiments with propagated error presented as standard error of the mean. Statistical significance was calculated by two-way ANOVA with Dunnett's multiples comparison test. *, $p \leq 0.05$; ** $p \leq 0.01$. UT, untreated; Tm, Tunicamycin-treated.

The mRNA levels of *HSP5* and *XBP1s/XBP1t* were increased in DENV2-infected continuous low-dose and single high-dose treated cells. In contrast, transcript levels of *ATF4* only significantly increased in single high-dose treatment compared to untreated cells at 96 hpi (**Figure 39A**) in mock- and DENV2-infected cells. For *DDIT3* this was only the case for DENV2-infected cells (**Figure 39B)**. This suggests that the PERK pathway is activated in single high-dose treated cells. However, in mock-infection Vero E6 cells have a lower protein burden in the ER and might be able to recover from the overload of the ER. Whereas in DENV2-infected and single high-dose treated cells the protein burden in the ER might be too high, inducing transcription of the pro-apoptotic *DDIT3* gene, which encodes the CHOP protein, leading to cell death. However, this needs to be proven by measuring protein levels rather than transcription levels.

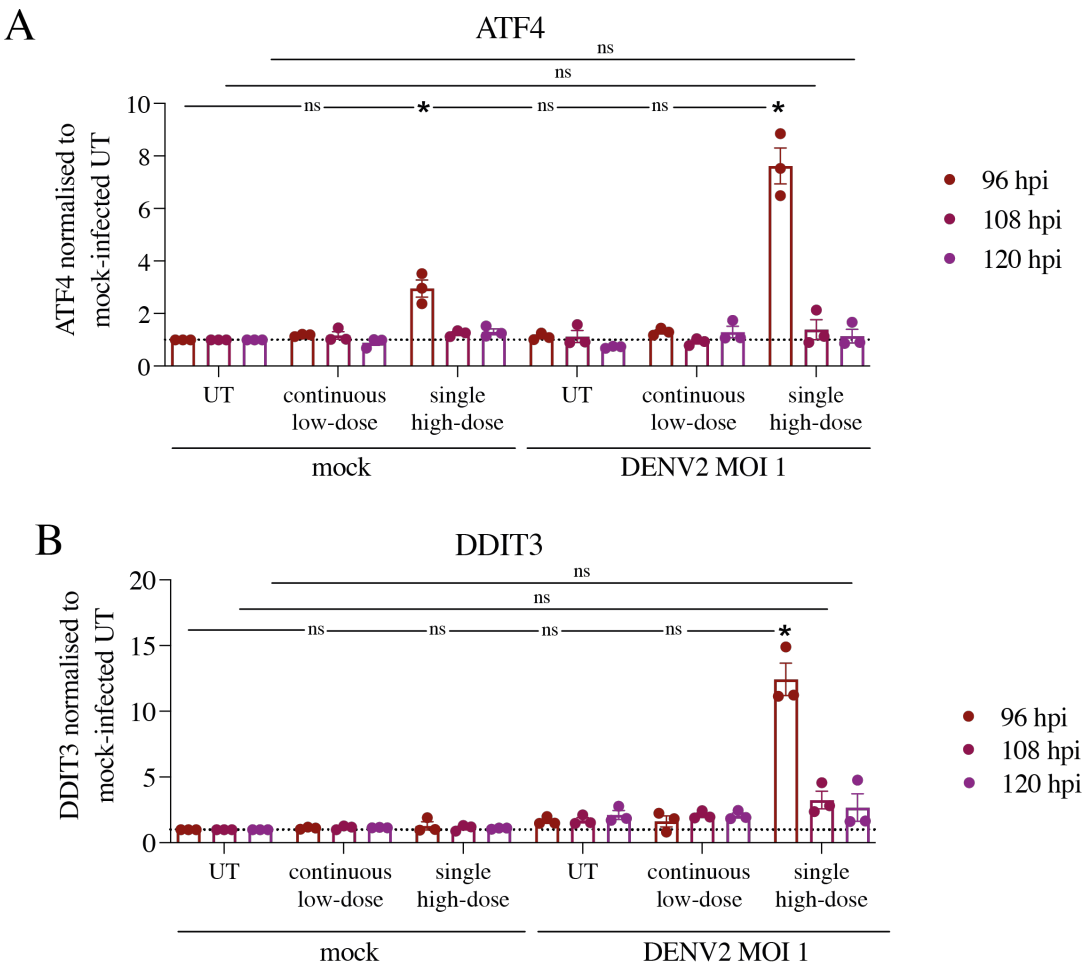

Figure 39: Transcript mRNA level of the UPR genes *ATF4* and *DDIT3*. Vero E6 cells were mock- or DENV2-infected and treated with described dosing regimen. (A) mRNA level of *ATF4* and (B) *DDIT3*. Values are shown as the mean of three biological independent experiments with propagated error presented as standard error of the mean. Statistical significance was calculated by two-way ANOVA with Dunnett's multiples comparison test. *, p≤ 0.05. UT, untreated; Tm, Tunicamycin-treated.

6.4 Discussion

In this chapter a suitable cell culture model was established to recreate the long-lasting antiviral effect against DENV and IVA after a single and/or double high-dose iminosugar treatment in mice (203), to start unravelling the mechanism of action of this treatment regimen. While developing this cell culture model, unexpectedly ER αGluI inhibition was observed in both continuous low-dose and single high-dose

treatment in DENV2-infected Vero E6 cells. An increased protein flux in the ER during infection might overload the ER capacity leading to triglucosylated FOS levels in DENV2-infected continuous low-dose treated cells. In such scenario, even low concentrations of *N*B-DNJ seem to be sufficient to give rise to an observable ER αGluI inhibition. However, ER αGluI inhibition is not enough to provide an antiviral effect similar to that seen in single high-dose treatment up to 0.5 mM *N*B-DNJ. *N*B-DNJ is a competitive inhibitor by mimicking monosaccharides and substrate concentration can out-compete inhibition, which could be the case for high-dose treated cells as well as low-dose treated cells, compared to untreated cells. However, ER stress may limit substrate concentration through UPR by either trying to rescue the cell survival and inducing expression of folding and ERAD-associated proteins or by inducing cell apoptosis, which might cause the difference observed in low-dose and high-dose treated cells.

Also, when DNJ-based iminosugars were used at IC_{50} concentrations (as used here for the continuous low-dose treatment) in primary macrophages and immature dendritic cells these were not sufficient to reach an αGluI inhibition (333,511), showing cell type specific differences.

A long-lasting antiviral effect after administering a single high-dose (4 mM *N*B-DNJ) for 8 hours at 88 hpi, with a decrease of virion secretion for further 24 hours without iminosugar present (120 hpi) was observed. No antiviral effect was measured for *N*B-DGJ treated control cells. In the continuous low-dose treatment, an antiviral effect was detected up to 120 hpi, whereas for later time points (144 hpi, 168 hpi) no reduction of virion secretion was detected. This is surprising since iminosugars are not

metabolised (290). However, another explanation may be that as secretion of virions was normalised to untreated cells that the levels of virions in untreated cells dropped. The raw GE/mL values suggest that at 144 hpi virions in untreated cells are either degraded or cells are starting to die so less virus is produced (raw values for UT 120 hpi: $6.2x10^9$ GE/mL, UT 144 hpi: $3.8x10^9$ GE/mL). Even though the secretion of virions at 144 hpi was not significantly decreased for the single high-dose treatment the specific infectivity was decreased. A decrease of specific infectivity has not been evaluated for all viruses susceptible to iminosugar treatments, however it has been demonstrated for HIV-1 (273,514,515), CMV (275) and Kunjin virus (258). In these studies, cells were continuously treated with iminosugars and no information is available if only αGluII was inhibited or αGluII and αGluI. In contrast, a dominant effect on secretion was described for HBV (516) and IVA (517). Interestingly, high concentration of *N*B-DNJ, M*O*N-DNJ and 2THO-DNJ does reduce the specific infectivity for DENV2-infected primary macrophages and immature dendritic cells in a continuous treatment (333,511). The lowest dose tested for the single high-dose treatment was 0.25 mM *N*B-DNJ (**Figure 30**), which was enough to induce accumulation of triglycosylated FOS but not sufficient to cause an antiviral effect (**Figure 31A, B**). A difference in the specific infectivity was not observed in continuous low-dose treated cells (**Figure 31C**).

Another effect of single high-dose treatment was the punctate pattern formation of potentially misfolded protein aggregates of E, prM and NS1, glycoproteins which get secreted in DENV2-infection. For the other DENV glycoprotein, NS4b, no aggregates were detected, potentially because this protein does not get secreted. If ER glycoproteins are not secreted from the ER to the Golgi compartment or degraded

through ERAD, they can aggregate (518). It is hypothesized that protein complexes or aggregates are too large to pass through the ERAD translocation pore, and hence must either be dissociated into monomers before ERAD, degraded via a different process e.g., autophagy (518), or glycans can be released by a mechanism involving another PNGase-like activity and hence protein can get degraded (294). This overload of the ER with misfolded/unfolded protein can trigger the UPR (519).

This response has been shown to have cell specific and drug specific differences (333). Here, the mRNA levels of the UPR arms *ATF6*, *XBP1* (downstream of the IRE1 pathway) as well as of *ATF4* (downstream of the PERK pathway) and *DDIT3* (downstream of mainly PERK but continuous stress also downstream of IRE1 and ATF6) were evaluated in both treatment regimens. No differences were observed for *ATF6* and *XBP1* between the two treatments. However, *ATF4* was expressed to higher levels at 96 hpi directly after single high-dose treatment in mock- and DENV2-infected cells, whereas an increase of *DDIT3* was only detected in DENV2-infected cells. *DDIT3* encodes for the pro-apoptotic protein CHOP, which activates the intrinsic apoptotic pathway through the suppression of B-cell lymphoma protein 2 (BCL-2), BCL-XL, and myeloid leukemia cell differentiation protein 1 (MCL-1), as well as the overexpression of BCL-2 like protein 1, which regulates mitochondrial outer membrane permeabilization. This leads to cytochrome c release and the activation of the caspase cascade for apoptosis (520).

However, only mRNA levels were determined, therefore one cannot rule out the possibility that ATF6 does play a role in the MOA of the single high-dose treatment. The activated ATF6 protein is cleaved leading to ATF6p50 which translocates to the

nucleus to regulate the expression of genes in the ERAD pathway (319), which is not possible to detect via qRT-PCR. Their protein levels need to be measured. Based on the data, the single high-dose treatment activates the IRE1-XBP1 and PERK pathway leading to an increase of the *XBP1s* and *XBP1t* (higher increase of *XBP1s*) transcripts as well as of the *ATF4* and *DDIT3* levels. In untreated DENV2-infected cells PERK is activated and catalyses phosphorylation of eIF2α which inhibits protein translation. However, DENV transiently activates and then inhibits eIF2α activation to overcome protein translation attenuation. ATF4 is induced by eIF2α and activates CHOP which can mediate apoptosis. Potentially, single high-dose *N*B-DNJ treated DENV2-infected cells may overcome the inhibition of eIF2α, because of high protein accumulation and aggregate formation, leading to activation of the apoptosis pathway (**Figure 40**). This is supported by cytotoxicity measurements, in which mock-infected single high-dose treated cells show an impact of their metabolic rate at 108 hpi, while this seems to be resolved at 120 hpi, whereas for DENV2-infected cells in this treatment a significant reduction from 108 hpi is detectable compared to untreated cells (**Figure 35**).

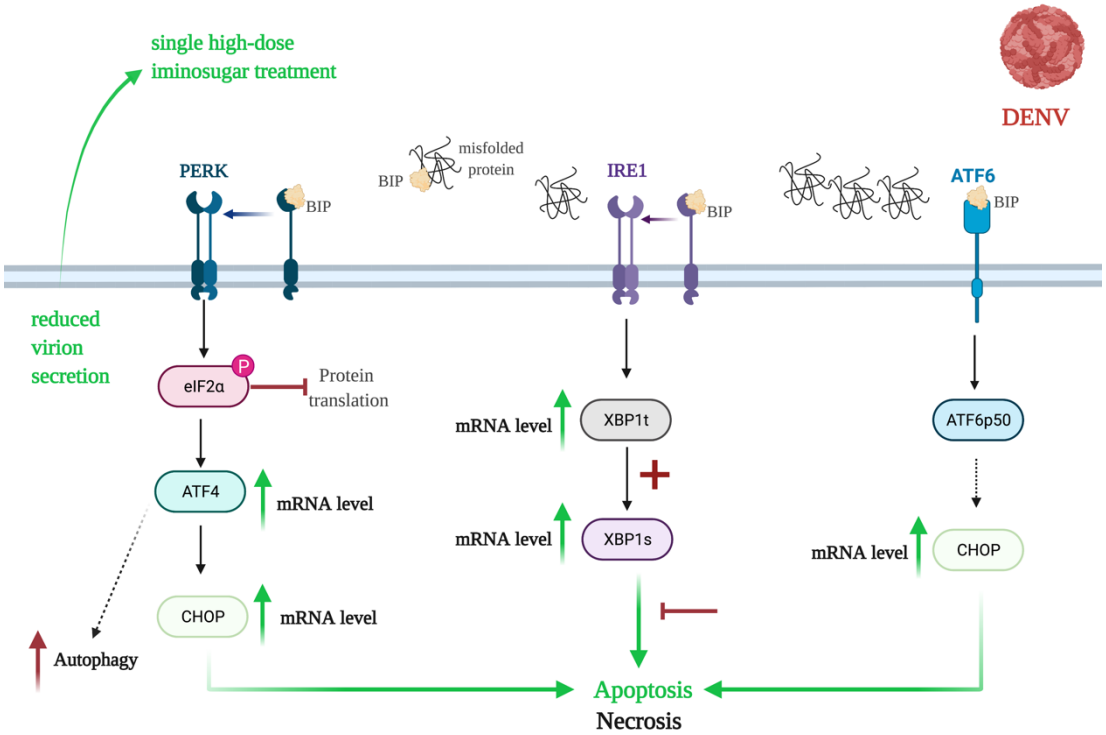

Figure 40: Hypothesis of MOA of single high-dose treated DENV2-infected cells. Increase of total and spliced XBP1 (*XBP1t*, *XBP1s*) was detected, with a ratio above 1 for *XBP1s*, in continuous low-dose and single high-dose DENV2-infected cells. Whereas *ATF4* and *DDIT3* (CHOP) mRNA levels are only detected in single high-dose treated DENV2-infected cells, potentially initiating the intrinsic apoptosis pathway. Increase of *ATF4* but not *DDIT3* (CHOP) was measured in mock-infected cells, suggesting that release of high-dose *N*B-DNJ treatment increased ER stress, but ER homeostasis could nevertheless be restored. Red shows the effects of DENV2 infection, green shows the effect single high-dose treatment of DENV2-infected cells based on the initial results.

Although Vero E6 cells are a good model to investigate the effects of viral infection and replication, it is known that the UPR can differ between cell types, especially between cell lines and primary cells (333,342). DENV triggers signalling pathways that result in the generation of antiviral mediators. DENV eradication is aided by these pro-inflammatory cytokines and chemokines. Its ability to evade these defences leads to increased viral replication, whereas overexpression of these mediators can be harmful to the host (341,521) and may contribute to the cytokine storm, which is linked to increased vascular permeability in severe dengue illness. The pro-inflammatory

cytokine TNFα was significantly reduced in response to single/double high-dose treatment in DENV ADE model mice, in which αGluI was inhibited (203). In primary immature dendritic cells treated continuously with concentrations of *N*N-DNJ capable of causing αGluI inhibition TNFα secretion was reduced, whereas for reduction of infectious virions αGluII inhibition was sufficient (333). In a physiological scenario, with infected cells carrying various virus loads, high dose iminosugar treatment might only lead to apoptosis of cells with high virus load. However, apoptotic cells were shown to have a beneficial effect on the cytokine storm downregulating both anti- and pro-inflammatory cytokines (522,523). A decrease of cytokines was measured in DENV-infected and high-dose iminosugar-treated mice, which lead to survival of the animals up to 14 days (end of experiment) (203). Therefore, single/double high-dose treatment might provide a new avenue to treat DENV infection.

Cytokine effects cannot be studied in Vero E6 cells but may be crucial for the understanding of the antiviral MOA in cells treated with a single high dose. To examine and comprehend this complex cascade of events involving DENV infection and iminosugar treatment, a primary human UPR-knockout cell culture model might be beneficial. The only knockout cells currently accessible are murine embryonic fibroblasts, and understanding the cell-type specific changes in DENV-induced UPR activation requires the development of a more physiological human cell culture model. Therefore, work on hiPSCs knockouts was initiated and is discussed in future work.

6.5 Future work

The COVID-19 pandemic impacted the work described in this chapter. Additional experiments were planned and are listed here:

6.5.1 Intracellular location of viral proteins in the presence and absence of iminosugar treatment

Final IF staining needs to be performed to differentiate between the different localization in the cell (ER, Golgi, lysosome) for the viral glycoproteins after continuous low-dose and single high-dose treatment, to identify where the protein aggregates are located and if they are cleared over time.

6.5.2 The unfolded protein response in DENV-infected and iminosugar-treated cells

So far, I measured the UPR signature of mRNA levels for *XBP1, ATF4, DDIT3* and *ATF6*. However, the protein levels associated with affected transcripts still need to be determined. The active version of ATF6 is spliced and translocated from the nucleus, therefore confocal microscopy might be required.

6.5.3 Identification of triglucosylated proteins in αGluI inhibited cells

FOS analysis measured the accumulation of glycans detached from proteins. However, it has not been shown which proteins might be triglucosylated inside the cells after the different treatment regimens. Besides, it is most likely the viral glycoproteins E, prM

and NS1 will be detected and host glycoproteins which might play a role in the long-lasting antiviral effect might be detected. Therefore, the inactive version (active site mutant D580N) of the αGluI protein has been expressed, purified and will be coupled to a column to perform pull-down experiments and subsequent identification of binding partners using mass spectrometry.

If any triglucosylated proteins were identified, measuring their longevity might be of interest to identify what happens to the triglucosylated unfolded proteins after the αGluI block is released and to exclude (or discover) any other MOA of high-dose iminosugar treatment besides inhibition of αGluI and αGluII. An inducible αGluI expression cell line will be created with a Vero αGluI knockout cell line, which is already established in the lab (524). Unfortunately, a degron system with a degradation tag on the protein is not possible for ER resident/secreted proteins. Therefore, we chose the Tet-on/Tef-off system, in which the expression of the gene can be influenced.

6.5.4 Cell death in DENV-virus and iminosugar-treated cells

In DENV-infected cells unfolded/misfolded proteins accumulate in the ER as the host glycosylation pathways are trying to cope with the additional burden of viral glycoprotein folding. Administering a high dose of iminosugar at a late stage of infection (when viral protein production is at a high level) leads to an even more overwhelming overload of unfolded proteins. As a consequence, I hypothesize that apoptosis will be initiated by the UPR in infected cells only. To prove this concept, I

need to demonstrate activation of a cell death pathway (apoptosis, autophagy, necrosis) and that only high-dose-treated DENV-infected cells are dying.

6.5.5 Induced iPSCs knockouts

6.5.5.1 Phenotypical description of hiPSCs-derived knockout macrophages

Human iPSCs CRISPR-Cas9 knockouts of the genes *MOGS, GANAB*, *EIF2AK3, ERN1, XBP1 and ATF6* were created for further elucidation of the role of the UPR in DENV infection and the single high-dose treatment. A double-cutting strategy was adopted to knock out genes of interest using gRNAs.

Genome editing by CRISPR-Cas9 or other genome editing tools induces DNA double strand breaks (DSBs) at particular loci. To reconstruct the DSB lesion site, endogenous repair machinery is recruited, which results in either non-homologous end-joining (NHEJ) or homology directed repair (HDR). NHEJ causes error-prone small indels, resulting in non-functional truncated proteins or mRNA degradation due to nonsense-mediated decay (525). To create knockouts, the hiPSCs were transfected utilising a RNP, consisting of Cas9 protein and gRNA, delivery technique and electroporation. Using screening primers, transfected cells were screened for gene knockout and sequenced to detect and validate the gene deletion (**Figure 41**).

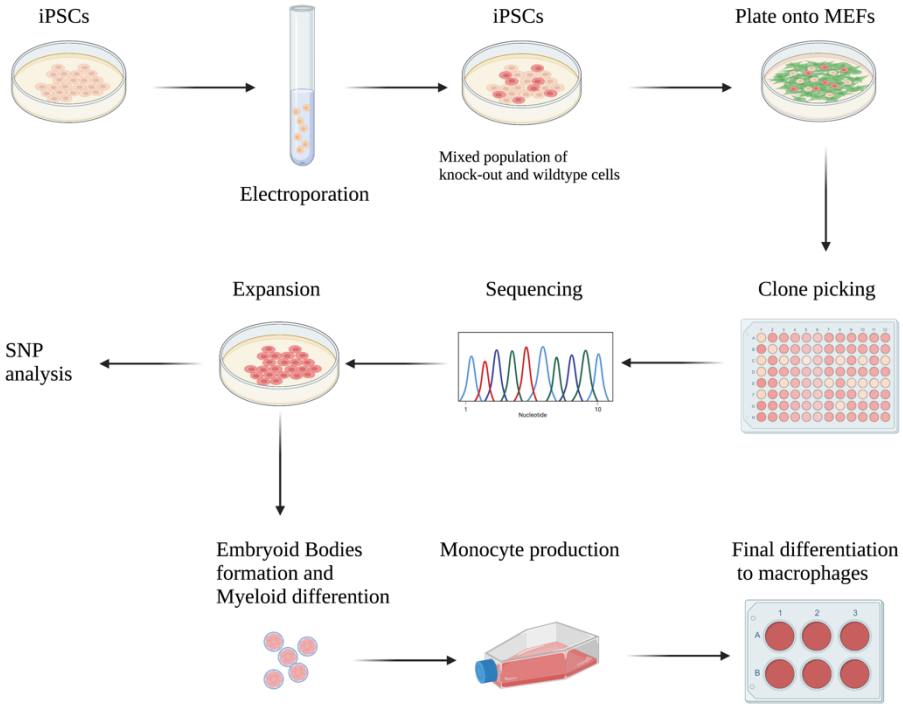

Figure 41: Schematic representation of the CRISPR-Cas9 based knockout strategy in hiPSCs. Human iPSCs generated from a healthy donor were propagated under feeder-free conditions and electroporated with a gRNA pair utilising RNP delivery system. Transfected cells were cultured under feeder-free conditions and after validation if knockout was successful for some cells, they were plated at low density onto mouse embryonic fibroblast (MEF) feeder cells, which are not able to divide. After ~4 – 6 days of expansion, individual single cell colonies were picked into a 96-well plate directly under feeder-free conditions and clones were expanded. Human iPSC clones were pre-screened for deletions and sequenced to determine exact sequence of each clone. The knockout cell clone was expanded, and SNP analysis was performed. If cells were karyotypically normal, cells were differentiated into embryoid bodies, which produces monocytes after 4 – 6 weeks. Monocytes will be finally differentiated into macrophages.

No knockout in hiPSCs were found in the literature for any of our genes of interest. Here, exemplary the creation of the *MOGS* knockout is shown in **Figure 42** (other genes are shown in **Appendix** III**, Figure 59-60**). Not only are there no hiPSCs for *MOGS* available, but also no transgenic mice. Even though knockouts are available in cell lines such as Vero E6 (524) and Huh7.5 (267), it is possible that the *MOGS* gene is important for development for hiPSCs growth or differentiation into final cell

phenotypes. Nevertheless, hiPSCs knockouts were attempted by targeting independently three different exons (exon 2, 3, 4b, **Figure 42**). To ensure chromosomal stability of the knockouts SNP analysis was performed (**Appendix III, Figure 65-71**), and one cell clone was taken through the transfection process without inducing a knockout (ERN1-15 9A$^{+/+}$) as a control.

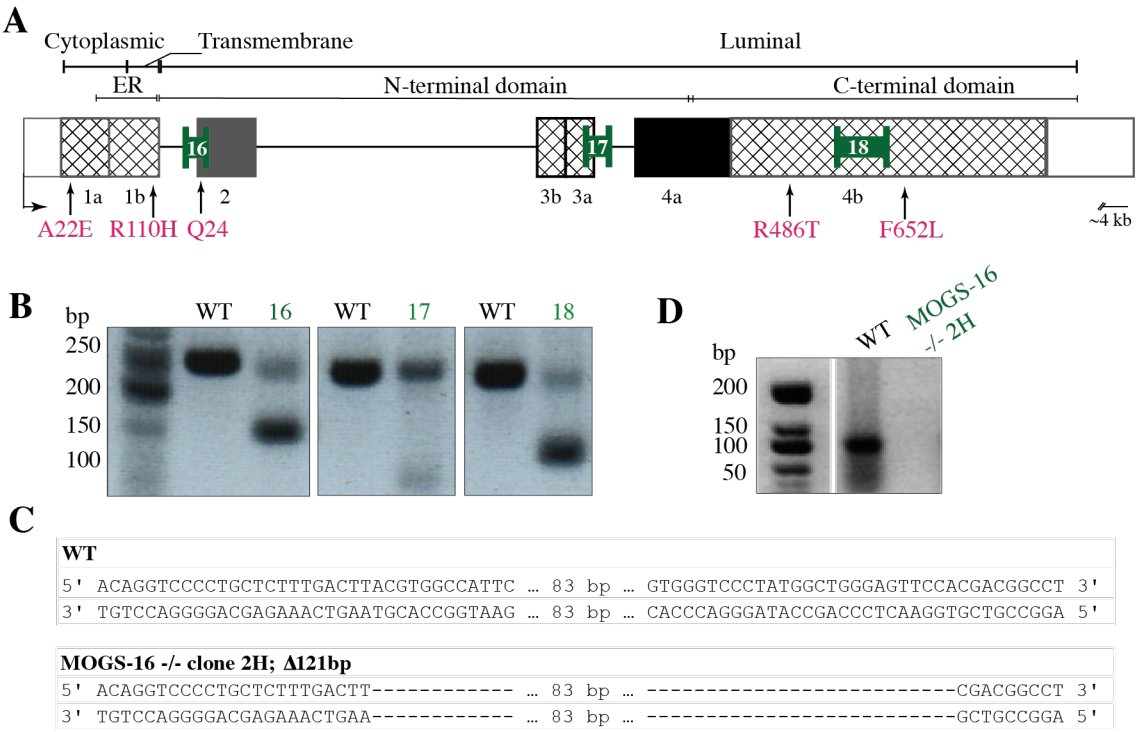

Figure 42:Genomic structure of *MOGS* and CRISPR/Cas9 targeting. (A) Human *MOGS* genomic structures, containing 4 exons, of which some are alternatively spliced (grey), in non-coding regions (grid). Functional domains are highlighted and known patient mutations are shown in pink. (B) Human iPSCs transfected with the designed gRNA pair, cells were expanded for ~4 days before half of cells were lysed and analysed via PCR for potential knockout cells or frozen down. (C) Mixed cell populations of knockout and wild-type cells were plated on mouse embryonic fibroblast feeder cells. After ~7 days expansion, individual single cell colonies were picked into 96-well plate in feeder-free conditions and clones were expanded. Single hiPSCs clones were screened for insertions, deletions and potential cross-contamination with a second clone by PCR with primers targeting the knockout area (D) and sequencing was performed to identify the exact knockout.

After confirming the knockout cell lines displaying no chromosomal abnormalities, they were differentiated into precursor macrophages. Out of the 6 knockouts, all were producing precursor macrophages, except for the *MOGS* knockout cell line. Even though these cells showed no abnormalities in their chromosomal stability, it seems, similar to CDG-IIB patients, that this gene might be essential for macrophage differentiation. If the gene is not essential, potentially, knockouts in a different exon might lead to successful macrophage *MOGS* knockouts cells.

Due to the pandemic the following experiments were not possible: The next steps would have been to determine the macrophage phenotype, by identifying the expression of key markers of the macrophage lineage – the LPS co-receptor CD14 and the pan-leukocyte marker CD45 – and determination if truncated proteins are still expressed in the knockout cell line and potentially active.

6.5.5.2 Dengue virus infection and UPR in hiPSC-derived knockout macrophages

Preliminary data showed that wildtype hiPSC-derived macrophages could be infected with DENV and secreted $1.5x10^6$ viral GE copies/mL. Infection levels, secretion and infectivity of virions need to be investigated for the knockout cells.

UPR-induced ERAD was thought to be an antiviral response produced by cells to combat invading infections. However, recent evidence suggests that the UPR response could also be hijacked by viruses to have a favourable outcome for the virus. The UPR

initiates molecules (IRE1, PERK and ATF6) that reside in the ER membrane and are kept in an inactive state by the folding chaperone BiP. When ER stress occurs, BiP is competitively sequestered by misfolded proteins in the ER and released from the initiation molecule, leading to the activation of the downstream signalling cascades. These downstream processes will be further analysed in the knockout cells, including the activation and expression of ERAD proteins and analysis of the cytokine response.

Chapter 7 Towards the identification of specific inhibitors of ER alpha-glucosidase I

7.1 Introduction

ER αGluI is the first enzyme to act on N-linked glycans after they have been attached to protein by the OST inside the ER lumen. ER αGluI is a type II single-pass transmembrane protein (526) and removes the outermost glucose from N-glycans attached to nascent polypeptides entering the ER. The enzyme acts with an inverting mechanism specific for α(1,2) glycosidic bonds (220,527). Iminosugars with a glucose-stereospecific analogue in the headgroup (DNJ and derivatives) are inhibitors of ER alpha-glucosidases I and II and often have an antiviral effect as shown in clinical trials against HIV, HCV and DENV infections (285–287,289,290). However, as glucose mimetics, iminosugars have undesirable side effects due to their lack of specificity and broad range of target enzymes. Most clinical studies have found some gastrointestinal side effects as a result of inhibition of intestinal alpha-glucosidases, which may be alleviated by dietary changes (289,290). These side effects necessitate the development of more specific ER α-glucosidase inhibitors. The first specific ER αGluII inhibitor, tocopherol-DNJ (ToP-DNJ), was reported in 2018 (507). A second compound (3,7a-di*epi*-alexine) has been speculated to specifically target ER αGluI, since it did not show inhibitory activity in ER microsomes against purified *Chaetomium thermophilum* αGluII, but prevented N-glycan trimming of a model

glycoprotein (528). However, its specificity for ER αGluI has not been formally demonstrated.

Here, I investigated potential avenues for a future ER αGluI specific inhibitor. To date, two structures of ER αGluI are available, one from yeast (PDB ID: 4J5T), and the murine (mus musculus, *Mm*) αGluI in complex with the iminosugar M*O*N-DNJ (PDB ID: 5MHF), reported by our laboratory (203). The overall structure of ER αGluI consists of two domains; the N-terminal super-beta-sandwich domain (*Mm* ER αGluI residues 94-339) and a C-terminal glycosyl hydrolase domain (*Mm* ER αGluI residues 381-838;

Figure 43A). The N-terminal domain belongs to the Pfam family PF1923 and its role is unknown. The C-terminal domain belongs to the GH63 family (Pfam family: PF03200) and contains the active site of the enzyme at the centre of the helical barrel. An α-helix (*Mm* ER αGluI residues 350-374) connects the N-terminal and C-terminal domains (

Figure 43B). Comparison of the structures of the GH63 family member *E.coli* YgjK in complex with glucose in the active site (PDB ID: 3W7S, (529)) with the one of the *Mm* ER αGluI complexed with M*O*N-DNJ (PDB ID: 5MHF, (203)) indicated that the DNJ-ring of the iminosugar binds *Mm* ER αGluI (203) in the same orientation as that of glucose in *Ec*YgjK.

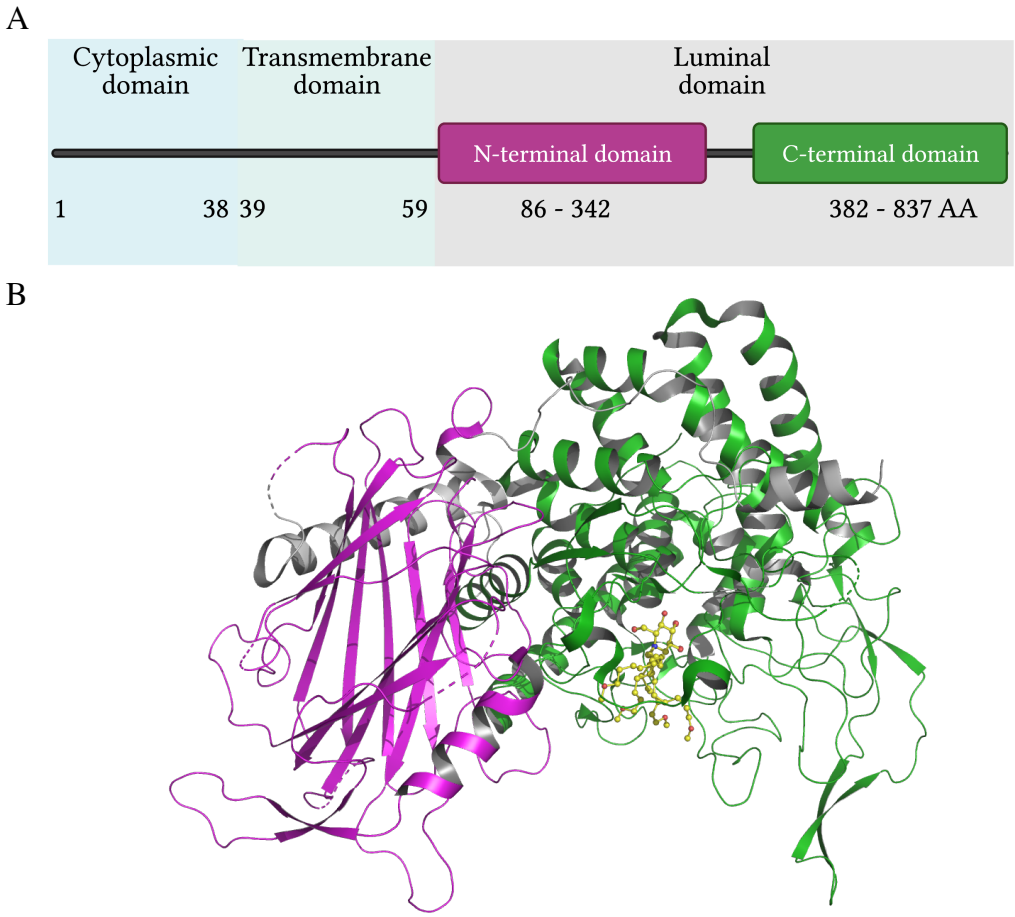

Figure 43: Overall architecture of the ER αGluI. (A) Schematic diagram of human αGluI, showing the cytoplasmic, transmembrane and luminal domain. (B) *Mm* αGluI with the N-terminal domain in magenta and the C-terminal catalytic domain in green. The iminosugar M*O*N-DNJ bound to the active site is shown in yellow, ball and stick representation (PDB ID: 5MHF). The α-helix connecting the two domains is coloured in grey.

There are several approaches to develop a specific inhibitor for a given target protein. This includes different screening methods, such as focused screens to validate compounds similar to known inhibitors, physiological screens using tissue-based methods, as well as structure-based and ligand-based drug discovery approaches using computational tools (reviewed in (530)).

In this chapter, I describe three different approaches to identify specific molecules binding to ER αGluI. First, based on previous results from our laboratory, I performed co-crystallisation of *Mm* ER αGluI with the known inhibitor *N*B-DNJ. The presence of an inhibitor is required to form crystals, as evidenced by previous failed attempts to crystallise the apoprotein. The idea was to subsequently soak these crystals with molecules from a chemical library – to identify additional binders that might be linked to the iminosugar. Once chemically linked to the iminosugar, such ligands would give rise to a new generation of more specific ligands. However, as it was difficult to consistently obtain crystals of *Mm* ER αGluI, even in the same crystallisation condition and in the stabilising presence of *N*B-DNJ, I decided to explore an *in vitro* approach to enrich the ligand repertoire of ER αGluI. A fluorescence-based thermal shift assay (TSA, or differential scanning fluorimetry) was optimised and employed to identify a set of binders for ER αGluI. This method measures the change in melting temperature (T_m) of ER αGluI, upon binding of a compound. An increase in melting temperature in the presence of a compound that is equal to, or higher than that induced by the known inhibitor *N*B-DNJ, points to the given compound as a potential tight binder (531).

Lastly, I used a DNA-encoded chemical library-based screen (DELopen) - one of the most recent technologies employed in the early phases of drug discovery (532). This method involves incubation of ER αGluI in solution with 2.9 billion different compounds that are all linked to specific DNA tags in the same tube, followed by a protein pull down assay. The presence of specific DNA tags enables the identification of those compounds that bound ER αGluI using next generation sequencing (NGS).

7.2 Methods

7.2.1 Protein construct *Mm* αGluI

The *Mm* ER αGluI (Uniprot entry Q80UM7) wild-type construct was originally cloned by Alessandro T. Caputo (533) with help from the Oxford Protein Production Facility (OPPF), for expression in mammalian cells. Primers were designed by Dr Bird and expression carried out under OPPF standard operating procedures (SOPs; see OPPF standard protocols: Cloning and Expression Screening, https://www.oppf.rc-harwell.ac.uk/OPPF/protocols/). To simplify protein production and crystallisation, the N-terminal region containing the transmembrane domain was removed. Therefore, the gene in the construct starts at residue 59 and ends at residue 834, and was cloned into the vector pOPINGS, with a C-terminal 6xhistidine-tag. The mature protein after cleavage of the signal peptide in the pOPINGS vector contains at the N-terminus a ETG and on the C-terminus a ASKWSHPQFEK-6xHIS-tag. Later, expression and purification was established by Johan Hill (524) using methods described in (203).

7.2.2 Protein purification

7.2.2.1 Sample preparation

The HEK 293F cells' supernatant containing the expressed protein of interest was harvested at day 4 after transfection (described in section 3.5.2) by centrifugation at 1500 x *g* for 20 minutes. Concentrated PBS to a final concentration of 1x PBS was added to the supernatant. pH of this sample was adjusted to 7.4 and the solution filtered through a 0.45 μm filter.

7.2.2.2 Affinity purification

Nickel-affinity chromatography was carried out using a HisTrap™ excel column (GE Healthcare Life Sciences). The column was equilibrated with 5 CV MilliQ water, 5 CV elution buffer and 5 CV binding buffer (**Table 22**). Clarified supernatant was loaded at 1 mL/minute onto the column, washed with 10 CV binding buffer and eluted with a gradient of elution buffer containing 500 mM imidazole (0 – 100%, 1 mL/minute, 20 CV). Fractions of eluted protein were collected and further processed for crystallography, differential scanning fluorimetry or DELopen compound library screening experiments.

Table 22: Concentration of binding and elution buffer for *Mm* ER αGluI using HisTrap™ excel.

Buffer	Component	Concentration
Binding buffer	PBS	1x
	glycerol	5%
	TCEP	0.1 mM
Elution buffer	PBS	1x
	glycerol	5%
	Imidazole	500 mM
	TCEP	0.1 mM

7.2.2.3 Size exclusion chromatography

Size exclusion chromatography (SEC) was the final step for *Mm* ER αGluI protein purification. Samples were dialysed to remove imidazole using Snakeskin Dialysis tubing (Thermo Fisher Scientific) with a 10 kDa MWCO against dialysing buffer (**Table 23**) twice for 1 hour and concentrated to 1-5 mg/mL in a spin concentrator (Sartorius Vivaspin) with a MWCO cut-off of 50 kDa. The Superdex 200 16/600 column (GE Lifesciences) was equilibrated using filtered and degassed gel filtration buffer (**Table 23**) prior to the run. Samples were run at a flow rate of 1 mL/minute.

Peak fractions were collected, concentrated and flash-frozen in liquid nitrogen for storage. The identity of the protein samples was previously confirmed through SDS-PAGE, western blot analysis (533) and MS (524). All protein batches used in this thesis were confirmed by SDS-Page and western blots as described in 3.3.2 and 3.4.

Table 23: Concentration of dialysis and gel filtration buffer for *Mm* ER αGluI.

Buffer	Component	Concentration
Dialysis buffer	HEPES	20 mM
	NaCl	150 mM
	glycerol	5%
	pH 7.5	
Gel filtration buffer	HEPES	20 mM
	NaCl	100 mM
	TCEP	0.1 mM
	pH 7.5	

7.2.3 Protein methylation

To improve chances of crystallisation of *Mm* ER αGluI, a reductive methylation of the affinity purified protein was conducted. Reductive methylation of lysine residues increases the likelihood of protein-protein interactions by introducing some hydrophobicity to the surface of the protein (534). After the His-tag affinity purification step, the protein sample was dialysed using dialysis buffer (**Table 23**), concentrated to 1–5 mL and 2% v/v of 1 M dimethylamine borane (DMAB, Sigma-Aldrich) and 4% v/v 1 M formaldehyde was added. After 2 hours incubation with agitation, DMAB and formaldehyde at the same concentrations were added again and incubated for further 2 hours. Finally, 1% v/v of 1 M DMAB was added, and the sample incubated for 16 hours with agitation. All steps were carried out on samples kept either on ice or at 4°C. The reaction was quenched by the addition of 12.5% v/v 1 M glycine and 0.1% v/v 1 M dithiothreitol (DTT) and incubated for 2 hours with

agitation to stop the reaction. Methylated protein was purified using SEC (described in 7.2.2.3). Previously, Dr Abhinav Kumar from the Zitzmann laboratory confirmed methylated lysines and oxidised methionines on *Mm* ER αGluI protein samples prepared employing the above method, using in-gel tryptic digestion and MS (524).

7.2.4 Crystallisation

7.2.4.1 Set-up of crystallisation screens

Methylated *Mm* ER αGluI (5 mg/mL) with 1 mM *N*B-DNJ was dispensed into SwissSci MRC 2 drop 96 well plates containing 50 µL of custom-made C1 condition (0.09 M NPS consisting of 0.03 M sodium nitrate; 0.03 M sodium phosphate dibasic; 0.03 M ammonium sulfate, 0.1 M Buffer System 1 (imidazole, MES monohydrate) pH 7.5 and 30% v/v precipitant Mix 1 (40% ethylene glycol; 20% w/v PEG 20000) of the commercial Morpheus HT-96 screen (Molecular Dimension) in each well to co-crystallise *Mm* ER αGluI with 1 mM *N*B-DNJ. Sitting drops were set up with a Mosquito® system (TTP Labtech) with 0.1 µL protein and 0.1 µL screen condition. All crystallisation plates were stored in a Rigaku Minstrel HT crystallisation robot at 18°C, with images from drops recorded at regular intervals at visible and ultraviolet wavelengths.

7.2.4.2 Data collection

Mm ER αGluI crystals, appeared in various drops in the crystallisation plate, were picked using nylon loops and flash cooled in liquid nitrogen (the Morpheus crystallisation condition is self-cryoprotecting). Diffraction data was collected at 100

K on the I04 beamline at the Diamond Light Source, Harwell, UK. Data collection parameters are listed in **Table 24**.

Table 24: Data collection parameters of *Mm* ER αGluI *N*B-DNJ.

Beamline	DLS I04
Detector	Pilatus 6M-F
Wavelength (Å)	0.92
Oscillation per Image (º)	0.1
Number of images	1800
Exposure time (s)	0.1
Beam size (µm)	43x30
Transmission (%)	74.81

7.2.4.3 Data processing, model building and refinement

Diffraction data was processed using the autoPROC toolbox (Global Phasing) (535). Refinements were carried out using BUSTER (536). Structure was refined with non-crystallographic symmetry restraints (537). The thermal motion of each chain was modelled with Translation/Libration/Screw (TLS) parametrisation. Model building was performed using COOT (538). Restraints for the ligand, *N*B-DNJ, were prepared using Grade webserver. The preliminary analysis of this structure, detailed in this chapter, was carried out using various tools available in CCP4 suite and Phenix (539). The reflection file was checked for any anomalies using SFCHECK utility in CCP4 (540) and Xtriage in Phenix (541). All contacts involving protein and ligand were computed using the CONTACT utility in CCP4 suite. All interactions between potential hydrogen bond donor and acceptor in the distance range from 2.2 – 3.6 Å

were considered as hydrogen bonds. The molecular electrostatic potential was computed using the APBS webserver (542). LigPlot was used for 2D representation of the protein-ligand contacts (543). All figures were prepared using PyMOL (544) or Chimera (545).

7.2.5 Differential scanning fluorimetry

Differential scanning fluorimetry (DSF; or TSA) experiments were performed using 0.5 µM *Mm* ER αGluI in gel filtration buffer (**Table 23)**. Compounds were dissolved in DMSO to 10 µM and 50 µM, and trials were run using different DMSO concentrations to check if DMSO affected the protein. All experiments were carried out employing an Applied Biosystems 7500 FAST real-time PCR system (Thermo Fisher Scientific) using MicroAmp Fast 96-well reaction plates (Thermo Fisher Scientific) and MicroAmp optical adhesive film (Thermo Fisher Scientific). The protein solution was mixed with 5x SYPR Orange (Molecular Probes) in gel filtration buffer to a final volume of 20 µL. All samples were subjected to a thermal ramp from 25°C to 90°C with an increment of 1°C per minute and the secondary fluorescence from the dye was detected using FAM and ROX filters which correspond to λ_{ex} of 494 nm and λ_{em} of 602 nm. *N*B-DNJ, a known inhibitor of ER αGluI with a inhibitory constant (Ki) of 463 nM (524), was used as a positive control. The screening of *Mm* ER αGluI against the MicroSource Pharmacon 1600 FDA approved library (Daniel Ebner's group, Target Discovery Institute, Nuffield Department of Medicine, University of Oxford) was performed using the Lightcycler™ 480 (Roche). Compounds were dispensed at 50 µM and 10 µM in singlicates into 384-well

Lightcycler 480 multiwell plates (Roche) and protein-SYPRO Orange mix was added, using the same protocol as described above.

7.2.6 DNA-encoded library

DNA-encoded chemical library technology (DELopen; WuXi AppTec) was used to identify potential chemical compounds that bind *Mm* ER αGluI, with the aim of expanding its ligands' chemical space. A library of $2.9x10^9$ compounds was screened. Each compound in this library is conjugated to a unique DNA barcode (546). All experiments were performed according to manufacturer's instructions (547). Briefly, a total of 5 µg *Mm* αGluI in 100 µL washing buffer (WB, DELopen) was mixed with magnetic Ni^{2+} beads (HisPur Ni NTA, Thermo Fisher Scientific) and kept for binding at room temperature for 30 minutes on a rotating wheel. The magnetic beads were washed using WB prior to mixing with protein. Washed beads without added protein were used as negative control. The protein-bead mix was then washed once with 200 µL selection buffer (SB, DELopen) to remove unbound protein. Subsequently, 10 µL of the DEL library was added to 90 µL of protein-bead mix in SB buffer and incubated for 1 hour at room temperature on a rotating wheel. After incubation, samples were washed thrice with 200 µL SB. Protein, bound to the compounds, was then denatured and DNA-conjugated compounds were eluted by boiling the sample in 100 µL SB at 95°C for 10 minutes. To increase efficiency of compound identification, eluted DNA-conjugated compounds were cooled and incubated with fresh protein-bead mix for two further rounds. The eluted DNA-conjugated compounds were sent to WuXi Apptec for next generation sequencing to identify bound compounds.

7.3 Results

7.3.1 Crystal structure of *Mm* αGluI with *N*B-DNJ

ER αGluI is one of the most underexplored proteins in the ERQC in terms of structure-based drug discovery – mainly because of the challenges associated with its crystallisation.

In the crystals of *Mm* ER αGluI in complex with M*O*N-DNJ, the ligand is primarily held in the active site through interactions of the deoxynojirimycin ring with the protein, which is a common feature seen in glycosidases inhibited by iminosugars (524). The long hydrophobic alkyl chain tail makes a few specific contacts and was modelled in different conformations. However, consistent co-crystallisation of the protein with M*O*N-DNJ were not successful. Therefore, crystallisation with *N*B-DNJ, another iminosugar with a shorter tail compared to M*O*N-DNJ, was attempted here as a next step to understand the effect of tail orientation on binding and specificity. All batches of *Mm* ER αGluI protein used for this thesis have been analysed by SDS-PAGE and western blot (**Appendix IV**, **Figure 72**).

The crystallisation condition for *Mm* ER aGluI was obtained from the work done by a previous member of this laboratory (524). Although this crystallisation condition never produced crystals consistently, this was the only known condition that gave diffraction quality crystals to use as the starting point for further structural work. The protein sample used in these trials, was subjected to reductive methylation before

crystallisation which can change the surface properties of the protein, promoting better crystal packing. Therefore, methylated protein was also used for crystallisation of *Mm* αGluI with *N*B-DNJ described in this chapter.

7.3.1.1 Crystallisation and data collection

Crystallisation of *Mm* αGluI with *N*B-DNJ was first attempted using a commercial Morpheus HT-96 employing Swisssci MRC 2 drop 96 well crystallisation plate under the exact same conditions as reported for the earlier *Mm* αGluI M*O*N-DNJ complex. Unfortunately, no crystals appeared in this plate. However, after setting up a plate with only the Morpheus screen C1 condition, the condition used for crystallising the *Mm* αGluI M*O*N-DNJ complex, a few crystals were observed in some of the drops. Therefore, crystallisation of *Mm* ER αGluI complexed with *N*B-DNJ was attempted in a set of crystallisation screening conditions based on C1, varying the pH of 0.1 M NPS from 6.2 – 6.9, the MP1 concentration from 44 – 55%, and keeping the 0.09 M NPS mix.

For the custom-made screen, co-crystallisation was carried out using methylated *Mm* αGluI. A protein concentration of 4.89 mg/mL was used for the setup. Protein was mixed with 1 mM *N*B-DNJ prior to the setup. After 35 days crystals appeared in 2 wells (B1 and E1) in the plate and another two crystals appeared after 100 days (A2 and F1). Crystals from the wells E1 and F1 did not diffract, however crystals from wells B1 and A2 provided data sets of 3.6 Å and 2.6 Å, respectively. Considering the better resolution of the second data set, only these data were used for the next steps

towards structure determination. The crystal that appeared in well A2 is shown in **Figure 44**.

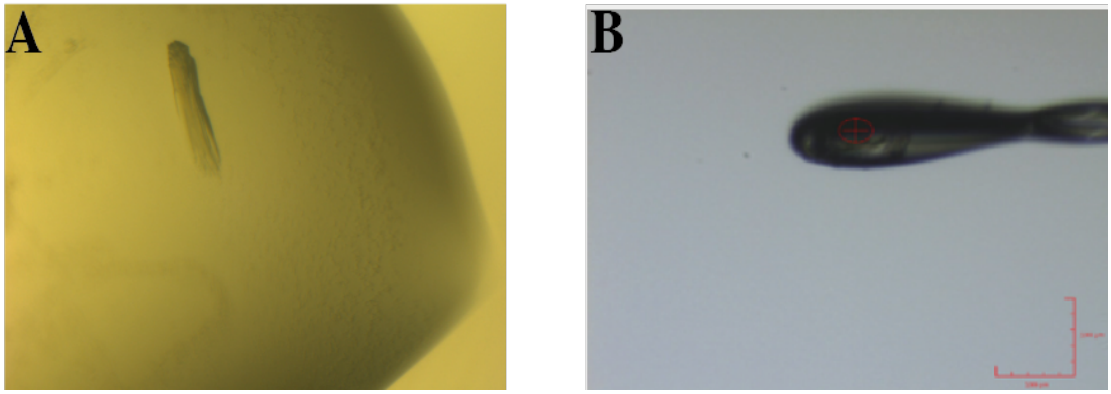

Figure 44: Rod-shaped crystal form of *Mm* ER αGluI co-crystallised with *N*B-DNJ. (A) Crystal as found in the drop after 100 days. (B) Single crystal mounted in a nylon loop. Picture taken during data collection at Diamond Light Source, beamline I04.

7.3.1.2 Data processing, structure resolution and refinement

Diffraction images from the crystal from well A2 were processed using the autoPROC suite of programs and the data processing statistics are given in **Table 25**. This crystal also belongs to the same space group as that of the previously reported *Mm* ER αGluI M*O*N-DNJ structure (PDB ID 5MHF).

Self-rotation maps generated using MOLREP (548) indicated the presence of NCS two-fold axes in addition to the crystallographic two folds confirming the presence of more than one molecule in the asymmetric unit. Estimation of the Matthews Coefficient values using the 'Cell Content Analysis' (549) utility from the CCP4 based on data and the molecular weight of *Mm* ER αGluI indicate the most probable number

of molecules in the asymmetric unit to be four with a solvent content of 52.34% and a Matthews Coefficient value of 2.54 $Å^3$/Da.

Table 25: Data processing statistics of the dataset obtained from the *Mm* ER αGluI *N*B-DNJ crystal in well A2. Values in brackets represent the data for the high-resolution data shell.

Resolution Range (Å)	92.21 - 2.60 (2.93 - 2.60)
Cell Dimension:	
a,b,c (Å)	106.73, 128.69, 134.18
α,β,ɣ (°)	90.00, 99.88, 90.00
Space group	$P2_1$
Total Reflections	200230 (9267)
Unique Reflections	58698 (2935)
R_{merge}	0.206 (0.521)
R_{meas}	0.245 (0.627)
R_{pim}	0.131 (0.344)
Completeness ellipsoidal (%)	92.3 (61.2)
Completeness spherical (%)	53.5 (8.9)
CC1/2	0.983 (0.828)
mean I / sd I	0.546 (0.558)

Data was checked for any further features/anomalies using the SFCHECK utility in CCP4. The output from this program indicated the presence of a translational non-crystallographic symmetry (tNCS). The presence of tNCS was further confirmed by calculating a native Patterson map using Fast Fourier transform (FFT). The native Patterson map showed a peak at fractional coordinates U = 0.45, V = 0.5, W = 0.26.

The initial phases were calculated after Rigid Body refinement of the model deposited in PDB ID: 5MHF. Refinement was carried out using BUSTER and manual model building between each round of refinement was carried out using COOT (550). Waters were added to maps at a sigma level of +3 for the Fo-Fc map and +1 for the 2Fo-Fc map. There was positive density to build $GlcNAc_2Man_1$ to the predicted N-glycosylation site on N654 into two chains, and $GlcNAc_2$ to the two others. After all

the protein chains were built, the map was checked for any unexplained blobs. There was positive density on the Fo-Fc map near the active site to which the co-crystallised *N*B-DNJ could be modelled. Sulfate (SO_4^{2-}) molecules (3 molecules in chain D and 2 in chains A, B, and C) were also modelled onto the density, all of which occurred at the interfaces between different chains. The current data refinement statistics are given in **Table 26** and the refinement is still in progress.

Table 26: Model building and refinement statistics.

Resolution Range (Å)	105.14 - 2.602
R_{work} (%)	20.41
R_{free} (%)	24.99
RMSD bond length (Å)	0.011
RMSD bond angels (°)	1.12
Ramachandran outliers	20
Ramachandran favoured (%)	95.76
MolProbity Clashscore	5.29 (99^{th} percentile)
MolProbity Score	2.13 (95^{th} percentile)
Good Rotamers (%)	86.47
B-factor (wilson plot) ($Å^2$)	36.02
Mean B value($Å^2$)	29.59
Residues modelled	A: 62 - 193, 198 - 220, 225 - 307, 311 - 339, 348 - 412, 421 - 838
Chain A-D	B: 62 - 193, 198 - 220, 225 - 307, 311 - 339, 348 - 412, 421 - 838
	C: 57 - 193, 198 - 220, 225 - 307, 311 - 339, 346 - 412, 421 - 838
	D: 57 - 193, 198 - 220, 225 - 307, 311 - 337, 349 - 412, 421 - 838
Methylated lysine	A-D: 111, 131, 227, 304, 366, 371, 376, 378, 553, 662, 736, 779
Oxidised methionine	A-D: 414, 421, 519

7.3.1.3 Structure analysis

A preliminary analysis was carried out with the structure in its current state of refinement. The root-mean-square deviation (RMSD) between the four chains in the asymmetric unit of this structure varies from 0.119 - 0.243 Å, indicating that the chains

were similar (**Figure 45A**). The overall structure of the *Mm* ER αGluI *N*B-DNJ complex (**Figure 45B**) is very similar to that of the only other structure of this protein, reported from our laboratory previously (524). Both structures have four chains in the asymmetric unit, arranged in the form of two dimers (**Figure 45C**).

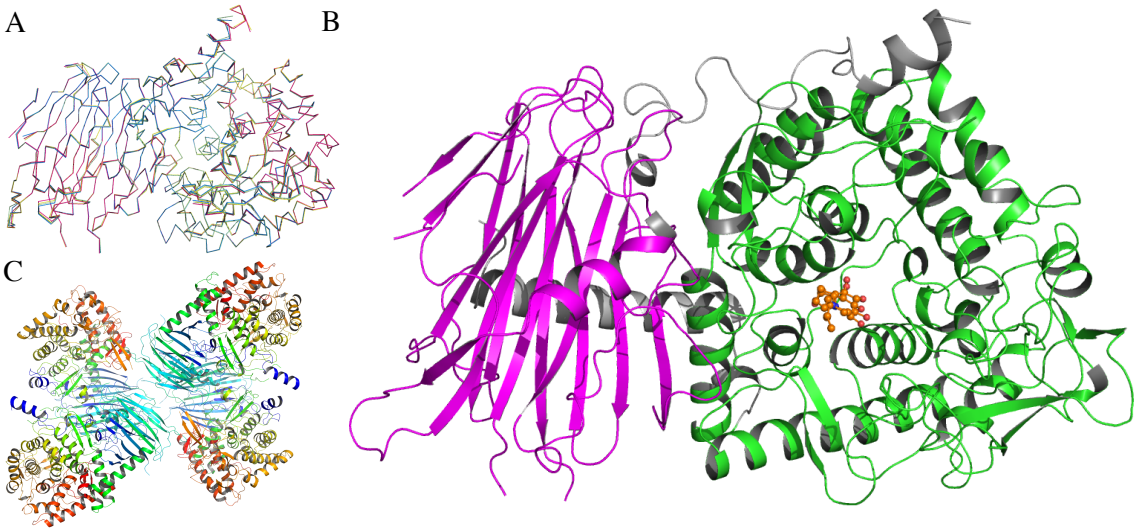

Figure 45: Overall structure of *Mm* ER αGluI with *N*B-DNJ in the active site. (A) Superposition of all four chains in the asymmetric unit, shown in ribbon representation. All images were prepared in Pymol. (B) The N-terminal domain is displayed in magenta and the C-terminal catalytic domain in green. The iminosugar *N*B-DNJ bound to the active site is shown in orange, in ball and stick representation. (C) Asymmetric unit of *Mm* ER αGluI *N*B-DNJ complex. Each chain is shown in rainbow colours with blue at the N-terminus and red at the C-terminus.

The *Mm* ER αGluI *N*B-DNJ chain A could be superposed over the *Mm* ER αGluI M*O*N-DNJ (PDB ID: 5MHF) chain A with an RMSD of 0.44 Å over 722 Cα atoms indicating no major differences between the two structures (**Figure 46**). *Mm* αGluI *N*B-DNJ chain A could also be superposed onto that of the homologue from yeast

(PDB ID: 4J5T) with a slightly higher RMSD of 1.75 Å over 588 Cα atoms, similar to what was reported previously with the *Mm* αGluI M*O*N-DNJ complex (203,524). The major differences lie in the loops in the N-terminal domain, the orientation of the N-terminal helix and a few loops distal to the active site within the catalytic domain.

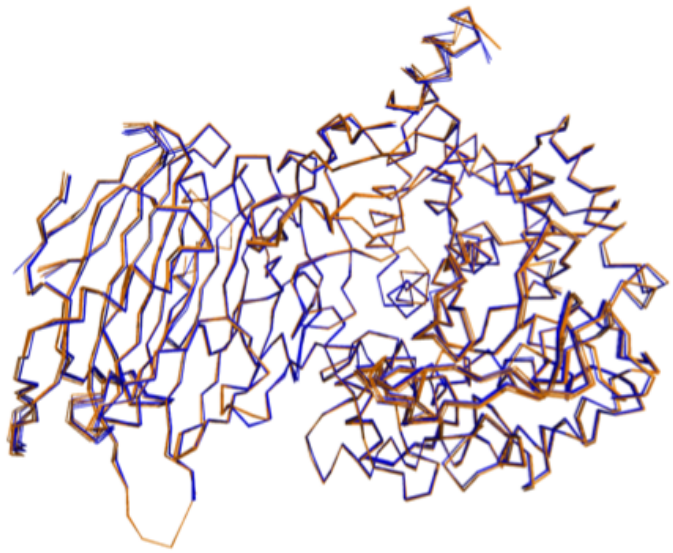

Figure 46: Superposition of *Mm* ER αGluI complexed with *N*B-DNJ (orange) and *Mm* ER αGluI complexed with M*O*N-DNJ (blue).

In the active site, there was strong density to model the deoxynojirimycin ring of *N*B-DNJ and the immediate surrounding water molecules, similar to what was reported for the *Mm* ER αGluI M*O*N-DNJ complex. There was no clear density to model the carbon-tail of the iminosugar. *N*B-DNJ is modelled in two slightly different orientations in the active site to indicate the possible conformers of the DNJ ring due the absence of a density for the tail region of *N*B-DNJ. The occupancies of each of the conformers were refined for every chain, with the constraint that they sum to 1.0. An

examination of the protein-ligand contacts in the structure shows that *N*B-DNJ is held in the active site mainly through hydrogen bonding interactions with the side chains of the residues W447, D448, D580, and W747, and with the main chain carbonyl oxygen of G578 (**Figure 47**). Both conformers make similar interactions with the protein in the active site. None of the methylated lysines were close to the active site, and therefore unlikely to affect the binding to the iminosugar.

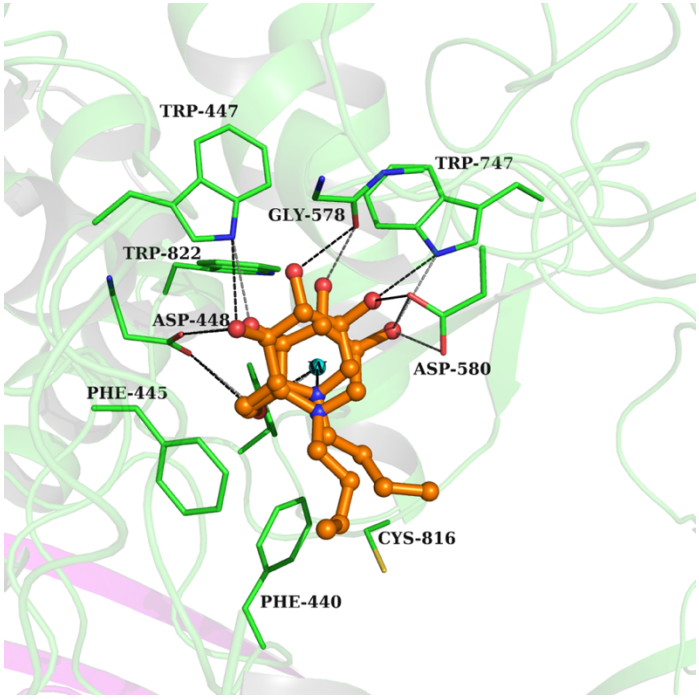

Figure 47: Active site of *Mm* ER αGluI in complex with *N*B-DNJ. The side chain amino acids within 5 Å radius of the ligand are shown as green sticks and the iminosugar in orange ball and stick representation. Hydrogen bonds between the DNJ ring of the two conformations of *N*B-DNJ and the amino acid residues W447, D448, G578, D580 and W747 of the protein are shown as black and grey dashes, respectively. The water molecule near the ligand is shown in cyan colour.

As expected, the DNJ ring of both the iminosugars, M*O*N-DNJ and *N*B-DNJ, binds to the *Mm* ER αGluI active site in a similar fashion. However, M*O*N-DNJ can form

additional interactions with other residues in the pocket through its longer alkyl tail which will not be possible for *N*B-DNJ (**Figure 48**). Previous isothermal calorimetry (ITC) data also showed a more favourable entropy change (ΔS) for binding to M*O*N-DNJ than to *N*B-DNJ, leading to a less inherently ordered system (524).

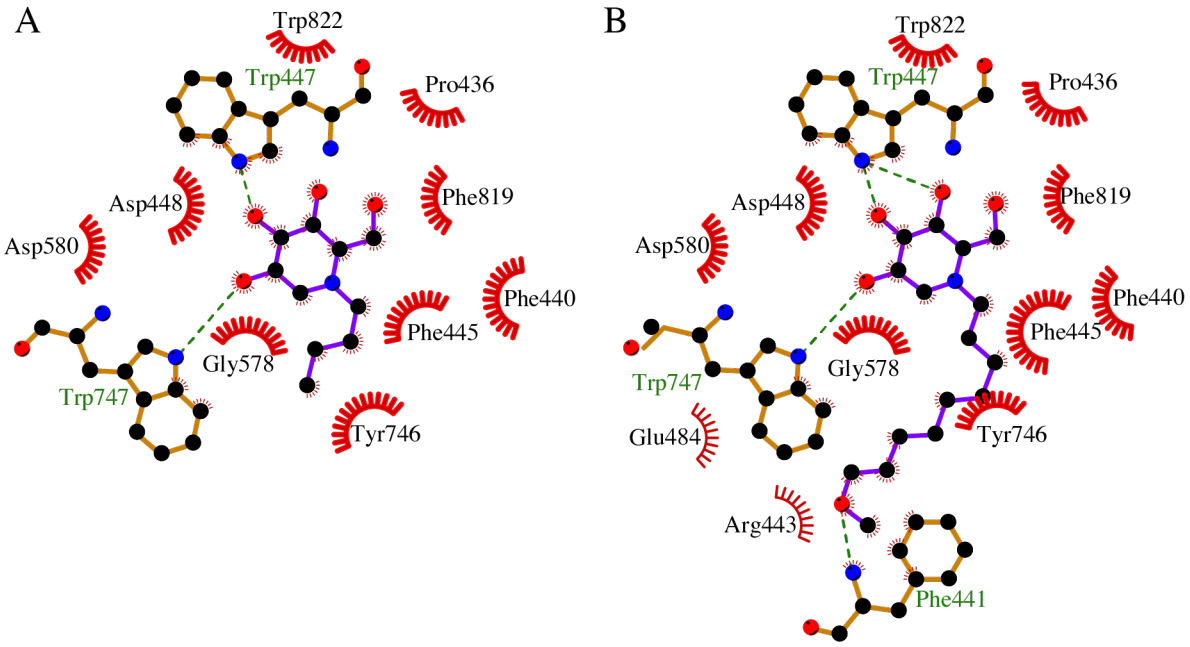

Figure 48: Two-dimensional diagram (LigPlot) showing interactions of *Mm* ER αGluI with (A) *N*B-DNJ (B) M*O*N-DNJ. Iminosugars are shown in purple colour. Dashed lines indicate interactions between main chain/ side chain of protein and ligand. Water molecules bound to the active site are not shown for clarity purposes. Interactions are only shown for chain A. Diagram created using Ligplot (543).

As mentioned above, there was no density to model the alkyl chain of the iminosugars. This indicates flexibility of the alkyl-chain of the iminosugars compared to the DNJ head-group. This stands in contrast to binding of the iminosugar to the ER αGluII, shown previously in our laboratory (533,551). In the structure of ER αGluII, the alkyl

tail had a defined conformation, interacting with the 'exclusion loop' of the protein, which is currently being used to direct the design of more specific inhibitors.

Mm ER αGluI contains a conserved cysteine (C816) from a neighbouring loop that is close to the active site. The sulphur atom of this cysteine is at a distance of 8.4 – 8.7 Å from the nitrogen atom of the DNJ ring in the *N*B-DNJ *Mm* ER αGluI complex and 7.2 Å from the M*O*N-DNJ *Mm* ER αGluI complex. Designing an iminosugar with a cysteine reactive tail to form a disulphide bond with this cysteine 816 could potentially lead to a more specific inhibitor (203).

7.3.1.4 Modelling of human alpha-glucosidase I

All structural work mentioned above was carried out using *Mm* ER αGluI mainly because of the difficulty associated with the expression of the full-length human ER αGluI. Expression of human (*Hs*) ER αGluI using a construct lacking the transmembrane domain (residue 1-59) was also not successful. Previous attempts using commercial full-length *Hs* ER αGluI did not give any diffraction quality crystals (524).

Mm ER αGluI and *Hs* ER αGluI share 87% sequence identity in the amino acid sequence. The residues that are different between the two proteins are spread over the entire length of the sequence rather than concentrating on specific regions of the protein. However, the active site residues are conserved between the two proteins.

In the absence of an experimental structure, a *Hs* ER αGluI model was created using the protein prediction tool Iterative Threading ASSEmbly Refinement (I-TASSER) web server (552). The sequence of the protein lacking the transmembrane region of *Hs* ER αGluI was used for modelling for direct comparison with the published *Mm* αGluI structure (PDB ID: 5MHF). The model of *Hs* ER αGluI, obtained from I-TASSER (C-score = 1.61) superposed with *Mm* ER αGluI with an RMSD of 0.436 Å over 605 Cα atoms (**Figure 49**) indicating no major differences between the model and the crystal structure. This was expected considering the high sequence identity.

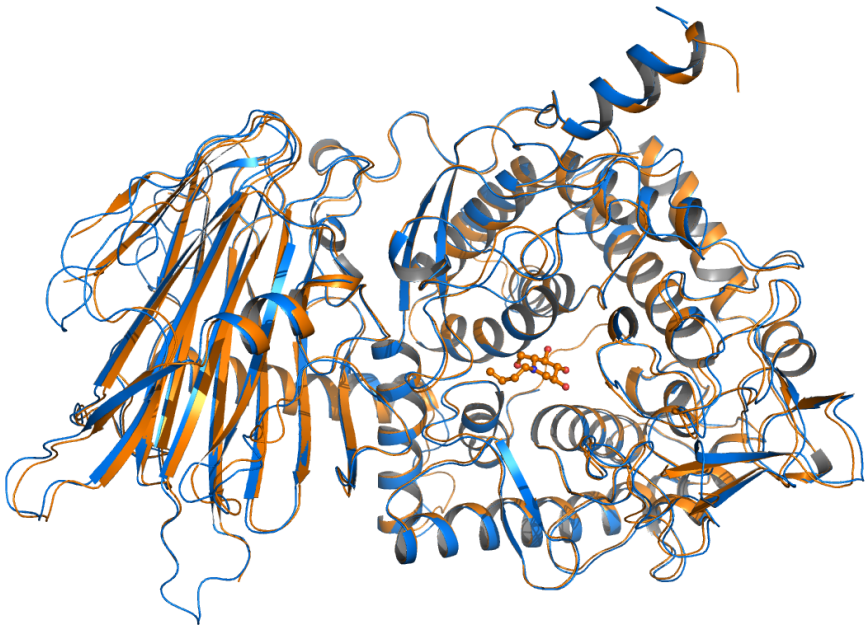

Figure 49: I-TASSER model of *Hs* ER aGluI. The *Hs* ER αGluI amino acid sequence without the transmembrane domain (residue 60-837; Uniprot Q13724) was used to model this structure. *Hs* αGluI (blue) shows high structural similarity to *Mm* ER αGluI (orange) sharing a sequence identify of 87%. *N*B-DNJ (orange) was modelled into the active site guided by the crystal structure described earlier in this thesis.

Next, the surface charge of the two homologues were computed using the Adaptive Poisson-Boltzmann Solver (APBS) web server (542). Vacuum electrostatics of *Mm* ER αGluI and the model of *Hs* ER αGluI showed no major differences (**Figure 50**).

The active sites of both molecules are negatively charged, consistent with a previous analysis from our laboratory, where a high degree of charge conservation was observed for 150 ER alpha-glucosidases derived from different species (524).

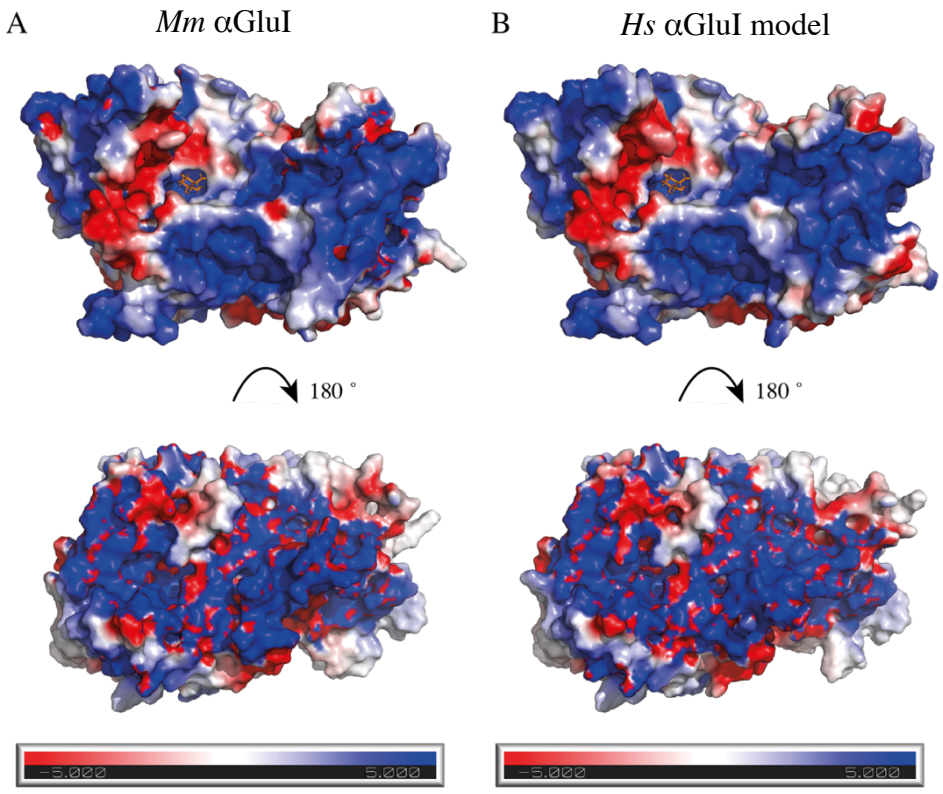

Figure 50: Vacuum electrostatic potential of human and murine ER αGluI. Electrostatic potential of (A) the crystal structure of *Mm* αGluI and (B) modelled *Hs* αGluI. Vacuum electrostatics were computed using the Adaptive Poisson-Boltzmann Solver (APBS) webserver.

7.3.2 Differential scanning fluorimetry of *Mm* αGluI with an FDA-approved compound library

DSF is a cost-effective method to screen the stability of a protein in the presence of different buffers, salt, pH and other components. It is also used in early drug discovery

to identify initial hits (553). In a DSF experiment, the protein is unfolded by increasing the temperature and the unfolding process is monitored as the secondary fluorescence from a suitable dye. As the protein unfolds, more and more hydrophobic patches will be exposed. Fluorescence of the dye on binding to the exposed hydrophobic patches is recorded in the experiment. The dye that is commonly used for carrying out DSF of soluble proteins is SYPRO orange. SYPRO orange has a high signal-to-noise ratio and a long excitation wavelength (near 500 nm), which minimizes the interference of small molecules, as they typically have an absorption maxima at shorter wavelengths (554).

In principle, as the temperature increases, the protein begins to unfold and expose hydrophobic areas, on which SYPRO orange can bind and emit fluorescence. The curve of fluorescence over temperature was fitted with a sigmoidal model, in which T_m is the temperature where 50% of the protein is denatured. With increasing temperature, aggregation occurs which excludes the dye from binding to the protein, causing a characteristic drop in the fluorescence at higher temperature (554).

DSF experiments carried out by a previous member of our group had shown an increase in T_m of *Mm* ER αGluI by 10°C in the presence of 100 μM *N*B-DNJ in water. I repeated DSF using a recently prepared batch of protein. The highest *N*B-DNJ concentration used here was 50 μM, as this was the highest concentration that could be dissolved in 0.5% DMSO, the highest DMSO concentration tolerated by the protein. I used DMSO as the solvent in the FDA chemical compound library I intended to screen , which is dissolved at 10 mM in 100% DMSO, resulting in a final concentration of 0.5% DMSO in the screen. Without ligand, *Mm* ER αGluI showed a T_m of 48.0°C and the melting temperature was increased by 6.69°C in the presence of 50 μM *N*B-

DNJ (T_m 54.7°C, **Figure 51**, **Table 27**), which was lower as previously described (533). No binding of SYPRO orange alone or autofluorescence was detected for samples containing *N*B-DNJ alone without protein. Therefore, *Mm* ER αGluI containing *N*B-DNJ was used as positive control in all DSF experiments.

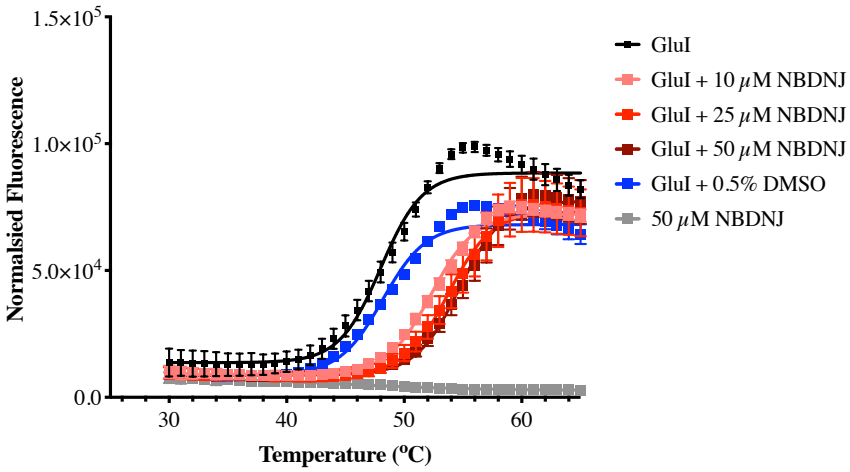

Figure 51: Differential scanning fluorimetry of *Mm* ER αGluI. Determination of the T_m of *Mm* αGluI with and without *N*B-DNJ or DMSO based on a sigmoidal fit (Boltzmann sigmoidal) of the normalised fluorescence. For each measurement 0.5 µM *Mm* αGluI and 5x SYPRO orange were used. Measurements were carried out in the temperature range from 20°C to 90°C with an increase of 1°C per minutes. All measurements were done in triplicates and error bars indicate standard deviations.

Table 27: Melting temperature (T_m) and relative melting temperature (ΔT_m) compared to native *Mm* αGluI from DSF.:

Sample	T_m (°C)	ΔT_m (*Mm* αGluI)
Mm αGluI	48.01	0
Mm αGluI + 10 µM *N*B-DNJ	52.30	4.29
Mm αGluI + 25 µM *N*B-DNJ	53.77	5.76
Mm αGluI + 50 µM *N*B-DNJ	54.70	6.69
Mm αGluI + 0.5% DMSO	48.17	0.16
50 µM *N*B-DNJ	45.16	na

DSF was then performed using a compound library with 1600 FDA-approved drugs (Pharmakon1600, MicroSource Discovery System, full list of compounds in **Appendix IV, Table 40**) in singlicates at 10 µM and 50 µM, corresponding to 20 times and 100 times excess of compound respectively, compared to protein (0.5 µM). The Z'-factor was calculated based on the 3x standard deviation of positive controls (*Mm* aGluI with 10 or 50 µM *N*B-DNJ) and with 10 or 50 µM DMSO as negative controls. The calculated Z'-factor for all plates were above ≥0.5 (ranging from 0.567 – 0.663), which indicates appropriate assay condition, where an ideal Z'-factor = 1 (555). To be considered for a tested compound as a positive hit, the T_m between the compound and the DMSO control (ΔT_m) has to be three times higher than the standard deviation of the DMSO control, which was 1.58°C for 0.1% and 1.85°C for 0.5% DMSO.

Even though a ΔT_m of 6.69°C was observed while testing *Mm* ER αGluI with 50 µM *N*B-DNJ, a *Mm* ER αGluI-*N*B-DNJ sample in high-throughput screening I performed at the Target Drug Discovery Institute (TDI) using their Eco dispensing robot, showed only an increase of 4.21°C and 3.64°C for 50 µM and 10 µM *N*B-DNJ, respectively. However, none of the compounds tested was identified as a significant hit when screened at the TDI. The highest ΔT_m measured was 1.45°C at 50 µM, whereas at 10 µM no substantial increase could be detected.

7.3.3 DNA-encoded chemical library screen to identify new compounds that bind *Mm* ER αGluI

DNA-encoded chemical library technology makes use of a library of 2.9 billion compounds, each with a unique DNA tag. The unique DNA tag helps to identify the compounds that bind the protein following a high throughput screen (556). Through several rounds of affinity selection, following binding on an immobilized protein, the library finally yields a mixture of compounds, enriched on the protein of interest. NGS of the DNA-tag identifies the bound compound (532,557–559). Purified *Mm* ER αGluI was immobilised onto beads and three cycles of affinity selection were performed. As a negative control, washed beads without protein were used. The specificity of *Mm* ER αGluI binding of the compounds was compared with that of the same compounds binding to *Mm* ER αGluII and *Hs* UGGT1, the other key players in the calnexin cycle.

A total 789,627 compounds out of 2.9 billion compounds were detected as bound to the proteins *Mm* ER αGluI, *Mm* ER αGluII and *Hs* UGGT1. After removing the background with the non-template control (NTC), 257,065 compounds were identified as hits. For *Mm* ER αGluI 10,090 compounds had an enrichment above 10 and 937 compounds had an enrichment above 100 (**Figure 52**, **Table 28**). Out of these latter compounds, 9 were chosen. Three out of these nine bound only to *Mm* αGluI, another compound with a high enrichment factor bound to all three (*Mm* αGluI, *Mm* αGluII and *Hs* UGGT1) and one compound bound to *Mm* αGluI and *Hs* UGGT1. Four compounds that were negative for binding *Mm* αGluI were included in the list of nine

compounds for validation in other experiments concerned with *Mm* αGluII and *Hs* UGGT1 drug development.

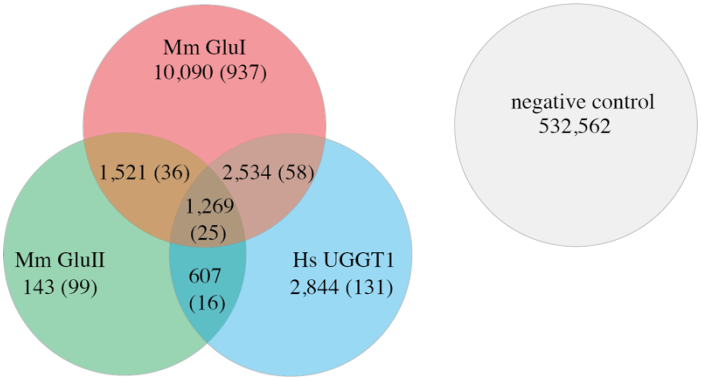

Figure 52: Venn diagram of compounds bound to *Mm* αGluI, *Mm* αGluII, *Hs* UGGT1 and a non-template control (negative control). The number of molecules found to be enriched >10 and >100 (in brackets) by sequencing are shown.

Table 28: Compounds binding to *Mm* ER αGluI chosen for further investigation.

	Enrichemnt				
NsynthonID	*Mm* αGluI	*Mm* αGluII	*Hs* UGGT1	neg. control	MW (Da)
10070-81-30-324-172	2957.05	4919.31	231.21	0.1	650.18
10008-267-468-102-0	2863.15	0.1	0.1	0.1	548.73
100690-315-3-21-468	2219.75	0.1	0.1	0.1	541.7
10070-81-35-205-172	2217.78	0.1	0.1	0.1	669.75
10070-183-17-324-382	0.1	0.1	1849.7	0.1	607.15
10069-336-44-6-143	0.1	0.1	613.42	0.1	665.61
10070-42-23-86-482	0.1	0.1	1387.28	0.1	626.16
10015-188-736-400-0	0.1	3745.21	0.1	0.1	623.46
10070-63-18-324-382	369.63	0.1	1156.07	0.1	633.19

Orthogonal methods that can validate binding such as surface plasmon resonance (SPR) and ITC have been initiated. However, they were affected by the pandemic. They have been restarted and are in progress at the time of writing.

7.4 Discussion

This chapter describes three different sets of experiments employed to potentially identify a novel inhibitor for ER αGluI, and their outcomes.

Structure-based inhibitor design was attempted first. *Mm* ER αGluI turned out to be a difficult protein to crystallise. Lack of consistency in obtaining crystals is one of the main bottlenecks in using this approach for *Mm* ER αGluI. In spite of all difficulties, a complex of *Mm* ER αGluI and the iminosugar *N*B-DNJ was obtained. Structure analysis indicated that *N*B-DNJ and M*O*N-DNJ (previously reported from this laboratory) bind to the catalytic site of *Mm* ER αGluI in a similar manner despite the varying lengths of their alkyl tails. In both cases, there was strong density only to model the DNJ-ring. Any density to build the molecule past the DNJ ring was completely absent, emphasising the flexibility of the alkyl chain.

A detailed analysis of the protein-ligand interactions indicated no major difference between the binding modes of the two ligands. Notably, the Cys816 residue that is close to the nitrogen of the iminosugar (8.4 – 8.7 Å and 7.1 Å, respectively from the sulphur atom of the C816) could be utilised in the future to design a strong and specific inhibitor for ER αGluI (203). An extended iminosugar tail with a cysteine thiol reactive group that could form a covalent bond with C816, may lead to an irreversible, but specific αGluI inhibitor.

The structure of *Mm* ER αGluI and *Hs* ER αGluI indicated no major differences between each other at molecular level. A few amino acid differences that are spread out across the whole length of the sequence did not lead to any difference in the surface charge distribution of the protein. High sequence similarity plus the structural similarity from the modelling study further supports our use of *Mm* αGluI as a model for efforts towards a specific human targeted antiviral. A combination approach involving ligand-based screen to identify new chemical moieties together with a high throughput virtual screening using *Mm* ER αGluI as the receptor may be another useful strategy towards a specific inhibitor.

A DSF screen against a library of FDA-approved compounds resulted in the identification of a few compounds that increased the stability of *Mm* ER αGluI above the threshold. The increase in stability, even though small, may provide another route towards developing a specific inhibitor. However, none of the compounds were superior to the known inhibitor *N*B-DNJ in stabilising the protein. Next steps involve understanding the binding and inhibition of these compounds and furthermore, screening against a much larger compound library to identify stronger hits.

Through DNA-encoded chemical library based high throughput screening, I identified 937 compounds that specifically bind *Mm* ER αGluI. These results provide a strong starting point towards identifying new *Mm* ER αGluI pharmacophores and binding sites. A similar approach was used previously to identify a specific inhibitor of the receptor-interacting protein kinase 1, a regulator of necrosis and inflammation: the initial hit was identified using the DNA-encoded chemical library approach (560).

After hit to lead optimisation, the compound successfully completed a phase II clinical study against ulcerative colitis (NCT02903966). Using the DELopen library we identified a few potential binders of ER αGluI. However, such hits do not provide information regarding the location of the binding and its binding mode. Biophysical methods such as SPR or ITC and structural studies using Saturation transfer difference nuclear magnetic resonance spectroscopy (STD-NMR) or X-ray crystallography are required to determine the binding affinity and binding site, and functional studies will be necessary to establish if this binding results in an inhibition of ER αGluI.

Even though no specific inhibitor for ER αGluI could be identified in this chapter, the DELopen compounds found to bind ER *Mm* αGluI but not ER *Mm* αGluII or *Hs* UGGT1 could potentially lead to such an inhibitor. Screening of ER αGluI against larger compound libraries might be necessary to identify additional starting points. Another potential strategy could be extending the alkyl chain of M*O*N-DNJ to react with the sulphur atom at C816, thereby increasing the specificity of the iminosugar binding to ER αGluI.

Conclusion

The current COVID-19 pandemic has underscored the urgent need for vaccines and antiviral drugs. The speed at which the COVID-19 vaccines were developed was not only unprecedented and impressive but has saved countless numbers of lives. On the other hand, drug development lags behind, and the absence of broad-spectrum antivirals that is available to patients before thorough study of a novel emerging virus has become even more evident. The first part of my DPhil was aimed at elucidating the mechanism of action of one such potential broad-spectrum antiviral, but the COVID-19 pandemic limited these efforts. Conversely, I was able to apply my knowledge and skill sets in viral glycobiology towards understanding glycosylation of SARS-CoV-2, vaccine antigen design, and antiviral drug screening.

All current vaccine development efforts and various vaccine platforms focus on the SARS-CoV-2 S glycoprotein as the immunodominant part of the virus. An effective vaccine that is designed to elicit neutralising antibody responses (B-cell vaccines) needs to mimic the viral immunogenic epitopes as closely as possible to produce a B-cell response that is sufficiently broad to provide lasting protection against virus exposure. In this regard, one first needs to know the physiologically relevant glycosylation of the wildtype virus. To address this question, I cultured in a human lung epithelial cell line, harvested and purified the wildtype England/02/2020 strain SARS-CoV-2. Together with colleagues from my group, we worked to expedite this

important project and analysed the N- and O-glycans of this virus, which is arguably the most physiologically relevant dataset to date. At around the same time of purifying the wildtype virus for glycan analysis, the first reports of the ChAdOx1 nCoV-19 (AZD1222) vaccine candidate appeared, and I became interested in the way the S antigen would be presented by vaccinated cells that express the antigen from the shuttle vector used in the creation of the ChAdOx1 nCoV-19 vaccine. We were particularly interested in the absence of the stabilising proline mutations, the presence of the furin cleavage site and the use of a tPA leader sequence present in front of the wildtype S leader sequence. Our hypothesis was that these factors could cause the S antigen to become unstable or otherwise differ from the wildtype S trimer on virions in ways that may be suboptimal in a vaccine antigen. We characterised site-specific glycosylation of both N- and O-glycans, which is a very useful indicator of glycoprotein secretion and three-dimensional shape. While preparing S proteins from both secreted virions as well as from cells transfected with the ChAdOx1 nCoV-19 shuttle vector, the different fates and cellular locations of the resulting proteins became evident. Specifically, one of my main observations was that the majority of the S1 subunit is shed from the cell in the form of soluble monomers when expressed from the ChAdOx1 nCoV-19 shuttle vector. Whether or not monomeric S1 shedding has an effect on the vaccine antibody response or could be implicated in the observed rare side effects, such as Vaccine-induced Thrombotic Thrombocytopenia, remains to be investigated. However, such analysis would require access to vaccinee sera, to which we did not have access during my DPhil.

The glycan analysis further highlighted differences in glycosylation between the various S proteins, indicating various oligomerisation states (trimers or monomers), and whether S had been originally present in more compact, artificially stabilised trimers or in the more accessible, flexible trimers as present on wildtype virus. Glycan analysis can be used to judge antigens as presented by the various vaccine platforms and could be informative in guiding an optimised design that most closely resembles the wildtype antigen.

With regards to antiviral drugs, we still do not have any compounds that could bridge the period between a new virus emerging and vaccines being developed. Faced with a pandemic situation similar to what we are currently experiencing, the only option for testing anti-SARS-CoV-2 drugs was to explore already approved drugs as antivirals, which could be repurposed. At the same time, more specific drugs need to be developed as repurposed drugs may be good as a stop gap, but they will never be more than that, as their development is not specifically aimed at the target virus. Usually, the development of such specific direct acting drugs from scratch takes 7 – 10 years, and the attrition rate is significant, with on average one compound being approved for every 5,000 – 10,000 early molecules. In this pandemic, academic and industry groups of scientists from Oxford and from all over the world, got together in early 2020 to crowdsource ideas and developed a strategy to test toxicity and potency of antivirals as a novel way of accelerated antiviral drug development. This was dubbed the "COVID-19 Moonshot," and our group was an instrumental contributor. I helped to set up the antiviral screening platform of the COVID-19 core facility in the Dunn School of Pathology, University of Oxford. Specifically, I contributed to establish a

physiologically relevant cellular screen with human lung epithelial cells as host cells and plaque or focus forming assays as antiviral readouts capable of detecting any kind of antiviral effect (i.e., not just direct replication inhibition but also creation of less or non-infectious particles) apart from those mediated by the immune system. We shared the data we obtained in nearly 'real time' with the rest of the world by setting up the "SARS-CoV-2 Cellular Tracker" webpage (http://sarscov2.assaytracker.net/), where we collated all antiviral information that was published by other groups around the world, as well as our own experimental results. We did this as cellular antiviral screens were (and still are) a major bottleneck in the worldwide efforts to identify potent drugs against SARS-CoV-2. Reporting negative results was as important as positive ones to avoid repetition of efforts elsewhere. We were also in contact with clinical committees, such as the UK steering group for therapeutics for COVID-19 and the Nuffield Department of Orthopaedics, Rheumatology and Musculoskeletal Sciences (NDORMS) committee in Oxford, for a two-way exchange of information where, for example, we were asked to screen specific drugs against SARS-CoV-2 that were being evaluated to potentially enter human trials and report to these committees commonly administered drugs that appeared potentially proviral in our hands as well as to alert GPs of these findings so they could monitor the patient databases for adverse events. As of now (June 2020) we screened and reported 253 drugs, helping several other research groups in the process.

In our screening efforts, we identified iminosugars as one of the two most promising class of drugs that have not entered clinical SARS-CoV-2 trials at the time of writing. Iminosugars were the focus of my DPhil before the COVID-19 pandemic, specifically

with the aim of developing a broad-spectrum antiviral that could be used in situations like this. Indeed, in a paper published by the Zitzmann group in January of 2020 (203), the discussion of M*O*N-DNJ given in a single or double high-dose regimen stated explicitly 'the prolonged antiviral effect by inhibiting ER αGluI demonstrated here suggest a strong potential benefit of using inhibitors of ER αGluI as a means of controlling viral infections, especially those that pose a threat of rapid global spreading.'. Of course, SARS-CoV-2 was not known at the time of writing that paper. During my DPhil I was interested in DENV; however, I used *N*B-DNJ instead of M*O*N-DNJ as this was a drug that could have been immediately repurposed if found to work against DENV in humans when given in the single high-dose regime; a situation reminiscent of what became even more relevant with the arrival of COVID-19.

The aim of my project was to find out how a single high-dose treatment could lead to the observed prolonged antiviral effect. To this end, I first needed to establish a cellular model that could recapitulate the main observations from the DENV infection mouse model. Using DENV-infected Vero E6 cells, I gathered preliminary data that led me to hypothesize that high-dose iminosugar treatment in virus-infected cells may lead to such an unfolded/misfolded protein overload in the ER. This overlay may induce apoptosis in infected cells only, unlike uninfected cells exposed to the same iminosugar concentration.

My investigations progressed as far as identifying the PERK arm of UPR as a likely contributor to the antiviral effects seen with this dosing regimen. However, to confirm this in a more relevant system, I then proceeded to create hiPSC lines that were

knocked out for factors of all three main UPR arms, as well as two calnexin cycle enzymes. I validated the knockouts by sequencing and was starting to differentiate them into macrophages, ready for initial experiments (e.g., DENV infection) when this work was halted due to the first COVID-19-induced shutdown. Unfortunately, all the cells I created died because differentiated iPSCs-derived macrophages cannot be cryopreserved. Nevertheless, I started again and grew the stem cells for differentiation when COVID-19 restrictions were temporarily lifted. However, the second shutdown forced me to sacrifice these iPSCs for a second time, resulting in the loss of several month of work. I remain committed to this work, and I will re-start this project as soon as possible.

However, even though we still do not know how a single high-dose treatment of iminosugar exerts its long-lasting antiviral effect, we do know that it correlates with the inhibition of ER αGluI. Specifically, it correlates with the presence of triglucosylated FOS that arise from the inhibition of ER αGluI and remain present after enzyme inhibition is reversed. Therefore, inhibiting ER αGluI is a desirable objective, as is the case with inhibition of ER αGluII. However, using monosaccharide mimics such as iminosugars to inhibit these enzymes can lead to unintended off-target effects, as many enzymes in the body recognise glucose. Therefore, I was interested in identifying or developing novel inhibitors of αGluI, sampling a broader chemical space. Although I managed to crystallise *Mm* αGluI once with *N*B-DNJ in the active site, crystallisation of this enzyme was difficult and not reproducible, which did not bode well for crystallisation-based screens, such as FBLD or full compound library screens. Therefore, I proceeded to screen a library of FDA-approved compounds

against the soluble enzyme using a thermal shift assay, but none of the 1600 compounds exhibited sufficient binding to observe a change in melting temperature. I then screened a library of 2.9 billion DNA-tagged molecules against the enzyme in-solution and found 937 potential binders (with enrichment >100). Three potential specific binders for αGluI were ordered for future experiments aimed at validating their binding to the target. If they do interact, the next step is to determine the structure of the enzyme-ligand complex and investigate whether the binding site would lend itself to developing the compounds into inhibitors. These experiments were also interrupted by the COVID-19 pandemic and will be re-started again at the earliest possible opportunity.

If we have learned anything from COVID-19 it is the value and need for a broad-spectrum antiviral drug, and the longer we prolong research toward achieving this principal aim, we will remain as underprepared as we were in early 2020. This viewpoint is not an exaggeration as the rate of emerging and deadly viruses continues to grow which means we live in a world where it is increasingly a question of when rather than if a new pandemic outbreak will occur.

References

1. Rouse BT, Sehrawat S. Immunity and immunopathology to viruses: What decides the outcome? Vol. 10, Nature Reviews Immunology. Nature Publishing Group; 2010. p. 514–26.
2. Fajgenbaum DC, June CH. Cytokine Storm. N Engl J Med. 2020 Dec 3;383(23):2255–73.
3. Raj Kumar Patro A, Mohanty S, Prusty BK, Singh DK, Gaikwad S, Saswat T, et al. Cytokine signature associated with disease severity in dengue. Viruses. 2019 Jan 1;11(1).
4. Guzman MG, Halstead SB, Artsob H, Buchy P, Farrar J, Gubler DJ, et al. Dengue: A continuing global threat. Nat Rev Microbiol. 2010;8(12):S7–16.
5. Bhatt S, Gething PW, Brady OJ, Messina JP, Farlow AW, Moyes CL, et al. The global distribution and burden of dengue. Nature. 2013 Apr 25;496(7446):504–7.
6. Dengue and severe dengue [Internet]. [cited 2021 Jun 14]. Available from: https://www.who.int/news-room/fact-sheets/detail/dengue-and-severe-dengue
7. Basu A, Chaturvedi UC. Vascular endothelium: The battlefield of dengue viruses. Vol. 53, FEMS Immunology and Medical Microbiology. FEMS Immunol Med Microbiol; 2008. p. 287–99.
8. Messina JP, Brady OJ, Golding N, Kraemer MUG, Wint GRW, Ray SE, et al. The current and future global distribution and population at risk of dengue. Nat Microbiol. 2019 Sep 1;4(9):1508–15.
9. Dengue shock syndrome at the emergency room of Queen Sirikit National Institute of Child Health, Bangkok, Thailand | Request PDF [Internet]. [cited 2021 Jun 12]. Available from: https://www.researchgate.net/publication/51761539_Dengue_shock_syndrome_at_the_emergency_room_of_Queen_Sirikit_National_Institute_of_Child_Health_Bangkok_Thailand
10. Arima Y, Edelstein ZR ebecc., Han HK wan., Matsui T. Epidemiologic update on the dengue situation in the Western Pacific Region, 2011. West Pacific Surveill response J WPSAR. 2013 Apr 1;4(2):47–54.
11. Mia MS, Begum RA, Er AC, Abidin RDZRZ, Pereira JJ. Trends of dengue infections in Malaysia, 2000-2010. Asian Pac J Trop Med. 2013 Jun;6(6):462–6.
12. Jessie K, Fong MY, Devi S, Lam SK, Wong KT. Localization of dengue virus in naturally infected human tissues, by immunohistochemistry and in situ hybridization. J Infect Dis. 2004 Apr 15;189(8):1411–8.
13. Cruz-Oliveira C, Freire JM, Conceição TM, Higa LM, Castanho MARB, Da Poian AT. Receptors and routes of dengue virus entry into the host cells. Vol. 39, FEMS Microbiology Reviews. Oxford University Press; 2015. p. 155–70.
14. Van Der Schaar HM, Rust MJ, Chen, Van Der Ende-Metselaar H, Wilschut J, Zhuang X, et al. Dissecting the cell entry pathway of dengue virus by single-particle tracking in living cells. PLoS Pathog. 2008;4(12):e1000244.
15. Acosta EG, Castilla V, Damonte EB. Alternative infectious entry pathways for dengue virus serotypes into mammalian cells. Cell Microbiol. 2009

Oct;11(10):1533–49.
16. Chen Y, Maguire T, Hileman RE, Fromm JR, Esko JD, Linhardt RJ, et al. Dengue virus infectivity depends on envelope protein binding to target cell heparan sulfate. Nat Med. 1997 Aug;3(8):866–71.
17. Martínez-Barragán J de J, del Angel RM. Identification of a Putative Coreceptor on Vero Cells That Participates in Dengue 4 Virus Infection. J Virol. 2001 Sep;75(17):7818–27.
18. Chen Y-C, Wang S-Y, King C-C. Bacterial Lipopolysaccharide Inhibits Dengue Virus Infection of Primary Human Monocytes/Macrophages by Blockade of Virus Entry via a CD14-Dependent Mechanism. J Virol. 1999 Apr;73(4):2650–7.
19. Miller JL, DeWet BJM, Martinez-Pomares L, Radcliffe CM, Dwek RA, Rudd PM, et al. The mannose receptor mediates dengue virus infection of macrophages. PLoS Pathog. 2008 Feb;4(2):e17.
20. Reyes-del Valle J, Chávez-Salinas S, Medina F, del Angel RM. Heat Shock Protein 90 and Heat Shock Protein 70 Are Components of Dengue Virus Receptor Complex in Human Cells. J Virol. 2005 Apr 15;79(8):4557–67.
21. Lozach PY, Burleigh L, Staropoli I, Navarro-Sanchez E, Harriague J, Virelizier JL, et al. Dendritic cell-specific intercellular adhesion molecule 3-grabbing non-integrin (DC-SIGN)-mediated enhancement of dengue virus infection is independent of DC-SIGN internalization signals. J Biol Chem. 2005 Jun 24;280(25):23698–708.
22. Navarro-Sanchez E, Altmeyer R, Amara A, Schwartz O, Fieschi F, Virelizier JL, et al. Dendritic-cell-specific ICAM3-grabbing non-integrin is essential for the productive infection of human dendritic cells by mosquito-cell-derived dengue viruses. EMBO Rep. 2003 Jul 1;4(7):723–8.
23. Tassaneetrithep B, Burgess TH, Granelli-Piperno A, Trumpfheller C, Finke J, Sun W, et al. DC-SIGN (CD209) mediates dengue virus infection of human dendritic cells. J Exp Med. 2003 Apr;197(7):823–9.
24. Lo YL, Liou GG, Lyu JH, Hsiao M, Hsu TL, Wong CH. Dengue virus infection is through a cooperative interaction between a mannose receptor and CLEC5A on macrophage as a multivalent hetero-complex. PLoS One. 2016 Nov 1;11(11).
25. Meertens L, Carnec X, Lecoin MP, Ramdasi R, Guivel-Benhassine F, Lew E, et al. The TIM and TAM families of phosphatidylserine receptors mediate dengue virus entry. Cell Host Microbe. 2012 Oct 18;12(4):544–57.
26. Ayala-Nunez N V., Hoornweg TE, Van De Pol DPI, Sjollema KA, Flipse J, Van Der Schaar HM, et al. How antibodies alter the cell entry pathway of dengue virus particles in macrophages. Sci Rep. 2016 Jul 7;6(1):1–15.
27. Flipse J, Diosa-Toro MA, Hoornweg TE, Van De Pol DPI, Urcuqui-Inchima S, Smit JM. Antibody-Dependent Enhancement of Dengue Virus Infection in Primary Human Macrophages; Balancing Higher Fusion against Antiviral Responses. Sci Rep. 2016 Jul 6;6(1):1–13.
28. Flipse J, Wilschut J, Smit JM. Molecular mechanisms involved in antibody-dependent enhancement of dengue virus infection in humans. Traffic. 2013 Jan;14(1):25–35.
29. Fischl W, Bartenschlager R. Exploitation of cellular pathways by Dengue virus. Vol. 14, Current Opinion in Microbiology. Curr Opin Microbiol; 2011. p. 470–

5.
30. Jain B, Chaturvedi UC, Jain A. Role of intracellular events in the pathogenesis of dengue; An overview. Vols. 69–70, Microbial Pathogenesis. Academic Press; 2014. p. 45–52.
31. Zaitseva E, Yang ST, Melikov K, Pourmal S, Chernomordik L V. Dengue virus ensures its fusion in late endosomes using compartment-specific lipids. PLoS Pathog. 2010 Oct;6(10):e1001131.
32. Modis Y, Ogata S, Clements D, Harrison SC. Structure of the dengue virus envelope protein after membrane fusion. Nature. 2004 Jan 22;427(6972):313–9.
33. Stiasny K, Heinz FX. Flavivirus membrane fusion. Vol. 87, Journal of General Virology. J Gen Virol; 2006. p. 2755–66.
34. Clyde K, Kyle JL, Harris E. Recent Advances in Deciphering Viral and Host Determinants of Dengue Virus Replication and Pathogenesis. J Virol. 2006 Dec;80(23):11418–31.
35. Paul D, Bartenschlager R. Flaviviridae Replication Organelles: Oh, What a Tangled Web We Weave. Vol. 2, Annual Review of Virology. Annual Reviews Inc.; 2015. p. 289–310.
36. Kuhn RJ, Zhang W, Rossmann MG, Pletnev S V., Corver J, Lenches E, et al. Structure of dengue virus: Implications for flavivirus organization, maturation, and fusion. Cell. 2002 Mar 8;108(5):717–25.
37. Zhang W, Chipman PR, Corver J, Johnson PR, Zhang Y, Mukhopadhyay S, et al. Visualization of membrane protein domains by cryo-electron microscopy of dengue virus. Nat Struct Biol. 2003 Nov;10(11):907–12.
38. Guzman MG, Harris E. Dengue. In: The Lancet. Lancet Publishing Group; 2015. p. 453–65.
39. Rodenhuis-Zybert IA, van der Schaar HM, lia da Silva Voorham JM, van der Ende-Metselaar H, Lei H-Y, Wilschut J, et al. Immature Dengue Virus: A Veiled Pathogen? 2010;
40. Dejnirattisai W, Jumnainsong A, Onsirisakul N, Fitton P, Vasanawathana S, Limpitikul W, et al. Cross-reacting antibodies enhance dengue virus infection in humans. Science. 2010 May 7;328(5979):745–8.
41. Rodenhuis-Zybert IA, Moesker B, Voorham JM da S, Ende-Metselaar H van der, Diamond MS, Wilschut J, et al. A Fusion-Loop Antibody Enhances the Infectious Properties of Immature Flavivirus Particles. J Virol. 2011 Nov 15;85(22):11800.
42. da Silva Voorham JM, Rodenhuis-Zybert IA, Nuñez NVA, Colpitts TM, van der Ende-Metselaar H, Fikrig E, et al. Antibodies against the Envelope Glycoprotein Promote Infectivity of Immature Dengue Virus Serotype 2. PLoS One. 2012 Mar 14;7(3):e29957.
43. Wirawan M, Fibriansah G, Marzinek JK, Lim XX, Ng TS, Sim AYL, et al. Mechanism of Enhanced Immature Dengue Virus Attachment to Endosomal Membrane Induced by prM Antibody. Structure. 2019 Feb 5;27(2):253-267.e8.
44. S Richter MK, lia da Silva Voorham JM, Torres Pedraza S, Hoornweg TE, I van de Pol DP, Rodenhuis-Zybert IA, et al. Immature Dengue Virus Is Infectious in Human Immature Dendritic Cells via Interaction with the Receptor Molecule DC-SIGN.
45. Pierson TC, Diamond MS. Degrees of maturity: The complex structure and

biology of flaviviruses. Vol. 2, Current Opinion in Virology. Elsevier B.V.; 2012. p. 168–75.
46. Stohlman SA, Eylar OR, Wisseman CL. Isolation of the dengue virus envelope glycoprotein from membranes of infected cells by concanavalin A affinity chromatography. J Virol. 1976 Apr;18(1):132–40.
47. Shapiro D, Brandt WE, Russell PK. Change involving a viral membrane glycoprotein during morphogenesis of group B arboviruses. Virology. 1972 Dec 1;50(3):906–11.
48. Russell PK, Chiewsilp D, Brandt WE. Immunoprecipitation Analysis of Soluble Complement-Fixing Antigens of Dengue Viruses. J Immunol. 1970;105(4).
49. Smith GW, Wright PJ. Synthesis of proteins and glycoproteins in Dengue type 2 virus-infected Vero and Aedes albopictus cells. J Gen Virol. 1985;66(3):559–71.
50. Naik NG, Wu H-N. Mutation of Putative N-Glycosylation Sites on Dengue Virus NS4B Decreases RNA Replication. J Virol. 2015 Jul 1;89(13):6746–60.
51. Zhang X, Ge P, Yu X, Brannan JM, Bi G, Zhang Q, et al. Cryo-EM structure of the mature dengue virus at 3.5-Å resolution. Nat Struct Mol Biol. 2013 Jan 16;20(1):105–10.
52. Mondotte JA, Lozach P-Y, Amara A, Gamarnik A V. Essential Role of Dengue Virus Envelope Protein N Glycosylation at Asparagine-67 during Viral Propagation. J Virol. 2007 Jul;81(13):7136–48.
53. Bryant JE, Calvert AE, Mesesan K, Crabtree MB, Volpe KE, Silengo S, et al. Glycosylation of the dengue 2 virus E protein at N67 is critical for virus growth in vitro but not for growth in intrathoracically inoculated Aedes aegypti mosquitoes. Virology. 2007 Sep 30;366(2):415–23.
54. Lee E, Leang SK, Davidson A, Lobigs M. Both E Protein Glycans Adversely Affect Dengue Virus Infectivity but Are Beneficial for Virion Release. J Virol. 2010 May 15;84(10):5171–80.
55. Beasley DWC, Whiteman MC, Zhang S, Huang CY-H, Schneider BS, Smith DR, et al. Envelope Protein Glycosylation Status Influences Mouse Neuroinvasion Phenotype of Genetic Lineage 1 West Nile Virus Strains. J Virol. 2005 Jul;79(13):8339–47.
56. Miagostovich MP, Ramos RG, Nicol AF, Nogueira RMR, Cuzzi-Maya T, Oliveira A V., et al. Retrospective study on dengue fatal cases. Vol. 16, Clinical Neuropathology. 1997. p. 204–8.
57. Ramos C, Sánchez G, Hernández Pando R, Baquera J, Hernández D, Mota J, et al. Dengue virus in the brain of a fatal case of hemorrhagic dengue fever. J Neurovirol. 1998;4(4):465–8.
58. Hacker K, White L, de Silva AM. N-linked glycans on dengue viruses grown in mammalian and insect cells. J Gen Virol. 2009;90(9):2097–106.
59. Johnson AJ, Guirakhoo F, Roehrig JT. The envelope glycoproteins of dengue 1 and dengue 2 viruses grown in mosquito cells differ in their utilization of potential glycosylation sites. Virology. 1994;203(2):241–9.
60. Lei Y, Yu H, Dong Y, Yang J, Ye W, Wang Y, et al. Characterization of N-glycan structures on the surface of mature dengue 2 virus derived from insect cells. PLoS One. 2015 Jul 24;10(7):e0132122.
61. Nowak T, Wengler G. Analysis of disulfides present in the membrane proteins of the West Nile flavivirus. Virology. 1987 Jan 1;156(1):127–37.

62. Zai J, Mei L, Wang C, Cao S, Fu ZF, Chen H, et al. N-glycosylation of the premembrane protein of Japanese encephalitis virus is critical for folding of the envelope protein and assembly of virus-like particles. Acta Virol. 2013;57(1):27–33.
63. Lorenz IC, Allison SL, Heinz FX, Helenius A. Folding and Dimerization of Tick-Borne Encephalitis Virus Envelope Proteins prM and E in the Endoplasmic Reticulum. J Virol. 2002 Jun 1;76(11):5480–91.
64. Yu IM, Zhang W, Holdaway HA, Li L, Kostyuchenko VA, Chipman PR, et al. Structure of the immature dengue virus at low pH primes proteolytic maturation. Science (80-). 2008 Mar 28;319(5871):1834–7.
65. Pokidysheva E, Zhang Y, Battisti AJ, Bator-Kelly CM, Chipman PR, Xiao C, et al. Cryo-EM reconstruction of dengue virus in complex with the carbohydrate recognition domain of DC-SIGN. Cell. 2006 Feb 10;124(3):485–93.
66. Yap SSL, Nguyen-Khuong T, Rudd PM, Alonso S. Dengue virus glycosylation: What do we know? Vol. 8, Frontiers in Microbiology. Frontiers Media S.A.; 2017. p. 1415.
67. Desprès P, Frenkiel MP, Deubel V. Differences between cell membrane fusion activities of two dengue type-1 isolates reflect modifications of viral structure. Virology. 1993 Jan 1;196(1):209–19.
68. Markoff L. In vitro processing of dengue virus structural proteins: cleavage of the pre-membrane protein. J Virol. 1989 Aug;63(8):3345–52.
69. Muller DA, Young PR. The flavivirus NS1 protein: Molecular and structural biology, immunology, role inpathogenesis and application asadiagnostic biomarker. Vol. 98, Antiviral Research. Elsevier B.V.; 2013. p. 192–208.
70. Glasner DR, Puerta-Guardo H, Beatty PR, Harris E. The good, the bad, and the shocking: The multiple roles of dengue virus nonstructural protein 1 in protection and pathogenesis. Annu Rev Virol. 2018 Sep 29;5(1):227–53.
71. Mackenzie JM, Jones MK, Young PR. Immunolocalization of the dengue virus nonstructural glycoprotein NS1 suggests a role in viral RNA replication. Virology. 1996 Jun 1;220(1):232–40.
72. Lindenbach BD, Rice CM. Genetic interaction of flavivirus nonstructural proteins NS1 and NS4A as a determinant of replicase function. J Virol. 1999 Jun;73(6):4611–21.
73. Welsch S, Miller S, Romero-Brey I, Merz A, Bleck CKE, Walther P, et al. Composition and Three-Dimensional Architecture of the Dengue Virus Replication and Assembly Sites. Cell Host Microbe. 2009 Apr 23;5(4):365–75.
74. Avirutnan P, Punyadee N, Noisakran S, Komoltri C, Thiemmeca S, Auethavornanan K, et al. Vascular leakage in severe dengue virus infections: A potential role for the nonstructural viral protein NS1 and complement. J Infect Dis. 2006 Apr 15;193(8):1078–88.
75. Young PR, Hilditch PA, Bletchly C, Halloran W. An antigen capture enzyme-linked immunosorbent assay reveals high levels of the dengue virus protein NS1 in the sera of infected patients. J Clin Microbiol. 2000;38(3):1053–7.
76. Avirutnan P, Zhang L, Punyadee N, Manuyakorn A, Puttikhunt C, Kasinrerk W, et al. Secreted NS1 of dengue virus attaches to the surface of cells via interactions with heparan sulfate and chondroitin sulfate E. PLoS Pathog. 2007 Nov;3(11):1798–812.
77. Falconar AKI. The dengue virus nonstructural-1 protein (NS1) generates

antibodies to common epitopes on human blood clotting, integrin/adhesin proteins and binds to human endothelial cells: Potential implications in haemorrhagic fever pathogenesis. Arch Virol. 1997;142(5):897–916.
78. Sun DS, King CC, Huang HS, Shih YL, Lee CC, Tsai WJ, et al. Antiplatelet autoantibodies elicited by dengue virus non-structural protein 1 cause thrombocytopenia and mortality in mice. J Thromb Haemost. 2007 Nov;5(11):2291–9.
79. Adikari TN, Gomes L, Wickramasinghe N, Salimi M, Wijesiriwardana N, Kamaladasa A, et al. Dengue NS1 antigen contributes to disease severity by inducing interleukin (IL)-10 by monocytes. Clin Exp Immunol. 2016 Apr 1;184(1):90–100.
80. Malavige GN, Jeewandara C, Alles KML, Salimi M, Gomes L, Kamaladasa A, et al. Suppression of Virus Specific Immune Responses by IL-10 in Acute Dengue Infection. PLoS Negl Trop Dis. 2013;7(9):e2409.
81. Pryor MJ, Wright PJ. Glycosylation mutants of dengue virus NS1 protein. J Gen Virol. 1994;75(5):1183–7.
82. Somnuke P, Hauhart RE, Atkinson JP, Diamond MS, Avirutnan P. N-linked glycosylation of dengue virus NS1 protein modulates secretion, cell-surface expression, hexamer stability, and interactions with human complement. Virology. 2011 May 10;413(2):253–64.
83. Pryor MJ, Gualano RC, Lin B, Davidson AD, Wright PJ. Growth restriction of dengue virus type 2 by site-specific mutagenesis of virus-encoded glycoproteins. J Gen Virol. 1998;79(11):2631–9.
84. Umareddy I, Pluquet O, Wang QY, Vasudevan SG, Chevet E, Gu F. Dengue virus serotype infection specifies the activation of the unfolded protein response. Virol J. 2007;4.
85. Vaughn DW, Green S, Kalayanarooj S, Innis BL, Nimmannitya S, Suntayakorn S, et al. Dengue viremia titer, antibody response pattern, and virus serotype correlate with disease severity. J Infect Dis. 2000 Jan 1;181(1):2–9.
86. Fried JR, Gibbons R V., Kalayanarooj S, Thomas SJ, Srikiatkhachorn A, Yoon IK, et al. Serotype-specific differences in the risk of dengue hemorrhagic fever: An analysis of data collected in Bangkok, Thailand from 1994 to 2006. PLoS Negl Trop Dis. 2010 Mar;4(3).
87. Simmons CP, McPherson K, Van Vinh Chau N, Hoai Tam DT, Young P, Mackenzie J, et al. Recent advances in dengue pathogenesis and clinical management. Vaccine. 2015 Dec 10;33(50):7061–8.
88. Halstead SB. Dengue. Vol. 370, Lancet. Elsevier B.V.; 2007. p. 1644–52.
89. Pang T, Cardosa MJ, Guzman MG. Of cascades and perfect storms: The immunopathogenesis of dengue haemorrhagic fever-dengue shock syndrome (DHF/DSS). Vol. 85, Immunology and Cell Biology. Immunol Cell Biol; 2007. p. 43–5.
90. Rathakrishnan A, Wang SM, Hu Y, Khan AM, Ponnampalavanar S, Lum LCS, et al. Cytokine Expression Profile of Dengue Patients at Different Phases of Illness. PLoS One. 2012 Dec 20;7(12).
91. Beltramello M, Williams KL, Simmons CP, MacAgno A, Simonelli L, Quyen NTH, et al. The human immune response to dengue virus is dominated by highly cross-reactive antibodies endowed with neutralizing and enhancing activity. Cell Host Microbe. 2010 Sep 16;8(3):271–83.

92. Schieffelin JS, Costin JM, Nicholson CO, Orgeron NM, Fontaine KA, Isern S, et al. Neutralizing and non-neutralizing monoclonal antibodies against dengue virus e protein derived from a naturally infected patient. Virol J. 2010;7.
93. de Alwis R, Beltramello M, Messer WB, Sukupolvi-Petty S, Wahala WMPB, Kraus A, et al. In-depth analysis of the antibody response of individuals exposed to primary dengue virus infection. PLoS Negl Trop Dis. 2011 Jun;5(6).
94. De Alwis R, Smith SA, Olivarez NP, Messer WB, Huynh JP, Wahala WMPB, et al. Identification of human neutralizing antibodies that bind to complex epitopes on dengue virions. Proc Natl Acad Sci U S A. 2012 May 8;109(19):7439–44.
95. Wahala WMPB, de Silva AM. The human antibody response to dengue virus infection. Vol. 3, Viruses. Viruses; 2011. p. 2374–95.
96. Wilder-Smith A, Ooi EE, Horstick O, Wills B. Dengue. Vol. 393, The Lancet. Lancet Publishing Group; 2019. p. 350–63.
97. Mongkolsapaya J, Dejnirattisai W, Xu XN, Vasanawathana S, Tangthawornchaikul N, Chairunsri A, et al. Original antigenic sin and apoptosis in the pathogenesis of dengue hemorrhagic fever. Nat Med. 2003 Jul 1;9(7):921–7.
98. Midgley CM, Bajwa-Joseph M, Vasanawathana S, Limpitikul W, Wills B, Flanagan A, et al. An In-Depth Analysis of Original Antigenic Sin in Dengue Virus Infection. J Virol. 2011 Jan 1;85(1):410–21.
99. Tan GK, Alonso S. Pathogenesis and prevention of dengue virus infection: State-of-the-art. Vol. 22, Current Opinion in Infectious Diseases. Curr Opin Infect Dis; 2009. p. 302–8.
100. Arredondo-García JL, Hadinegoro SR, Reynales H, Chua MN, Rivera Medina DM, Chotpitayasunondh T, et al. Four-year safety follow-up of the tetravalent dengue vaccine efficacy randomized controlled trials in Asia and Latin America. Clin Microbiol Infect. 2018 Jul 1;24(7):755–63.
101. Hadinegoro SR, Arredondo-García JL, Capeding MR, Deseda C, Chotpitayasunondh T, Dietze R, et al. Efficacy and Long-Term Safety of a Dengue Vaccine in Regions of Endemic Disease. N Engl J Med. 2015 Sep 24;373(13):1195–206.
102. Gailhardou S, Skipetrova A, Dayan GH, Jezorwski J, Saville M, Van der Vliet D, et al. Safety Overview of a Recombinant Live-Attenuated Tetravalent Dengue Vaccine: Pooled Analysis of Data from 18 Clinical Trials. PLoS Negl Trop Dis. 2016 Jul 14;10(7):e0004821.
103. Plennevaux E, Moureau A, Arredondo-García JL, Villar L, Pitisuttithum P, Tran NH, et al. Impact of Dengue Vaccination on Serological Diagnosis: Insights from Phase III Dengue Vaccine Efficacy Trials. Clin Infect Dis. 2018 Apr 3;66(8):1164–72.
104. Deen J. The Dengue Vaccine Dilemma: Balancing the Individual and Population Risks and Benefits. PLoS Med. 2016 Nov 1;13(11):e1002182.
105. Biswal S, Borja-Tabora C, Martinez Vargas L, Velásquez H, Theresa Alera M, Sierra V, et al. Efficacy of a tetravalent dengue vaccine in healthy children aged 4–16 years: a randomised, placebo-controlled, phase 3 trial. Lancet. 2020 May 2;395(10234):1423–33.
106. López-Medina E, Biswal S, Saez-Llorens X, Borja-Tabora C, Bravo L, Sirivichayakul C, et al. Efficacy of a Dengue Vaccine Candidate (TAK-003) in

Healthy Children and Adolescents 2 Years after Vaccination. J Infect Dis. 2020 Dec 15;
107. Biswal S, Reynales H, Saez-Llorens X, Lopez P, Borja-Tabora C, Kosalaraksa P, et al. Efficacy of a Tetravalent Dengue Vaccine in Healthy Children and Adolescents. N Engl J Med. 2019 Nov 21;381(21):2009–19.
108. Botta L, Rivara M, Zuliani V, Radi M. Drug repurposing approaches to fight Dengue virus infection and related diseases. Front Biosci - Landmark. 2018 Jan 1;23(6):997–1019.
109. Yang X, Yu Y, Xu J, Shu H, Xia J, Liu H, et al. Clinical course and outcomes of critically ill patients with SARS-CoV-2 pneumonia in Wuhan, China: a single-centered, retrospective, observational study. Lancet Respir Med. 2020 May 1;8(5):475–81.
110. Gorbalenya AE, Baker SC, Baric RS, de Groot RJ, Drosten C, Gulyaeva AA, et al. The species Severe acute respiratory syndrome-related coronavirus: classifying 2019-nCoV and naming it SARS-CoV-2. Vol. 5, Nature Microbiology. Nature Research; 2020. p. 536–44.
111. WHO Coronavirus (COVID-19) Dashboard | WHO Coronavirus (COVID-19) Dashboard With Vaccination Data [Internet]. [cited 2021 Jun 14]. Available from: https://covid19.who.int/
112. Huang C, Wang Y, Li X, Ren L, Zhao J, Hu Y, et al. Clinical features of patients infected with 2019 novel coronavirus in Wuhan, China. Lancet. 2020 Feb 15;395(10223):497–506.
113. Cui J, Li F, Shi ZL. Origin and evolution of pathogenic coronaviruses. Vol. 17, Nature Reviews Microbiology. Nature Publishing Group; 2019. p. 181–92.
114. De Wit E, Van Doremalen N, Falzarano D, Munster VJ. SARS and MERS: Recent insights into emerging coronaviruses. Vol. 14, Nature Reviews Microbiology. Nature Publishing Group; 2016. p. 523–34.
115. Lu R, Zhao X, Li J, Niu P, Yang B, Wu H, et al. Genomic characterisation and epidemiology of 2019 novel coronavirus: implications for virus origins and receptor binding. Lancet. 2020 Feb 22;395(10224):565–74.
116. Domingo E, Holland JJ. RNA virus mutations and fitness for survival. Vol. 51, Annual Review of Microbiology. Annu Rev Microbiol; 1997. p. 151–78.
117. Emma C Wall, Mary Wu, Ruth Harvey, Gavin Kelly, Scott Warchal, Chelsea Sawyer, Rodney Daniels, Philip Hobson, Emine Hatipoglu, Yenting Ngai, Saira Hussain, Jerome Nicod, Robert Goldstone, Karen Ambrose, Steve Hindmarsh, Rupert Beale, Andrew Riddell, Steve and DLB. Neutralising antibody activity against SARS-CoV-2 VOCs B.1.617.2 and B.1.351 by BNT162b2 vaccination. Lancet. 2021;
118. Gordon DE, Jang GM, Bouhaddou M, Xu J, Obernier K, White KM, et al. A SARS-CoV-2 protein interaction map reveals targets for drug repurposing. Nature. 2020 Jul 16;583(7816):459–68.
119. Perlman S, Netland J. Coronaviruses post-SARS: Update on replication and pathogenesis. Vol. 7, Nature Reviews Microbiology. Nat Rev Microbiol; 2009. p. 439–50.
120. Fehr AR, Perlman S. Coronaviruses: An overview of their replication and pathogenesis. In: Coronaviruses: Methods and Protocols. Springer New York; 2015. p. 1–23.
121. Chan JFW, Kok KH, Zhu Z, Chu H, To KKW, Yuan S, et al. Genomic

characterization of the 2019 novel human-pathogenic coronavirus isolated from a patient with atypical pneumonia after visiting Wuhan. Emerg Microbes Infect. 2020 Jan 1;9(1):221–36.
122. Walls AC, Park YJ, Tortorici MA, Wall A, McGuire AT, Veesler D. Structure, Function, and Antigenicity of the SARS-CoV-2 Spike Glycoprotein. Cell. 2020 Apr 16;181(2):281-292.e6.
123. Hoffmann M, Kleine-Weber H, Schroeder S, Krüger N, Herrler T, Erichsen S, et al. SARS-CoV-2 Cell Entry Depends on ACE2 and TMPRSS2 and Is Blocked by a Clinically Proven Protease Inhibitor. Cell. 2020 Apr 16;181(2):271-280.e8.
124. Bosch BJ, Bartelink W, Rottier PJM. Cathepsin L Functionally Cleaves the Severe Acute Respiratory Syndrome Coronavirus Class I Fusion Protein Upstream of Rather than Adjacent to the Fusion Peptide. J Virol. 2008 Sep 1;82(17):8887–90.
125. Shirato K, Kawase M, Matsuyama S. Middle East Respiratory Syndrome Coronavirus Infection Mediated by the Transmembrane Serine Protease TMPRSS2. J Virol. 2013 Dec;87(23):12552–61.
126. Zhou Y, Vedantham P, Lu K, Agudelo J, Carrion R, Nunneley JW, et al. Protease inhibitors targeting coronavirus and filovirus entry. Antiviral Res. 2015;116:76–84.
127. Hoffmann M, Mösbauer K, Hofmann-Winkler H, Kaul A, Kleine-Weber H, Krüger N, et al. Chloroquine does not inhibit infection of human lung cells with SARS-CoV-2. Nature. 2020 Sep 24;585(7826):588–90.
128. Padmanabhan P, Desikan R, Dixit NM. Targeting TMPRSS2 and Cathepsin B/L together may be synergistic against SARSCoV- 2 infection. PLoS Comput Biol. 2020 Dec 8;16(12):e1008461.
129. Daly JL, Simonetti B, Klein K, Chen KE, Williamson MK, Antón-Plágaro C, et al. Neuropilin-1 is a host factor for SARS-CoV-2 infection. Science (80-). 2020 Nov 13;370(6518):861–5.
130. Cantuti-Castelvetri L, Ojha R, Pedro LD, Djannatian M, Franz J, Kuivanen S, et al. Neuropilin-1 facilitates SARS-CoV-2 cell entry and infectivity. Science (80-). 2020 Nov 13;370(6518):856–60.
131. Tortorici MA, Beltramello M, Lempp FA, Pinto D, Dang H V., Rosen LE, et al. Ultrapotent human antibodies protect against SARS-CoV-2 challenge via multiple mechanisms. Science (80-). 2020 Nov 20;370(6519):950–7.
132. Letko M, Marzi A, Munster V. Functional assessment of cell entry and receptor usage for SARS-CoV-2 and other lineage B betacoronaviruses. Nat Microbiol. 2020;5(4):562–9.
133. Romano M, Ruggiero A, Squeglia F, Maga G, Berisio R. A Structural View of SARS-CoV-2 RNA Replication Machinery: RNA Synthesis, Proofreading and Final Capping. Vol. 9, Cells. NLM (Medline); 2020.
134. Cohen JR, Lin LD, Machamer CE. Identification of a Golgi Complex-Targeting Signal in the Cytoplasmic Tail of the Severe Acute Respiratory Syndrome Coronavirus Envelope Protein. J Virol. 2011 Jun 15;85(12):5794–803.
135. McBride CE, Li J, Machamer CE. The Cytoplasmic Tail of the Severe Acute Respiratory Syndrome Coronavirus Spike Protein Contains a Novel Endoplasmic Reticulum Retrieval Signal That Binds COPI and Promotes Interaction with Membrane Protein. J Virol. 2007 Mar 1;81(5):2418–28.

136. Siu YL, Teoh KT, Lo J, Chan CM, Kien F, Escriou N, et al. The M, E, and N Structural Proteins of the Severe Acute Respiratory Syndrome Coronavirus Are Required for Efficient Assembly, Trafficking, and Release of Virus-Like Particles. J Virol. 2008 Nov 15;82(22):11318–30.
137. de Haan CAM, Kuo L, Masters PS, Vennema H, Rottier PJM. Coronavirus Particle Assembly: Primary Structure Requirements of the Membrane Protein. J Virol. 1998 Aug 1;72(8):6838–50.
138. Stertz S, Reichelt M, Spiegel M, Kuri T, Martínez-Sobrido L, García-Sastre A, et al. The intracellular sites of early replication and budding of SARS-coronavirus. Virology. 2007;361(2):304–15.
139. Klein S, Cortese M, Winter S, Wachsmuth-Melm M, Neufeldt C, Cerikan B, et al. SARS-CoV-2 structure and replication characterized by in situ cryo-electron tomography. bioRxiv. 2020 Aug 16;2020.06.23.167064.
140. Ghosh S, Dellibovi-Ragheb TA, Kerviel A, Pak E, Qiu Q, Fisher M, et al. β-Coronaviruses use lysosomes for egress instead of the biosynthetic secretory pathway. Cell. 2020;1–16.
141. Hoffmann M, Kleine-Weber H, Pöhlmann S. A Multibasic Cleavage Site in the Spike Protein of SARS-CoV-2 Is Essential for Infection of Human Lung Cells. Mol Cell. 2020 May 21;78(4):779-784.e5.
142. Ou X, Liu Y, Lei X, Li P, Mi D, Ren L, et al. Characterization of spike glycoprotein of SARS-CoV-2 on virus entry and its immune cross-reactivity with SARS-CoV. Nat Commun. 2020 Dec 1;11(1).
143. Coutard B, Valle C, de Lamballerie X, Canard B, Seidah NG, Decroly E. The spike glycoprotein of the new coronavirus 2019-nCoV contains a furin-like cleavage site absent in CoV of the same clade. Antiviral Res. 2020 Apr 1;176.
144. Wölfel R, Corman VM, Guggemos W, Seilmaier M, Zange S, Müller MA, et al. Virological assessment of hospitalized patients with COVID-2019. Nature. 2020 May 28;581(7809):465–9.
145. Ziegler CGK, Allon SJ, Nyquist SK, Mbano IM, Miao VN, Tzouanas CN, et al. SARS-CoV-2 Receptor ACE2 Is an Interferon-Stimulated Gene in Human Airway Epithelial Cells and Is Detected in Specific Cell Subsets across Tissues. Cell. 2020 May 28;181(5):1016-1035.e19.
146. Blanco-Melo D, Nilsson-Payant BE, Liu WC, Uhl S, Hoagland D, Møller R, et al. Imbalanced Host Response to SARS-CoV-2 Drives Development of COVID-19. Cell. 2020 May 28;181(5):1036-1045.e9.
147. Williamson EJ, Walker AJ, Bhaskaran K, Bacon S, Bates C, Morton CE, et al. Factors associated with COVID-19-related death using OpenSAFELY. Nature. 2020 Aug 20;584(7821):430–6.
148. Guan W, Ni Z, Hu Y, Liang W, Ou C, He J, et al. Clinical Characteristics of Coronavirus Disease 2019 in China. N Engl J Med. 2020 Apr 30;382(18):1708–20.
149. Pung R, Chiew CJ, Young BE, Chin S, Chen MIC, Clapham HE, et al. Investigation of three clusters of COVID-19 in Singapore: implications for surveillance and response measures. Lancet. 2020 Mar 28;395(10229):1039–46.
150. Lauer SA, Grantz KH, Bi Q, Jones FK, Zheng Q, Meredith HR, et al. The incubation period of coronavirus disease 2019 (CoVID-19) from publicly reported confirmed cases: Estimation and application. Ann Intern Med. 2020

May 5;172(9):577–82.
151. Wang D, Hu B, Hu C, Zhu F, Liu X, Zhang J, et al. Clinical Characteristics of 138 Hospitalized Patients with 2019 Novel Coronavirus-Infected Pneumonia in Wuhan, China. JAMA - J Am Med Assoc. 2020 Mar 17;323(11):1061–9.
152. Zhou F, Yu T, Du R, Fan G, Liu Y, Liu Z, et al. Clinical course and risk factors for mortality of adult inpatients with COVID-19 in Wuhan, China: a retrospective cohort study. Lancet. 2020 Mar 28;395(10229):1054–62.
153. Zhou Y, Fu B, Zheng X, Wang D, Zhao C, Qi Y, et al. Pathogenic T-cells and inflammatory monocytes incite inflammatory storms in severe COVID-19 patients. Vol. 7, National Science Review. Oxford University Press; 2020. p. 998–1002.
154. Taefehshokr N, Taefehshokr S, Hemmat N, Heit B. Covid-19: Perspectives on Innate Immune Evasion. Front Immunol. 2020;11.
155. Vibhuti Kumar Shah, Priyanka Firmal, Aftab Alam, Dipyaman Ganguly SC. Overview of Immune Response During SARS-CoV-2 Infection: Lessons From the Past. Front Immunol. 2020;11.
156. No Title [Internet]. [cited 2021 May 1]. Available from: https://www.who.int/blueprint/priority-diseases/key-action/WHO_Target_Product_Profiles_for_COVID-19_web.pdf
157. Poland GA, Ovsyannikova IG, Kennedy RB. SARS-CoV-2 immunity: review and applications to phase 3 vaccine candidates. Vol. 396, The Lancet. Lancet Publishing Group; 2020. p. 1595–606.
158. Who PQ. Status of COVID-19 Vaccines within WHO EUL/PQ evaluation process Manufacturer / WHO EUL holder Name of Vaccine NRA of Record Platform EOI accepted Pre-submission meeting held Dossier accepted for review* Status of assessment** Decision date***. 2021.
159. Xia S, Zhang Y, Wang Y, Wang H, Yang Y, Gao GF, et al. Safety and immunogenicity of an inactivated SARS-CoV-2 vaccine, BBIBP-CorV: a randomised, double-blind, placebo-controlled, phase 1/2 trial. Lancet Infect Dis. 2021 Jan 1;21(1):39–51.
160. Zhang Y, Zeng G, Pan H, Li C, Hu Y, Chu K, et al. Safety, tolerability, and immunogenicity of an inactivated SARS-CoV-2 vaccine in healthy adults aged 18–59 years: a randomised, double-blind, placebo-controlled, phase 1/2 clinical trial. Lancet Infect Dis. 2021 Feb 1;21(2):181–92.
161. Baden LR, El Sahly HM, Essink B, Kotloff K, Frey S, Novak R, et al. Efficacy and Safety of the mRNA-1273 SARS-CoV-2 Vaccine. N Engl J Med. 2021 Feb 4;384(5):403–16.
162. Wall EC, Wu M, Harvey R, Kelly G, Warchal S, Sawyer C, et al. Neutralising antibody activity against SARS-CoV-2 VOCs B.1.617.2 and B.1.351 by BNT162b2 vaccination. Lancet. 2021 Jun;0(0).
163. Folegatti PM, Ewer KJ, Aley PK, Angus B, Becker S, Belij-Rammerstorfer S, et al. Safety and immunogenicity of the ChAdOx1 nCoV-19 vaccine against SARS-CoV-2: a preliminary report of a phase 1/2, single-blind, randomised controlled trial. Lancet. 2020 Aug 15;396(10249):467–78.
164. Sadoff J, Le Gars M, Shukarev G, Heerwegh D, Truyers C, de Groot AM, et al. Interim Results of a Phase 1–2a Trial of Ad26.COV2.S Covid-19 Vaccine. N Engl J Med. 2021 May 13;384(19):1824–35.
165. Ella R, Reddy S, Jogdand H, Sarangi V, Ganneru B, Prasad S, et al. Safety and

immunogenicity of an inactivated SARS-CoV-2 vaccine, BBV152: interim results from a double-blind, randomised, multicentre, phase 2 trial, and 3-month follow-up of a double-blind, randomised phase 1 trial. Lancet Infect Dis. 2021 Mar;0(0).
166. Al Kaabi N, Zhang Y, Xia S, Yang Y, Al Qahtani MM, Abdulrazzaq N, et al. Effect of 2 Inactivated SARS-CoV-2 Vaccines on Symptomatic COVID-19 Infection in Adults: A Randomized Clinical Trial. JAMA. 2021 May 26;
167. A Phase 1/2 Safety and Immunogenicity Trial of COVID-19 Vaccine COVIVAC - Full Text View - ClinicalTrials.gov [Internet]. [cited 2021 Jun 17]. Available from: https://clinicaltrials.gov/ct2/show/NCT04830800
168. Immunogenicity, Efficacy and Safety of QazCovid-in® COVID-19 Vaccine - Full Text View - ClinicalTrials.gov [Internet]. [cited 2021 Jun 17]. Available from: https://clinicaltrials.gov/ct2/show/NCT04691908
169. A Safety and Immunogenicity Study of Inactivated SARS-CoV-2 Vaccine (Vero Cells) in Healthy Population Aged 18 Years and Above(COVID-19) - Full Text View - ClinicalTrials.gov [Internet]. [cited 2021 Jun 17]. Available from: https://clinicaltrials.gov/ct2/show/NCT04758273
170. Shinde V, Bhikha S, Hoosain Z, Archary M, Bhorat Q, Fairlie L, et al. Efficacy of NVX-CoV2373 Covid-19 Vaccine against the B.1.351 Variant. N Engl J Med. 2021 May 20;384(20):1899–909.
171. Yang S, Li Y, Dai L, Wang J, He P, Li C, et al. Safety and immunogenicity of a recombinant tandem-repeat dimeric RBD-based protein subunit vaccine (ZF2001) against COVID-19 in adults: two randomised, double-blind, placebo-controlled, phase 1 and 2 trials. Lancet Infect Dis. 2021;0(0).
172. Study of the Tolerability, Safety, Immunogenicity and Preventive Efficacy of the EpiVacCorona Vaccine for the Prevention of COVID-19 - Full Text View - ClinicalTrials.gov [Internet]. [cited 2021 Jun 17]. Available from: https://clinicaltrials.gov/ct2/show/NCT04780035
173. Logunov DY, Dolzhikova I V., Shcheblyakov D V., Tukhvatulin AI, Zubkova O V., Dzharullaeva AS, et al. Safety and efficacy of an rAd26 and rAd5 vector-based heterologous prime-boost COVID-19 vaccine: an interim analysis of a randomised controlled phase 3 trial in Russia. Lancet. 2021 Feb 20;397(10275):671–81.
174. CTRI [Internet]. [cited 2021 Jun 17]. Available from: http://ctri.nic.in/Clinicaltrials/showallp.php?mid1=46186&EncHid=&userName=covid-19 vaccine
175. Krammer F. SARS-CoV-2 vaccines in development. Vol. 586, Nature. Nature Research; 2020. p. 516–27.
176. Dai L, Gao GF. Viral targets for vaccines against COVID-19. Vol. 21, Nature Reviews Immunology. Nature Research; 2021. p. 73–82.
177. Randomised Evaluation of COVID-19 Therapy - Full Text View - ClinicalTrials.gov [Internet]. [cited 2021 Jun 17]. Available from: https://clinicaltrials.gov/ct2/show/NCT04381936
178. Dexamethasone in Hospitalized Patients with Covid-19. N Engl J Med. 2021 Feb 25;384(8):693–704.
179. Beigel JH, Tomashek KM, Dodd LE, Mehta AK, Zingman BS, Kalil AC, et al. Remdesivir for the Treatment of Covid-19 — Final Report. N Engl J Med. 2020 Nov 5;383(19):1813–26.

180. Dyer O. Covid-19: Remdesivir has little or no impact on survival, WHO trial shows. BMJ. 2020 Oct 19;371:m4057.
181. Search of: COVID-19 - List Results - ClinicalTrials.gov [Internet]. [cited 2021 Jun 14]. Available from: https://clinicaltrials.gov/ct2/results?cond=COVID-19
182. Choi JH, Croyle MA. Emerging targets and novel approaches to ebola virus prophylaxis and treatment. Vol. 27, BioDrugs. Springer International Publishing; 2013. p. 565–83.
183. Ioos S, Mallet HP, Leparc Goffart I, Gauthier V, Cardoso T, Herida M. Current Zika virus epidemiology and recent epidemics. Vol. 44, Medecine et Maladies Infectieuses. Elsevier Masson SAS; 2014. p. 302–7.
184. Wu D, Wu T, Liu Q, Yang Z. The SARS-CoV-2 outbreak: What we know. Vol. 94, International Journal of Infectious Diseases. Elsevier B.V.; 2020. p. 44–8.
185. Scott LJ. Tetravalent Dengue Vaccine: A Review in the Prevention of Dengue Disease. Drugs. 2016 Sep 1;76(13):1301–12.
186. Wu F, Zhao S, Yu B, Chen YM, Wang W, Song ZG, et al. A new coronavirus associated with human respiratory disease in China. Nature. 2020 Mar 12;579(7798):265–9.
187. Ghosn J, Taiwo B, Seedat S, Autran B, Katlama C. HIV. Lancet. 2018 Aug 25;392(10148):685–97.
188. Gubareva L V., Kaiser L, Hayden FG. Influenza virus neuraminidase inhibitors. Vol. 355, Lancet. Elsevier B.V.; 2000. p. 827–35.
189. Hayden FG, Sugaya N, Hirotsu N, Lee N, de Jong MD, Hurt AC, et al. Baloxavir Marboxil for Uncomplicated Influenza in Adults and Adolescents. N Engl J Med. 2018 Sep 6;379(10):913–23.
190. Rosenke K, Feldmann H, Westover JB, Hanley PW, Martellaro C, Feldmann F, et al. Use of favipiravir to treat lassa virus infection in Macaques. Emerg Infect Dis. 2018 Sep 1;24(9):1696–9.
191. Sissoko D, Laouenan C, Folkesson E, M'Lebing AB, Beavogui AH, Baize S, et al. Experimental Treatment with Favipiravir for Ebola Virus Disease (the JIKI Trial): A Historically Controlled, Single-Arm Proof-of-Concept Trial in Guinea. PLoS Med. 2016 Mar 1;13(3).
192. MacArthur RD, Novak RM. Maraviroc: The first of a new class of antiretroviral agents. Vol. 47, Clinical Infectious Diseases. Clin Infect Dis; 2008. p. 236–41.
193. Ikeda M, Kato N. Modulation of host metabolism as a target of new antivirals. Adv Drug Deliv Rev. 2007;59(12).
194. Mathur P, Kottilil S, Wilson E. Use of ribavirin for hepatitis c treatment in the modern direct-acting antiviral era. Vol. 6, Journal of Clinical and Translational Hepatology. Xia and He Publishing Inc.; 2018. p. 431–7.
195. Yau AHL, Yoshida EM. Hepatitis C drugs: The end of the pegylated interferon era and the emergence of all-oral, interferon-free antiviral regimens: a concise review. Vol. 28, Canadian Journal of Gastroenterology and Hepatology. Pulsus Group Inc.; 2014. p. 445–51.
196. Arends JE, Lieveld FI, Ahmad S, Ustianowski A. New Viral and Immunological Targets for Hepatitis B Treatment and Cure: A Review. Vol. 6, Infectious Diseases and Therapy. Springer Healthcare; 2017. p. 461–76.
197. Iyidogan P, Anderson KS. Current perspectives on HIV-1 antiretroviral drug resistance. Vol. 6, Viruses. MDPI AG; 2014. p. 4095–139.
198. Ahmed A, Felmlee DJ. Mechanisms of hepatitis C viral resistance to direct

acting antivirals. Vol. 7, Viruses. MDPI AG; 2015. p. 6716–29.
199. Sayce AC, Alonzi DS, Killingbeck SS, Tyrrell BE, Hill ML, Caputo AT, et al. Iminosugars Inhibit Dengue Virus Production via Inhibition of ER Alpha-Glucosidases—Not Glycolipid Processing Enzymes. PLoS Negl Trop Dis. 2016 Mar 14;10(3).
200. Perry ST, Buck MD, Plummer EM, Penmasta RA, Batra H, Stavale EJ, et al. An iminosugar with potent inhibition of dengue virus infection in vivo. Antiviral Res. 2013 Apr 1;98(1):35–43.
201. Wu S-F, Lee C-J, Liao C-L, Dwek RA, Zitzmann N, Lin Y-L. Antiviral effects of an iminosugar derivative on flavivirus infections. J Virol. 2002 Apr;76(8):3596–604.
202. Warfield KL, Warren TK, Qiu X, Wells J, Mire CE, Geisbert JB, et al. Assessment of the potential for host-targeted iminosugars UV-4 and UV-5 activity against filovirus infections in vitro and in vivo. Antiviral Res. 2017 Feb 1;138:22–31.
203. Warfield KL, Alonzi DS, Hill JC, Caputo AT, Roversi P, Kiappes JL, et al. Targeting Endoplasmic Reticulum α-Glucosidase i with a Single-Dose Iminosugar Treatment Protects against Lethal Influenza and Dengue Virus Infections. J Med Chem. 2020 Apr 23;63(8):4205–14.
204. Sayce AC. Iminosugars as dengue virus therapeutics: Molecular mechanisms of action of a drug entering clinical trials. University of Oxford; 2014.
205. Parodi A, Cummings RD, Aebi M. Chapter 39 Glycans in Glycoprotein Quality Control. Cold Spring Harb (NY. 2017;039:2015–7.
206. Hebert DN, Lamriben L, Powers ET, Kelly JW. The intrinsic and extrinsic effects of N-linked glycans on glycoproteostasis. Vol. 10, Nature Chemical Biology. Nature Publishing Group; 2014. p. 902–10.
207. Wormald MR, Dwek RA. Glycoproteins: Glycan presentation and protein-fold stability. Vol. 7, Structure. Current Biology Ltd; 1999.
208. Apweiler R, Hermjakob H, Sharon N. On the frequency of protein glycosylation, as deduced from analysis of the SWISS-PROT database. Biochim Biophys Acta - Gen Subj. 1999 Dec 17;1473(1):4–8.
209. Chatterjee S, Mayor S. The GPI-anchor and protein sorting. Vol. 58, Cellular and Molecular Life Sciences. Birkhauser Verlag Basel; 2001. p. 1969–87.
210. Mohan GS, Li W, Ye L, Compans RW, Yang C. Antigenic Subversion: A Novel Mechanism of Host Immune Evasion by Ebola Virus. PLoS Pathog. 2012 Dec;8(12).
211. Moore PL, Crooks ET, Porter L, Zhu P, Cayanan CS, Grise H, et al. Nature of Nonfunctional Envelope Proteins on the Surface of Human Immunodeficiency Virus Type 1. J Virol. 2006 Mar;80(5):2515–28.
212. Klimstra WB, Nangle EM, Smith MS, Yurochko AD, Ryman KD. DC-SIGN and L-SIGN Can Act as Attachment Receptors for Alphaviruses and Distinguish between Mosquito Cell- and Mammalian Cell-Derived Viruses. J Virol. 2003 Nov 15;77(22):12022–32.
213. Crispin MDM, Ritchie GE, Critchley AJ, Morgan BP, Wilson IA, Dwek RA, et al. Monoglucosylated glycans in the secreted human complement component C3: Implications for protein biosynthesis and structure. FEBS Lett. 2004 May 21;566(1–3):270–4.
214. Loke I, Kolarich D, Packer NH, Thaysen-Andersen M. Emerging roles of

protein mannosylation in inflammation and infection. Vol. 51, Molecular Aspects of Medicine. Elsevier Ltd; 2016. p. 31–55.
215. Murin CD, Julien J-P, Sok D, Stanfield RL, Khayat R, Cupo A, et al. Structure of 2G12 Fab2 in Complex with Soluble and Fully Glycosylated HIV-1 Env by Negative-Stain Single-Particle Electron Microscopy. J Virol. 2014 Sep 1;88(17):10177–88.
216. Qi L, Tsai B, Arvan P. New Insights into the Physiological Role of Endoplasmic Reticulum-Associated Degradation. Vol. 27, Trends in Cell Biology. Elsevier Ltd; 2017. p. 430–40.
217. Kornfeld R, Kornfeld S. Assembly of asparagine-linked oligosaccharides. Annu Rev Biochem. 1985;VOL. 54:631–64.
218. Mellquist JL, Kasturi L, Spitalnik SL, Shakin-Eshleman SH. The amino acid following an Asn-X-Ser/Thr sequon is an important determinant of N-linked core glycosylation efficiency. Biochemistry. 1998 May 12;37(19):6833–7.
219. Helenius A, Aebi M. Intracellular functions of N-linked glycans. Vol. 291, Science. American Association for the Advancement of Science; 2001. p. 2364–9.
220. Schweden J, Borgmann C, Legler G, Bause E. Characterization of calf liver glucosidase I and its inhibition by basic sugar analogs. Arch Biochem Biophys. 1986 Jul 1;248(1):335–40.
221. Schallus T, Jaeckh C, Fehér K, Palma AS, Liu Y, Simpson JC, et al. Malectin: A novel carbohydrate-binding protein of the endoplasmic reticulum and a candidate player in the early steps of protein N-glycosylation. Mol Biol Cell. 2008 Aug;19(8):3404–14.
222. Galli C, Bernasconi R, Soldà T, Calanca V, Molinari M. Malectin participates in a backup glycoprotein quality control pathway in the mammalian ER. PLoS One. 2011;6(1):16304.
223. Chen Y, Hu D, Yabe R, Tateno H, Qin SY, Matsumoto N, et al. Role of malectin in Glc 2Man 9GlcNAc 2-dependent quality control of α1-antitrypsin. Mol Biol Cell. 2011 Oct 1;22(19):3559–70.
224. Hebert DN, Foellmer B, Helenius A. Glucose trimming and reglucosylation determine glycoprotein association with calnexin in the endoplasmic reticulum. Vol. 81, Cell. Cell; 1995. p. 425–33.
225. Nauseef WM, McCormick SJ, Clark RA. Calreticulin functions as a molecular chaperone in the biosynthesis of myeloperoxidase. J Biol Chem. 1995;270(9):4741–7.
226. D'Alessio C, Caramelo JJ, Parodi AJ. UDP-GlC:glycoprotein glucosyltransferase-glucosidase II, the ying-yang of the ER quality control. Vol. 21, Seminars in Cell and Developmental Biology. Elsevier Ltd; 2010. p. 491–9.
227. Hebert DN, Molinari M. Flagging and docking: Dual roles for N-glycans in protein quality control and cellular proteostasis. Trends Biochem Sci. 2012 Oct;37(10):404–10.
228. Herscovics A, Romero PA, Tremblay LO. The specificity of the yeast and human class I ER α1,2-mannosidases involved in ER quality control is not as strict as previously reported. Vol. 12, Glycobiology. Glycobiology; 2002.
229. Ward BK, Rea SL, Magno AL, Pedersen B, Brown SJ, Mullin S, et al. The endoplasmic reticulum-associated protein, OS-9, behaves as a lectin in targeting

the immature calcium-sensing receptor. J Cell Physiol. 2018 Jan 1;233(1):38–56.
230. Olivari S, Molinari M. Glycoprotein folding and the role of EDEM1, EDEM2 and EDEM3 in degradation of folding-defective glycoproteins. Vol. 581, FEBS Letters. FEBS Lett; 2007. p. 3658–64.
231. Kukushkin N V., Alonzi DS, Dwek RA, Butters TD. Demonstration that endoplasmic reticulum-associated degradation of glycoproteins can occur downstream of processing by endomannosidase. Biochem J. 2011 Aug 15;438(1):133–42.
232. Bertozzi CR, Rabuka D. Structural Basis of Glycan Diversity. Essentials of Glycobiology. Cold Spring Harbor Laboratory Press; 2009.
233. Syed GH, Khan M, Yang S, Siddiqui A. Hepatitis C Virus Lipoviroparticles Assemble in the Endoplasmic Reticulum (ER) and Bud off from the ER to the Golgi Compartment in COPII Vesicles. J Virol. 2017 Aug;91(15).
234. Watanabe T, Sorensen EM, Naito A, Schott M, Kim S, Ahlquist P. Involvement of host cellular multivesicular body functions in hepatitis B virus budding. Proc Natl Acad Sci U S A. 2007 Jun 12;104(24):10205–10.
235. Sundquist WI, Kräusslich HG. HIV-1 assembly, budding, and maturation. Vol. 2, Cold Spring Harbor Perspectives in Medicine. Cold Spring Harbor Laboratory Press; 2012.
236. Nayak DP, Hui EKW, Barman S. Assembly and budding of influenza virus. Virus Res. 2004;106(2 SPEC.ISS.):147–65.
237. Ghosh S, Dellibovi-Ragheb TA, Kerviel A, Pak E, Qiu Q, Fisher M, et al. β-Coronaviruses Use Lysosomes for Egress Instead of the Biosynthetic Secretory Pathway. Cell. 2020 Dec 10;183(6):1520-1535.e14.
238. Brockhausen, I. & Stanley, P. ed. Varki A et al. . Essentials of Glycobiology (. Cold Spring Harbor Laboratory Press; 2009. 113–123 p.
239. Molloy SS, Thomas L, VanSlyke JK, Stenberg PE, Thomas G. Intracellular trafficking and activation of the furin proprotein convertase: localization to the TGN and recycling from the cell surface. EMBO J. 1994;13(1):18.
240. Bachert C, Linstedt AD. A Sensor of Protein O-Glycosylation Based on Sequential Processing in the Golgi apparatus. Traffic. 2013 Jan;14(1):47.
241. Paulsen H. Carbohydrates Containing Nitrogen or Sulfur in the “Hemiacetal” Ring. Angew Chemie Int Ed English. 1966 May 1;5(5):495–510.
242. Yagi, M., Kouno, T., Aoyagi, Y. and M. The Structure of Moranoline, a Piperidine Alkaloid rom Morus species. Nippon Nogeik Kaishi. 1976;50, 571–57.
243. Inouye S, Tsuruoka T, Ito T, Niida T. Structure and synthesis of nojirimycin. Tetrahedron. 1968 Jan 1;24(5):2125–44.
244. Inouye S, Tsuruoka T, Nida T. The structure of nojirimycin, a piperidinose sugar antibiotic. J Antibiot (Tokyo). 1966 Nov 1;19(6):288–92.
245. Alonzi DS, Scott KA, Dwek RA, Zitzmann N. Iminosugar antivirals: the therapeutic sweet spot. Biochem Soc Trans. 2017;45(2):571–82.
246. Dwek RA, Butters TD, Platt FM, Zitzmann N. Targeting glycosylation as a therapeutic approach. Nat Rev Drug Discov. 2002;1(1):65–75.
247. Horne G, Wilson FX, Tinsley J, Williams DH, Storer R. Iminosugars past, present and future: Medicines for tomorrow. Vol. 16, Drug Discovery Today. Drug Discov Today; 2011. p. 107–18.

248. Compain P, Martin OR. Iminosugars: From Synthesis to Therapeutic Applications. Iminosugars: From Synthesis to Therapeutic Applications. John Wiley and Sons; 2008. 1–467 p.
249. Kingma PJ, Menheere PPCA, Sels JP, Nieuwenhuijzen Kruseman AC. α-Glucosidase inhibition by miglitol in NIDDM patients. Diabetes Care. 1992;15(4):478–83.
250. Cox T, Lachmann R, Hollak C, Aerts J, Van Weely S, Hrebícek M, et al. Novel oral treatment of Gaucher's disease with N-butyldeoxynojirimycin (OGT 918) to decrease substrate biosynthesis. Lancet. 2000 Apr 29;355(9214):1481–5.
251. Campbell LK, Baker DE, Campbell RK. Miglitol: Assessment of its role in the treatment of patients with diabetes mellitus. Vol. 34, Annals of Pharmacotherapy. Ann Pharmacother; 2000. p. 1291–301.
252. Zitzmann N, Mehta AS, Carrouée S, Butters TD, Platt FM, McCauley J, et al. Imino sugars inhibit the formation and secretion of bovine viral diarrhea virus, a pestivirus model of hepatitis C virus: Implications for the development of broad spectrum anti-hepatitis virus agents. Proc Natl Acad Sci U S A. 1999 Oct 12;96(21):11878–82.
253. Wu S-F, Lee C-J, Liao C-L, Dwek RA, Zitzmann N, Lin Y-L. Antiviral Effects of an Iminosugar Derivative on Flavivirus Infections. J Virol. 2002 Apr 15;76(8):3596–604.
254. Miller JL, Lachica R, Sayce AC, Williams JP, Bapat M, Dwek R, et al. Liposome-mediated delivery of iminosugars enhances efficacy against dengue virus in vivo. Antimicrob Agents Chemother. 2012 Dec;56(12):6379–86.
255. Gu B, Mason P, Wang L, Norton P, Bourne N, Moriarty R, et al. Antiviral profiles of novel iminocyclitol compounds against bovine viral diarrhea virus, West Nile virus, dengue virus and hepatitis B virus. Antivir Chem Chemother. 2007;18(1):49–59.
256. Whitby K, Pierson TC, Geiss B, Lane K, Engle M, Zhou Y, et al. Castanospermine, a Potent Inhibitor of Dengue Virus Infection In Vitro and In Vivo. J Virol. 2005 Jul;79(14):8698–706.
257. Chang J, Wang L, Ma D, Qu X, Guo H, Xu X, et al. Novel imino sugar derivatives demonstrate potent antiviral activity against flavivirusesv. Antimicrob Agents Chemother. 2009 Apr;53(4):1501–8.
258. Mackenzie JM, Westaway EG. Assembly and Maturation of the Flavivirus Kunjin Virus Appear To Occur in the Rough Endoplasmic Reticulum and along the Secretory Pathway, Respectively. J Virol. 2001 Nov 15;75(22):10787–99.
259. Moore SEH, Spiro RG. Demonstration that Golgi endo-α-D-mannosidase provides a glucosidase-independent pathway for the formation of complex N-linked oligosaccharides of glycoproteins. J Biol Chem. 1990 Aug 5;265(22):13104–12.
260. Qu X, Pan X, Weidner J, Yu W, Alonzi D, Xu X, et al. Inhibitors of endoplasmic reticulum α-glucosidases potently suppress hepatitis C virus virion assembly and release. Antimicrob Agents Chemother. 2011 Mar;55(3):1036–44.
261. Steinmann E, Whitfield T, Kallis S, Dwek RA, Zitzmann N, Pietschmann T, et al. Antiviral effects of amantadine and iminosugar derivatives against hepatitis C virus. Hepatology. 2007 Aug 1;46(2):330–8.
262. Miller JL, Spiro SG, Dowall SD, Taylor I, Rule A, Alonzi DS, et al. No Minimal In Vivo Efficacy of Iminosugars in a Lethal Ebola Virus Guinea Pig Model.

Kuhn JH, editor. PLoS One. 2016 Nov;11(11):e0167018.
263. Chang J, Warren TK, Zhao X, Gill T, Guo F, Wang L, et al. Small molecule inhibitors of ER α-glucosidases are active against multiple hemorrhagic fever viruses. Antiviral Res. 2013 Jun 1;98(3):432–40.
264. Mehta A, Lu X, Block TM, Blumberg BS, Dwek RA. Hepatitis B virus (HBV) envelope glycoproteins vary drastically in their sensitivity to glycan processing: Evidence that alteration of a single N-linked glycosylation site can regulate HBV secretion. Proc Natl Acad Sci U S A. 1997 Mar 4;94(5):1822–7.
265. Mehta A, Carrouée S, Conyers B, Jordan R, Butters T, Dwek RA, et al. Inhibition of hepatitis B virus DNA replication by imino sugars without the inhibition of the DNA polymerase: Therapeutic implications. Hepatology. 2001 Jun 1;33(6):1488–95.
266. Hussain S, Miller JL, Harvey DJ, Gu Y, Rosenthal PB, Zitzmann N, et al. Strain-specific antiviral activity of iminosugars against human influenza A viruses. J Antimicrob Chemother. 2015 Jan 1;70(1):136–52.
267. Ma J, Zhang X, Soloveva V, Warren T, Guo F, Wu S, et al. Enhancing the antiviral potency of ER α-glucosidase inhibitor IHVR-19029 against hemorrhagic fever viruses in vitro and in vivo. Antiviral Res. 2018 Feb 1;150:112–22.
268. Miller JL, Tyrrell BE, Zitzmann N. Mechanisms of antiviral activity of iminosugars against dengue virus. In: Advances in Experimental Medicine and Biology. Springer New York LLC; 2018. p. 277–301.
269. Liang PH, Cheng WC, Lee YL, Yu HP, Wu YT, Lin YL, et al. Novel five-membered iminocyclitol derivatives as selective and potent glycosidase inhibitors: New structures for antivirals and osteoarthritis. ChemBioChem. 2006 Jan 9;7(1):165–73.
270. Courageot M-P, Frenkiel M-P, Duarte Dos Santos C, Deubel V, Desprès P. α-Glucosidase Inhibitors Reduce Dengue Virus Production by Affecting the Initial Steps of Virion Morphogenesis in the Endoplasmic Reticulum. J Virol. 2000 Jan 1;74(1):564–72.
271. Caputo AT, Alonzi DS, Marti L, Reca IB, Kiappes JL, Struwe WB, et al. Structures of mammalian ER α-glucosidase II capture the binding modes of broad-spectrum iminosugar antivirals. Proc Natl Acad Sci U S A. 2016 Aug 9;113(32):E4630–8.
272. Warfield KL, Plummer EM, Sayce AC, Alonzi DS, Tang W, Tyrrell BE, et al. Inhibition of endoplasmic reticulum glucosidases is required for in vitro and in vivo dengue antiviral activity by the iminosugar UV-4. Antiviral Res. 2016 May 1;129:93–8.
273. Dedera D, Vander Heyden N, Ratner L. Attenuation of HIV-1 Infectivity by an Inhibitor of Oligosaccharide Processing. AIDS Res Hum Retroviruses. 1990;6(6):785–94.
274. Fischer PB, Karlsson GB, Butters TD, Dwek RA, Platt FM, Fischer B, et al. N-butyldeoxynojirimycin-mediated inhibition of human immunodeficiency virus entry correlates with changes in antibody recognition of the V1/V2 region of gp120. J Virol. 1996 Oct;70(10):7143.
275. Taylor DL, Fellows LE, Farrar GH, Nash RJ, Taylor-Robinson D, Mobberley MA, et al. Loss of cytomegalovirus infectivity after treatment with castanospermine or related plant alkaloids correlates with aberrant glycoprotein

synthesis. Antiviral Res. 1988 Nov 1;10(1–3):11–26.
276. Lazar C, Durantel D, Macovei A, Zitzmann N, Zoulim F, Dwek RA, et al. Treatment of hepatitis B virus-infected cells with alpha-glucosidase inhibitors results in production of virions with altered molecular composition and infectivity. Antiviral Res. 2007 Oct;76(1):30–7.
277. Block TM, Lu X, Platt FM, Foster GR, Gerlich WH, Blumberg BS, et al. Secretion of human hepatitis B virus is inhibited by the imino sugar N-butyldeoxynojirimycin. Proc Natl Acad Sci U S A. 1994;91(6):2235–9.
278. Griffin SDC, Beales LP, Clarke DS, Worsfold O, Evans SD, Jaeger J, et al. The p7 protein of hepatitis C virus forms an ion channel that is blocked by the antiviral drug, Amantadine. In: FEBS Letters. Elsevier; 2003. p. 34–8.
279. Steinmann E, Penin F, Kallis S, Patel AH, Bartenschlager R, Pietschmann T. Hepatitis C virus p7 protein is crucial for assembly and release of infectious virions. PLoS Pathog. 2007 Jul;3(7):0962–71.
280. Sakai A, St. Claire M, Faulk K, Govindarajan S, Emerson SU, Purcell RH, et al. The p7 polypeptide of hepatitis C virus is critical for infectivity and contains functionally important genotype-specific sequences. Proc Natl Acad Sci U S A. 2003 Sep 30;100(20):11646–51.
281. Pavlovic D, Neville DCA, Argaud O, Blumberg B, Dwek RA, Fischer WB, et al. The hepatitis C virus p7 protein forms an ion channel that is inhibited by long-alkyl-chain iminosugar derivatives. Proc Natl Acad Sci U S A. 2003 May 13;100(10):6104–8.
282. Foster TL, Verow M, Wozniak AL, Bentham MJ, Thompson J, Atkins E, et al. Resistance mutations define specific antiviral effects for inhibitors of the hepatitis C virus p7 ion channel. Hepatology. 2011 Jul;54(1):79–90.
283. Myers MW. New antiretroviral agents in the clinic. Rev Infect Dis. 1990;12(5):944–50.
284. McHutchison JG, Bartenschlager R, Patel K, Pawlotsky JM. The face of future hepatitis C antiviral drug development: Recent biological and virologic advances and their translation to drug development and clinical practice. Vol. 44, Journal of Hepatology. J Hepatol; 2006. p. 411–21.
285. Kaita K, Yoshida E, Kunimoto D, Anderson F, Morris S, Marotta P, et al. [127] Phil PROOF OF CONCEPT STUDY OF CELGOSIVIR IN COMBINATION WITH PEGINTERFERON o-2b AND RIBAVIRIN IN CHRONIC HEPATITIS C GENOTYPE-1 NON-RESPONDER PATIENTS. J Hepatol. 2007 Apr 1;46:S56–7.
286. Safety and Pharmacokinetics of UV-4B Solution Administered Orally as Multiple Ascending Doses to Healthy Subjects - Full Text View - ClinicalTrials.gov [Internet]. [cited 2021 Apr 22]. Available from: https://clinicaltrials.gov/ct2/show/NCT02696291
287. Sung C, Wei Y, Watanabe S, Lee HS, Khoo YM, Fan L, et al. Extended Evaluation of Virological, Immunological and Pharmacokinetic Endpoints of CELADEN: A Randomized, Placebo-Controlled Trial of Celgosivir in Dengue Fever Patients. PLoS Negl Trop Dis. 2016 Aug 10;10(8).
288. Fleet GWJ, Karpas A, Dwek RA, Fellows LE, Tyms AS, Petursson S, et al. Inhibition of HIV replication by amino-sugar derivatives. FEBS Lett. 1988 Sep 12;237(1–2):128–32.
289. Fischl MA, Resnick L, Coombs R, Kremer AB, Pottage JC, Fass RJ, et al. The

safety and efficacy of combination yv-butyl-deoxynojirimycin (Sc-48334) and zidovudine in patients with hiv-1 infection and 200-500 cd4 cells/mm3. J Acquir Immune Defic Syndr. 1994 Feb 1;7(2):139–47.
290. Tierney M, Pottage J, Kessler H, Fischl M, Richman D, Merigan T, et al. The tolerability and pharmacokinetics of N-butyl-deoxynojirimycin in patients with advanced HIV disease (ACTG 100). J Acquir Immune Defic Syndr Hum Retrovirology. 1995 Dec 1;10(5):549–53.
291. Warfield KL, Plummer E, Alonzi DS, Wolfe GW, Sampath A, Nguyen T, et al. A novel iminosugar UV-12 with activity against the diverse viruses influenza and dengue (Novel iminosugar antiviral for influenza and dengue). Viruses. 2015 May 13;7(5):2404–27.
292. Spiro RG. Role of N-linked polymannose oligosaccharides in targeting glycoproteins for endoplasmic reticulum-associated degradation. Vol. 61, Cellular and Molecular Life Sciences. Cell Mol Life Sci; 2004. p. 1025–41.
293. Moore SEH, Bauvy C, Codogno P. Endoplasmic reticulum-to-cytosol transport of free polymannose oligosaccharides in permeabilized HepG2 cells. EMBO J. 1995;14(23):6034–42.
294. Alonzi DS, Kukushkin N V., Allman SA, Hakki Z, Williams SJ, Pierce L, et al. Glycoprotein misfolding in the endoplasmic reticulum: Identification of released oligosaccharides reveals a second ER-associated degradation pathway for Golgi-retrieved proteins. Cell Mol Life Sci. 2013 Aug;70(15):2799–814.
295. Porath B, Gainullin VG, Cornec-Le Gall E, Dillinger EK, Heyer CM, Hopp K, et al. Mutations in GANAB, Encoding the Glucosidase IIα Subunit, Cause Autosomal-Dominant Polycystic Kidney and Liver Disease. Am J Hum Genet. 2016 Jun 2;98(6):1193–207.
296. Sadat MA, Moir S, Chun T-W, Lusso P, Kaplan G, Wolfe L, et al. Glycosylation, Hypogammaglobulinemia, and Resistance to Viral Infections. N Engl J Med. 2014 Apr 24;370(17):1615–25.
297. De Praeter CM, Gerwig GJ, Bause E, Nuytinck LK, Vliegenthart JFG, Breuer W, et al. A novel disorder caused by defective biosynthesis of N-linked oligosaccharides due to glucosidase I deficiency. Am J Hum Genet. 2000;66(6):1744–56.
298. Kim Y-M, Hun Seo G, Jung E, Jang J-H, Za Kim S, Hee Lee B. Characteristic dysmorphic features in congenital disorders of glycosylation type IIb. J Hum Genet. 2018;63:383–6.
299. Li M, Xu Y, Wang Y, Yang X-A, Jin D. Compound heterozygous variants in MOGS inducing congenital disorders of glycosylation (CDG) IIb. J Hum Genet. 2019;64:265–8.
300. Ota M, Miyahara J, Itano A, Sugiura H, Ohki S. Mannosyl-oligosaccharide glucosidase – congenital disorder of glycosylation: A patient with novel variants. Pediatr Int. 2020 Mar 1;62(3):417–8.
301. Peiwei Zhao, Peng X, Luo S, Huang Y, Tan L, Shao J, et al. Identification and characterization of novel mutations in MOGS in a Chinese patient with infantile spams. Neurogenetics. 2020 Apr 1;21(2):97–104.
302. Anzai R, Tsuji M, Yamashita S, Wada Y, Okamoto N, Saitsu H, et al. Congenital disorders of glycosylation type IIb with MOGS mutations cause early infantile epileptic encephalopathy, dysmorphic features, and hepatic dysfunction. Brain Dev. 2021 Mar 1;43(3):402–10.

303. Alonzi DS, Neville DCA, Lachmann RH, Dwek RA, Butters TD. Glucosylated free oligosaccharides are biomarkers of endoplasmic-reticulum α-glucosidase inhibition. Biochem J. 2008 Jan 15;409(2):571–80.
304. Miyazaki T, Nishikawa A, Tonozuka T. Crystal structure of the enzyme-product complex reveals sugar ring distortion during catalysis by family 63 inverting α-glycosidase. J Struct Biol. 2016 Dec 1;196(3):479–86.
305. Tappe D, Pérez-Girón JV, Zammarchi L, Rissland J, Ferreira DF, Jaenisch T, et al. Cytokine kinetics of Zika virus-infected patients from acute to reconvalescent phase. Med Microbiol Immunol. 2016 Jun 1;205(3):269–73.
306. Diwaker D, Mishra KP, Ganju L. Effect of modulation of unfolded protein response pathway on dengue virus infection. Acta Biochim Biophys Sin (Shanghai). 2015 Jun 24;47(12):960–8.
307. Smith JA. A new paradigm: Innate immune sensing of viruses via the unfolded protein response. Vol. 5, Frontiers in Microbiology. Frontiers Research Foundation; 2014.
308. Smith JA. Regulation of cytokine production by the unfolded protein response; Implications for infection and autoimmunity. Vol. 9, Frontiers in Immunology. Frontiers Media S.A.; 2018. p. 1.
309. Hetz C, Zhang K, Kaufman RJ. Mechanisms, regulation and functions of the unfolded protein response. Vol. 21, Nature Reviews Molecular Cell Biology. Nature Research; 2020. p. 421–38.
310. Walter P, Ron D. The unfolded protein response: From stress pathway to homeostatic regulation. Vol. 334, Science. American Association for the Advancement of Science; 2011. p. 1081–6.
311. Schindler AJ, Schekman R. In vitro reconstitution of ER-stress induced ATF6 transport in COPII vesicles. Proc Natl Acad Sci U S A. 2009 Oct 20;106(42):17775–80.
312. Diehl JA, Fuchs SY, Koumenis C. The cell biology of the unfolded protein response. Gastroenterology. 2011;141(1).
313. Novoa I, Zeng H, Harding HP, Ron D. Feedback inhibition of the unfolded protein response by GADD34-mediated dephosphorylation of eIF2α. J Cell Biol. 2001 May 25;153(5):1011–21.
314. Iranpour M, Moghadam AR, Yazdi M, Ande SR, Alizadeh J, Wiechec E, et al. Apoptosis, autophagy and unfolded protein response pathways in arbovirus replication and pathogenesis. Vol. 18, Expert Reviews in Molecular Medicine. Cambridge University Press; 2016.
315. Chan SW. Unfolded protein response in hepatitis C virus infection. Vol. 5, Frontiers in Microbiology. Frontiers Research Foundation; 2014.
316. Peña J, Harris E. Dengue virus modulates the unfolded protein response in a time-dependent manner. J Biol Chem. 2011 Apr 22;286(16):14226–36.
317. Upton JP, Wang L, Han D, Wang ES, Huskey NE, Lim L, et al. IRE1α cleaves select microRNAs during ER stress to derepress translation of proapoptotic caspase-2. Science (80-). 2012 Nov 9;338(6108):818–22.
318. Chen H, Yang H, Pan L, Wang W, Liu X, Ren X, et al. The molecular mechanisms of XBP-1 gene silencing on IRE1α-TRAF2-ASK1-JNK pathways in oral squamous cell carcinoma under endoplasmic reticulum stress. Biomed Pharmacother. 2016 Feb 1;77:108–13.
319. Grootjans J, Kaser A, Kaufman RJ, Blumberg RS. The unfolded protein

response in immunity and inflammation. Vol. 16, Nature Reviews Immunology. Nature Publishing Group; 2016. p. 469–84.
320. Yoshida H, Matsui T, Yamamoto A, Okada T, Mori K. XBP1 mRNA is induced by ATF6 and spliced by IRE1 in response to ER stress to produce a highly active transcription factor. Cell. 2001 Dec 28;107(7):881–91.
321. Balakrishnan B, Sen D, Hareendran S, Roshini V, David S, Srivastava A, et al. Activation of the Cellular Unfolded Protein Response by Recombinant Adeno-Associated Virus Vectors. PLoS One. 2013 Jan 8;8(1).
322. Isler JA, Skalet AH, Alwine JC. Human Cytomegalovirus Infection Activates and Regulates the Unfolded Protein Response. J Virol. 2005 Jun 1;79(11):6890–9.
323. Lee DY, Lee J, Sugden B. The Unfolded Protein Response and Autophagy: Herpesviruses Rule! J Virol. 2009 Feb 1;83(3):1168–72.
324. Kazemi S, Papadopoulou S, Li S, Su Q, Wang S, Yoshimura A, et al. Control of α Subunit of Eukaryotic Translation Initiation Factor 2 (eIF2α) Phosphorylation by the Human Papillomavirus Type 18 E6 Oncoprotein: Implications for eIF2α-Dependent Gene Expression and Cell Death. Mol Cell Biol. 2004 Apr 15;24(8):3415–29.
325. Hassan IH, Zhang MS, Powers LS, Shao JQ, Baltrusaitis J, Rutkowski DT, et al. Influenza A viral replication is blocked by inhibition of the inositol-requiring enzyme 1 (IRE1) stress pathway. J Biol Chem. 2012 Feb 10;287(7):4679–89.
326. Medigeshi GR, Lancaster AM, Hirsch AJ, Briese T, Lipkin WI, DeFilippis V, et al. West Nile Virus Infection Activates the Unfolded Protein Response, Leading to CHOP Induction and Apoptosis. J Virol. 2007 Oct 15;81(20):10849–60.
327. Su H-L, Liao C-L, Lin Y-L. Japanese Encephalitis Virus Infection Initiates Endoplasmic Reticulum Stress and an Unfolded Protein Response. J Virol. 2002 May 1;76(9):4162–71.
328. Ke PY, Chen SSL. Hepatitis C virus and cellular stress response: Implications to molecular pathogenesis of liver diseases. Vol. 4, Viruses. Viruses; 2012. p. 2251–90.
329. Alfano C, Gladwyn-Ng I, Couderc T, Lecuit M, Nguyen L. The unfolded protein response: A key player in zika virus-associated congenital microcephaly. Front Cell Neurosci. 2019 Jan 29;13.
330. Gladwyn-Ng I, Cordón-Barris L, Alfano C, Creppe C, Couderc T, Morelli G, et al. Stress-induced unfolded protein response contributes to Zika virus-associated microcephaly. Vol. 21, Nature Neuroscience. Nature Publishing Group; 2018. p. 63–73.
331. Liao Y, Fung TS, Huang M, Fang SG, Zhong Y, Liu DX. Upregulation of CHOP/GADD153 during Coronavirus Infectious Bronchitis Virus Infection Modulates Apoptosis by Restricting Activation of the Extracellular Signal-Regulated Kinase Pathway. J Virol. 2013 Jul 15;87(14):8124–34.
332. Klomporn P, Panyasrivanit M, Wikan N, Smith DR. Dengue infection of monocytic cells activates ER stress pathways, but apoptosis is induced through both extrinsic and intrinsic pathways. Virology. 2011 Jan 20;409(2):189–97.
333. Perera N. Evaluating the effects of dengue virus and iminosugar treatment on cellular unfolded protein response and redox homeostasis. University of Oxford; 2019.

334. Paradkar PN, Ooi EE, Hanson BJ, Gubler DJ, Vasudevan SG. Unfolded protein response (UPR) gene expression during antibody-dependent enhanced infection of cultured monocytes correlates with dengue disease severity. Biosci Rep. 2011 Jun;31(3):221–30.
335. Thepparit C, Khakpoor A, Khongwichit S, Wikan N, Fongsaran C, Chingsuwanrote P, et al. Dengue 2 infection of HepG2 liver cells results in endoplasmic reticulum stress and induction of multiple pathways of cell death. BMC Res Notes. 2013;6(1).
336. Lee YR, Kuo SH, Lin CY, Fu PJ, Lin YS, Yeh TM, et al. Dengue virus-induced ER stress is required for autophagy activation, viral replication, and pathogenesis both in vitro and in vivo. Sci Rep. 2018 Dec 1;8(1).
337. Fraser JE, Watanabe S, Wang C, Chan WKK, Maher B, Lopez-Denman A, et al. A nuclear transport inhibitor that modulates the unfolded protein response and provides in vivo protection against lethal dengue virus infection. J Infect Dis. 2014 Dec 1;210(11):1780–91.
338. Cheng YL, Lin YS, Chen CL, Tsai TT, Tsai CC, Wu YW, et al. Activation of Nrf2 by the dengue virus causes an increase in CLEC5A, which enhances TNF-α production by mononuclear phagocytes. Sci Rep. 2016 Aug 26;6(1):1–15.
339. Yu C-Y, Hsu Y-W, Liao C-L, Lin Y-L. Flavivirus Infection Activates the XBP1 Pathway of the Unfolded Protein Response To Cope with Endoplasmic Reticulum Stress. J Virol. 2006 Dec;80(23):11868–80.
340. Valadão ALC, Aguiar RS, de Arruda LB. Interplay between inflammation and cellular stress triggered by Flaviviridae viruses. Vol. 7, Frontiers in Microbiology. Frontiers Media S.A.; 2016. p. 1233.
341. Jaiyen Y, Masrinoul P, Kalayanarooj S, Pulmanausahakul R, Ubol S. Characteristics of dengue virus-infected peripheral blood mononuclear cell death that correlates with the severity of illness. Microbiol Immunol. 2009 Aug;53(8):442–50.
342. Perera N, Miller JL, Zitzmann N. The role of the unfolded protein response in dengue virus pathogenesis. Vol. 19, Cellular Microbiology. Blackwell Publishing Ltd; 2017.
343. Rathore APS, Paradkar PN, Watanabe S, Tan KH, Sung C, Connolly JE, et al. Celgosivir treatment misfolds dengue virus NS1 protein, induces cellular pro-survival genes and protects against lethal challenge mouse model. Antiviral Res. 2011 Dec;92(3):453–60.
344. Beevers JE, Lai MC, Collins E, Booth HDE, Zambon F, Parkkinen L, et al. MAPT Genetic Variation and Neuronal Maturity Alter Isoform Expression Affecting Axonal Transport in iPSC-Derived Dopamine Neurons. Stem Cell Reports. 2017 Aug 8;9(2):587–99.
345. Morrison M, Klein C, Clemann N, Collier DA, Hardy J, Heiβerer B, et al. StemBANCC: Governing Access to Material and Data in a Large Stem Cell Research Consortium. Stem Cell Rev Reports. 2015 Oct 10;11(5):681–7.
346. Vaughan-Jackson A, Stodolak S, Ebrahimi KH, Browne C, Reardon PK, Pires E, et al. Differentiation of Human induced Pluripotent Stem Cells to Authentic Macrophages using Fully Defined, Serum Free, Open Source Media. bioRxiv. bioRxiv; 2020. p. 2020.10.27.357632.
347. Wilgenburg B van, Browne C, Vowles J, Cowley SA. Efficient, Long Term Production of Monocyte-Derived Macrophages from Human Pluripotent Stem

Cells under Partly-Defined and Fully-Defined Conditions. Covas DT, editor. PLoS One. 2013 Aug 12;8(8):e71098.
348. Zor T, Selinger Z. Linearization of the Bradford protein assay increases its sensitivity: Theoretical and experimental studies. Anal Biochem. 1996 May 1;236(2):302–8.
349. Gasteiger E, Hoogland C, Gattiker A, Duvaud S, Wilkins MR, Appel RD, et al. Protein Identification and Analysis Tools on the ExPASy Server. In: The Proteomics Protocols Handbook. Humana Press; 2005. p. 571–607.
350. Draft landscape and tracker of COVID-19 candidate vaccines [Internet]. [cited 2021 Mar 22]. Available from: https://www.who.int/publications/m/item/draft-landscape-of-covid-19-candidate-vaccines
351. Shang J, Wan Y, Luo C, Ye G, Geng Q, Auerbach A, et al. Cell entry mechanisms of SARS-CoV-2. Proc Natl Acad Sci U S A. 2020 May 26;117(21):11727–34.
352. Wrapp D, Wang N, Corbett KS, Goldsmith JA, Hsieh CL, Abiona O, et al. Cryo-EM structure of the 2019-nCoV spike in the prefusion conformation. Science (80-). 2020;367(6483):1260–3.
353. Bosch BJ, van der Zee R, de Haan CAM, Rottier PJM. The Coronavirus Spike Protein Is a Class I Virus Fusion Protein: Structural and Functional Characterization of the Fusion Core Complex. J Virol. 2003 Aug 15;77(16):8801–11.
354. Xia S, Zhu Y, Liu M, Lan Q, Xu W, Wu Y, et al. Fusion mechanism of 2019-nCoV and fusion inhibitors targeting HR1 domain in spike protein. Vol. 17, Cellular and Molecular Immunology. Springer Nature; 2020. p. 765–7.
355. Walls AC, Tortorici MA, Snijder J, Xiong X, Bosch BJ, Rey FA, et al. Tectonic conformational changes of a coronavirus spike glycoprotein promote membrane fusion. Proc Natl Acad Sci U S A. 2017 Oct 17;114(42):11157–62.
356. Pallesen J, Wang N, Corbett KS, Wrapp D, Kirchdoerfer RN, Turner HL, et al. Immunogenicity and structures of a rationally designed prefusion MERS-CoV spike antigen. Proc Natl Acad Sci U S A. 2017 Aug 29;114(35):E7348–57.
357. Walls AC, Xiong X, Park YJ, Tortorici MA, Snijder J, Quispe J, et al. Unexpected Receptor Functional Mimicry Elucidates Activation of Coronavirus Fusion. Cell. 2019 Feb 21;176(5):1026-1039.e15.
358. Cai Y, Zhang J, Xiao T, Peng H, Sterling SM, Walsh RM, et al. Distinct conformational states of SARS-CoV-2 spike protein. Science (80-). 2020 Sep 25;369(6511):1586–92.
359. Henderson R, Edwards RJ, Mansouri K, Janowska K, Stalls V, Gobeil SMC, et al. Controlling the SARS-CoV-2 spike glycoprotein conformation. Nat Struct Mol Biol. 2020 Oct 1;27(10):925–33.
360. Yuan Y, Cao D, Zhang Y, Ma J, Qi J, Wang Q, et al. Cryo-EM structures of MERS-CoV and SARS-CoV spike glycoproteins reveal the dynamic receptor binding domains. Nat Commun. 2017 Apr 10;8.
361. Gui M, Song W, Zhou H, Xu J, Chen S, Xiang Y, et al. Cryo-electron microscopy structures of the SARS-CoV spike glycoprotein reveal a prerequisite conformational state for receptor binding. Cell Res. 2017 Jan 1;27(1):119–29.
362. VanBlargan LA, Goo L, Pierson TC. Deconstructing the Antiviral Neutralizing-Antibody Response: Implications for Vaccine Development and Immunity.

Microbiol Mol Biol Rev. 2016 Dec 1;80(4):989–1010.
363. Rossmann MG. The canyon hypothesis. Hiding the host cell receptor attachment site on a viral surface from immune surveillance. Vol. 264, Journal of Biological Chemistry. Elsevier; 1989. p. 14587–90.
364. Kwong PD, Doyle ML, Casper DJ, Cicala C, Leavitt SA, Majeed S, et al. HIV-1 evades antibody-mediated neutralization through conformational masking of receptor-binding sites. Nature. 2002 Dec 12;420(6916):678–82.
365. Vigerust DJ, Shepherd VL. Virus glycosylation: role in virulence and immune interactions. Vol. 15, Trends in Microbiology. Elsevier Current Trends; 2007. p. 211–8.
366. Watanabe Y, Bowden TA, Wilson IA, Crispin M. Exploitation of glycosylation in enveloped virus pathobiology. Vol. 1863, Biochimica et Biophysica Acta - General Subjects. Elsevier B.V.; 2019. p. 1480–97.
367. Casalino L, Gaieb Z, Dommer AC, Harbison AM, Fogarty CA, Barros EP, et al. Shielding and beyond: The roles of glycans in SARS-CoV-2 spike protein. bioRxiv. bioRxiv; 2020.
368. Bosshart H, Humphrey J, Deignan E, Davidson J, Drazba J, Yuan L, et al. The cytoplasmic domain mediates localization of furin to the trans-golgi network en route to the endosomal/lysosomal system. J Cell Biol. 1994 Sep;126(5):1157–72.
369. Thaysen-Andersen M, Packer NH. Site-specific glycoproteomics confirms that protein structure dictates formation of N-glycan type, core fucosylation and branching. Glycobiology. 2012 Nov;22(11):1440–52.
370. Hang I, Lin CW, Grant OC, Fleurkens S, Villiger TK, Soos M, et al. Analysis of site-specific N-glycan remodeling in the endoplasmic reticulum and the Golgi. Glycobiology. 2015 Dec 1;25(12):1335–49.
371. Watanabe Y, Allen JD, Wrapp D, McLellan JS, Crispin M. Site-specific glycan analysis of the SARS-CoV-2 spike. Science (80-). 2020 Jul 17;369(6501):330–3.
372. Sanders RW, Derking R, Cupo A, Julien JP, Yasmeen A, de Val N, et al. A Next-Generation Cleaved, Soluble HIV-1 Env Trimer, BG505 SOSIP.664 gp140, Expresses Multiple Epitopes for Broadly Neutralizing but Not Non-Neutralizing Antibodies. PLoS Pathog. 2013 Sep;9(9).
373. Amanat F, Stadlbauer D, Strohmeier S, Nguyen THO, Chromikova V, McMahon M, et al. A serological assay to detect SARS-CoV-2 seroconversion in humans. 2020 p. 1033–6.
374. Amanat F, Stadlbauer D, Strohmeier S, Nguyen THO, Chromikova V, McMahon M, et al. A serological assay to detect SARS-CoV-2 seroconversion in humans. Nat Med. 2020 Jul;26(7):1033–6.
375. Alonzi DS, Neville DCA, Lachmann RH, Dwek RA, Butters TD. Glucosylated free oligosaccharides are biomarkers of endoplasmic-reticulum α-glucosidase inhibition. Biochem J. 2008;409(2).
376. Bukreyev A, Yang L, Fricke J, Cheng L, Ward JM, Murphy BR, et al. The Secreted Form of Respiratory Syncytial Virus G Glycoprotein Helps the Virus Evade Antibody-Mediated Restriction of Replication by Acting as an Antigen Decoy and through Effects on Fc Receptor-Bearing Leukocytes. J Virol. 2008 Dec 15;82(24):12191–204.
377. Rerks-Ngarm S, Pitisuttithum P, Nitayaphan S, Kaewkungwal J, Chiu J, Paris

R, et al. Vaccination with ALVAC and AIDSVAX to Prevent HIV-1 Infection in Thailand. N Engl J Med. 2009 Dec 3;361(23):2209–20.
378. Zhang S, Go EP, Ding H, Anang S, Kappes JC, Desaire H, et al. Glycosylation and disulfide bonding of wild-type SARS-CoV-2 spike glycoprotein. J Virol. 2021 Nov 24;
379. Behrens A-J, Harvey DJ, Milne E, Cupo A, Kumar A, Zitzmann N, et al. Molecular Architecture of the Cleavage-Dependent Mannose Patch on a Soluble HIV-1 Envelope Glycoprotein Trimer. J Virol. 2017 Jan 15;91(2).
380. Yao H, Song Y, Chen Y, Wu N, Xu J, Sun C, et al. Molecular Architecture of the SARS-CoV-2 Virus. Cell. 2020 Oct 29;183(3):730-738.e13.
381. Sanda M, Morrison L, Goldman R. N- And O-Glycosylation of the SARS-CoV-2 Spike Protein. Anal Chem. 2021 Feb 2;18:35.
382. Shajahan A, Supekar NT, Gleinich AS, Azadi P. Deducing the N- And O-glycosylation profile of the spike protein of novel coronavirus SARS-CoV-2. Glycobiology. 2020 Dec 1;30(12):981–8.
383. Reily C, Stewart TJ, Renfrow MB, Novak J. Glycosylation in health and disease. Nat Rev Nephrol 2019 156. 2019 Mar 11;15(6):346–66.
384. Zielinska DF, Gnad F, Wiśniewski JR, Mann M. Precision mapping of an in vivo N-glycoproteome reveals rigid topological and sequence constraints. Cell. 2010;141(5):897–907.
385. Thaysen-Andersen M, Packer NH. Site-specific glycoproteomics confirms that protein structure dictates formation of N-glycan type, core fucosylation and branching. Glycobiology. 2012 Nov;22(11):1440–52.
386. Hirst J, Futter CE, Hopkins CR. The kinetics of mannose 6-phosphate receptor trafficking in the endocytic pathway in HEp-2 cells: The receptor enters and rapidly leaves multivesicular endosomes without accumulating in a prelysosomal compartment. Mol Biol Cell. 1998;9(4):809–16.
387. van Doremalen N, Lambe T, Spencer A, Belij-Rammerstorfer S, Purushotham J, Port J, et al. ChAdOx1 nCoV-19 vaccination prevents SARS-CoV-2 pneumonia in rhesus macaques. bioRxiv Prepr Serv Biol. 2020;
388. Ramasamy MN, Minassian AM, Ewer KJ, Flaxman AL, Folegatti PM, Owens DR, et al. Safety and immunogenicity of ChAdOx1 nCoV-19 vaccine administered in a prime-boost regimen in young and old adults (COV002): a single-blind, randomised, controlled, phase 2/3 trial. Lancet. 2020 Dec 19;396(10267):1979–93.
389. Ramasamy MN, Minassian AM, Ewer KJ, Flaxman AL, Folegatti PM, Owens DR, et al. Safety and immunogenicity of ChAdOx1 nCoV-19 vaccine administered in a prime-boost regimen in young and old adults (COV002): a single-blind, randomised, controlled, phase 2/3 trial. Lancet. 2020;0(0).
390. Folegatti PM, Ewer KJ, Aley PK, Angus B, Becker S, Belij-Rammerstorfer S, et al. Safety and immunogenicity of the ChAdOx1 nCoV-19 vaccine against SARS-CoV-2: a preliminary report of a phase 1/2, single-blind, randomised controlled trial. Lancet. 2020 Aug;396(10249):467–78.
391. van Doremalen N, Lambe T, Spencer A, Belij-Rammerstorfer S, Purushotham JN, Port JR, et al. ChAdOx1 nCoV-19 vaccine prevents SARS-CoV-2 pneumonia in rhesus macaques. Nature. 2020;586(7830):578–82.
392. M T, C F, E H, H R, J S. Lack of correlation between soluble CD4-induced shedding of the human immunodeficiency virus type 1 exterior envelope

glycoprotein and subsequent membrane fusion events. J Virol. 1992 Sep;66(9):5516–24.
393. Ruprecht CR, Krarup A, Reynell L, Mann AM, Brandenberg OF, Berlinger L, et al. MPER-specific antibodies induce gp120 shedding and irreversibly neutralize HIV-1. J Exp Med. 2011 Mar 14;208(3):439–54.
394. Rhea EM, Logsdon AF, Hansen KM, Williams LM, Reed MJ, Baumann KK, et al. The S1 protein of SARS-CoV-2 crosses the blood–brain barrier in mice. Nat Neurosci. 2020 Mar 1;24(3):368–78.
395. Grobbelaar LM, Venter C, Ngoepe M, Laubscher GJ, Lourens J, Steenkamp J, et al. SARS-CoV-2 spike protein S1 induces fibrin(ogen) resistant to fibrinolysis: Implications for microclot formation in COVID-19. medRxiv. 2021 Mar 8;2021.03.05.21252960.
396. Letarov A V., Babenko V V., Kulikov EE. Free SARS-CoV-2 Spike Protein S1 Particles May Play a Role in the Pathogenesis of COVID-19 Infection. Biochem. 2020 Mar 1;86(3):257–61.
397. Sanders RW, Vesanen M, Schuelke N, Master A, Schiffner L, Kalyanaraman R, et al. Stabilization of the Soluble, Cleaved, Trimeric Form of the Envelope Glycoprotein Complex of Human Immunodeficiency Virus Type 1. J Virol. 2002 Sep 1;76(17):8875–89.
398. Tortorici MA, Veesler D. Structural insights into coronavirus entry. In: Advances in Virus Research. Academic Press Inc.; 2019. p. 93–116.
399. Barnes CO, Jette CA, Abernathy ME, Dam KMA, Esswein SR, Gristick HB, et al. SARS-CoV-2 neutralizing antibody structures inform therapeutic strategies. Nature. 2020 Dec 24;588(7839):682–7.
400. Casalino L, Gaieb Z, Goldsmith JA, Hjorth CK, Dommer AC, Harbison AM, et al. Beyond shielding: The roles of glycans in the SARS-CoV-2 spike protein. ACS Cent Sci. 2020 Oct 28;6(10):1722–34.
401. Watanabe Y, Mendonça L, Allen ER, Howe A, Lee M, Allen JD, et al. Native-like SARS-CoV-2 spike glycoprotein expressed by ChAdOx1 nCoV-19/AZD1222 vaccine. bioRxiv Prepr Serv Biol. 2021 Jan 19;2021.01.15.426463.
402. Kowarz E, Krutzke L, Reis J, Bracharz S, Kochanek S, Marschalek R. "Vaccine-Induced Covid-19 Mimicry" Syndrome:Splice reactions within the SARS-CoV-2 Spike open reading frame result in Spike protein variants that may cause thromboembolic events in patients immunized with vector-based vaccines. 2021 May 26;
403. Kirchdoerfer RN, Wang N, Pallesen J, Wrapp D, Turner HL, Cottrell CA, et al. Stabilized coronavirus spikes are resistant to conformational changes induced by receptor recognition or proteolysis. Sci Rep. 2018 Dec 1;8(1):1–11.
404. Walsh EE, Frenck RW, Falsey AR, Kitchin N, Absalon J, Gurtman A, et al. Safety and Immunogenicity of Two RNA-Based Covid-19 Vaccine Candidates. N Engl J Med. 2020 Dec 17;383(25):2439–50.
405. Sanders RW, Moore JP. Virus vaccines: proteins prefer prolines. Vol. 29, Cell Host and Microbe. Cell Press; 2021. p. 327–33.
406. Brun J, Vasiljevic S, Gangadharan B, Hensen M, V. Chandran A, Hill ML, et al. Assessing Antigen Structural Integrity through Glycosylation Analysis of the SARS-CoV-2 Viral Spike. ACS Cent Sci. 2021 Apr 28;7(4):586–93.
407. Keech C, Albert G, Cho I, Robertson A, Reed P, Neal S, et al. Phase 1–2 Trial

of a SARS-CoV-2 Recombinant Spike Protein Nanoparticle Vaccine. N Engl J Med. 2020 Dec 10;383(24):2320–32.
408. Mercado NB, Zahn R, Wegmann F, Loos C, Chandrashekar A, Yu J, et al. Single-shot Ad26 vaccine protects against SARS-CoV-2 in rhesus macaques. Nature. 2020 Oct 22;586(7830):583–8.
409. Bos R, Rutten L, van der Lubbe JEM, Bakkers MJG, Hardenberg G, Wegmann F, et al. Ad26 vector-based COVID-19 vaccine encoding a prefusion-stabilized SARS-CoV-2 Spike immunogen induces potent humoral and cellular immune responses. npj Vaccines. 2020 Dec 1;5(1):1–11.
410. Braakman I, Hebert DN. Protein Folding in the Endoplasmic Reticulum. Cold Spring Harb Perspect Biol. 2013;5(5).
411. Ren X, Glende J, Al-Falah M, de Vries V, Schwegmann-Wessels C, Qu X, et al. Analysis of ACE2 in polarized epithelial cells: Surface expression and function as receptor for severe acute respiratory syndrome-associated coronavirus. J Gen Virol. 2006 Jun;87(6):1691–5.
412. Aguiar JA, Tremblay BJM, Mansfield MJ, Woody O, Lobb B, Banerjee A, et al. Gene expression and in situ protein profiling of candidate SARS-CoV-2 receptors in human airway epithelial cells and lung tissue. Eur Respir J. 2020 Sep 1;56(3).
413. Graham FL, Smiley J, Russell WC, Nairn R. Characteristics of a human cell line transformed by DNA from human adenovirus type 5. J Gen Virol. 1977;36(1):59–72.
414. Riquelme C, Acuña MJ, Torrejón J, Rebolledo D, Cabrera D, Santos RA, et al. ACE2 is augmented in dystrophic skeletal muscle and plays a role in decreasing associated fibrosis. PLoS One. 2014 Apr 2;9(4).
415. Hassan AO, Kafai NM, Dmitriev IP, Fox JM, Smith BK, Harvey IB, et al. A Single-Dose Intranasal ChAd Vaccine Protects Upper and Lower Respiratory Tracts against SARS-CoV-2. Cell. 2020 Oct 1;183(1):169.
416. King RG, Silva-Sanchez A, Peel JN, Botta D, Meza-Perez S, Allie SR, et al. Single-dose intranasal administration of AdCOVID elicits systemic and mucosal immunity against SARS-CoV-2 in mice. bioRxiv. 2020 Oct 11;2020.10.10.331348.
417. Ramasamy MN, Minassian AM, Ewer KJ, Flaxman AL, Folegatti PM, Owens DR, et al. Safety and immunogenicity of ChAdOx1 nCoV-19 vaccine administered in a prime-boost regimen in young and old adults (COV002): a single-blind, randomised, controlled, phase 2/3 trial. Lancet. 2020 Dec 19;396(10267):1979–93.
418. Polack FP, Thomas SJ, Kitchin N, Absalon J, Gurtman A, Lockhart S, et al. Safety and Efficacy of the BNT162b2 mRNA Covid-19 Vaccine. N Engl J Med. 2020 Dec 31;383(27):2603–15.
419. Yang J, Wang W, Chen Z, Lu S, Yang F, Bi Z, et al. A vaccine targeting the RBD of the S protein of SARS-CoV-2 induces protective immunity. Nature. 2020 Oct 22;586(7830):572–7.
420. Richmond P, Hatchuel L, Dong M, Ma B, Hu B, Smolenov I, et al. Safety and immunogenicity of S-Trimer (SCB-2019), a protein subunit vaccine candidate for COVID-19 in healthy adults: a phase 1, randomised, double-blind, placebo-controlled trial. Lancet. 2021 Feb 20;397(10275):682–94.
421. Minor PD. Live attenuated vaccines: Historical successes and current

challenges. Vols. 479–480, Virology. Academic Press Inc.; 2015. p. 379–92.
422. Liu STH, Aberg JA. Convalescent plasma in patients hospitalised with COVID-19. Lancet. 2021 May 29;397(10289):2024–5.
423. Taylor PC, Adams AC, Hufford MM, de la Torre I, Winthrop K, Gottlieb RL. Neutralizing monoclonal antibodies for treatment of COVID-19. Vol. 21, Nature Reviews Immunology. Nature Research; 2021. p. 382–93.
424. Seeland S, Török M, Kettiger H, Treiber A, Hafner M, Huwyler J. A cell-based, multiparametric sensor approach characterises drug-induced cytotoxicity in human liver HepG2 cells. Toxicol Vitr. 2013 Apr;27(3):1109–20.
425. Woodcock J, Woosley R. The FDA critical path initiative and its influence on new drug development. Vol. 59, Annual Review of Medicine. Annu Rev Med; 2008. p. 1–12.
426. Fact Sheet: FDA at a Glance | FDA [Internet]. [cited 2021 Jun 7]. Available from: https://www.fda.gov/about-fda/fda-basics/fact-sheet-fda-glance
427. Achdout H, Aimon A, Bar-David E, Barr H, Ben-Shmuel A, Bennett J, et al. COVID moonshot: Open science discovery of SARS-CoV-2 main protease inhibitors by combining crowdsourcing, high-throughput experiments, computational simulations, and machine learning. bioRxiv. bioRxiv; 2020. p. 2020.10.29.339317.
428. Dexamethasone in Hospitalized Patients with Covid-19. N Engl J Med. 2021 Feb 25;384(8):693–704.
429. Jin Z, Du X, Xu Y, Deng Y, Liu M, Zhao Y, et al. Structure of Mpro from SARS-CoV-2 and discovery of its inhibitors. Nature. 2020 Jun 11;582(7811):289–93.
430. Douangamath A, Fearon D, Gehrtz P, Krojer T, Lukacik P, Owen CD, et al. Crystallographic and electrophilic fragment screening of the SARS-CoV-2 main protease. Nat Commun. 2020 Dec 1;11(1):1–11.
431. De Madrid AT, Porterfield JS. A simple micro-culture method for the study of group B arboviruses. Bull World Health Organ. 1969;40(1):113–21.
432. Miao X, Luo Y, Huang X, Lee SMY, Yuan Z, Tang Y, et al. A novel biparatopic hybrid antibody-ACE2 fusion that blocks SARS-CoV-2 infection: implications for therapy. MAbs. 2020 Jan 1;12(1).
433. Ammerman NC, Beier-Sexton M, Azad AF. Growth and maintenance of vero cell lines. Vol. APPENDIX, Current Protocols in Microbiology. NIH Public Access; 2008. p. Appendix.
434. (No Title) [Internet]. [cited 2021 Jun 12]. Available from: http://sarscov2.assaytracker.net/
435. Dittmar M, Lee JS, Whig K, Segrist E, Li M, Kamalia B, et al. Drug repurposing screens reveal cell-type-specific entry pathways and FDA-approved drugs active against SARS-Cov-2. Cell Rep. 2021 Apr 6;35(1):108959.
436. Hui KPY, Cheung MC, Perera RAPM, Ng KC, Bui CHT, Ho JCW, et al. Tropism, replication competence, and innate immune responses of the coronavirus SARS-CoV-2 in human respiratory tract and conjunctiva: an analysis in ex-vivo and in-vitro cultures. Lancet Respir Med. 2020 Jul 1;8(7):687–95.
437. Shen BQ, Finkbeiner WE, Wine JJ, Mrsny RJ, Widdicombe JH. Calu-3: A human airway epithelial cell line that shows cAMP-dependent Cl- secretion. Am J Physiol - Lung Cell Mol Physiol. 1994;266(5 10-5).

438. Saedisomeolia A, Wood LG, Garg ML, Gibson PG, Wark PAB. Lycopene enrichment of cultured airway epithelial cells decreases the inflammation induced by rhinovirus infection and lipopolysaccharide. J Nutr Biochem. 2009 Aug;20(8):577–85.
439. Grantham ML, Wu W-H, Lalime EN, Lorenzo ME, Klein SL, Pekosz A. Palmitoylation of the Influenza A Virus M2 Protein Is Not Required for Virus Replication In Vitro but Contributes to Virus Virulence. J Virol. 2009 Sep 1;83(17):8655–61.
440. Harcourt JL, Caidi H, Anderson LJ, Haynes LM. Evaluation of the Calu-3 cell line as a model of in vitro respiratory syncytial virus infection. J Virol Methods. 2011 Jun 1;174(1–2):144–9.
441. Yoshikawa T, Hill T, Li K, Peters CJ, Tseng C-TK. Severe Acute Respiratory Syndrome (SARS) Coronavirus-Induced Lung Epithelial Cytokines Exacerbate SARS Pathogenesis by Modulating Intrinsic Functions of Monocyte-Derived Macrophages and Dendritic Cells. J Virol. 2009 Apr 1;83(7):3039–48.
442. Pollock S, Dwek RA, Burton DR, Zitzmann N. N-Butyldeoxynojirimycin is a broadly effective anti-HIV therapy significantly enhanced by targeted liposome delivery. AIDS. 2008;22(15):1961–9.
443. Bush CO, Pokrovskii M V., Saito R, Morganelli P, Canales E, Clarke MO, et al. A small-Molecule inhibitor of hepatitis C virus infectivity. Antimicrob Agents Chemother. 2014 Jan 1;58(1):386–96.
444. Chang MH, Gordon LA, Fung HB. Boceprevir: A Protease Inhibitor for the Treatment of Hepatitis C. Vol. 34, Clinical Therapeutics. Clin Ther; 2012. p. 2021–38.
445. Levenson AS, Wolf DM, Catherino WH, Takei H, Craig Jordan V. Understanding the antiestrogenic actions of raloxifene and a mechanism of drug resistance to tamoxifen. Vol. 5, Breast Cancer. Springer; 1998. p. 99–106.
446. EU/3/10/782 | European Medicines Agency [Internet]. [cited 2021 Jun 13]. Available from: https://www.ema.europa.eu/en/medicines/human/orphan-designations/eu310782
447. Choi JY, Kang YJ, Jang HM, Jung HY, Cho JH, Park SH, et al. Nafamostat mesilate as an anticoagulant during continuous renal replacement therapy in patients with high bleeding risk a randomized clinical trial. Med (United States). 2015;94(52).
448. Munshi PN, Lubin M, Bertino JR. 6-Thioguanine: A Drug With Unrealized Potential for Cancer Therapy. Oncologist. 2014 Jul;19(7):760–5.
449. Tchounwou PB, Dasari S, Noubissi FK, Ray P, Kumar S. Advances in Our Understanding of the Molecular Mechanisms of Action of Cisplatin in Cancer Therapy. J Exp Pharmacol. 2021 Mar;Volume 13:303–28.
450. Dasari S, Bernard Tchounwou P. Cisplatin in cancer therapy: Molecular mechanisms of action. Vol. 740, European Journal of Pharmacology. Elsevier; 2014. p. 364–78.
451. Gowda C, Sachdev M, Muthisami S, Kapadia M, Petrovic-Dovat L, Hartman M, et al. Casein kinase II (CK2) as a therapeutic target for hematological malignancies. Curr Pharm Des. 2016 Oct 6;22(999):1–1.
452. Welford RWD, Mühlemann A, Garzotti M, Rickert V, Groenen PMA, Morand O, et al. Glucosylceramide synthase inhibition with lucerastat lowers globotriaosylceramide and lysosome staining in cultured fibroblasts from Fabry

patients with different mutation types. Hum Mol Genet. 2018 Oct 1;27(19):3392–403.
453. CAS-ViewAlert [Internet]. [cited 2021 Jun 15]. Available from: https://www.cas.mhra.gov.uk/ViewandAcknowledgment/ViewAlert.aspx?AlertID=103054
454. Hempel T, Raich L, Olsson S, Azouz NP, Klingler AM, Hoffmann M, et al. Molecular mechanism of inhibiting the SARS-CoV-2 cell entry facilitator TMPRSS2 with camostat and nafamostat. Chem Sci. 2021 Jan 21;12(3):983–92.
455. Yamamoto M, Matsuyama S, Li X, Takeda M, Kawaguchi Y, Inoue JI, et al. Identification of nafamostat as a potent inhibitor of middle east respiratory syndrome Coronavirus s protein-mediated membrane fusion using the split-protein-based cell-cell fusion assay. Antimicrob Agents Chemother. 2016 Nov 1;60(11):6532–9.
456. Wang M, Cao R, Zhang L, Yang X, Liu J, Xu M, et al. Remdesivir and chloroquine effectively inhibit the recently emerged novel coronavirus (2019-nCoV) in vitro. Vol. 30, Cell Research. Springer Nature; 2020. p. 269–71.
457. Ko M, Jeon S, Ryu W, Kim S. Comparative analysis of antiviral efficacy of FDA-approved drugs against SARS-CoV-2 in human lung cells. J Med Virol. 2021 Mar 16;93(3):1403–8.
458. Hwang SD, Hyun YK, Moon SJ, Lee SC, Yoon SY. Nafamostat mesilate for anticoagulation in continuous renal replacement therapy. Vol. 36, International Journal of Artificial Organs. Int J Artif Organs; 2013. p. 208–16.
459. Rentsch CT, Beckman JA, Tomlinson L, Gellad WF, Alcorn C, Kidwai-Khan F, et al. Early initiation of prophylactic anticoagulation for prevention of coronavirus disease 2019 mortality in patients admitted to hospital in the United States: Cohort study. BMJ. 2021 Feb 11;372.
460. Takahashi W, Yoneda T, Koba H, Ueda T, Tsuji N, Ogawa H, et al. Potential mechanisms of nafamostat therapy for severe COVID-19 pneumonia with disseminated intravascular coagulation. Int J Infect Dis. 2021 Jan 1;102:529–31.
461. Garcia-Dorival I, Cuesta-Geijo MÁ, Barrado-Gil L, Galindo I, Urquiza J, del Puerto A, et al. Identification of NPC1 as a novel SARS-CoV-2 intracellular target. bioRxiv. bioRxiv; 2020. p. 2020.12.19.423584.
462. Vanier MT, Latour P. Laboratory diagnosis of Niemann-Pick disease type C: The filipin staining test. Methods Cell Biol. 2015;126:357–75.
463. Carette JE, Raaben M, Wong AC, Herbert AS, Obernosterer G, Mulherkar N, et al. Ebola virus entry requires the cholesterol transporter Niemann-Pick C1. Nature. 2011 Sep 15;477(7364):340–3.
464. Côté M, Misasi J, Ren T, Bruchez A, Lee K, Filone CM, et al. Small molecule inhibitors reveal Niemann-Pick C1 is essential for Ebola virus infection. Nature. 2011 Sep 15;477(7364):344–8.
465. Daniloski Z, Jordan TX, Wessels HH, Hoagland DA, Kasela S, Legut M, et al. Identification of Required Host Factors for SARS-CoV-2 Infection in Human Cells. Cell. 2021 Jan 7;184(1):92-105.e16.
466. Zhu Y, Feng F, Hu G, Wang Y, Yu Y, Zhu Y, et al. A genome-wide CRISPR screen identifies host factors that regulate SARS-CoV-2 entry. Nat Commun. 2021 Dec 1;12(1):1–11.

467. Chokesuwattanaskul R, Shah N, Chokesuwattanaskul S, Liu Z, Thakur R. Low-dose Amiodarone Is Safe: A Systematic Review and Meta-analysis. J Innov Card Rhythm Manag. 2020 Apr 1;11(4):4054–61.
468. Yilmaz S, Yilmaz Sezer N, Gönenç İM, İlhan SE, Yilmaz E. Safety of clomiphene citrate: a literature review. Vol. 70, Cytotechnology. Springer Netherlands; 2018. p. 489–95.
469. Marsh W. Imipramine. In: xPharm: The Comprehensive Pharmacology Reference. Elsevier Inc.; 2007. p. 1–5.
470. Tsai YC, Tsai TF. Itraconazole in the Treatment of Nonfungal Cutaneous Diseases: A Review. Vol. 9, Dermatology and Therapy. Springer Healthcare; 2019. p. 271–80.
471. Heringa M. Review on raloxifene: Profile of a selective estrogen receptor modulator. Vol. 41, International Journal of Clinical Pharmacology and Therapeutics. Dustri-Verlag Dr. Karl Feistle; 2003. p. 331–45.
472. Vogel CL, Johnston MA, Capers C, Braccia D. Toremifene for breast cancer: A review of 20 years of data. Vol. 14, Clinical Breast Cancer. Elsevier Inc.; 2014. p. 1–9.
473. Appelqvist H, Nilsson C, Garner B, Brown AJ, Kågedal K, Öllinger K. Attenuation of the lysosomal death pathway by lysosomal cholesterol accumulation. Am J Pathol. 2011 Feb 1;178(2):629–39.
474. Johansen LM, Brannan JM, Delos SE, Shoemaker CJ, Stossel A, Lear C, et al. FDA-approved selective estrogen receptor modulators inhibit ebola virus infection. Sci Transl Med. 2013 Jun 19;5(190).
475. Xiong HL, Cao JL, Shen CG, Ma J, Qiao XY, Shi TS, et al. Several FDA-Approved Drugs Effectively Inhibit SARS-CoV-2 Infection in vitro. Front Pharmacol. 2021 Feb 5;11.
476. Schloer S, Brunotte L, Goretzko J, Mecate-Zambrano A, Korthals N, Gerke V, et al. Targeting the endolysosomal host-SARS-CoV-2 interface by clinically licensed functional 1 inhibitors of acid sphingomyelinase (FIASMA) including the antidepressant fluoxetine 2. bioRxiv. 2020 Aug 16;2020.07.27.222836.
477. Nakagawa K, Narayanan K, Wada M, Makino S. Inhibition of Stress Granule Formation by Middle East Respiratory Syndrome Coronavirus 4a Accessory Protein Facilitates Viral Translation, Leading to Efficient Virus Replication. J Virol. 2018 Aug 1;92(20):902–20.
478. Raaben M, Groot Koerkamp MJA, Rottier PJM, de Haan CAM. Mouse hepatitis coronavirus replication induces host translational shutoff and mRNA decay, with concomitant formation of stress granules and processing bodies. Cell Microbiol. 2007 Sep;9(9):2218–29.
479. Reineke LC, Tsai W-C, Jain A, Kaelber JT, Jung SY, Lloyd RE. Casein Kinase 2 Is Linked to Stress Granule Dynamics through Phosphorylation of the Stress Granule Nucleating Protein G3BP1. Mol Cell Biol. 2017 Feb 15;37(4).
480. Bouhaddou M, Memon D, Meyer B, White KM, Rezelj V V., Correa Marrero M, et al. The Global Phosphorylation Landscape of SARS-CoV-2 Infection. Cell. 2020 Aug 6;182(3):685-712.e19.
481. Malla TR, Tumber A, John T, Brewitz L, Strain-Damerell C, Owen CD, et al. Mass spectrometry reveals potential of β-lactams as SARS-CoV-2 Mproinhibitors. Chem Commun. 2021 Feb 11;57(12):1430–3.
482. Chou CY, Chien CH, Han YS, Prebanda MT, Hsieh HP, Turk B, et al.

Thiopurine analogues inhibit papain-like protease of severe acute respiratory syndrome coronavirus. Biochem Pharmacol. 2008 Apr 15;75(8):1601–9.
483. Cheng KW, Cheng SC, Chen WY, Lin MH, Chuang SJ, Cheng IH, et al. Thiopurine analogs and mycophenolic acid synergistically inhibit the papain-like protease of Middle East respiratory syndrome coronavirus. Antiviral Res. 2015;115:9–16.
484. Swaim CD, Perng YC, Zhao X, Canadeo LA, Harastani HH, Darling TL, et al. 6-Thioguanine blocks SARS-CoV-2 replication by inhibition of PLpro protease activities. bioRxiv. bioRxiv; 2020.
485. Lugea A, Gerloff A, Su HY, Xu Z, Go A, Hu C, et al. The Combination of Alcohol and Cigarette Smoke Induces Endoplasmic Reticulum Stress and Cell Death in Pancreatic Acinar Cells. Gastroenterology. 2017 Dec 1;153(6):1674–86.
486. Rothan HA, Stone S, Natekar J, Kumari P, Arora K, Kumar M. The FDA-approved gold drug auranofin inhibits novel coronavirus (SARS-COV-2) replication and attenuates inflammation in human cells. Virology. 2020 Aug 1;547:7–11.
487. Yuan S, Wang R, Chan JFW, Zhang AJ, Cheng T, Chik KKH, et al. Metallodrug ranitidine bismuth citrate suppresses SARS-CoV-2 replication and relieves virus-associated pneumonia in Syrian hamsters. Nat Microbiol. 2020 Nov 1;5(11):1439–48.
488. Perwitasari O, Torrecilhas AC, Yan X, Johnson S, White C, Tompkins SM, et al. Targeting Cell Division Cycle 25 Homolog B To Regulate Influenza Virus Replication. J Virol. 2013 Dec 15;87(24):13775–84.
489. Brozovic A, Ambriović-Ristov A, Osmak M. The relationship between cisplatin-Induced reactive oxygen species, glutathione, and BCL-2 and resistance to cisplatin. Vol. 40, Critical Reviews in Toxicology. Crit Rev Toxicol; 2010. p. 347–59.
490. Elbein AD. Glycosidase inhibitors: inhibitors of N-linked oligosaccharide processing. FASEB J. 1991 Dec 1;5(15):3055–63.
491. Miller JL, Spiro SG, Dowall SD, Taylor I, Rule A, Alonzi DS, et al. Minimal In Vivo Efficacy of Iminosugars in a Lethal Ebola Virus Guinea Pig Model. Kuhn JH, editor. PLoS One. 2016 Nov 23;11(11):e0167018.
492. Andersson U, Butters TD, Dwek RA, Platt FM. N-butyldeoxygalactonojirimycin: A more selective inhibitor of glycosphingolipid biosynthesis than N-butyldeoxynojirimycin, in vitro and in vivo. Biochem Pharmacol. 2000 Apr 1;59(7):821–9.
493. Rajasekharan S, Bonotto RM, Kazungu Y, Alves LN, Poggianella M, Orellana PM, et al. Repurposing of Miglustat to inhibit the coronavirus Severe Acquired Respiratory Syndrome SARS-CoV-2. bioRxiv. bioRxiv; 2020. p. 2020.05.18.101691.
494. Clarke EC, Nofchissey RA, Ye C, Bradfute SB. The iminosugars celgosivir, castanospermine and UV-4 inhibit SARS-CoV-2 replication. Glycobiology. 2020 Sep 26;2020:1–7.
495. Fukushi M, Yoshinaka Y, Matsuoka Y, Hatakeyama S, Ishizaka Y, Kirikae T, et al. Monitoring of S Protein Maturation in the Endoplasmic Reticulum by Calnexin Is Important for the Infectivity of Severe Acute Respiratory Syndrome Coronavirus. J Virol. 2012 Nov 1;86(21):11745–53.

496. Holwerda M, Vkovski P, Wider M, Thiel V, Dijkman R. Identification of five antiviral compounds from the pandemic response box targeting SARS-CoV-2. bioRxiv. bioRxiv; 2020. p. 2020.05.17.100404.
497. Carbajo-Lozoya J, Müller MA, Kallies S, Thiel V, Drosten C, Von Brunn A. Replication of human coronaviruses SARS-CoV, HCoV-NL63 and HCoV-229E is inhibited by the drug FK506. Virus Res. 2012 Apr;165(1):112–7.
498. Bramante CT, Ingraham NE, Murray TA, Marmor S, Hovertsen S, Gronski J, et al. Metformin and risk of mortality in patients hospitalised with COVID-19: a retrospective cohort analysis. Lancet Heal Longev. 2021 Jan 1;2(1):e34–41.
499. Neubauer A, Wiesmann T, Vogelmeier CF, Mack E, Skevaki C, Gaik C, et al. Ruxolitinib for the treatment of SARS-CoV-2 induced acute respiratory distress syndrome (ARDS). Vol. 34, Leukemia. Springer Nature; 2020. p. 2276–8.
500. Veras FP, Pontelli MC, Silva CM, Toller-Kawahisa JE, de Lima M, Nascimento DC, et al. SARS-CoV-2-triggered neutrophil extracellular traps mediate COVID-19 pathology. J Exp Med. 2020 Dec 7;217(12).
501. Konrad M, Nieman DC. Evaluation of Quercetin as a Countermeasure to Exercise-Induced Physiological Stress. In: Antioxidants in Sport Nutrition. CRC Press; 2014. p. 155–70.
502. Treiber A, Morand O, Clozel M. The pharmacokinetics and tissue distribution of the glucosylceramide synthase inhibitor miglustat in the rat. Xenobiotica. 2007 Mar;37(3):298–314.
503. Gurukumar K, Priyadarshini D, Patil J, Bhagat A, Singh A, Shah P, et al. Development of real time PCR for detection and quantitation of Dengue Viruses. Virol J. 2009 Jan 23;6(1):10.
504. Russell PK, Nisalak A, Sukhavachana P, Vivona S. A plaque reduction test for dengue virus neutralizing antibodies. J Immunol. 1967 Aug 1;99(2):285–90.
505. by Kenny Moore C, Martin J, William S. Electroporation of human pluripotent or embryonic stem cells with CRISPR reagents Ribonucleoprotein delivery using the Alt-R ® CRISPR-Cas9 System for homology-directed repair or other genome editing applications.
506. Kaliwantoro N, Soesatyo MH, Indarto, Juffrie M, Dharmastiti R. Effect of dengue virus infection on the permeability of vero cells line. In: AIP Conference Proceedings. American Institute of Physics Inc.; 2016. p. 10002.
507. Kiappes JL, Hill ML, Alonzi DS, Miller JL, Iwaki R, Sayce AC, et al. ToP-DNJ, a Selective Inhibitor of Endoplasmic Reticulum α-Glucosidase II Exhibiting Antiflaviviral Activity. ACS Chem Biol. 2018 Jan 19;13(1):60–5.
508. Cumpstey I, Butters TD, Tennant-Eyles RJ, Fairbanks AJ, France RR, Wormald MR. Synthesis of fluorescence-labelled disaccharide substrates of glucosidase II. Carbohydr Res. 2003 Sep 10;338(19):1937–49.
509. Kaushal GP, Pan YT, Tropea JE, Mitchell M, Liu P, Elbein AD. Selective inhibition of glycoprotein-processing enzymes. Differential inhibition of glucosidases I and II in cell culture. J Biol Chem. 1988 Nov 25;263(33):17278–83.
510. Petrescu AJ, Butters TD, Reinkensmeier G, Petrescu S, Platt FM, Dwek RA, et al. The solution NMR structure of glucosylated N-glycans involved in the early stages of glycoprotein biosynthesis and folding. EMBO J. 1997 Jul 16;16(14):4302–10.
511. Tyrrell BE. Antiviral and immunomodulatory activities of iminosugars:

candidate therapeutics for arbovirus infections. University of Oxford; 2018.
512. Boigard H, Cimica V, Galarza JM. Dengue-2 virus-like particle (VLP) based vaccine elicits the highest titers of neutralizing antibodies when produced at reduced temperature. Vaccine. 2018 Nov 29;36(50):7728–36.
513. Nemésio H, Palomares-Jerez F, Villalaín J. NS4A and NS4B proteins from dengue virus: Membranotropic regions. Biochim Biophys Acta - Biomembr. 2012 Nov 1;1818(11):2818–30.
514. Gruters RA, Neefjes JJ, Tersmette M, De Goede REY, Tulp A, Huisman HG, et al. Interference with HIV-induced syncytium formation and viral infectivity by inhibitors of trimming glucosidase. Nature. 1987;330(6143):74–7.
515. Bowlin TL, Tyms AS, Taylor DL, Sunkara PS, Liu PS, Kang MS. 6-O-Butanoylcastanospermine (MDL 28,574) inhibits glycoprotein processing and the growth of HIVs. AIDS. 1991 Jun 1;5(6):693–8.
516. Mellor HR, Nolan J, Pickering L, Wormald MR, Platt FM, Dwek RA, et al. Preparation, biochemical characterization and biological properties of radiolabelled N-alkylated deoxynojirimycins. Biochem J. 2002 Aug 15;366(1):225–33.
517. Chang J, Block TM, Guo JT. Antiviral therapies targeting host ER alpha-glucosidases: Current status and future directions. Vol. 99, Antiviral Research. Antiviral Res; 2013. p. 251–60.
518. Ferris SP, Kodali VK, Kaufman RJ. Glycoprotein folding and quality-control mechanisms in protein-folding diseases. Vol. 7, DMM Disease Models and Mechanisms. Company of Biologists Ltd; 2014. p. 331–41.
519. García-González P, Cabral-Miranda F, Hetz C, Osorio F. Interplay Between the Unfolded Protein Response and Immune Function in the Development of Neurodegenerative Diseases. Front Immunol. 2018 Nov 2;9(NOV):2541.
520. Hu H, Tian M, Ding C, Yu S. The C/EBP homologous protein (CHOP) transcription factor functions in endoplasmic reticulum stress-induced apoptosis and microbial infection. Vol. 10, Frontiers in Immunology. Frontiers Media S.A.; 2019. p. 3083.
521. Valadão ALC, Aguiar RS, de Arruda LB. Interplay between inflammation and cellular stress triggered by Flaviviridae viruses. Vol. 7, Frontiers in Microbiology. Frontiers Media S.A.; 2016.
522. Trahtemberg U, Mevorach D. Apoptotic Cells Induced Signaling for Immune Homeostasis in Macrophages and Dendritic Cells. Front Immunol. 2017 Oct 25;8(OCT).
523. Elliott MR, Ravichandran KS. Clearance of apoptotic cells: implications in health and disease. J Cell Biol. 2010 Jun 28;189(7):1059–70.
524. Hill JC. Structural chracterisation of calnexin cycle components and assessment as antiviral target. University of Oxford; 2018.
525. Hentze MW, Kulozik AE. A perfect message: RNA surveillance and nonsense-mediated decay. Vol. 96, Cell. Elsevier B.V.; 1999. p. 307–10.
526. Shailubhai K, Pukazhenthi BS, Saxena ES, Varma GM, Vijay IK. Glucosidase I, a transmembrane endoplasmic reticular glycoprotein with a luminal catalytic domain. J Biol Chem. 1991 Sep 5;266(25):16587–93.
527. Deprez P, Gautschi M, Helenius A. More than one glycan is needed for ER glucosidase II to allow entry of glycoproteins into the calnexin/calreticulin cycle. Mol Cell. 2005 Jul 22;19(2):183–95.

528. O'Keefe S, Roebuck QP, Nakagome I, Hirono S, Kato A, Nash R, et al. Characterizing the selectivity of ER α-glucosidase inhibitors. Glycobiology. 2019 Jul 1;29(7):530–42.
529. Kurakata Y, Uechi A, Yoshida H, Kamitori S, Sakano Y, Nishikawa A, et al. Structural Insights into the Substrate Specificity and Function of Escherichia coli K12 YgjK, a Glucosidase Belonging to the Glycoside Hydrolase Family 63. J Mol Biol. 2008 Aug 1;381(1):116–28.
530. Hughes JP, Rees SS, Kalindjian SB, Philpott KL. Principles of early drug discovery. Vol. 162, British Journal of Pharmacology. Wiley-Blackwell; 2011. p. 1239–49.
531. Lo MC, Aulabaugh A, Jin G, Cowling R, Bard J, Malamas M, et al. Evaluation of fluorescence-based thermal shift assays for hit identification in drug discovery. Anal Biochem. 2004 Sep 1;332(1):153–9.
532. Kunig V, Potowski M, Gohla A, Brunschweiger A. DNA-encoded libraries-an efficient small molecule discovery technology for the biomedical sciences. Vol. 399, Biological Chemistry. Walter de Gruyter GmbH; 2018. p. 691–710.
533. Caputo AT. Structural and Biochemical Characterisation of the Endoplasmic Reticulum a-Glucosidases. University of Oxford; 2015.
534. Walter TS, Meier C, Assenberg R, Au KF, Ren J, Verma A, et al. Lysine Methylation as a Routine Rescue Strategy for Protein Crystallization. Structure. 2006 Nov;14(11):1617–22.
535. Vonrhein C, Flensburg C, Keller P, Sharff A, Smart O, Paciorek W, et al. Data processing and analysis with the autoPROC toolbox. Acta Crystallogr Sect D Biol Crystallogr. 2011 Apr 18;67(4):293–302.
536. Womack, T. O., Smart, O. S., Sharff, A., Flensburg, C., Keller, P., Paciorek, W., Vonrhein, C. & Bricogne G. . rhofit v.1.2.1. http://www.globalphasing.com. 2010;
537. Smart OS, Womack TO, Flensburg C, Keller P, Paciorek W, Sharff A, et al. Exploiting structure similarity in refinement: Automated NCS and target-structure restraints in BUSTER. Acta Crystallogr Sect D Biol Crystallogr. 2012 Apr 16;68(4):368–80.
538. Emsley P, Lohkamp B, Scott WG, Cowtan K. Features and development of Coot. Acta Crystallogr Sect D Biol Crystallogr. 2010;66(4):486–501.
539. P.H. Zwart, R.W. Grosse-Kunstleve and PDA. Xtriage and Fest: automatic assessment of X-ray data and substructure structure factor estimation. CCP4 Newsl. 2005;Winter Con.
540. A.A.Vaguine, J.Richelle SJW. .SFCHECK: a unified set of procedure for evaluating the quality of macromolecular stracture-factor data and their agreement with atomic model. Acta Crystallogr Sect B. 1999;D55, 191–2.
541. Zwart P, Grosse-Kunstleve RW, Adams P. Xtriage and Fest : automatic assessment of X-ray data and substructure structure factor estimation. 2005;
542. APBS | Home [Internet]. [cited 2021 Jun 7]. Available from: https://server.poissonboltzmann.org/
543. Wallace AC, Laskowski RA, Thornton JM. Ligplot: A program to generate schematic diagrams of protein-ligand interactions. Protein Eng Des Sel. 1995 Feb;8(2):127–34.
544. Schrodinger L. The PyMOL Molecular Graphics System.
545. Pettersen EF, Goddard TD, Huang CC, Couch GS, Greenblatt DM, Meng EC,

et al. UCSF Chimera - A visualization system for exploratory research and analysis. J Comput Chem. 2004 Oct;25(13):1605–12.
546. Su W, Ge R, Ding D, Chen W, Wang W, Yan H, et al. Triaging of DNA-Encoded Library Selection Results by High-Throughput Resynthesis of DNA–Conjugate and Affinity Selection Mass Spectrometry. Bioconjug Chem. 2021 May 19;32(5):1001–7.
547. (No Title) [Internet]. [cited 2021 Jun 17]. Available from: https://wuxi-rsd.com/Media/Default/ServicesSolutionsImages/HitS/DELopen Protocol _approved_20200601.pdf
548. Vagin A, Teplyakov A. MOLREP: An Automated Program for Molecular Replacement. J Appl Crystallogr. 1997 Dec 1;30(6):1022–5.
549. Kantardjieff KA, Rupp B. Matthews coefficient probabilities: Improved estimates for unit cell contents of proteins, DNA, and protein-nucleic acid complex crystals. Protein Sci. 2003 Sep;12(9):1865–71.
550. Emsley P, Cowtan K. Coot: Model-building tools for molecular graphics. Acta Crystallogr Sect D Biol Crystallogr. 2004 Dec;60(12 I):2126–32.
551. Hensen M. Structural and functional studies of the antiviral target proteins HCV p7 and ER alpha-glucosidase II. University of Oxford; 2019.
552. I-TASSER server for protein structure and function prediction [Internet]. [cited 2021 Dec 23]. Available from: https://zhanggroup.org/I-TASSER/
553. Bai N, Roder H, Dickson A, Karanicolas J. Isothermal Analysis of ThermoFluor Data can readily provide Quantitative Binding Affinities. Sci Rep. 2019 Dec 1;9(1):1–15.
554. Niesen FH, Berglund H, Vedadi M. The use of differential scanning fluorimetry to detect ligand interactions that promote protein stability. Nat Protoc. 2007 Sep 13;2(9):2212–21.
555. Zhang JH, Chung TDY, Oldenburg KR. A simple statistical parameter for use in evaluation and validation of high throughput screening assays. J Biomol Screen. 1999;4(2):67–73.
556. Brenner S, Lerner RA. Encoded combinatorial chemistry. Proc Natl Acad Sci U S A. 1992 Jun 15;89(12):5381–3.
557. Neri D, Lerner RA. DNA-Encoded Chemical Libraries: A Selection System Based on Endowing Organic Compounds with Amplifiable Information. Vol. 87, Annual Review of Biochemistry. Annual Reviews Inc.; 2018. p. 479–502.
558. Yuen LH, Franzini RM. Achievements, Challenges, and Opportunities in DNA-Encoded Library Research: An Academic Point of View. ChemBioChem. 2017 May 4;18(9):829–36.
559. Favalli N, Bassi G, Scheuermann J, Neri D. DNA-encoded chemical libraries - achievements and remaining challenges. FEBS Lett. 2018 Jun 1;592(12):2168–80.
560. Harris PA, Berger SB, Jeong JU, Nagilla R, Bandyopadhyay D, Campobasso N, et al. Discovery of a First-in-Class Receptor Interacting Protein 1 (RIP1) Kinase Specific Clinical Candidate (GSK2982772) for the Treatment of Inflammatory Diseases. J Med Chem. 2017 Feb 23;60(4):1247–61.
561. Schuller M, Correy GJ, Gahbauer S, Fearon D, Wu T, Díaz RE, et al. Fragment Binding to the Nsp3 Macrodomain of SARS-CoV-2 Identified Through Crystallographic Screening and Computational Docking. bioRxiv. bioRxiv; 2020.

562. Krafcikova P, Silhan J, Nencka R, Boura E. Structural analysis of the SARS-CoV-2 methyltransferase complex involved in RNA cap creation bound to sinefungin. Nat Commun. 2020 Dec 1;11(1):1–7.
563. Walker AP, Fan H, Keown JR, Margitich V, Grimes JM, Fodor E, et al. Enisamium is a small molecule inhibitor of the influenza A virus and SARS-CoV-2 RNA polymerases. bioRxiv. bioRxiv; 2020.
564. DeDiego ML, Nieto-Torres JL, Regla-Nava JA, Jimenez-Guardeno JM, Fernandez-Delgado R, Fett C, et al. Inhibition of NF- B-Mediated Inflammation in Severe Acute Respiratory Syndrome Coronavirus-Infected Mice Increases Survival. J Virol. 2014 Jan 15;88(2):913–24.
565. Shahripour AB, Plummer MS, Lunney EA, Sawyer TK, Stankovic CJ, Connolly MK, et al. Structure-based design of caspase-1 inhibitor containing a diphenyl ether sulfonamide. Bioorganic Med Chem Lett. 2001 Oct 22;11(20):2779–82.
566. Redondo N, García-Moreno M, Sanz MA, Carrasco L. Translation of viral mRNAs that do not require eIF4E is blocked by the inhibitor 4EGI-1. Virology. 2013 Sep;444(1–2):171–80.
567. Gopalakrishnan R, Matta H, Chaudhary PM. A purine scaffold HSP90 inhibitor BIIB021 has selective activity against KSHV-associated primary effusion lymphoma and blocks vFLIP k13-induced NF-κB. Clin Cancer Res. 2013 Sep 15;19(18):5016–26.
568. Bakewell S, Conde I, Fallah Y, McCoy M, Jin L, Shajahan-Haq AN. Inhibition of DNA repair pathways and induction of ROS are potential mechanisms of action of the small molecule inhibitor bold-100 in breast cancer. Cancers (Basel). 2020 Sep 1;12(9):1–19.
569. Jin Z, Zhao Y, Sun Y, Zhang B, Wang H, Wu Y, et al. Structural basis for the inhibition of SARS-CoV-2 main protease by antineoplastic drug carmofur. Nat Struct Mol Biol. 2020 Jun 1;27(6):529–32.
570. Baddock HT, Brolih S, Yosaatmadja Y, Ratnaweera M, Bielinski M, Swift LP, et al. Characterisation of the SARS-CoV-2 ExoN (nsp14^{ExoN}-nsp10) complex: implications for its role in viral genome stability and inhibitor identification. bioRxiv. Cold Spring Harbor Laboratory; 2020. p. 2020.08.13.248211.
571. Xie C, Gao X, Sun D, Zhang Y, Krausz KW, Qin X, et al. Metabolic profiling of the novel hypoxia-inducible factor 2α inhibitor PT2385 in vivo and in vitro. Drug Metab Dispos. 2018 Apr 1;46(4):336–45.
572. Piplani S, Singh P, Petrovsky N, Winkler DA. Computational screening of repurposed drugs and natural products against SARS-Cov-2 main protease (Mpro) as potential COVID-19 therapies. 2020 Sep 1;
573. A Study of Telaglenastat (CB-839) in Combination With Palbociclib in Patients With Solid Tumors - Full Text View - ClinicalTrials.gov [Internet]. [cited 2021 Apr 1]. Available from: https://clinicaltrials.gov/ct2/show/NCT03965845
574. Curtin N, Bányai K, Thaventhiran J, Le Quesne J, Helyes Z, Bai P. Repositioning PARP inhibitors for SARS-CoV-2 infection(COVID-19); a new multi-pronged therapy for acute respiratory distress syndrome? Vol. 177, British Journal of Pharmacology. John Wiley and Sons Inc; 2020. p. 3635–45.
575. Kilbourne ED. Inhibition of influenza virus multiplication with a glucose antimetabolite (2-deoxy-D-glucose). Nature. 1959;183(4656):271–2.
576. Newburg DS, Shea TB, Yatziv S, Raghavan SS, McCluer RH. Macrophages exposed in vitro to conduritol B epoxide resemble Gaucher cells. Exp Mol

Pathol. 1988;48(3):317–23.
577. Beckmann N, Becker KA. Ceramide and Related Molecules in Viral Infections. Int J Mol Sci. 2021 May 26;22(11):5676.
578. Gong M jiao, Chang Y yan, Shao J jun, Li S fang, Zhang Y guang, Chang H yun. Antiviral effect of amiloride on replication of foot and mouth disease virus in cell culture. Microb Pathog. 2019 Oct 1;135:103638.
579. Wilson L, Gage P, Ewart G. Hexamethylene amiloride blocks E protein ion channels and inhibits coronavirus replication. Virology. 2006 Sep 30;353(2):294–306.
580. Von Nussbaum F, Li VMJ. Neutrophil elastase inhibitors for the treatment of (cardio)pulmonary diseases: Into clinical testing with pre-adaptive pharmacophores. Vol. 25, Bioorganic and Medicinal Chemistry Letters. Elsevier Ltd; 2015. p. 4370–81.
581. Hu L, Li J, Cai H, Yao W, Xiao J, Li YP, et al. Avasimibe: A novel hepatitis C virus inhibitor that targets the assembly of infectious viral particles. Antiviral Res. 2017 Dec 1;148:5–14.
582. Lawson MA, Ebetino FH, Mazur A, Chantry AD, Paton-Hough J, Evans HR, et al. The Pharmacological Profile of a Novel Highly Potent Bisphosphonate, OX14 (1-Fluoro-2-(Imidazo-[1,2-α]Pyridin-3-yl)-Ethyl-Bisphosphonate). J Bone Miner Res. 2017 Sep 1;32(9):1860–9.
583. Wing PA, Keeley TP, Zhuang X, Lee JY, Prange-Barczynska M, Tsukuda S, et al. Hypoxic and pharmacological activation of HIFs inhibits SARS-CoV-2 infection of lung epithelial cells. Cell Rep. 2021 Apr 5;109020.
584. Zhuang X, Tsukuda S, Wrensch F, Wing PA, Borrmann H, Harris JM, et al. Circadian regulation of SARS-CoV-2 infection in lung epithelial cells. bioRxiv. 2021 Mar 21;2021.03.20.436163.
585. Eleftheriou P, Amanatidou D, Petrou A, Geronikaki A. In silico evaluation of the effectivity of approved protease Inhibitors against the main protease of the novel SARS-CoV-2 virus. Molecules. 2020 Jun 1;25(11).

Appendix I

Table 29: Glycoform abundances observed across $S1_{virus}$.

	N17	N61	N74	N122	N149	N165	N234	N282	N331	N343	N603	N616	N657
Unoccupied	0	0	0	0	0	0	0	0	0	0	0	0	0.16061
Man9	0	0	0	0	0	0	0	0	0	0	0	0	0
Man8	5.63	0	0	1.5	0	0	23.44	0	1.39	1.02	0	0	0
Man7	0	0.74	2.39	19.23	0	0	20.32	0	4.69	1.79	0	0	0
Man6	20.07	3.73	2.66	5.52	0	0	16.31	0	2.26	1.39	0	0	0
Man5	0	93.9	24.47	32.96	11.6	0	39.93	23	11.34	17.71	82.81	27.44	0.12975
hybrid	0	0	0	0	0	0	0	0	0	0	0	2.29	0
Mono	0	0	1.85	0	0	0	0	0	0.78	0	0	0	0
Di	74.30	0	0.59	24.8	0	0	0	1.47	5.82	2.67	0	0	0
Tri	0	1.62	63.38	16	88.4	100	0	75.53	72.94	75.42	17.19	70.27	0.70964
Tetra	0	0	4.66	0	0		0	0	0.78	0	0	0	0

	T323/S325	T678
Unoccupied		
GalNac	82.774	
Core-1	0	
Core-1+Sial	3.108	
Core-2	14.119	
Core-2+Sial	0	
Core-2+2Sial	0	

Table 30: Glycoform abundances observed across $S_{recombinant\ trimer}$.

	N17	N61	N74	N122	N149	N165	N234	N282	N331	N343	N603	N616	N657
Un-occupied	0	0	0	0	0	0	0	0	0	0.167	0	0	0
Man9	0	0	0	0	0	0	21.924	0	0	0	0	0	0
Man8	0	0	0	0	0	0	42.863	5.11	0	0	0	0	0
Man7	0	0	0	0.791	0	0	15.071	0	0	0	0	0	0
Man6	0	0	0	0.327	0	0	7.672	0	0	0.256	0	0	0
Man5	0	81.771	0.627	30.576	0	41.16	12.469	1.607	1.288	1.323	6.306	0	0
hybrid	0	0	0	14.794	0	0	0	0	0	0.987	0	0	0
Mono	0	4.694	0.296	11.206	0	0	0	9.673	3.521	0	0	0	0.504
Bi	0	11.994	9.541	39.902	25.527	7.889	0	22.124	57.598	67.541	93.694	98.529	74.726
Tri	100	1.541	61.022	2.404	74.473	31.842	0	59.456	36.282	29.725	0	1.471	18.935
Tetra	0	0	12.651	0	0	19.11	0	2.031	1.311	0	0	0	5.835

	N709	N717	N801	N1074	N1098	N1134	N1158	N1173	N1194
Un-occupied	0	0	4.23E-02	13.625	12.024	0		0	37.61
Man9	0	0	0	0	0	0		0	0
Man8	0	0	0.119	0	0	0		0	0
Man7	0	5.678	1.64	0	0	0		0	0
Man6	0	10.014	1.234	0	0	0		0	0
Man5	92.325	39.216	49.753	39.957	2.381	0		0	0
hybrid	7.675	25.526	9.446	4.503	9.97	0		0	0
Mono	0	7.935	3.491	9.641	12.809	0		0	0
Bi	0	1.653	26.448	16.209	40.311	51.909		0	12.534
Tri	0	0.484	7.826	13.328	15.54	35.478		0	7.108
Tetra	0	9.494	0	2.348	6.7	12.612		100	42.748

	T323/ S325	T678
Unoccupied	99.085	10.877
GalNac	0.636	7.857
Core-1	0.197	15.787
Core-1+Sial	3.06E-03	9.96
Core-1+2Sial	0	26.563
Core-2	7.97E-02	0.903
Core-2+Sial	0	13.539
Core-2+2Sial	0	14.515

Table 31: Glycoform abundances observed across $S1_{\text{vaccine antigen}}$.

	N17	N61	N74	N122	N149	N165	N234	N282	N331	N343	N603	N616	N657
Un-occupied	46.641	0	6.582	0.203	96.277	0	0	0	0	0	0	0	65.732
Man9	0	0	0	0	0	0	0	0	0	0	0	0	0
Man8	0	0	0	0	0	0	0.738	0	0	0	0	0	0
Man7	0	0	0	0	0	0	1.747	0	0	0	0	0	0
Man6	0	0	0	0	0	0	0.693	0	0	0	0	0	0
Man5	0	11.991	0	1.871	0	0	71.57	0	0	0.676	17.66	0	0
hybrid	0	4.351	0	4.507	0	0	0	0	0	0	0	0	0
Mono	0	0.623	0	8.234	0	0	3.152	0	0	0.541	12.24	0	0
Di	4.192	30.75	0	57.682	1.187	30.917	18.568	4.377	48.045	15.067	51.66	27.424	0
Tri	49.168	48.745	93.418	26.936	2.537	50.215	3.532	77.323	50.766	83.717	18.441	68.489	34.268
Tetra	0	3.54	0	0.566	0	18.868	0	18.3	1.189	0	0	4.087	0

	T323/S325	T678
Un-occupied	95.417	10.877
GalNac	1.574	7.857
Core-1	0.894	15.787
Core-1+Sial	0.419	9.96
Core-1+2Sial	0.954	26.563
Core-2	0.254	1.86E+09
Core-2+Sial	0.441	13.539
Core-2+2Sial	4.70E-02	14.515

Table 32: Glycoform abundances observed across $S1_{\text{recombinant monomer}}$.

	N17	N61	N74	N122	N149	N165	N234	N282	N331	N343	N603	N616	N657
Un-occupied	0	0	60.992	0	94.761	0	0	0	1.47	0	0	0	99.71
Man9	0	0	0	0	0	0	0	0	0	0	0	0	0
Man8	0	0	0	0	0	0	0	0	0	0	0	0	0
Man7	0	0	0	0.182	0	0	0	0	0	0	0	0	0
Man6	0	0	0	0.21	0	0	0	0	0	0	0	0	0
Man5	0	2.469	0	3.725	0	1.328	0	0	0.15	10.07	0	0	0
hybrid	0	0	0	0	0	0	0	0	0	0	0	0	0
Mono	0	0	0	0	0	0	0	0	0	0	0	0	0
Di	3.648	35.126	15.124	66.996	5.239	44.267	37.631	0	70.856	58.4	76.671	0	0.29
Tri	57.628	25.212	20.418	26.066	0	32.748	39.199	0	23.874	31.53	9.806	0	0
Tetra	38.723	37.193	3.466	2.821	0	21.657	23.171	100	3.65	0	13.523	100	0

	T323/S325	T678
Un-occupied	71.76	0
GalNac	1.922	4.751
Core-1	5.73	0
Core-1+Sial	2.293	0
Core-1+2Sial	7.778	67.214
Core-2	0.712	0
Core-2+Sial	7.197	2.975
Core-2+2Sial	2.607	25.06

Table 33: Gibson assembly and sequencing primers to clone $S_{vaccine\ antigen}$.

Name	Sequence 5' – 3'
Gibson Assembly forward primer	gcccggttcagacggggtaccTTTGTTTTCTTGGTTCTTTTG
Gibson Assembly reverse primer	ctctagatgcatgctcgagcggccgcTTACGTGTAGTGCAATTTTAC
Sequencing 1 forward	cataaatataaccaggttccagacactgctcg
Sequencing 2 forward	gttaagcaactgagctccaacttcgg
Sequencing 3 reverse	ccgaagttggagctcagttgcttaac
Sequencing 4 reverse	gaatctcctggagtaaggtagctccg

```
   1 MFVFLVLLPL VSSQCVNLTT RTQLPPAYTN SFTRGVYYPD KVFRSSVLHS
  51 TQDLFLPFFS NVTWFHAIHV SGTNGTKRFD NPVLPFNDGV YFASTEKSNI
 101 IRGWIFGTTL DSKTQSLLIV NNATNVVIKV CEFQFCNDPF LGVYYHKNNK
 151 SWMESEFRVY SSANNCTFEY VSQPFLMDLE GKQGNFKNLR EFVFKNIDGY
 201 FKIYSKHTPI NLVRDLPQGF SALEPLVDLP IGINITRFQT LLALHRSYLT
 251 PGDSSSGWTA GAAAYYVGYL QPRTFLLKYN ENGTITDAVD CALDPLSETK
 301 CTLKSFTVEK GIYQTSNFRV QPTESIVRFP NITNLCPFGE VFNATRFASV
 351 YAWNRKRISN CVADYSVLYN SASFSTFKCY GVSPTKLNDL CFTNVYADSF
 401 VIRGDEVRQI APGQTGKIAD YNYKLPDDFT GCVIAWNSNN LDSKVGGNYN
 451 YLYRLFRKSN LKPFERDIST EIYQAGSTPC NGVEGFNCYF PLQSYGFQPT
 501 NGVGYQPYRV VVLSFELLHA PATVCGPKKS TNLVKNKCVN FNFNGLTGTG
 551 VLTESNKKFL PFQQFGRDIA DTTDAVRDPQ TLEILDITPC SFGGVSVITP
 601 GTNTSNQVAV LYQDVNCTEV PVAIHADQLT PTWRVYSTGS NVFQTRAGCL
 651 IGAEHVNNSY ECDIPIGAGI CASYQTQTNS PRRARSVASQ SIIAYTMSLG
 701 AENSVAYSNN SIAIPTNFTI SVTTEILPVS MTKTSVDCTM YICGDSTECS
 751 NLLLQYGSFC TQLNRALTGI AVEQDKNTQE VFAQVKQIYK TPPIKDFGGF
 801 NFSQILPDPS KPSKRSFIED LLFNKVTLAD AGFIKQYGDC LGDIAARDLI
 851 CAQKFNGLTV LPPLLTDEMI AQYTSALLAG TITSGWTFGA GAALQIPFAM
 901 QMAYRFNGIG VTQNVLYENQ KLIANQFNSA IGKIQDSLSS TASALGKLQD
 951 VVNQNAQALN TLVKQLSSNF GAISSVLNDI LSRLDKVEAE VQIDRLITGR
1001 LQSLQTYVTQ QLIRAAEIRA SANLAATKMS ECVLGQSKRV DFCGKGYHLM
1051 SFPQSAPHGV VFLHVTYVPA QEKNFTTAPA ICHDGKAHFP REGVFVSNGT
1101 HWFVTQRNFY EPQIITTDNT FVSGNCDVVI GIVNNTVYDP LQPELDSFKE
1151 ELDKYFKNHT SPDVDLGDIS GINASVVNIQ KEIDRLNEVA KNLNESLIDL
1201 QELGKYEQYI KWPWYIWLGF IAGLIAIVMV TIMLCCMTSC CSCLKGCCSC
1251 GSCCKFDEDD SEPVLKGVKL HYT
```

Figure 53: Sequence coverage of S_{virus} by Mascot. Total sequence coverage for S_{virus} for the three combined proteases (trypsin, chymotrypsin, and alpha lytic protease) used for bottom-up MS. Peptides for S1 covering 588 amino acids for S_{virus} (88% coverage). Mascot peptides are outlined in red. Potential N-glycosylation sites are highlighted in blue. S1 is bolded. S2 in italics. Not italics/underlining: Signal peptide.

Figure 54: Sequence coverage of $S_{vaccine\ antigen}$ by Mascot. Total sequence coverage for $S_{vaccine\ antigen}$ for the three combined proteases (trypsin, chymotrypsin, and alpha lytic protease) used for bottom-up MS. Peptides for S1 covering 586 amino acids for S_{virus} (87% coverage). Mascot peptides are outlined in red. Potential N-glycosylation sites are highlighted in blue. S1 is bolded. S2 in italics. Not italics/underlining: Signal peptide.

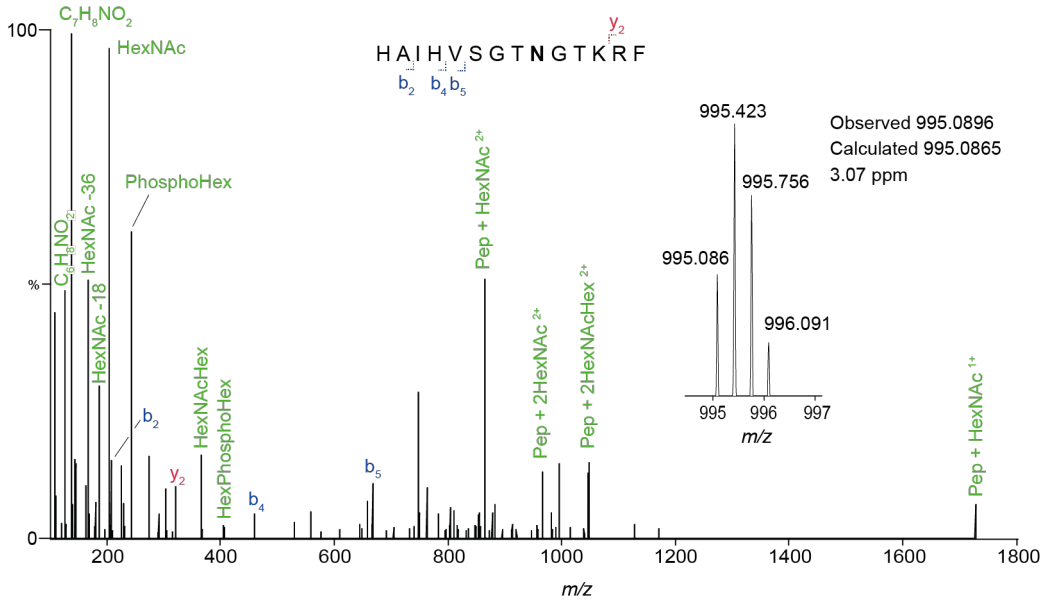

Figure 55: MS/MS spectrum of the N74 glycopeptide from S1$_{\text{vaccine antigen}}$.

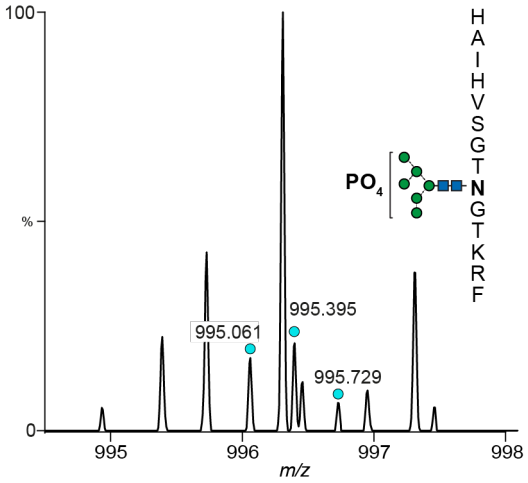

Figure 56: MS spectrum of N74 containing glycopeptide from S1$_{\text{virus}}$. MS spectrum displays the existence of the mannose-6-phosphate glycan at N74 (N-glycopeptide from chymotrypsin digestion) on S1$_{\text{virus}}$. The distribution of isotopes is labelled (blue circles).

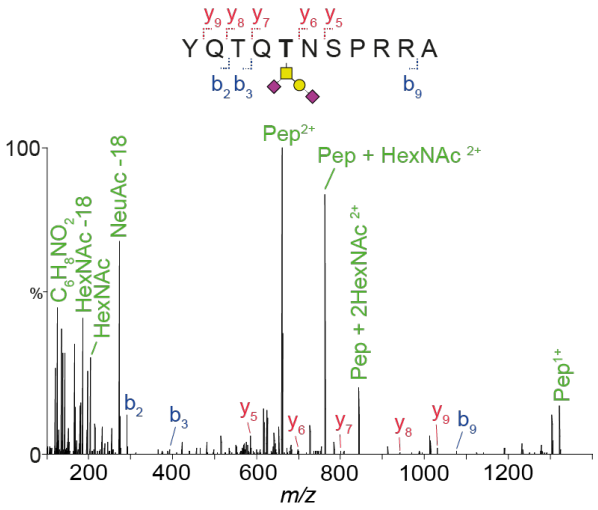

Figure 57: MS/MS spectrum of the T678 glycopeptide from S1$_{\text{vaccine antigen}}$.

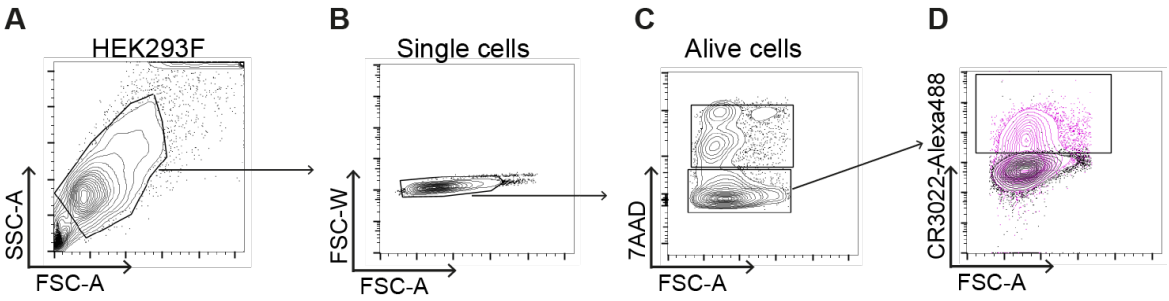

Figure 58: Flow cytometry analysis. Representative flow cytometry plots demonstrating the gating technique used to analyse the expression of S1 and S2. (A) HEK293F gate, (B) excluding of doublets in (C) final gating for live cells. (D) Non-transfected HEK293F cells (black) and S1-positive cells (pink) are seen in a representative map.

Appendix II

Table 34: FDA-approved DAAs used in the drug screening against SARS-CoV-2. GP, general practitioners; Pc, personal communication/interest with proposed MOA; CT, in clinical trial.

Compound name	Used for	Mechanism of action	Drug (µM)	% infection vs. UT	SEM	CC_{50} (µM)	CC_{10} (µM)	Plaque: IC_{50} (µM)	Plaque: IC_{90} (µM)	FFU: IC_{50} (µM)	FFU: IC_{90} (µM)	SI1	SI2	Ref
Aztreonam	Antibiotic	Bacterial cell wall synthesis inhibitor	50	82.0	2.5									GP
Chloramphenicol	Antibiotic	Binds to L16 protein of the 50S subunit of bacterial ribosomes	1000	130.8	34.4									GP
Ciprofloxacin	Antibiotic	Acts on bacterial topoisomerase II and IV	66.7	90.0	4.0	217.2	90.5							GP
Linezolid	Antibiotic	Bacterial protein synthesis inhibitor	1000	147.8	20.0									GP
Nitroxoline	Antibiotic	Bacterial gyrases inhibitor	1	109.8	13.1	82.3	33.9							GP, (481)
Tigecycline hydrate	Antibiotic	Bacterial protein translation	10	105.5	6.3	83.6	8.1							GP
Boceprevir	Antiviral	HCV NS3/4 protease inhibitor	100	56.9	19.6	>100		89.1				>1.1		(444,481)

Indinavir	Antiviral	HIV protease inhibitor	10	99.4	8.0	144.1	80.9						(197)
Enisamium	Antiviral	RNA polymerase inhibitor	10	102.8	11.2		396.0						(563)
Ribavirin	Synthetic guanosine nucleoside	Interferes with viral mRNA synthesis	10	167.5	58.9	222.9	17.3						(194)
Itraconazole	Antifungal	Ergosterol synthesis inhibitor	1.325	98.6	7.2		4.4						(470, 497)

Table 35: FDA-approved HTAs used in the drug screening against SARS-CoV-2. Pc, personal communication/interest with proposed MOA; CT, in clinical trial. *EMA not FDA-approve.

Compound name	Used for	Mechanism of action	Drug (µM)	% infection vs. UT	SEM	CC_{50} (µM)	CC_{10} (µM)	Plaque: IC_{50} (µM)	Plaque: IC_{90} (µM)	FFU: IC_{50} (µM)	FFU: IC_{90} (µM)	SI1	SI2	Ref
Nafamostat*	Anti-coagulant	Serine protease inhibitor	10	4.2	1.9	196.6	44.8	2.6	5.0			75.0	6.9	(458)
Rivaroxaban	Anti-coagulant	Factor Xa inhibitor	1	106.9	4.3		5.8							Pc
Alendronate	Bone loss	Binds to bone hydroxyapatite	1	81.5	5.2		11.1							Pc
Clodronate	Bone loss	Binds to bone hydroxyapatite	10	98.8	3.9		10.1							Pc
Raloxifene	Osteoporosis	NPC1 inhibitor	81.2	17.6	3.7	82.8	70.1							(471)
Zoledronate	Bone loss	Binds to bone hydroxyapatite	1	90.7	4.2	29.2	2.8							Pc
5-Thioguanine	Cancer	Hypoxanthine competitor	1	46.8	10.2	96.6	0.04							(481)
Cisplatin	Cancer	Alkylating agent	100	60.7	21.1	>100		96.2				>1.0		(481)
Daunorubicin	Cancer	Complex forming with DNA, topoisomerase II inhibitor	0.1	104.7	25.8	0.227	0.014							(561)
Fludarabine	Cancer	DNA synthesis inhibitor	1	94.9	5.6	51.48	6.36							(561)
Midostaurin	Cancer	Kinase inhibitor	1	134.8	12.9	61.9	6.8							(561)

Olaparib	Cancer	PARP inhibitor	1	113.0	6.8					(561)
Ponatinib	Cancer	Kinase inhibitor	10	72.3	25.8	90.3	89.1			(561)
Ruxolitinib	Cancer	Janus kinase inhibitor	10	262.5	10.0	531.4	439.0			(561)
Silmitasertib	Cancer	Casein kinase 2 inhibitor	10	0.50	0.14	22.8	9.0	0.24	93.4	(561)
Talazoparib	Cancer	PARP inhibitor	0.05	116.7	6.8					(561)
Tamoxifene	Cancer	Binding to oestrogen receptor	1	269.1	7.7	10.05	4.5			(472)
Toremifene	Cancer	NPC1 inhibitor	12.7	106.3	10.5	26.6	14.4			(472)
Amiodarone	Anti-arrhythmic drug	Potassium blocker	24.5	133.4	8.6	27.74	24.3			(467)
Dronedarone	Cardiac arrythmias	Multichannel blocker	1	95.0	12.4	46.8	31.5			Pc
Verapamil	Cardiac arrythmias	Calcium channel blocker	86.7	264.7	39.4	97.4	88.7			Pc
Amiloride	Hypertension	Sodium reabsorption inhibition	100	11.5	1.5	310.7	174.7			(478, 479)
Lercanidipine	Hypertension	Calcium channel blocker	1	85.3	7.2	19.75	2.4			Pc
Mycophenolic Acid	Immuno-suppression	Inhibitor of inosine monophosphate dehydrogenase	0.1	82.0	14.0	1.78	0.16			Pc
Rapamycin	Immuno-suppression	Cytokine production inhibitor	0.001	97.9	17.7		0.002			CT
Tacrolimus	Immuno-suppression	Reduces Peptidyl-prolyl isomerase activity	1	143.8	19.1	12.22	4.5			CT
Eliglustat	Gaucher disease	Glucosylceramide inhibitor	10	93.8	14.5	432.4	499.0			Pc
Migalastat	Gaucher disease	Glucosylceramide inhibitor	1000	70.6	9.6					Pc
Miglustat	Gaucher disease	Glucosylceramide inhibitor	1000	12.5	1.7	>1000	>1000	169.5	>5.9	(502)
Auranofin	Anti-inflammatory	Heme oxygenase-1 inducer	1	116.0	9.2	71.8	52.9			(485)

Celecoxib	Nonsteroidal anti-inflammatory drug	Cyclooxygenase-2 inhibitor	10	71.2	5.6	92.01	63.6	Pc
Indomethacin	Nonsteroidal anti-inflammatory drug	Prostaglandin synthesis inhibitor	100	124.9	5.3	593	353.2	CT
Ambroxol	Cough	Inhibition of Nitric oxide-dependent activation of soluble guanylate cyclase	121	156.5	8.4	305.3	121.2	Pc
Atorvastatin	Dyslipidaemia	Competitive inhibitor of the HMG-CoA reductase	10	84.4	9.1	33.49	30.5	PC
Bismuth (III) Subsalicylate	Gastro-intestinal	N/A	10	73.2	26.2			(481)
Clomifene	Fertility treatment	Oestrogen agonist-antagonist	3.23	301.8	12.7	5.76	3.2	(468)
Folic acid	Vitamin B9	Cofactor for enzyme synthesis	51.5	79.1	8.5		343.7	Pc
Haloperidol	Antipsychotic	Antagonism of the dopamine receptor	100	111.9	10.3	265.8	210.7	Pc
Imipramine	Antidepressant	NPC1 inhibitor	11.4	212.0	8.3	85.3	16.0	(469)
Lomitapide	Homozygous familial hyper-cholesterolemia	Microsomal triglyceride transfer protein inhibitor	1	110.0	10.2	9.42	8.0	Pc
Melatonin	Insomnia	Tryptophan derivative - binds to melatonin receptor type-1A	100	110.2	27.2	958.2	506.9	(498), CT
Metformin HCl	Type 2 Diabetes	Unknown - Decrease of blood glucose level	100	102.3	19.8		875.2	(498), CT
Valproic Acid	Epilepsy, migraine, bipolar disorder	Unknown - Succinic semialdehyde dehydrogenases	100	141.9	16.9		950.1	Pc

		inhibitor, interferes with ERK pathway, non-competitive inhibitor of myo-inosital-1-phosphate synthetase											
Quercetin	Dietary supplement	Quinone reductase 2 inhibitor	100	140.6	12.7								(501)

Table 36: Experimental proposed DAAs used in the drug screening against SARS-CoV-2. Pc, personal communication/interest with proposed MOA; CT, in clinical trial.

Compound name	Used for	Mechanism of action	Drug (µM)	% infection vs. UT	SEM	CC_{50} (µM)	CC_{10} (µM)	Plaque: IC_{50} (µM)	Plaque: IC_{90} (µM)	FFU: IC_{50} (µM)	FFU: IC_{90} (µM)	SI1	SI2	Ref
IAL-MD0128	Antibiotic	Bacterial cell wall synthesis inhibitor	10	89.68%	68.10%	127	37.3							(561)
IAL-MD0131	Antibiotic	Bacterial cell wall synthesis inhibitor	50	91.05%	41.64%	346	252							(561)
PLTV	Antibiotic	Beta-lactamases inhibitor	100	88.54%	31.70%									(481)
TSF_217	Antibiotic	Beta-lactamases inhibitor	100	150.15%	55.95%									(481)
BI41	Antibiotic	Bacteria cell wall synthesis inhibitor	100	82.23%	30.36%									(481)
BI50	Antibiotic	Bacteria cell wall synthesis inhibitor	100	73.56%	27.60%									(481)
BI63	Antibiotic	Bacteria cell wall synthesis inhibitor	100	76.25%	27.81%									(481)
BI71-2	Antibiotic	Bacteria cell wall synthesis inhibitor	100	87.43%	32.92%									(481)
Sinefungin	Antibiotic	SAM-dependent methyltransferases inhibitor	500	73.18%	25.38%									(562)
VR17-04	Antiviral	RNA polymerase inhibitor	10	102.84%	44.22%		50.6							
Antipain	Antipain	potential anti-trypanosomatid drug	100	28.67%	10.59%		71.7							(481)

MED-COV-4280ac29-15	Antiviral	Mpro inhibitor	1	103.07%	14.50%	16.8	3.51						(427)
SIM-SYN-f15aaa3a-1	Antiviral	Mpro inhibitor	1	81.40%	26.20%	40.2	20.5						(427)
MAT-POS-916a2c5a-1	Antiviral	Mpro inhibitor	1	93.43%	16.63%	42.9	21.7						(427)
MAT-POS-916a2c5a-2	Antiviral	Mpro inhibitor	1	54.98%	17.78%			52.9	90.7	>0.02	>0.01		(427)
LON-WEI-8f408cad-3	Antiviral	Mpro inhibitor	1	115.31%	36.00%	19.9	2.96						(427)
LON-WEI-adc59df6-47	Antiviral	Mpro inhibitor	1	115.45%	17.61%	38.5	21.3						(427)
MED-COV-4280ac29-31	Antiviral	Mpro inhibitor	1	116.58%	24.94%	7.1	0.414						(427)
LON-WEI-ff7b210a-4	Antiviral	Mpro inhibitor	10	101.25%	13.53%	89	73.3						(427)
LOR-NEU-c8f11034-5	Antiviral	Mpro inhibitor	100	39.47%	11.91%			15.2	46.5	>6.58	>2.15		(427)
LON-WEI-babf2c61-1	Antiviral	Mpro inhibitor	10	111.63%	10.21%								(427)
LOR-NEU-c8f11034-2	Antiviral	Mpro inhibitor	10	110.25%	12.03%		74.5						(427)
TRY-UNI-2eddb1ff-7	Antiviral	Mpro inhibitor	10	99.58%	11.19%		61.8						(427)
ALP-POS-c59291d4-5	Antiviral	Mpro inhibitor	100	79.65%	17.01%								(427)
ALP-POS-c59291d4-6	Antiviral	Mpro inhibitor	100	137.50%	17.46%		0.0161						(427)
ALP-POS-d2866bdf-1	Antiviral	Mpro inhibitor	100	31.77%	10.92%			15.3	26.8	>6.54	>3.73		(427)
JOR-UNI-2fc98d0b-12	Antiviral	Mpro inhibitor	100	31.37%	13.53%	21.4	12.3	14.9		1.44			(427)
LOR-NOR-30067bb9-7	Antiviral	Mpro inhibitor	10	65.22%	1.71%		71.2						(427)
DAN-LON-a5fc619e-8	Antiviral	Mpro inhibitor	10	106.22%	7.18%	77.7	64						(427)
DAN-LON-a5fc619e-3	Antiviral	Mpro inhibitor	10	100.45%	6.31%	79.2	65.5						(427)
LON-WEI-babf2c61-9	Antiviral	Mpro inhibitor	10	86.62%	5.50%	77.3	60.9						(427)
MED-COV-4280ac29-30	Antiviral	Mpro inhibitor	10	96.57%	8.73%	87.1	76.6						(427)
JAN-GHE-5a013bed-2	Antiviral	Mpro inhibitor	10	113.17%	5.78%	104	73.6						(427)

EDJ-MED-6af13d92-3	Antiviral	Mpro inhibitor	100	9.39%	4.63%				15.3	45.4	>6.54	>2.20	(427)
ADA-UCB-6c2cb422-1	Antiviral	Mpro inhibitor	10	107.82%	6.88%		59						(427)
EDJ-MED-6af13d92-1	Antiviral	Mpro inhibitor	10	86.77%	6.65%								(427)
JAG-UCB-a3ef7265-20	Antiviral	Mpro inhibitor	100	87.97%	9.77%								(427)
TAT-ENA-80bfd3e5-1 MAT-POS-e10a589d-2	Antiviral	Mpro inhibitor	100	86.92%	18.62%								(427)
MAT-POS-e10a589d-1	Antiviral	Mpro inhibitor	1	90.95%	6.69%	8.97							(427)
PAU-UNI-8cdd41c7-1	Antiviral	Mpro inhibitor	10	90.83%	6.85%	32.2	30.9						(427)
LON-WEI-2e27a2e5-1	Antiviral	Mpro inhibitor	10	69.87%	6.35%	81.7	58.5						(427)
TRY-UNI-714a760b-3	Antiviral	Mpro inhibitor	10	119.33%	10.39%								(427)
AGN-NEW-891393a6-1	Antiviral	Mpro inhibitor	10	91.88%	4.58%								(427)
ALP-POS-c59291d4-2	Antiviral	Mpro inhibitor	100	11.13%	5.78%		49.6		31.5	32.7	>3.17	1.52	(427)
ALP-POS-91609ae9-3	Antiviral	Mpro inhibitor	10	98.68%	7.62%	86.1	20						(427)
DAV-CRI-14a23e73-1	Antiviral	Mpro inhibitor	10	94.88%	3.85%	81.8	71.5						(427)
BEN-DND-93268d01-8	Antiviral	Mpro inhibitor	10	67.38%	10.57%								(427)
ALP-POS-3b848b35-2	Antiviral	Mpro inhibitor	10	130.73%	42.39%				9.89E-03	8.86E-03	>1011.12	>1128.67	(427)
VLA-UCB-1dbca3b4-15	Antiviral	Mpro inhibitor	10	116.61%	39.98%								(427)
EDJ-MED-c314995a-1	Antiviral	Mpro inhibitor	10	124.67%	11.11%	12.9	9.52						(427)
MAT-POS-11b63608-1	Antiviral	Mpro inhibitor	10	139.67%	22.89%	26	17.6						(427)
MAT-POS-9ff17035-3	Antiviral	Mpro inhibitor	1	115.83%	7.31%	2.08	1.2						(427)
MAT-POS-bbbbc21a-3	Antiviral	Mpro inhibitor	100	71.83%	9.21%								(427)

MAT-POS-f2460aef-3	Antiviral	Mpro inhibitor	10	169.50%	27.12%	79.3	59.2						(427)
MAT-POS-f2460aef-4	Antiviral	Mpro inhibitor	1	139.50%	11.43%	9.79	7.85						(427)
MAT-POS-f7918075-2	Antiviral	Mpro inhibitor	1	135.00%	14.78%		1.11						(427)
MAT-POS-fa06b69f-6	Antiviral	Mpro inhibitor	100	101.72%	22.90%		70.4						(427)
PET-UNK-1901c25b-1	Antiviral	Mpro inhibitor	1	131.67%	10.09%	24.5	8.22						(427)
EDJ-MED-00c1612e-1	Antiviral	Mpro inhibitor	1	164.67%	16.37%	4.9	1.12						(427)
MAT-POS-b3e365b9-1	Antiviral	Mpro inhibitor	100	0.70%	2.47%					1.99			(427)
MAT-POS-f2460aef-1	Antiviral	Mpro inhibitor	10	9.68%	4.12%	14.5	12.5			2.89	5.02		(427)
ALP-POS-c59291d4-1	Antiviral	Mpro inhibitor	100	228.00%	24.31%								(427)
MAT-POS-3b92565d-1	Antiviral	Mpro inhibitor	10	99.77%	5.99%	13.7	10.5						(427)
ERI-UCB-ce40166b-17	Antiviral	Mpro inhibitor	100	88.40%	14.59%		80.6						(427)

Table 37: Experimental proposed HTAs used in the drug screening against SARS-CoV-2. Screened for: Pc, personal communication/interest; CT, in clinical trial

Compound name	Used for	Mechanism of action	Drug (µM)	% infection vs. UT	SEM	CC_{50} (µM)	CC_{10} (µM)	Plaque: IC_{50} (µM)	Plaque: IC_{90} (µM)	FFU: IC_{50} (µM)	FFU: IC_{90} (µM)	SI1	SI2	Ref
BAY-11 7082	Anti-inflammatory	Kinase inhibitor	1	99.40%	42.60 %	9.59	2.48							Pc
SDZ-224-015	Anti-inflammatory	Interleukin-1β inhibitor	0.1	110.90%	27.87 %	1.97	0.058							Pc
TLCK N-alpha-Tosyl-L-lysine chloromethyl ketone hydrochloride	Cancer	NFκB activation inhibitor	100	112.55%	23.94 %									(481)
TPCK N-p-Tosyl-L-phenylalanine	Antiviral	NFκB activation inhibitor	1	64.09%	30.96 %	17.4	3.72							(481)

chloromethyl ketone														
4EGI-1	Cancer	eIF4E/eIF4H interaction inhibitor	1	140.97%	36.64 %	19.3	8.27							(566)
BIIB021	Cancer	HSP90 inhibitor	0.01	126.73%	47.56 %	0.348	0.009 67							(567)
BOLD100	Cancer	GRP78 inhibition	10	83.23%	17.37 %	246	107							Pc
Carmofur	Cancer	Acid ceramidase inhibitor	0.1	104.52%	54.56 %	67.8	7.3							(569)
IPA3	Cancer	Pak1 inhibitor	100	76.03%	67.81 %									(481)
NSC95397	Cancer	MKP-1 inhibitor, CtBP-1 inhibitor	1	129.83%	32.27 %	8.67	2.42							(488)
PDD0001727 3	Cancer	Poly(ADP-ribose) glycohydrolase inhibitor	5	134.13%	15.93 %									(561)
PT2385	Cancer	hypoxia-inducible factor-2α (HIF-2α)	200	79.13%	20.86 %									(571)
Tarloxotinib	Cancer	Pan-HER tyrosine kinase inhibitor	100	81.87%	23.74 %		1.14			1.35		>74.0 7		Pc
Telaglenastat	Cancer	Glutaminase inhibitor	1	79.98%	27.69 %		3.67							Pc
Veliparib	Cancer	PARP inhibitor	5	93.60%	7.08%									(561)
2-Deoxyglucose	Cancer, Antiviral	Glycolysis inhibitor	100	88.82%	50.63 %	359	109							Pc
CBE Conduritol-B-epoxide	For studying: Gaucher diseases, Parkinson's disease	GBA 1inhibitor	200	128.37%	43.20 %									Pc
(D)-PDMP	Anti-inflammatory	Glucosylceramide inhibitor	10	50.57%	27.42 %									Pc
Lucerastat	Gaucher disease	Glucosylceramide inhibitor	2000	1.37%	0.55%			316	1180			>6.33	>1.67	(452)
MON-DGJ	Glycolipid inhibitor		250	258.38%	29.47 %	380	2.69							Pc
M*O*N-DNJ	Antiviral	ER glycosidases inhibitor	100	26.39%	6.67%					12.2	71.9			(200,2 03, 254,27 2)

***N*AP-DNJ**	Antiviral	ER glycosidases inhibitor	100	3.51%	1.72%	132	97		9.92	143	13.31	0.68	Pc
***N*N-DGJ**	Glycolipid inhibitor		500	2.95%	1.40%				158	215	>3.16	>2.33	(261)
***N*N-DNJ**	Antiviral	ER glycosidases inhibitor	500	2.80%	0.40%						>108.00	>8.32	(261,497)
Dimethyl amiloride	Hypertension	Sodium channel blocker	10	63.83%	16.60 %	92.8	30.9						(578)
HMA Hexamethylene Amiloride	Hypertension	Sodium reabsorption inhibition	1	130.83%	33.08 %	8.09	5.86						(579)
Alvelestat	Pulmonary Disease	Neutrophil elastase inhibitor	1	107.28%	15.27 %		8.43						(580)
Avasimibe	Antihyperlipidemic	Acyl-Coenzyme A: cholesterol acyltransferase inhibitor	1	79.67%	18.85 %	9.15	1.04						(581)
Ox14	Bone loss	FFPS inhibitor	1	93.60%	7.08%	16	9.79						(582)
Roxadustat	Anaemia	HIF-PH inhibitor	100	91.45%	20.16 %								Pc
SR9009	Circadian clock	REV-ERB agonist	1	122.60%	32.62 %		6.61						Pc
Teneligliptin	Type 2 Diabetes	Dipeptidyl Peptidase 4 inhibitor	47.7	130.78%	26.75 %	467	458						Pc
U18666a	Niemen-Pick type C disease	NPC1 inhibitor	0.202	134.65%	33.84 %	7.28	0.322						(473)

Appendix III

Table 38: List of gRNAs used to create hiPSCs knockouts.

gRNA pair	Name	Sequence 5' – 3'
11	ATF6_20	CTCTTCAGCGGAGCCACTGA
	ATF6_21	TTTGTTGTGAGTGATTACCG
12	ATF6_22	GAATAAGAGTCCACTGACCG
	ATF6_23	GGAGGAAAGGTTTTACCCAC
13	XBP1_24	CCAAGCGCTGTCTTAACTCC
	XBP1_26	TTGGAACCAGTACTCACATG
14	XBP1_25	ACTCCTGGTTCTCAACTACA
	XBP1_27	AATCGCTGGGTCATGTCACT
15	ERN1_28	CTTGTTGTTTGTGTCAACGC
	ERN1_29	GGACGTTTATAGCTTTGCTG
16	MOGS_30	TATGGCTGGGAGTTCCACGA
	MOGS_31	CCCCTGCTCTTTGACTTACG
17	MOGS_32	GCGGAAGTCACCAAGTTCAC
	MOGS_33	AAAGTGTTCAGGAGTCAGGT
18	MOGS_34	CACTGCCACTATCTTACCGC
	MOGS_35	CCAGTGCCACCCAACATCGC
19	GANAB_36	ACATCTGGTACACGGTATCG
	GANAB_37	ATTAGGCTGGGACAAGATGT
20	GANAB_38	AAAGACTTCGGTCCTCTAGT
	GANAB_39	GTGTTGTGAGGTCTGGCACG
NP5	ERN1_8 (T3)	TTCAGGAAGCGTCACTGTGC
	ERN1_11 (T6)	GCAAATGTCCATGTCGCCCA

Table 39: List of primers for sequencing CRISPR-Cas9 knockouts, or primer to detect DNA between CRISPR cut sites.

	Name	Sequence 5' – 3'
Sequencing primer	61 ATF6-11 forward	TTCTAGTTCTCAGATGTCTCCCCT
	62 ATF6-11 reverse	TGAAGATGGTGGGGTCTGAGT
	63 ATF6-12 forward	TTCTGCATCTTTCATTTTCACTCGT
	64 ATF6-12 reverse	TGTAAAAGACTGGCTACTCACAGG
	65 XBP1-13/14 forward	TCCAGAACCAAAAACTTTTGCTAGA
	66 XBP1-13/14 reverse	ACGCTCTTGATCAGAAGTCCA
	67 ERN1-15 forward	AAGTACCAGCACAGTGACGC
	68 ERN1-15 reverse	ACATGAAGTCTAAACAGAAGCAAAA
	69 MOGS-16 forward	GGAAGGAATGGATCAGGAGAGTT
	70 MOGS-16 reverse	CCCAGGCCTCTTGACGAAC
	71 MOGS-17 forward	CCAAGGGGCAGTTGAAGTTTAT
	72 MOGS-17 reverse	GAAGGCAGTGGGCATTATAAAGAG
	73 MOGS-18 forward	CCTGGTTTTCCTGGCTCCAT
	74 MOGS-18 reverse	CTACCTCAGCCTCACCCAGA
	75 GANAB-19 forward	GGAAAGGGGGAAATTGTGGC
	76 GANAB-19 reverse	TTTGGGAAAGAATATCAGCAACC
	77 GANAB-20 forward	ATCTTGACAGCACGGCCATT
	78 GANAB-20 reverse	GACAGAGAGCTTCTCCCAGC
Internal primer	92_ATF6-11_Internal_forward	GATAAGCCTGTCACTGGTCC
	93_ATF6-11_Internal_reverse	AAACAGCAAGCCAGCCTAAT
	96_XBP1-13_Internal_forward	AGGCGGAAGCCAAGGTAAATC
	97_XBP1-13_Internal_reverse	GTACTCACATGAGGCACCAAA
	100_ERN1-15_Internal_forward	CAGCAAGAGGACAGGCTCAA
	101_ERN1-15_Internal_reverse	GCCTTTTCCTCTCTTGATCCCA
	104_MOGS-16_Internal_forward	CATTCTACCCCCAGGACTGATG
	105_MOGS-16_Internal_reverse	GCCTGAGCTTAGGAGTCCCC
	108_GANAB-20_Internal_forward	TGTCAATGCCCGAGGACTCT
	109_GANAB-20_Internal_reverse	ACCCCTGTACTCACGAGACC
	120_EIF2AK3-NP10_Internal_forward	AGACATCCTGCTTCTACAGCGT
	121_EIF2AK3-NP10_Internal_reverse	CGAGGTCCGACAGCTCTAACA

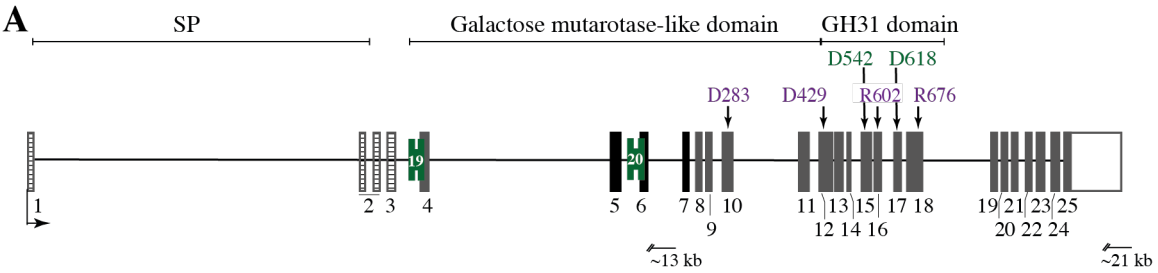

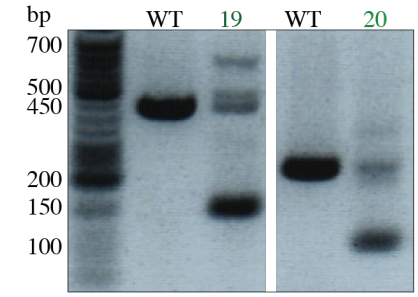

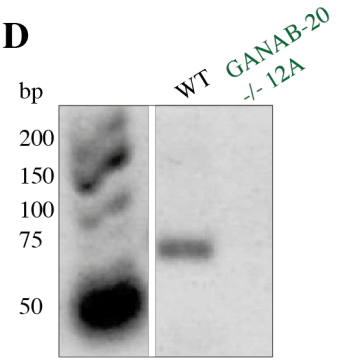

C

WT
5' CTTGACCTACTAGAGGACCGAAGTCTTT … 112 bp … GTGTTGTGAGGTCTGGCACGGGGAGGAG 3'
3' TTTCTGAAGCCAGGAGATCATCCAGTTC … 112 bp … CACAACACTCCAGACCGTGCCCCTCCTC 5'
GANAB-20 -/- clone 12A; Δ145 bp
5' CTTGACCTACT---------- … 112 bp … ----------CACGGGGAGGAG 3'
3' TTTCTGAAGCC---------- … 112 bp … ----------GTGCCCCTCCTC 5'

Figure 59: Genomic structure of *GANAB* and CRISPR-Cas9 targeting. (A) Human *GANAB* genomic structures, containing 25 exons, of which are some alternatively spliced (grey) and non-coding region (grid). Functional domains are highlighted and known patient mutations are shown in green and purple. (B) Transfected iPSCs with specific gRNA pair, cells were expanded and for ~4 days before half of the cells were lysed and analysed via PCR for potential knockout cells. (C) Mixed cell populations of knockout and wild-type cells were plated on mouse embryonic fibroblast feeder cells. After ~7 days expansion, individual single cell colonies were picked into 96-well plate in feeder-free conditions and clones were expanded. Single hiPSCs clones were screened for insertions, deletions and potential cross-contamination with a second clone by PCR with primers targeting the knockout area and (D) sequencing was performed to identify exact knockout. SP, signal peptide; GH3, glycosyl-hydrolase domain of Glycoside hydrolyse family 31.

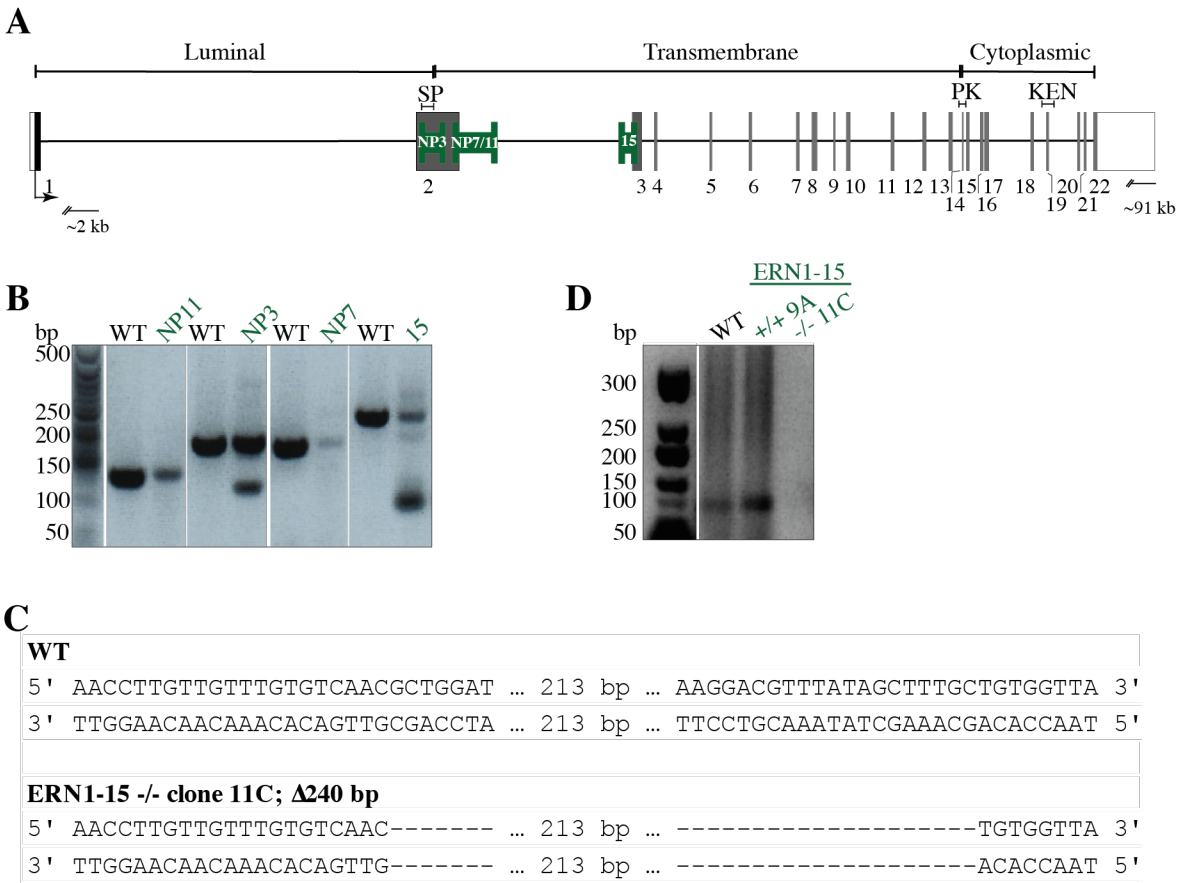

C

WT

```
5' AACCTTGTTGTTTGTGTCAACGCTGGAT … 213 bp … AAGGACGTTTATAGCTTTGCTGTGGTTA 3'
3' TTGGAACAACAAACACAGTTGCGACCTA … 213 bp … TTCCTGCAAATATCGAAACGACACCAAT 5'
```

ERN1-15 -/- clone 11C; Δ240 bp

```
5' AACCTTGTTGTTTGTGTCAAC------- … 213 bp … --------------------TGTGGTTA 3'
3' TTGGAACAACAAACACAGTTG------- … 213 bp … --------------------ACACCAAT 5'
```

Figure 60: Genomic structure of *ERN1* and CRISPR-Cas9 targeting. (A) Human *ERN1* genomic structures, containing 22 exons, of which are some alternatively spliced (grey) and non-coding region (grid), therefore not targeted for this approach. (B) Transfected hiPSCs with specific gRNA pair, cells were expanded and for ~4 days before half of the cells were lysed and analysed via PCR for potential knockout cells. (C) Mixed cell populations of knockout and wild-type cells were plated on mouse embryonic fibroblast feeder cells. After ~7 days expansion, individual single cell colonies were picked into 96-well plate in feeder-free conditions and clones were expanded. Single hiPSCs clones were screened for insertions, deletions and potential cross-contamination with a second clone by PCR with primers targeting the knockout area and (D) sequencing was performed to identify exact knockout. SP, signal peptide; PK, protein kinase domain; KEN, kinase-extension nuclease domain.

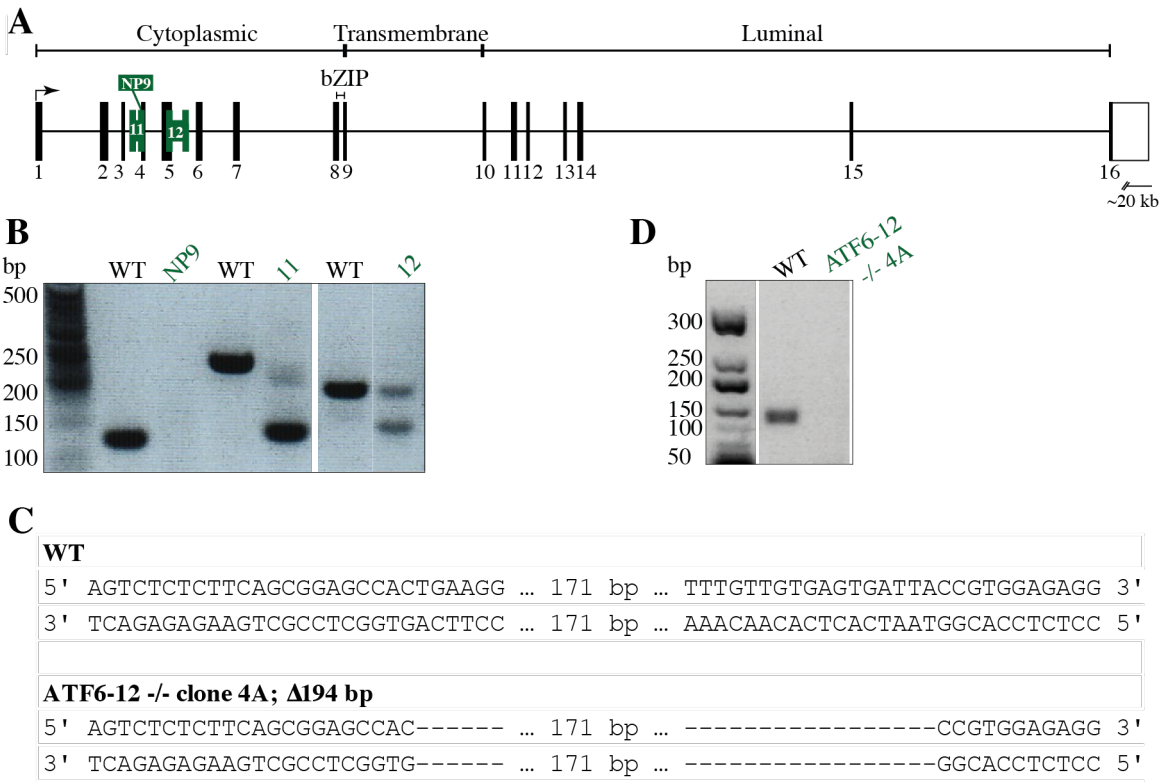

Figure 61: Genomic structure of *ATF6* and CRISPR-Cas9 targeting. (A) Human *ATF6* genomic structures, containing 16 exons, of which are some alternatively spliced (grey) and non-coding region (grid). (B) Transfected iPSCs with specific gRNA pair, cells were expanded and for ~4 days before half of the cells were lysed and analysed via PCR for potential knockout cells. (C) Mixed cell populations of knockout and wild-type cells were plated on mouse embryonic fibroblast feeder cells. After ~7 days expansion, individual single cell colonies were picked into 96-well plate in feeder-free conditions and clones were expanded. Single hiPSCs clones were screened for insertions, deletions and potential cross-contamination with a second clone by PCR with primers targeting the knockout area and (D) sequencing was performed to identify exact knockout. bZIP, basic leucine zipper domain.

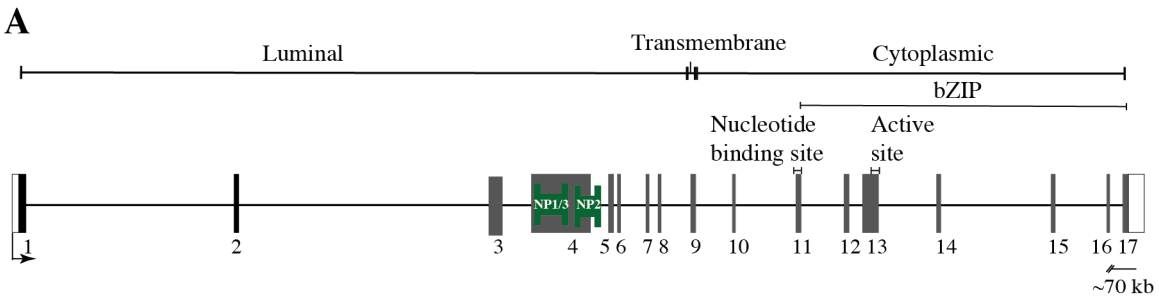

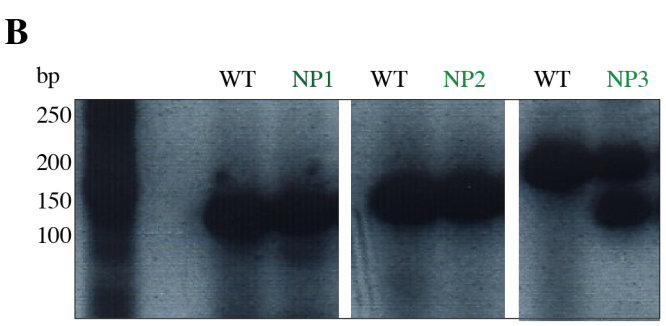

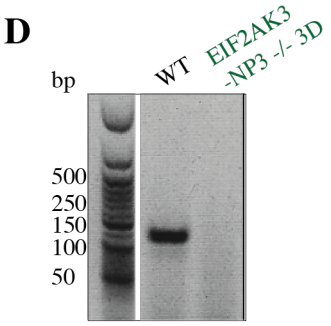

C

WT

```
5' GTCGCCAATGGGATAGTGACGAAATGGA … 46 bp … AGAGCTGTCGGACCTCGCAGTGGCAATG 3'
3' CAGCGGTTACCCTATCACTGCTTTACCT … 46 bp … TCTCGACAGCCTGGAGCGTCACCGTTAC 5'
```

EIF2AK3-NP3 -/- clone 3D; Δ81 bp

```
5' GTCGCCAATG------------------- … 46 bp … ----------------CAGTGGCAATG 3'
3' CAGCGGTTAC------------------- … 46 bp … ----------------GTCACCGTTAC 5'
```

Figure 62: Genomic structure of *EIF2AK3* and CRISPR-Cas9 targeting. (A) Human *EIF2AK3* genomic structures, containing 17 exons, of which are some alternatively spliced (grey) and non-coding region (grid). (B) Transfected iPSCs with specific gRNA pair, cells were expanded and for ~4 days before half of the cells were lysed and analysed via PCR for potential knockout cells. (C) Mixed cell populations of knockout and wild-type cells were plated on mouse embryonic fibroblast feeder cells. After ~7 days expansion, individual single cell colonies were picked into 96-well plate in feeder-free conditions and clones were expanded. Single hiPSCs clones were screened for insertions, deletions and potential cross-contamination with a second clone by PCR with primers targeting the knockout area and (D) sequencing was performed to identify exact knockout. bZIP, basic leucine zipper domain.

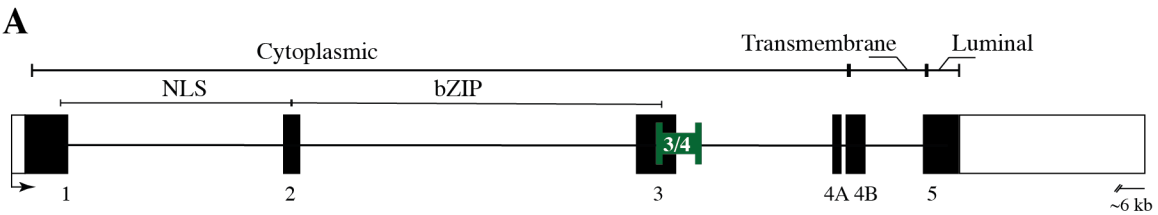

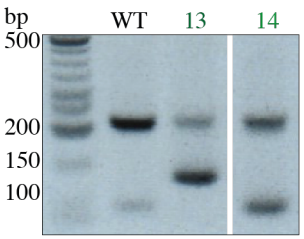

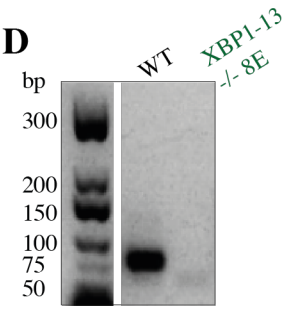

C

WT	
5' AACCAGGAGTTAAGACAGCGCTTGGGGA … 62 bp … CCTCATGTGAGTACTGGTTCCAAGTGAC 3'	
3' TTGGTCCTCAATTCTGTCGCGAACCCCT … 62 bp … GGAGTACACTCATGACCAAGGTTCACTG 5'	
XBP1-13 -/- clone 8E; Δ88 bp	
5' AACCAGGAGT---------- … 62 bp … --------GAGTACTGGTTCCAAGTGAC 3'	
3' TTGGTCCTC---------- … 62 bp … --------CTCATGACCAAGGTTCACTG 5'	

Figure 63: Genomic structure of *XBP1* and CRISPR-Cas9 targeting. (A) Human *XBP1* genomic structures, containing 5 exons, of which are some alternatively spliced (grey) and non-coding region (grid). (B) Transfected iPSCs with specific gRNA pair, cells were expanded and for ~4 days before half of the cells were lysed and analysed via PCR for potential knockout cells. (C) Mixed cell populations of knockout and wild-type cells were plated on mouse embryonic fibroblast feeder cells. After ~7 days expansion, individual single cell colonies were picked into 96-well plate in feeder-free conditions and clones were expanded. Single hiPSCs clones were screened for insertions, deletions and potential cross-contamination with a second clone by PCR with primers targeting the knockout area and (D) sequencing was performed to identify exact knockout. bZIP, basic leucine zipper domain; NLS, nuclear localisation signal.

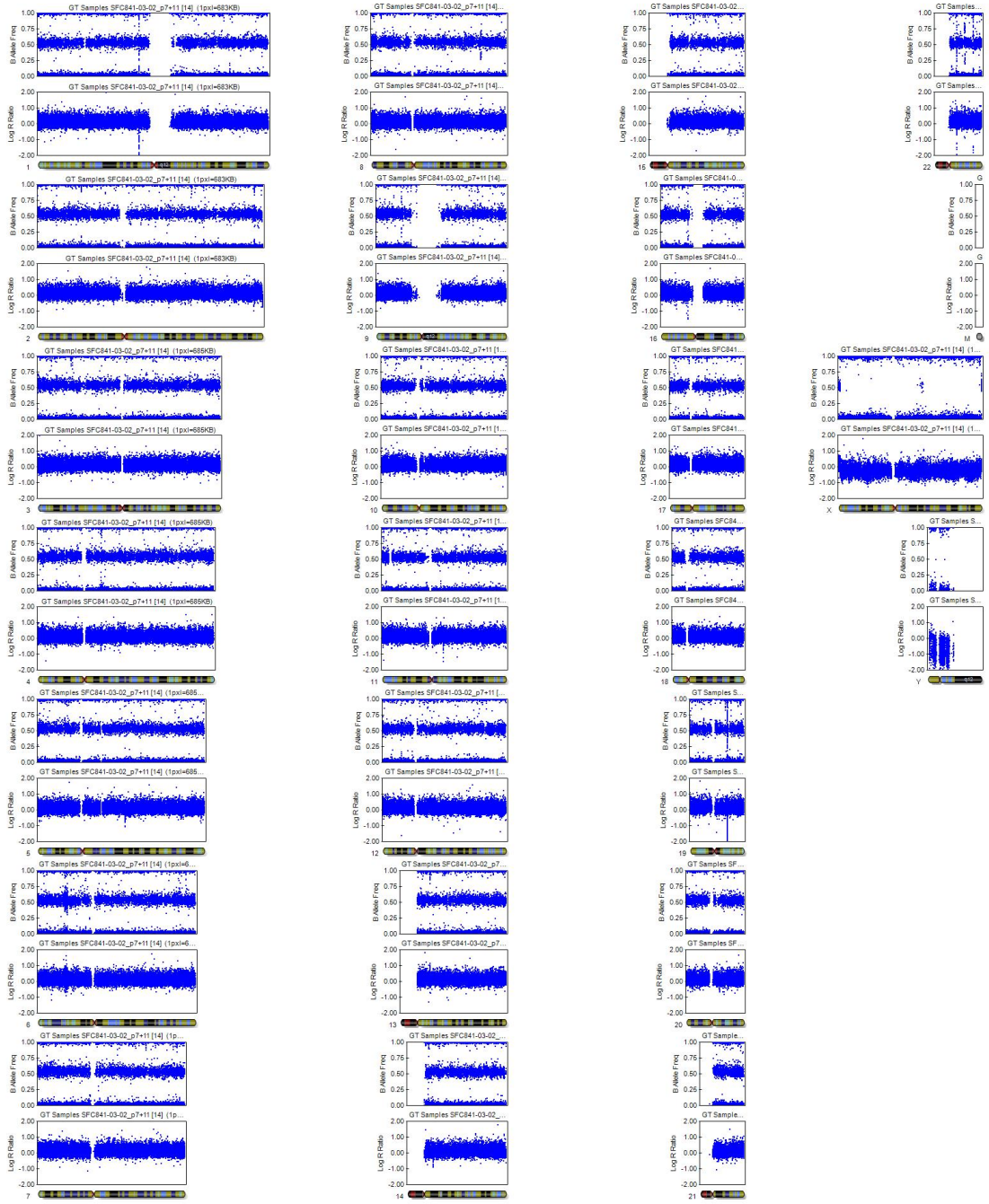

Figure 64: SNP analysis of parental SFC841-03-02 p7+11.

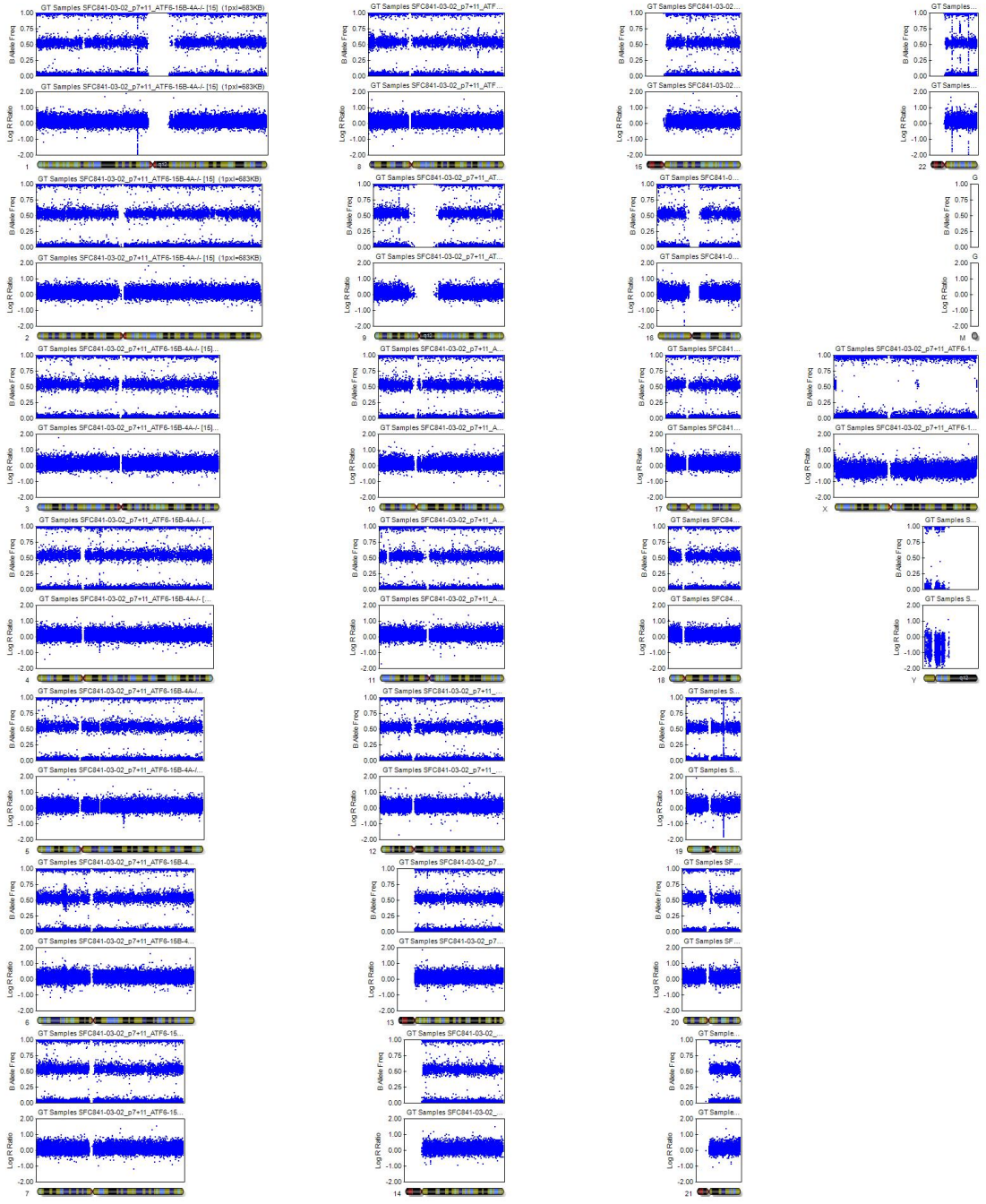

Figure 65: SNP analysis of SFC841-03-02 p7+11 ATF6-15B-4A$^{-/-}$.

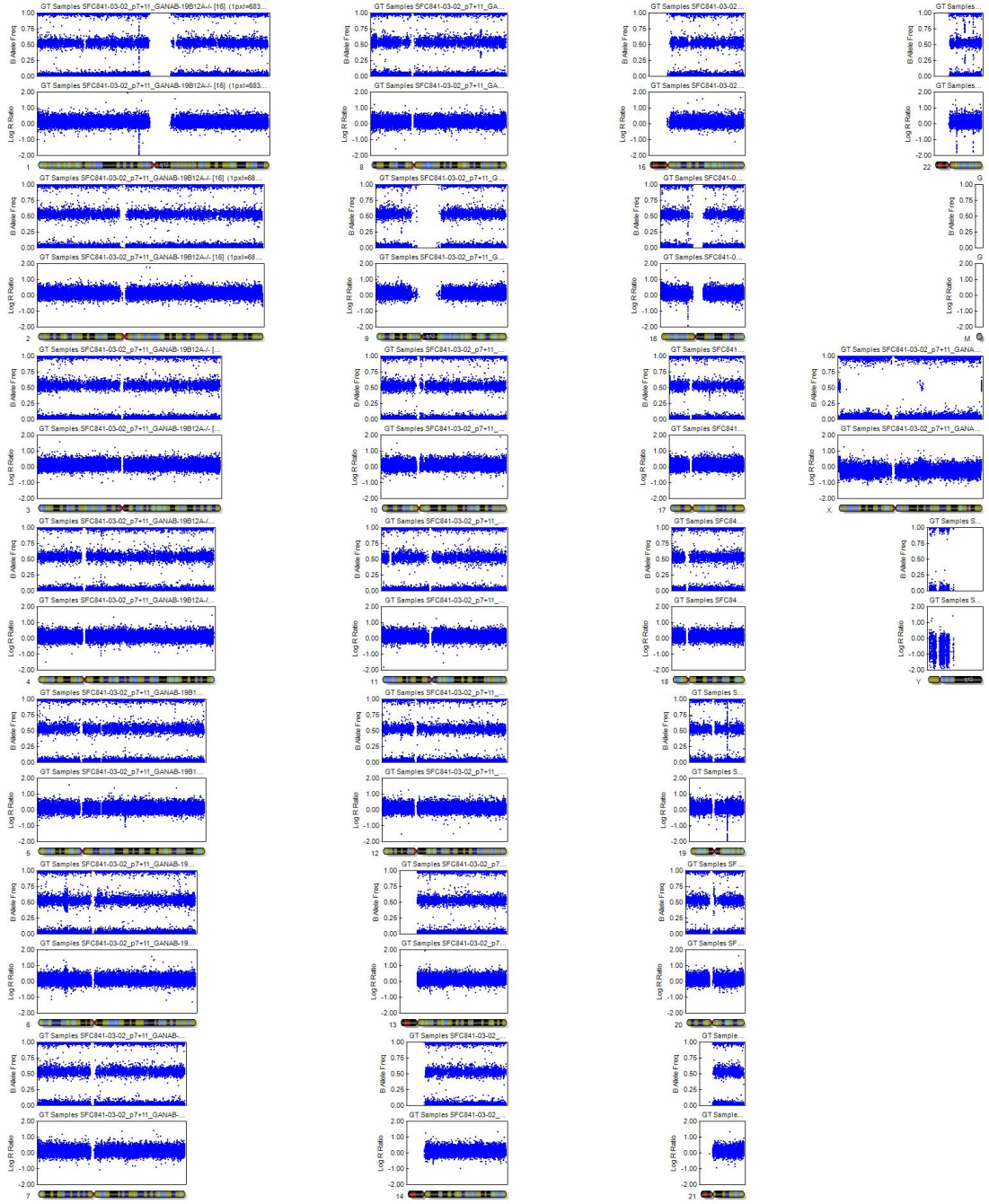

Figure 66: SNP analysis of SFC841-03-02 p7+11 GANAB-19B12A$^{-/-}$.

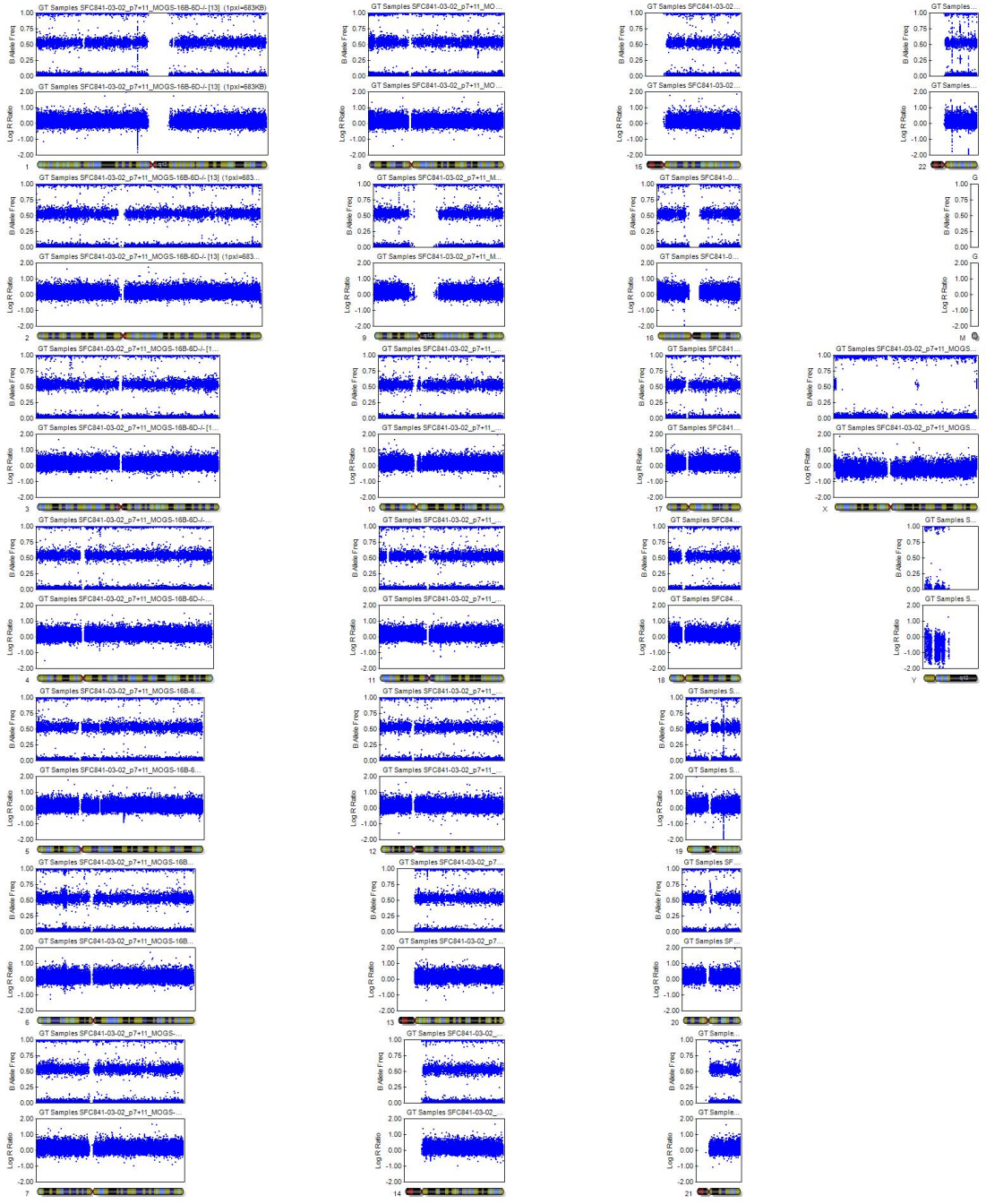

Figure 67: SNP analysis of SFC841-03-02 p7+11 MOGS-16B-6D $^{-/-}$.

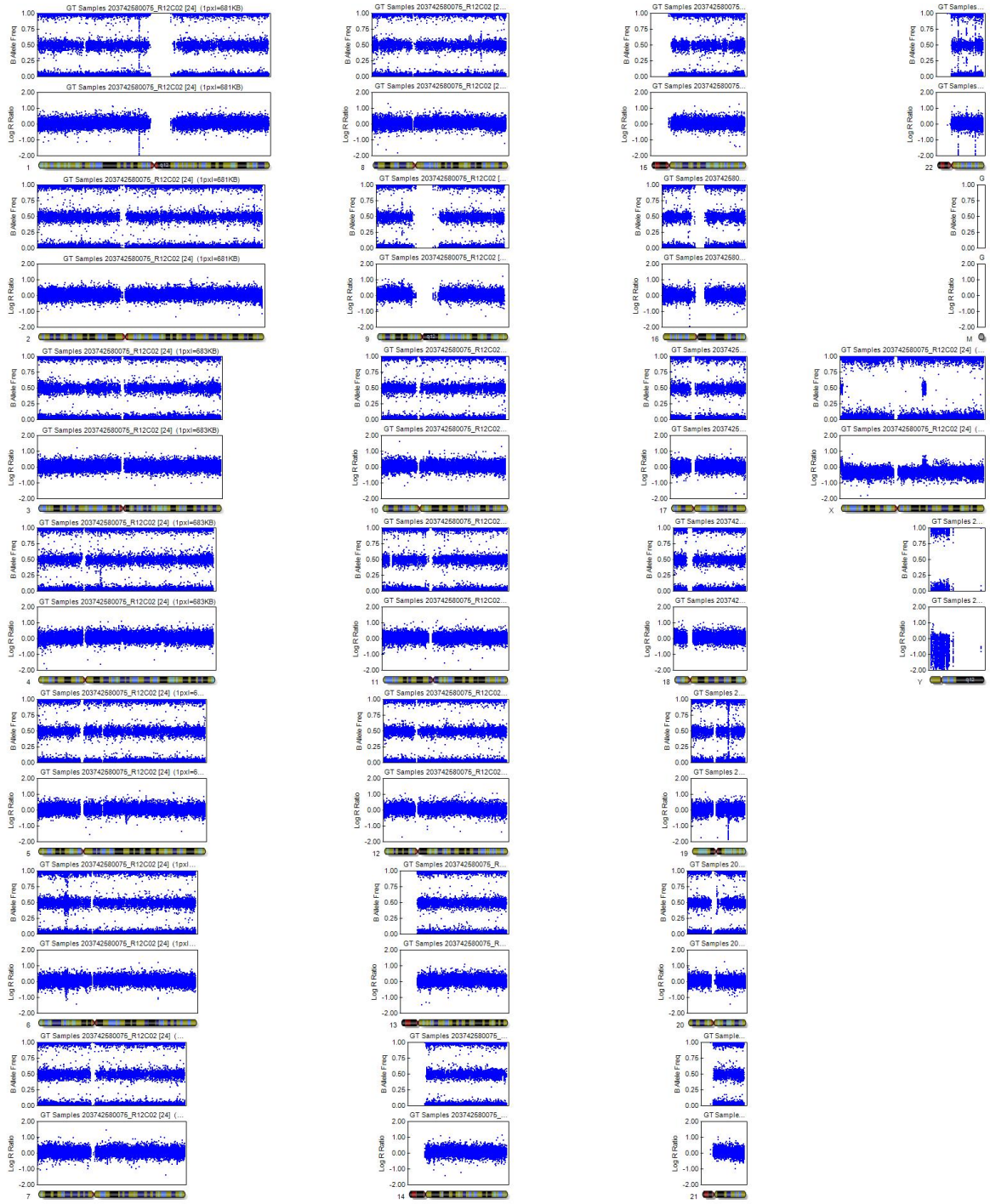

Figure 68: SNP analysis of SFC841-03-02_p7+11_ERN1-15B-11C$^{-/-}$.

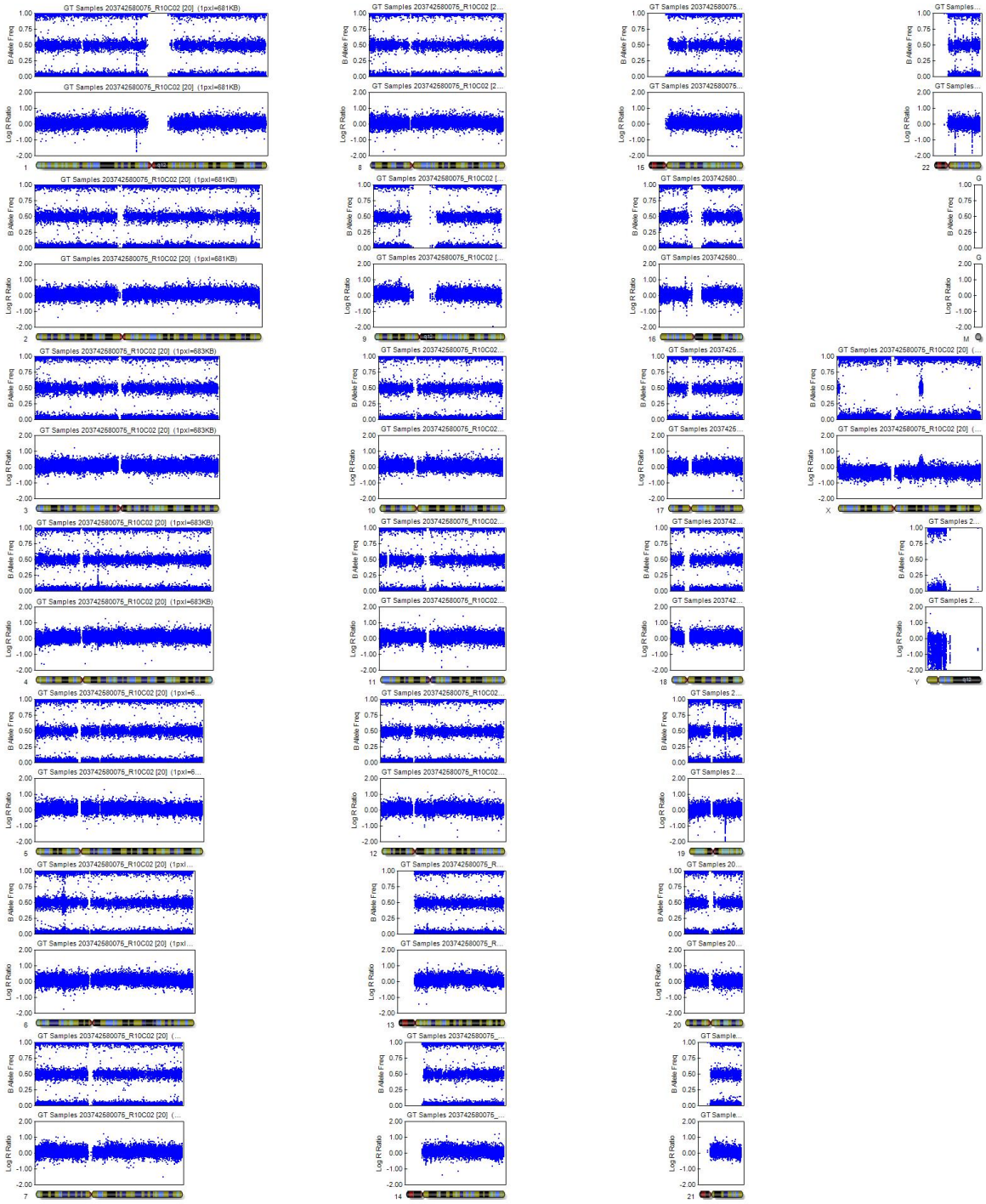

Figure 69: SNP analysis of SFC841-03-02_p7+11_EIF2AK3-NP-3D$^{-/-}$.

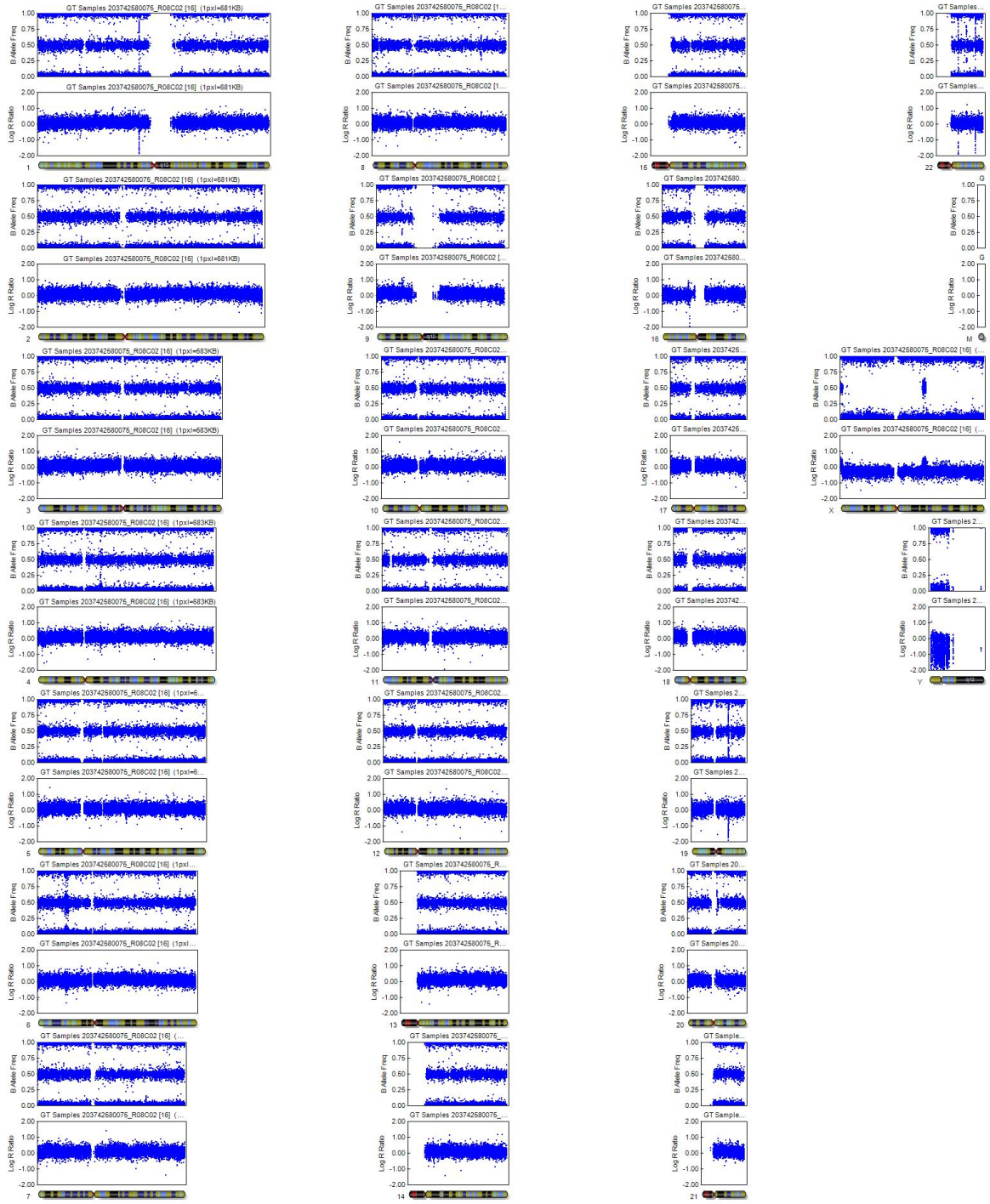

Figure 70: SNP analysis of SFC841-03-02_p7+11_XBP1-13B-8E$^{-/-}$.

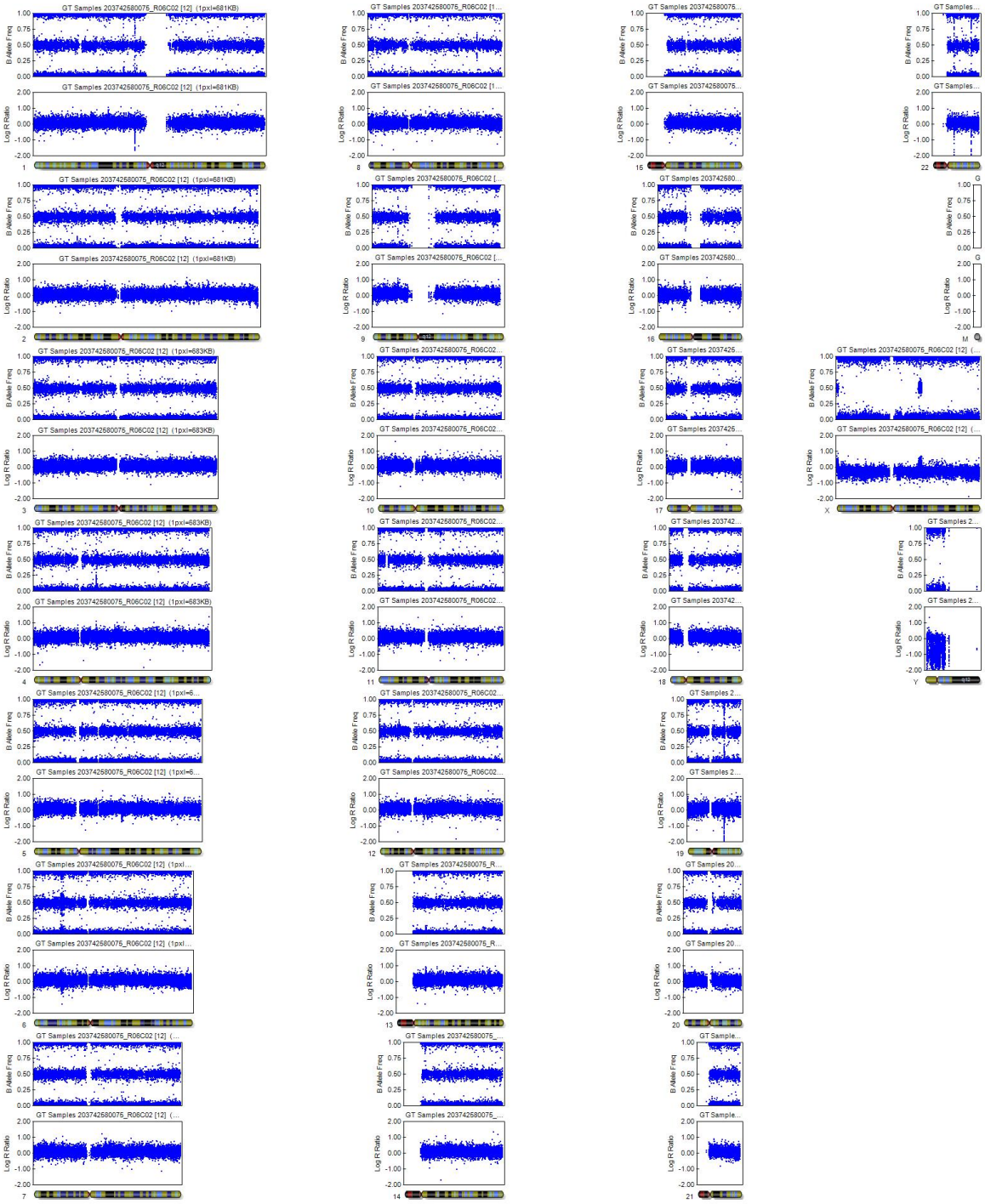

Figure 71: SNP analysis of SFC841-03-02_p7+11_ERNR1-15B-9A$^{+/+}$.

Appendix IV

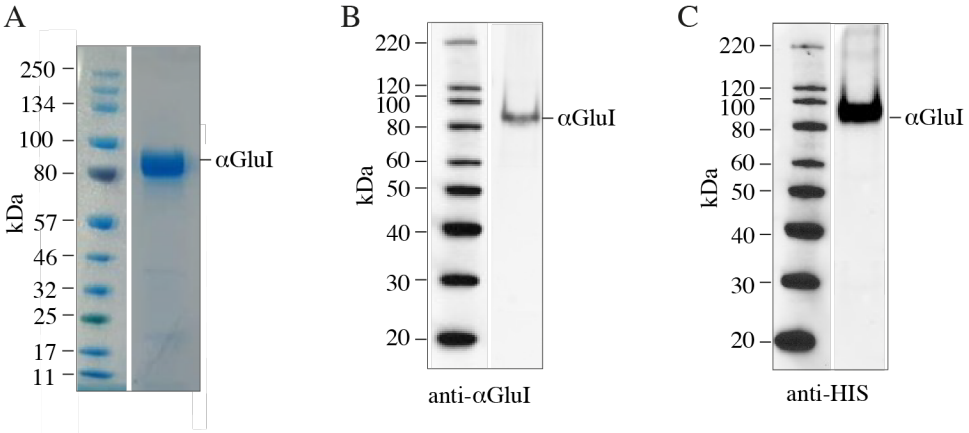

Figure 72: Confirmation of expression and purification of ER *Mm* αGluI. HEK293F cells transfected with secreted ER *Mm* αGluI-construct and harvested 4 days post transfection. Cells were spun down, and filtered supernatant applied to Nickel affinity column, followed by size exclusion chromatography. Concentrated protein was run on (A) SDS-PAGE, and western blot was performed and blotted against (B) anti-αGluI and (C) anti-HIS.

Table 40: FDA-approved drugs (Pharmakon1600, MicroSource Discovery System screened against soluble ER *Mm* αGluI. ΔT_m are shown for compounds screened at 10 µM and 50 µM.

Compound	10 µM	50 µM
*N*B-DNJ	3.64	4.21
CHLOROPHYLLIDE_Cu_COMPLEX_Na_SALT	-1.104	1.449
PROFLAVINE_HEMISULFATE	-8.311	1.398
SUCRALOSE	0.004	1.39
BUTOCONAZOLE	-0.415	1.373
CEFPIRAMIDE	-0.134	1.349
ZOMEPIRAC_SODIUM	-0.219	1.325
ROXARSONE	-0.062	1.322
DARIFENACIN_HYDROBROMIDE	-0.455	1.303
BENAZEPRIL_HYDROCHLORIDE	-0.627	1.277
NANOFIN	-0.216	1.263
DECAMETHONIUM_BROMIDE	0.052	1.256
MILNACIPRAN_HYDROCHLORIDE	0.038	1.234
PHENFORMIN_HYDROCHLORIDE	0.019	1.23
DYDROGESTERONE	-0.238	1.224
NITARSONE	-0.275	1.186
ENTACAPONE	-0.21	1.181
CEFTIOFUR_HYDROCHLORIDE	-0.32	1.167
MANIDIPINE_HYDROCHLORIDE	-0.248	1.158
ARSENIC_TRIOXIDE	-0.336	1.157
PHENAZOPYRIDINE_HYDROCHLORIDE	-0.161	1.146
FOMEPIZOLE	-0.358	1.144

RUTIN	-0.942	1.135
MECHLORETHAMINE	-0.282	1.13
IDOXURIDINE	0.184	1.125
CLINAFOXACIN_HYDROCHLORIDE	-0.477	1.124
ERGOTAMINE_TARTRATE	-0.267	1.092
PROPYLTHIOURACIL	-0.208	1.089
CEFUROXIME_SODIUM	-0.177	1.079
BETAXALOL_HYDROCHLORIDE	-0.126	1.075
OLSALAZINE_SODIUM	0.218	1.059
CYCLOHEXIMIDE	0.034	1.054
TRANDOLAPRIL	-0.105	1.044
THIABENDAZOLE	-0.071	1.039
MALATHION	-0.306	1.032
SUCRALFATE	-0.255	1.031
EPHEDRINE_(1R_2S)_HYDROCHLORIDE	-0.309	1.031
DIRITHROMYCIN	0.183	1.027
ALBUTEROL	-0.22	1.022
PUROMYCIN_DIHYDROCHLORIDE	-0.549	1.018
METHYLATROPINE_NITRATE	-0.255	1.017
SELEGILINE_HYDROCHLORIDE	-0.326	1.015
ACETANILIDE	-0.233	1.014
FEBUXOSTAT	-0.69	1.01
TIGECYCLINE	-0.422	1.007
ESOMEPRAZOLE_POTASSIUM	0.295	1.003
POTASSIUM_p-AMINOBENZOATE	-0.015	1
RACEPHEDRINE_HYDROCHLORIDE	-0.121	1
ETHOPABATE	-0.037	0.994
˙TAVUDINE	-0.403	0.993
˙ERROUS_FUMARATE	-0.45	0.988
˩THOTOIN	-0.023	0.98
BENOXINATE_HYDROCHLORIDE	-0.353	0.974
CYACETACIDE	-0.266	0.96
MONTELUKAST_SODIUM	-0.361	0.959
DEHYDROACETIC_ACID	-0.398	0.959
TORSEMIDE	0.259	0.958
PANTHENOL_(dl)	0.251	0.958
PROSCILLARIDIN	-0.752	0.957
CHLOROACETOXYQUINOLINE	-0.063	0.955
NALIDIXIC_ACID	-0.378	0.954
TAPENTADOL_HYDROCHLORIDE	-0.419	0.951
CHLORMEZANONE	-0.272	0.948
PHENELZINE_SULFATE	-0.123	0.946
METOCLOPRAMIDE_HYDROCHLORIDE	0.156	0.944
ACTINOQUINOL_SODIUM	-0.209	0.932
ISOSORBIDE_MONONITRATE	-0.074	0.932
MYCOPHENOLATE_MOFETIL	-0.412	0.931
CETIRIZINE_HYDROCHLORIDE	-0.024	0.929
TROSPIUM_CHLORIDE	-0.267	0.928
CLOZAPINE	-0.705	0.926
TETRAMIZOLE_HYDROCHLORIDE	-0.299	0.922
OXIDOPAMINE_HYDROCHLORIDE	-0.149	0.921
PROMETHAZINE_HYDROCHLORIDE	-0.123	0.919
AMITRAZ	-0.29	0.916
MINAPRINE_HYDROCHLORIDE	-0.381	0.915
ERYTHROSINE_SODIUM	-6.396	0.913
MOLSIDOMINE	-0.645	0.911
IFOSFAMIDE	-0.09	0.909
PEMETREXED	-0.255	0.908
CICLOPIROX_OLAMINE	-0.172	0.906
TELMISARTAN	-0.988	0.906
THIOSTREPTON	-0.186	0.893
SUMATRIPTAN_SUCCINATE	-0.274	0.891
EDITOL	-0.269	0.888
ARSANILIC_ACID	-0.322	0.883

ISOXSUPRINE_HYDROCHLORIDE	0.547	0.882
PARAMETHADIONE	-0.177	0.881
MECAMYLAMINE_HYDROCHLORIDE	-0.481	0.881
ABAMECTIN_(avermectin_B1a_shown)	-0.452	0.879
RESORCINOL	0.198	0.879
ISOPROPAMIDE_IODIDE	0.608	0.876
TOREMIPHENE_CITRATE	0.13	0.873
PERMETHRIN	-0.339	0.873
ETHYL_PARABEN	-0.046	0.872
NATAMYCIN	-0.522	0.872
FIPRONIL	-0.175	0.872
SILDENAFIL_CITRATE	-0.406	0.87
ISOPROTERENOL_HYDROCHLORIDE	0.389	0.869
TADALAFIL	-0.462	0.866
CYPROTERONE_ACETATE	0.151	0.863
METHYLTHIOURACIL	0.118	0.863
SOTALOL_HYDROCHLORIDE	-0.243	0.863
PENBUTOLOL_SULFATE	-0.409	0.861
TRICHLORFON	-0.144	0.86
HYDROCORTISONE_ACETATE	0.153	0.859
CARBADOX	-0.514	0.856
METHACYCLINE_HYDROCHLORIDE	-0.127	0.852
SODIUM_PHENYLACETATE	-0.256	0.851
MILRINONE	-0.276	0.846
AMPYZINE_SULFATE	-0.2	0.842
DICLORALUREA	-0.456	0.836
PIPERAZINE	-0.199	0.834
BRINZOLAMIDE	-0.312	0.83
OSELTAMIVIR_PHOSPHATE	-0.297	0.829
CRYOFLURANE	-0.357	0.829
SULFAQUINOXALINE_SODIUM	-0.044	0.828
CALCIUM_GLUCEPTATE	-0.247	0.826
CEFORANIDE	-0.28	0.822
AZACITIDINE	-0.881	0.821
FENTHION	-0.34	0.815
ISONIAZID	0.26	0.815
ALMOTRIPTAN	-0.156	0.814
OXYCLOZANIDE	-1.047	0.814
ISOXICAM	-0.422	0.812
CEFPROZIL	-0.341	0.811
SALICYL_ALCOHOL	0.082	0.811
AZATADINE_MALEATE	-0.225	0.808
LEVAMISOLE_HYDROCHLORIDE	-0.267	0.807
ESTRAMUSTINE	-0.743	0.805
PIROXICAM	0.304	0.803
TROLEANDOMYCIN	-0.284	0.8
AMMONIUM_LACTATE	0.162	0.792
OXYQUINOLINE_SULFATE	-0.171	0.79
DOXAZOSIN_MESYLATE	0.052	0.79
FLUROTHYL	-0.194	0.789
PHENIRAMINE_MALEATE	-0.094	0.788
CLOSANTEL	-0.084	0.782
DIETHYLCARBAMAZINE_CITRATE	-0.062	0.782
PHENYTOIN_SODIUM	-0.293	0.776
CITALOPRAM_HYDROBROMIDE	-0.226	0.774
PYRETHRINS	-0.621	0.774
ESCITALOPRAM_OXALATE	-0.252	0.774
HOMATROPINE_METHYLBROMIDE	0.148	0.768
ZOXAZOLAMINE	0.309	0.767
OXIGLUTATIONE_DISODIUM_SALT	-0.378	0.766
DICHLORVOS	-0.777	0.763
CEFOPERAZONE	-0.533	0.759
TACRINE_HYDROCHLORIDE	0.219	0.759
NALOXONE_HYDROCHLORIDE	0.259	0.758

GENTIAN_VIOLET	-7.127	0.751
FLUTICASONE_PROPIONATE	-0.415	0.742
MICONAZOLE_NITRATE	-0.754	0.734
MENBUTONE	-0.96	0.733
IODOQUINOL	0.299	0.728
METHENAMINE	0.667	0.727
RONIDAZOLE	-0.152	0.727
FENOFIBRIC_ACID	-0.41	0.726
DOXYLAMINE_SUCCINATE	0.351	0.726
RIVASTIGMINE_TARTRATE	-0.156	0.715
POLYMYXIN_B_SULFATE	-0.243	0.714
QUINAPRILAT	-0.212	0.713
CHENODIOL	-0.368	0.712
1S_2R-PHENYLPROPANOLAMINE	-0.202	0.71
SULBACTAM	0.092	0.708
DIMESNA	-0.324	0.706
WARFARIN	0.023	0.702
SCOPOLAMINE_HYDROBROMIDE	-0.188	0.699
HEXYLENE_GLYCOL	-0.402	0.693
RAMIPRIL	-0.354	0.691
PROBENECID	-0.43	0.69
DROSPIRENONE	-0.4	0.689
ACEBUTOLOL_HYDROCHLORIDE	-0.146	0.689
BEPHENIUM_HYDROXYNAPTHOATE	-0.219	0.688
DEXTROAMPHETAMINE_SULFATE	0.202	0.685
OXYTETRACYCLINE	-0.144	0.683
FAMCICLOVIR	-0.66	0.682
¯RAMIPROSATE	0.01	0.68
ȷALBUPHINE_HYDROCHLORIDE	-0.333	0.678
ATOVAQUONE	-0.22	0.676
ZINC_UNDECYLENATE	-0.404	0.676
PYRAZINAMIDE	0.416	0.674
LEVCYCLOSERINE	-0.011	0.671
ANETHOLE	0.098	0.667
TRIMIPRAMINE_MALEATE	-0.507	0.665
CLOPIDOL	-0.139	0.664
METOPROLOL_TARTRATE	0.095	0.664
CINNARAZINE	-0.002	0.661
OXYMETAZOLINE_HYDROCHLORIDE	-0.253	0.66
PENTAGASTRIN	0.081	0.654
CANRENONE	-0.406	0.653
DILAZEP_DIHYDROCHLORIDE	-0.24	0.649
SULFAPYRIDINE	0.259	0.648
ESTRADIOL	0.312	0.642
TRETINOIN	-0.114	0.64
VORICONAZOLE	0.012	0.639
SITAGLIPTIN_MONOPHOSPHATE_MONOHYDRATE	-0.483	0.636
MECLOCYCLINE_SULFOSALICYLATE	-0.345	0.635
ONDANSETRON	0.201	0.635
ETHACRYNIC_ACID	-0.548	0.634
SULFANILATE_ZINC	-0.355	0.632
FLUNARIZINE_HYDROCHLORIDE	-0.066	0.63
SALICYLIC_ACID	-0.082	0.629
MEXILETINE_HYDROCHLORIDE	-0.217	0.627
BLEOMYCIN	-0.181	0.623
BENZOYL_PEROXIDE	0.1	0.619
OXIBENDAZOLE	-0.139	0.619
BEMOTRIZINOL	-0.382	0.618
TRILOSTANE	0.062	0.618
LORNOXICAM	0.15	0.618
AMCINONIDE	-0.181	0.617
PROCARBAZINE_HYDROCHLORIDE	-0.377	0.617
PRAZOSIN_HYDROCHLORIDE	-0.655	0.616
IOVERSOL	-0.123	0.615

LEUCOVORIN_CALCIUM	0.309	0.61
RABEPRAZOLE_SODIUM	0.082	0.609
CASANTHRANOL	0.678	0.607
DILOXANIDE_FUROATE	-1.012	0.606
ESZOPICLONE	-0.94	0.604
COLESEVALAM_HYDROCHLORIDE	-0.527	0.599
HALOTHANE	0.139	0.599
ANISINDIONE	0.202	0.596
IBUPROFEN	-0.002	0.592
RALOXIFENE_HYDROCHLORIDE	0.104	0.592
DIBEKACIN	0.301	0.591
NICARDIPINE_HYDROCHLORIDE	-0.014	0.589
FLUROXENE	-0.006	0.589
DEXCHLORPHENIRAMINE_MALEATE	-0.656	0.588
IOXILAN	0.172	0.588
ETHYLNOREPINEPHRINE_HYDROCHLORIDE	-0.132	0.586
ETHOSUXIMIDE	0.282	0.583
CARVEDILOL_PHOSPHATE	-0.556	0.578
MANNITOL	-0.066	0.576
BUDESONIDE	0.259	0.573
IVERMECTIN	0.066	0.573
PAPAVERINE_HYDROCHLORIDE	-0.126	0.571
PENFLURIDOL	-0.38	0.571
CINTRIAMIDE	-0.72	0.569
DESLORATIDINE	-0.15	0.567
ISOTRETINON	-0.111	0.563
VALPROATE_SODIUM	-0.363	0.563
ESTRONE	-0.41	0.559
PHENOLPHTHALEIN	-0.498	0.558
SODIUM_LACTATE	-0.209	0.553
PAROXETINE_HYDROCHLORIDE	0.231	0.552
PRAMOXINE_HYDROCHLORIDE	-0.091	0.55
SALICIN	-0.146	0.547
SEMUSTINE	-0.132	0.546
CLOFIBRATE	-0.313	0.544
PROCYCLIDINE_HYDROCHLORIDE	-0.47	0.544
MOMETASONE_FUROATE	-0.277	0.544
IOTHALAMIC_ACID	-0.193	0.543
CARBOPLATIN	0.079	0.543
THONZYLAMINE_HYDROCHLORIDE	0.235	0.541
BEKANAMYCIN_SULFATE	0.364	0.54
NEOSTIGMINE_BROMIDE	0.416	0.54
PROGESTERONE	-0.026	0.539
CRESOL	0.036	0.539
VINCRISTINE_SULFATE	-0.186	0.539
DOCUSATE_SODIUM	-0.257	0.538
RIFAMPIN	0.061	0.536
BETAHISTINE_HYDROCHLORIDE	-0.435	0.531
DISOPYRAMIDE_PHOSPHATE	0.191	0.531
BENZOIC_ACID	-0.327	0.529
BROMPERIDOL	0.189	0.528
TAURINE	0.378	0.526
DESIPRAMINE_HYDROCHLORIDE	-0.243	0.525
BUTYLATED_HYDROXYANISOLE	-0.108	0.52
TETRAHYDROZOLINE_HYDROCHLORIDE	0.276	0.519
CINCHONIDINE	-0.392	0.518
TETRACYCLINE_HYDROCHLORIDE	0.272	0.517
TRIFLUPROMAZINE_HYDROCHLORIDE	0.105	0.514
NITAZOXANIDE	-0.706	0.509
ACONITINE	0.143	0.508
METHICILLIN_SODIUM	0.1	0.507
CANDICIDIN	-1.087	0.505
FLUPHENAZINE_HYDROCHLORIDE	-0.424	0.504
PYRVINIUM_PAMOATE	-0.259	0.501

THIAMYLAL_SODIUM	-0.938	0.501
THONZONIUM_BROMIDE	-0.716	0.498
ADENINE	0.243	0.497
DEXAMETHASONE_ACETATE	-0.113	0.497
ORNIDAZOLE	0.215	0.496
ETHYNODIOL_DIACETATE	0.35	0.494
BROMPHENIRAMINE_MALEATE	-0.004	0.494
KETANSERIN_TARTRATE	-1.244	0.493
ESTRADIOL_CYPIONATE	0.224	0.493
VENLAFAXINE_HYDROCHLORIDE	0.011	0.491
NICOTINE_BITARTRATE	-0.305	0.489
METHACHOLINE_CHLORIDE	0.242	0.489
RETINYL_PALMITATE	-0.411	0.487
INDOPROFEN	0.328	0.487
MEMANTINE_HYDROCHLORIDE	-0.116	0.486
BETAMETHASONE_ACETATE	-0.241	0.485
SENNOSIDE_A	0.362	0.485
PROTRYPTYLINE_HYDROCHLORIDE	-0.131	0.484
CYCLOSPORINE	-0.473	0.483
OMEPRAZOLE	0.018	0.479
ADAPALENE	-0.365	0.478
TYLOXAPOL	0.396	0.474
PIPERIDOLATE_HYDROCHLORIDE	0.251	0.474
MOXALACTAM_DISODIUM	-0.662	0.473
ECONAZOLE_NITRATE	-0.413	0.469
DILTIAZEM_HYDROCHLORIDE	0.001	0.468
ALTRENOGEST	-0.427	0.468
CEFACLOR	0.159	0.467
BENZYL_BENZOATE	0.042	0.467
CARBARSONE	-0.742	0.466
PARGYLINE_HYDROCHLORIDE	-0.168	0.465
MORANTEL_CITRATE	-0.072	0.465
DOXOFYLLINE	0.332	0.463
REPAGLINIDE	-0.561	0.462
LIDOCAINE_HYDROCHLORIDE	0.008	0.461
MANGAFODIPI 00R_TRISODIUM	-0.008	0.46
ACENOCOUMAROL	0.005	0.459
FLUDARABINE_PHOSPHATE	-0.37	0.458
ANAGRELIDE_HYDROCHLORIDE	0.154	0.458
LAMIVUDINE	-0.052	0.456
DIPYRIDAMOLE	0.242	0.453
IPRIFLAVONE	0.292	0.449
ALISKIREN_HEMIFUMARATE	0.019	0.448
FOSFOSAL	0.009	0.448
MELOXICAM_SODIUM	0.33	0.447
BUPIVACAINE_HYDROCHLORIDE	-0.068	0.446
DIPHENHYDRAMINE_HYDROCHLORIDE	0.573	0.446
PIPAMPERONE	-0.031	0.444
NIMESULIDE	-0.169	0.444
GRANISETRON_HYDROCHLORIDE	-0.053	0.444
BRUCINE	-0.166	0.443
EUGENOL	-0.022	0.442
NEOMYCIN_SULFATE	0.064	0.442
DANTROLENE_SODIUM	-0.066	0.44
ROLITETRACYCLINE	-0.201	0.44
SULFANITRAN	-0.481	0.434
PIRENZEPINE_HYDROCHLORIDE	-0.065	0.433
CEFEPIME_HYDROCHLORIDE	0.08	0.432
HYDRALAZINE_HYDROCHLORIDE	-0.168	0.432
PHENTOLAMINE_HYDROCHLORIDE	0.123	0.43
TRIACETIN	0.253	0.43
PREDNICARBATE	-0.517	0.429
CEPHALEXIN	0.06	0.427
METHYLERGONOVINE_MALEATE	0.135	0.427

ROFECOXIB	0.171	0.426
BUTACAINE	0.008	0.426
SULFASALAZINE	0.023	0.425
ACETRIAZOIC_ACID	-0.199	0.421
ESTRIOL	-1.309	0.42
DYCLONINE_HYDROCHLORIDE	0.213	0.418
EPRODISATE_DISODIUM	0.312	0.417
TOLTRAZURIL	0.172	0.417
ALLANTOIN	0.315	0.416
PHENYLMERCURIC_ACETATE	-0.019	0.414
QUIPAZINE_MALEATE	-0.425	0.414
PERINDOPRIL_ERBUMINE	-0.659	0.414
NADIDE	-0.253	0.413
CITICOLINE	-0.657	0.412
LANSOPRAZOLE	-0.194	0.41
NISOLDIPINE	0.09	0.405
PENICILLAMINE	0.366	0.404
ARGININE_HYDROCHLORIDE	-0.474	0.403
AZELASTINE_HYDROCHLORIDE	0.114	0.399
OXFENDAZOLE	-0.426	0.399
DACARBAZINE	0.305	0.398
DOXAPRAM_HYDROCHLORIDE	-0.253	0.398
CINCHONINE	-0.427	0.398
QUINAPRIL_HYDROCHLORIDE	0.218	0.394
INDOMETHACIN	0.232	0.393
IODIPAMIDE	0.313	0.392
CLOPIDOGREL_SULFATE	-0.074	0.391
‘ALFUZOSIN_HYDROCHLORIDE	0.031	0.39
)IZOCILPINE_MALEATE	-0.248	0.39
,ITROFURAZONE	0.143	0.388
DIETHYLTOLUAMIDE	0.381	0.388
PIPERACETAZINE	0.135	0.387
SACCHARIN	-0.522	0.385
ASTEMIZOLE	-0.135	0.384
SALICYLAMIDE	-0.042	0.383
CLOPERASTINE_HYDROCHLORIDE	0.213	0.383
DENATONIUM_BENZOATE	0.404	0.382
DOXYCYCLINE_HYDROCHLORIDE	0.19	0.381
CINOXACIN	0.245	0.38
BETAINE_HYDROCHLORIDE	0.062	0.379
THIOTEPA	-0.018	0.379
RIBAVIRIN	-0.558	0.377
LOXAPINE_SUCCINATE	0.25	0.377
VIGABATRIN	-0.162	0.374
LITHIUM_CITRATE	-0.298	0.373
BUTAMBEN	-0.064	0.373
BISOPROLOL_FUMARATE	-0.251	0.37
OLMESARTAN_MEDOXOMIL	-0.507	0.369
NABUMETONE	0.092	0.368
DERACOXIB	-0.981	0.364
AZITHROMYCIN	-0.062	0.364
AMIFOSTINE	-0.097	0.363
GEMFIBROZIL	-0.092	0.363
SULFABENZAMIDE	0.361	0.362
PHENOTHIAZINE	0.64	0.362
HYDROXYPROGESTERONE_CAPROATE	0.17	0.361
CYTARABINE	-0.254	0.361
ERYTHROMYCIN_ETHYLSUCCINATE	0.326	0.36
BETAMETHASONE_17_21-DIPROPIONATE	0.253	0.36
ATRACURIUM_BESYLATE	0.323	0.36
CEFONICID_SODIUM	0.345	0.359
DEXIBUPROFEN	0.039	0.359
THIAMINE	0.231	0.358
RAMOPLANIN_[A2_shown;_2mM]	-0.51	0.358

FLUOXETINE	0.078	0.357
RANOLAZINE	-0.111	0.355
SODIUM_NITROPRUSSIDE	-0.499	0.354
AMINOPENTAMIDE_SULFATE	-0.214	0.353
COLISTIN_SULFATE	0.079	0.353
ADIPHENINE_HYDROCHLORIDE	-0.268	0.352
HYDROFLUMETHIAZIDE	-0.257	0.35
DEHYDROCHOLIC_ACID	0.265	0.35
METHYCLOTHIAZIDE	-0.123	0.35
CEFAMANDOLE_SODIUM	0.138	0.349
HYDROXYZINE_PAMOATE	-0.494	0.349
CARBETAPENTANE_CITRATE	-0.691	0.348
METHYSERGIDE_MALEATE	-0.424	0.348
STREPTOMYCIN_SULFATE	0.121	0.348
ETHISTERONE	-0.267	0.347
SODIUM_MONOFLUOROPHOSPHATE	-0.085	0.347
ERYTHRITOL	0.077	0.346
IMEXON	0.3	0.346
CHLOROXINE	-0.124	0.346
THIRAM	-0.889	0.345
CEFTRIAXONE_SODIUM_TRIHYDRATE	-0.636	0.344
LAMOTRIGINE	0.007	0.343
SELAMECTIN	-0.279	0.343
AMINOGLUTETHIMIDE	0.029	0.341
RISEDRONATE_SODIUM	0.133	0.34
ETHAMBUTOL_HYDROCHLORIDE	-0.253	0.34
ΓENOXICAM	-0.006	0.34
ΓRISODIUM_ETHYLENEDIAMINE_TETRACETATE	0.505	0.339
ΓOLONIUM_CHLORIDE	0.332	0.338
ıNDAPAMIDE	0.606	0.338
FlUMAZENIL	-0.499	0.336
PYRIDOXINE	-0.422	0.335
KETOCONAZOLE	-0.069	0.334
DIGOXIN	0.334	0.334
IMATINIB	-0.204	0.333
TYLOSIN_TARTRATE	0.233	0.333
OUABAIN	0.041	0.332
CHOLECALCIFEROL	-0.021	0.332
TIAPRIDE_HYDROCHLORIDE	-0.178	0.332
CIPROFIBRATE	-0.278	0.331
D-LACTITOL_MONOHYDRATE	0.337	0.331
EDETATE_DISODIUM	0.323	0.33
STREPTOZOSIN	0.193	0.328
MEDROXYPROGESTERONE_ACETATE	0.126	0.327
ZALEPLON	-0.11	0.327
CAPECITABINE	0.384	0.325
LEVOCARNITINE_PROPIONATE_HYDROCHLORIDE	0.065	0.323
PYRANTEL_PAMOATE	-1.143	0.323
DOXEPIN_HYDROCHLORIDE	0.269	0.322
IMIPRAMINE_HYDROCHLORIDE	0.155	0.32
DORAMECTIN	0.094	0.32
PEFLOXACINE_MESYLATE	-0.629	0.319
OXALIPLATIN	-0.256	0.319
DIOXYBENZONE	0.368	0.317
RESORCINOL_MONOACETATE	-0.23	0.314
CITRIC_ACID	0.12	0.314
NAFCILLIN_SODIUM	0.23	0.314
SULFAMERAZINE	0.264	0.31
MERCAPTOPURINE	0.256	0.31
NICORANDIL	0.386	0.309
KETOROLAC_TROMETHAMINE	-0.344	0.307
NICOTINYL_ALCOHOL_TARTRATE	0.059	0.307
PIPERACILLIN_SODIUM	-0.019	0.306
PILOCARPINE_NITRATE	0.042	0.304

TINIDAZOLE	0.267	0.303
VANCOMYCIN_HYDROCHLORIDE	-1.24	0.303
CLOXACILLIN_SODIUM	-0.372	0.301
PRILOCAINE_HYDROCHLORIDE	-0.046	0.301
CELECOXIB	0.257	0.301
ERYTHROMYCIN_ESTOLATE	-0.416	0.3
DIAZOXIDE	0.092	0.3
TRIENTINE_HYDROCHLORIDE	-0.331	0.299
TRIPROLIDINE_HYDROCHLORIDE	0.077	0.298
DEFLAZACORT	0.283	0.298
OXICONAZOLE_NITRATE	-0.291	0.297
CEFPODOXIME_PROXETIL	0.188	0.295
PROTIRELIN	0.225	0.294
AMLODIPINE_BESYLATE	-1.078	0.293
HYDROCORTISONE_HEMISUCCINATE	-0.007	0.293
LEVOCARNITINE	0.326	0.292
THIAMPHENICOL	0.218	0.292
DICUMAROL	-0.602	0.29
CHLORPROTHIXENE_HYDROCHLORIDE	-0.14	0.29
SODIUM_OXYBATE	-0.588	0.288
LORATADINE	-0.104	0.288
COLFORSIN	-0.137	0.286
MEPHENYTOIN	0.065	0.286
SODIUM_PHENYLBUTYRATE	0.17	0.286
LINEZOLID	-0.497	0.286
CINROMIDE	-0.905	0.285
HEXACHLOROPHENE	-0.999	0.285
SULFACHLORPYRIDAZINE	-0.714	0.285
OXAPROZIN	-0.797	0.284
SPECTINOMYCIN_HYDROCHLORIDE	0.185	0.283
AMINACRINE	0.082	0.28
LOBENDAZOLE	-0.547	0.28
SARAFLOXACIN_HYDROCHLORIDE	0.166	0.28
CEFAZOLIN_SODIUM	-0.035	0.277
MENADIONE	-0.973	0.274
PERHEXILINE_MALEATE	0.225	0.272
HYDROCORTISONE_PHOSPHATE_TRIETHYLAMINE	0.068	0.272
FLORFENICOL	-0.387	0.272
ETHOPROPAZINE_HYDROCHLORIDE	-0.319	0.271
LINCOMYCIN_HYDROCHLORIDE	0.281	0.271
DOPAMINE_HYDROCHLORIDE	0.317	0.27
ASCORBIC_ACID	-0.23	0.269
ALCLOMETAZONE_DIPROPIONATE	-0.922	0.269
FENOTEROL_HYDROBROMIDE	-0.03	0.267
PERPHENAZINE	-0.393	0.266
DECOQUINATE	0.374	0.266
PIRENPERONE	0.077	0.264
SPIRAMYCIN	-0.38	0.263
LIPOAMIDE	0.073	0.262
ZIPRASIDONE_MESYLATE	-0.38	0.261
PROCHLORPERAZINE_EDISYLATE	-0.672	0.261
BIFONAZOLE	-0.556	0.26
CYCLOPHOSPHAMIDE	-0.227	0.259
ETOMIDATE	0.088	0.259
TETROQUINONE	0.348	0.258
TERPENE_HYDRATE	0.024	0.257
FUROSEMIDE	-0.329	0.257
CARSALAM	-1.252	0.257
SERTRALINE_HYDROCHLORIDE	-0.418	0.255
EDOXUDINE	-0.745	0.255
MINOCYCLINE_HYDROCHLORIDE	-0.533	0.255
MODAFINIL	-0.594	0.254
CILOSTAZOL	-0.823	0.254
HISTAMINE_DIHYDROCHLORIDE	-0.396	0.254

ISOVALERAMIDE	0.354	0.253
TICLOPIDINE_HYDROCHLORIDE	-0.278	0.253
LACTULOSE	0.102	0.252
MONENSIN_SODIUM_(monensin_A_is_shown)	0.136	0.252
DOCOSANOL	-0.095	0.251
APRAMYCIN_SULFATE	-0.621	0.251
HYDROCHLOROTHIAZIDE	-0.394	0.249
CIPROFLOXACIN	-0.05	0.248
ZIDOVUDINE_[AZT]	0.346	0.246
ALENDRONATE_SODIUM	0.011	0.246
URETHANE	-0.24	0.246
DEXAMETHASONE	-0.389	0.245
TRANYLCYPROMINE_SULFATE	0.517	0.245
ACTARIT	-0.125	0.245
SIROLIMUS	0.025	0.245
PIPENZOLATE_BROMIDE	0.265	0.243
TICARCILLIN_DISODIUM	-0.03	0.241
PIZOTYLINE_MALATE	0.125	0.24
YOHIMBINE_HYDROCHLORIDE	-0.018	0.239
SULFISOXAZOLE_ACETYL	0.291	0.239
KANAMYCIN_A_SULFATE	0.134	0.238
DIMETHADIONE	0.374	0.237
CEFDITORIN_PIVOXIL	0.097	0.237
SULFAMETHOXAZOLE	0.358	0.237
CHLORMIDAZOLE	-0.411	0.237
ˈENBUFEN	-0.213	0.236
ˋRIMETHADIONE	0.297	0.236
ˎMINOPYRINE	0.153	0.236
ˏICLOFENAC_SODIUM	-0.265	0.235
SPIRONOLACTONE	0.095	0.235
METHAPYRILENE_HYDROCHLORIDE	0.388	0.234
PROPOXYCAINE_HYDROCHLORIDE	-0.295	0.233
FLUTAMIDE	-0.406	0.232
BUMETANIDE	-0.125	0.232
CHOLESTEROL	0.066	0.232
BENZBROMARONE	-0.368	0.231
PAROMOMYCIN_SULFATE	0.344	0.231
ROSUVASTATIN_CALCIUM	-0.487	0.23
RETINOL	-0.394	0.23
QUINETHAZONE	-0.318	0.23
PHENACETIN	-0.406	0.229
MEBEVERINE_HYDROCHLORIDE	-0.699	0.229
ORLISTAT	0.296	0.229
TERFENADINE	-0.258	0.228
OCTINOXATE	-0.136	0.228
BROMHEXINE_HYDROCHLORIDE	-0.604	0.228
DEMECLOCYCLINE_HYDROCHLORIDE	-0.222	0.227
INOSITOL	0.016	0.226
SODIUM_GLUCONATE	0.287	0.226
CEFTIBUTEN	-0.649	0.226
DIPHENYLPYRALINE_HYDROCHLORIDE	0.207	0.224
PHENYLETHYL_ALCOHOL	-0.092	0.224
BEPRIDIL_HYDROCHLORIDE	-0.558	0.224
MEBENDAZOLE	-0.17	0.222
LEVALBUTEROL_HYDROCHLORIDE	-0.033	0.221
PIPOBROMAN	-0.322	0.22
CIMETIDINE	0.163	0.219
MEFLOQUINE	-0.359	0.219
NIACIN	-0.179	0.218
TELITHROMYCIN	-0.585	0.218
GADOTERIDOL	-0.11	0.215
MOXIFLOXACIN_HYDROCHLORIDE	0.169	0.215
SULFADIAZINE	0.317	0.212
TERBUTALINE_HEMISULFATE	0.38	0.211

PERGOLIDE_MESYLATE	-0.248	0.21
BACAMPICILLIN_HYDROCHLORIDE	-0.46	0.21
ISOETHARINE_MESYLATE	-0.274	0.209
SULFACETAMIDE	0.333	0.207
BUTYL_PARABEN	-0.542	0.206
ACARBOSE	-0.821	0.205
CAPTOPRIL	0.037	0.205
DYPHYLLINE	0.614	0.204
METFORMIN_HYDROCHLORIDE	-0.223	0.204
THIOGUANINE	0.599	0.202
HYDRASTINE_(1R_9S)	-0.028	0.202
CHLORMADINONE_ACETATE	-0.003	0.2
PIMAGEDINE_HYDROCHLORIDE	-0.202	0.199
RANITIDINE_HYDROCHLORIDE	-0.263	0.199
PYRILAMINE_MALEATE	0.418	0.198
DICYCLOMINE_HYDROCHLORIDE	0.08	0.197
DEFEROXAMINE_MESYLATE	-0.041	0.197
NETILMICIN_SULFATE	-0.387	0.197
STRYCHNINE	-0.115	0.195
CYANOCOBALAMIN	-0.041	0.195
TRIMEPRAZINE_TARTRATE	0.126	0.193
HYOSCYAMINE	0.056	0.192
AZELAIC_ACID	-0.011	0.191
CAMYLOFINE_DIHYDROCHLORIDE	-0.081	0.191
TETRACAINE_HYDROCHLORIDE	0.293	0.19
MEPARFYLON	0.351	0.19
GUANABENZ_ACETATE	-0.159	0.19
NIFEDIPINE	-0.127	0.188
DOXORUBICIN	-0.973	0.187
SIBUTRAMINE_HYDROCHLORIDE	-0.65	0.187
CLIOQUINOL	-0.356	0.187
AMPHOTERICIN_B	-0.185	0.186
GLUTAMINE_(L)	0.098	0.186
CLOBETASOL_PROPIONATE	-0.46	0.185
DICLOXACILLIN_SODIUM	0.055	0.185
gamma-AMINOBUTYRIC_ACID	-0.601	0.185
SULFAMETHIZOLE	0.279	0.184
DIBUTYL_PHTHALATE	-0.502	0.183
SYMCLOSENE	0.341	0.183
ALLYLISOTHIOCYANATE	-0.416	0.182
ZALCITABINE	-0.194	0.182
PIPERINE	-0.217	0.182
BIOTIN	-0.299	0.182
ACYCLOVIR	-0.206	0.182
DIGITOXIN	0.322	0.18
ETHENZAMIDE	-0.635	0.18
DAUNORUBICIN	-0.598	0.178
FIROCOXIB	-0.111	0.178
IOPANIC_ACID	-0.872	0.177
LEVOSIMENDAN	-0.179	0.177
LOMEFLOXACIN_HYDROCHLORIDE	0.217	0.174
NITHIAMIDE	-0.389	0.172
CHLORHEXIDINE_DIHYDROCHLORIDE	-0.213	0.172
ETIDRONATE_DISODIUM	-0.713	0.172
OXETHAZAINE	0.262	0.171
METICRANE	0.185	0.17
MEPHENESIN	-0.081	0.17
THALIDOMIDE	-0.377	0.169
EZETIMIBE	-0.629	0.168
SORBITOL	0.21	0.168
SULFAMETHAZINE	0.317	0.167
METHYLDOPA	-0.124	0.167
IOHEXOL	-0.267	0.167
PIRACETAM	-0.163	0.167

PROPANTHELINE_BROMIDE	-0.22	0.166
BENSERAZIDE_HYDROCHLORIDE	-0.228	0.166
AMINOHYDROXYBUTYRIC_ACID	0.014	0.165
ALTRETAMINE	0.039	0.163
NYSTATIN	-0.195	0.161
CAFFEINE	-0.024	0.16
DIBENZOTHIOPHENE	0.025	0.159
HETACILLIN_POTASSIUM	-0.338	0.157
ENROFLOXACIN	0.008	0.157
NIMODIPINE	-0.254	0.156
BENDROFLUMETHIAZIDE	-0.599	0.156
CHLORINDANOL	-0.628	0.154
SULFATHIAZOLE	0.244	0.153
PREDNISOLONE_HEMISUCCINATE	-0.418	0.153
METACETAMOL	0.179	0.152
DIMENHYDRINATE	0.215	0.152
URSODIOL	-0.264	0.152
COLCHICINE	-0.052	0.152
ETHANOLAMINE_OLEATE	-0.133	0.152
TRICLOSAN	0.264	0.151
GUANETHIDINE_MONOSULFATE	-0.175	0.151
DIFLUNISAL	0.003	0.149
CEFTAZIDIME	-0.092	0.149
PRAZIQUANTEL	-0.233	0.149
TENIPOSIDE	-0.189	0.148
IFENPRODIL_TARTRATE	0.088	0.147
QUINESTROL	-1.826	0.147
AMOROLFINE_HYDROCHLORIDE	-0.888	0.146
ADENOSINE_PHOSPHATE	-0.361	0.145
DEXLANSOPRAZOLE	-0.41	0.145
ROXITHROMYCIN	0.364	0.145
SIMVASTATIN	0.177	0.145
TIOCONAZOLE	0.028	0.143
DONEPEZIL_HYDROCHLORIDE	0.287	0.143
CANRENOIC_ACID_POTASSIUM_SALT	0.157	0.142
TRAZODONE_HYDROCHLORIDE	-0.814	0.142
NOSCAPINE_HYDROCHLORIDE	0.099	0.142
THIORIDAZINE_HYDROCHLORIDE	0.388	0.141
AZILSARTAN_KAMEDOXOMIL	-0.56	0.14
IODIXANOL	0.218	0.14
HYDROXYUREA	-0.052	0.139
CARBINOXAMINE_MALEATE	-0.233	0.139
FLOPROPIONE	-0.094	0.137
BIPERIDEN	-0.892	0.137
PENTYLENETETRAZOL	-0.486	0.136
MYCOPHENOLIC_ACID	-0.861	0.135
FURALTADONE	-0.147	0.134
VIDARABINE	-0.449	0.134
IMIPENEM	-0.09	0.134
SISOMICIN_SULFATE	0.086	0.132
BENZYDAMINE_HYDROCHLORIDE	-0.176	0.132
TRANILAST	0.507	0.131
ACEPROMAZINE_MALEATE	-0.496	0.128
DIOSMIN	0.388	0.127
NIFUROXAZIDE	0.282	0.127
NEVIRAPINE	-0.384	0.127
NIZATIDINE	-1.046	0.125
TERCONAZOLE	-0.231	0.123
TRICHLORMETHINE_HYDROCHLORIDE	0.08	0.122
ETHINYL_ESTRADIOL	-0.634	0.122
HYDROCORTISONE_VALERATE	-0.216	0.122
CEFDINIR	-0.652	0.122
MESNA	-0.353	0.122
PROTOPORPHYRIN_IX	0.362	0.12

GUAIACOL	0.155	0.12
ETHAMIVAN	-0.404	0.118
FLUNIXIN_MEGLUMINE	-0.101	0.118
ALTHIAZIDE	0.097	0.117
FAMOTIDINE	-0.252	0.113
GLUCOSAMINE_HYDROCHLORIDE	-0.173	0.112
TRIMETOZINE	-0.334	0.11
DESONIDE	-0.161	0.109
PREDNISOLONE	0.067	0.109
AMINOHIPPURIC_ACID	-0.35	0.109
AKLOMIDE	-0.067	0.108
BENZOCAINE	-0.131	0.107
EXEMESTANE	0.036	0.107
ETOSALAMIDE	-0.472	0.106
EUCALYPTOL	-0.026	0.104
BISACODYL	-0.052	0.104
ENOXACIN	0.456	0.103
SULFISOXAZOLE	0.391	0.101
LEVOFLOXACIN	-0.368	0.101
NONIVAMIDE	0.333	0.1
FELBINAC	-0.112	0.1
ETHAVERINE_HYDROCHLORIDE	0.146	0.098
EVANS_BLUE	-1.267	0.098
VALGANCICLOVIR_HYDROCHLORIDE	0.258	0.098
EPINEPHRINE_BITARTRATE	0.539	0.097
PYRIMETHAMINE	-0.371	0.097
RESERPINE	-0.384	0.096
URAZOLIDONE	-0.054	0.095
MEPENZOLATE_BROMIDE	0.037	0.095
PRAVASTATIN_SODIUM	0.013	0.095
HYDROCORTISONE_BUTYRATE	-0.179	0.094
TRIPELENNAMINE_CITRATE	0.293	0.093
PROPRANOLOL_HYDROCHLORIDE_(+/-)	0.058	0.093
QUINACRINE_HYDROCHLORIDE	-0.532	0.092
AMPROLIUM	-0.262	0.09
ETHIONAMIDE	-0.44	0.09
MEPIVACAINE_HYDROCHLORIDE	-0.023	0.088
DIPYRONE	0.283	0.088
DIENESTROL	-0.174	0.087
AUROTHIOGLUCOSE	0.163	0.086
SULFINPYRAZONE	0.307	0.086
LUMIRACOXIB	-0.564	0.084
GLICLAZIDE	-0.33	0.084
ACECAINIDE_HYDROCHLORIDE	0.239	0.083
ACETOPHENAZINE_MALEATE	-0.32	0.083
SOLIFENACIN_SUCCINATE	-0.291	0.081
TOCAINIDE_HYDROCHLORIDE	-0.198	0.08
NIACINAMIDE	-0.032	0.08
SULINDAC	0.168	0.08
TACROLIMUS	-0.242	0.079
ESTROPIPATE	-1.207	0.078
CHLORAMBUCIL	-0.34	0.078
DIBUCAINE_HYDROCHLORIDE	-0.297	0.078
SPIPERONE	-0.271	0.074
METOLAZONE	0.28	0.072
LOVASTATIN	-1.026	0.071
GALLAMINE_TRIETHIODIDE	0.058	0.071
ACECLOFENAC	-0.446	0.07
ORPHENADRINE_CITRATE	-0.263	0.07
FLOXURIDINE	-0.43	0.068
CYPROTERONE	-0.061	0.067
HEXYLRESORCINOL	-1.352	0.066
BENZTHIAZIDE	0.06	0.064
FTAXILIDE	-0.503	0.062

LOBELINE_HYDROCHLORIDE	-0.026	0.062
PREDNISOLONE_ACETATE	-0.319	0.061
RACTOPAMINE_HYDROCHLORIDE	-0.223	0.061
DIHYDROERGOTAMINE_MESYLATE	0.205	0.06
PRALIDOXIME_CHLORIDE	-0.253	0.059
ESCIN	-1.236	0.058
CLOFAZIMINE	-0.319	0.058
CARBACHOL	-0.161	0.058
CYCLOPENTOLATE_HYDROCHLORIDE	-0.454	0.057
FEXOFENADINE_HYDROCHLORIDE	-0.337	0.057
VALACYCLOVIR_HYDROCHLORIDE	-0.18	0.056
CARMUSTINE	-0.656	0.053
CARZENIDE	0.077	0.053
CYCLOTHIAZIDE	0.201	0.052
DISULFIRAM	0.242	0.052
OCTOPAMINE_HYDROCHLORIDE	0.513	0.05
QUETIAPINE	-0.984	0.05
OXELAIDIN_CITRATE	0.183	0.049
SODIUM_SALICYLATE	0.043	0.049
MOLINDONE_HYDROCHLORIDE	-0.059	0.048
FOMEPIZOLE_HYDROCHLORIDE	0.017	0.048
CEPHAPIRIN_SODIUM	-0.117	0.048
MIGLITOL	-0.513	0.047
TILMICOSIN	0.165	0.047
HALAZONE	-0.291	0.047
RITANSERIN	-0.145	0.046
MITOXANTRONE_HYDROCHLORIDE	0.284	0.045
ᵀUAMINOHEPTANE_SULFATE	-0.155	0.045
ᒪOLBUTAMIDE	0.43	0.044
CHLORTETRACYCLINE_HYDROCHLORIDE	0.135	0.042
SULFADOXINE	0.024	0.041
LEVONORGESTREL	-0.056	0.041
PENTAMIDINE_ISETHIONATE	-0.15	0.04
NEFIRACETAM	0.332	0.039
MESALAMINE	-1.26	0.039
LEVODOPA	-0.154	0.038
PARACHLOROPHENOL	0.013	0.038
ETODOLAC	-0.268	0.037
NITRENDIPINE	-0.354	0.036
QUININE_SULFATE	-0.412	0.035
beta-CAROTENE	-0.093	0.033
CHLORAMPHENICOL_SODIUM_SUCCINATE	-0.179	0.033
ACETOHEXAMIDE	-0.411	0.03
BENZOCLIDINE	0.08	0.03
FINASTERIDE	-0.274	0.029
EMETINE_DIHYDROCHLORIDE	0.434	0.028
CHLORAZANIL_HYDROCHLORIDE	-0.028	0.028
ACESULFAME_POTASSIUM	-0.94	0.028
FLUVASTATIN	0.091	0.027
MEBHYDROLIN_NAPHTHALENESULFONATE	-0.111	0.026
CHLORCYCLIZINE_HYDROCHLORIDE	-0.382	0.026
TANDUTINIB	0.252	0.026
CARBENICILLIN_DISODIUM	-0.22	0.025
TRIMETHOPRIM	0.275	0.025
CHLOROTHIAZIDE	-0.264	0.024
ATROPINE_SULFATE	0.009	0.022
ANIRACETAM	-0.094	0.022
PROADIFEN_HYDROCHLORIDE	-0.088	0.021
IPROHEPTINE	0.399	0.021
CYCLOBENZAPRINE_HYDROCHLORIDE	-0.037	0.019
METHOXSALEN	-0.108	0.019
SULCONAZOLE_NITRATE	-0.639	0.019
ALPRENOLOL	-0.625	0.018
MEGLUTOL	-0.104	0.018

NITROMIDE	0.021	0.017
UNDECYLENIC_ACID	-0.038	0.017
DEHYDROCHOLATE_SODIUM	-0.076	0.017
BUCETIN	-0.121	0.017
VIOMYCIN_SULFATE	0.292	0.015
PIROCTONE_OLAMINE	-0.186	0.014
TERBINAFINE_HYDROCHLORIDE	-0.083	0.013
AMODIAQUINE_DIHYDROCHLORIDE	-0.223	0.012
NITROFURANTOIN	-0.21	0.012
DAPSONE	0.104	0.011
PREDNISOLONE_TEBUTATE	-0.331	0.008
ADELMIDROL	-0.025	0.007
EUCATROPINE_HYDROCHLORIDE	0.008	0.007
CYCLIZINE	-0.59	0.004
CYCLANDELATE	0.371	0.004
NORGESTIMATE	0.018	0.003
CINOCTRAMIDE	0.195	0.003
DIHYDROSTREPTOMYCIN_SULFATE	0.531	0.002
AMOXAPINE	-0.231	0.001
METHSCOPOLAMINE_BROMIDE	0.019	0
PHTHALYLSULFACETAMIDE	-0.039	-0.001
METHAZOLAMIDE	-0.515	-0.002
TODRALAZINE_HYDROCHLORIDE	-0.154	-0.003
LINAGLIPTIN	0.258	-0.004
CEFOTAXIME_SODIUM	-0.175	-0.005
VILAZODONE_HYDROCHLORIDE	0.039	-0.006
SODIUM_CYCLAMATE	-0.273	-0.006
ROCLOSENE_POTASSIUM	-0.141	-0.008
CARBAMAZEPINE	-0.38	-0.008
THIOPENTAL_SODIUM	-0.914	-0.009
THIMEROSAL	-1.114	-0.011
TRIFLURIDINE	-0.305	-0.011
BETHANECHOL_CHLORIDE	0.017	-0.012
ACADESINE	0.018	-0.013
AJMALINE	-0.281	-0.013
ERGOCALCIFEROL	-0.351	-0.013
GEMIFLOXACIN_MESYLATE	-0.048	-0.014
PRASTERONE_ACETATE	-0.155	-0.015
CAPREOMYCIN_SULFATE	-0.039	-0.015
ALRESTATIN	-0.31	-0.015
DIETHYLSTILBESTROL	-0.047	-0.016
BETAMETHASONE	-0.003	-0.016
ETICLOPRIDE_HYDROCHLORIDE	0.259	-0.016
TAMOXIFEN_CITRATE	0.092	-0.016
NORETHINDRONE	-0.086	-0.016
CORTISONE_ACETATE	-0.359	-0.017
CARTEOLOL_HYDROCHLORIDE	-0.385	-0.017
NIKETHAMIDE	-0.086	-0.02
d-LIMONENE	0.22	-0.02
EFLOXATE	-0.014	-0.02
PIOGLITAZONE_HYDROCHLORIDE	0.297	-0.021
NAFRONYL_OXALATE	-0.023	-0.022
ERYTHROMYCIN_STEARATE	0.01	-0.022
BEZAFIBRATE	-0.086	-0.024
HALOPERIDOL	-0.302	-0.024
CARISOPRODOL	-0.328	-0.024
DEXPROPRANOLOL_HYDROCHLORIDE	-0.249	-0.024
CHLORAMPHENICOL	-0.407	-0.024
FLUMEQUINE	0.057	-0.025
TRANEXAMIC_ACID	0.146	-0.025
BORNYL_ACETATE	0.071	-0.026
ASCORBYL_PALMITATE	0.059	-0.027
FENOPROFEN	-0.093	-0.027
NICLOSAMIDE	-0.242	-0.028

TOBRAMYCIN	0.337	-0.029
LOPERAMIDE_HYDROCHLORIDE	-0.058	-0.03
PROPOFOL	-0.136	-0.03
SECNIDAZOLE	0.115	-0.03
ADIPIC_ACID	-0.122	-0.031
BUSULFAN	-0.023	-0.032
PROBUCOL	-0.098	-0.033
CLEMASTINE_FUMARATE	-0.304	-0.034
CARGLUMIC_ACID	0.188	-0.035
SPARFLOXACIN	-0.106	-0.037
BACITRACIN	-0.379	-0.037
CEFUROXIME_AXETIL	-0.378	-0.038
PENTETIC_ACID	-0.172	-0.038
HEXESTROL	-0.051	-0.041
DOBUTAMINE_HYDROCHLORIDE	-0.479	-0.041
PIPEMIDIC_ACID	0.341	-0.041
NIALAMIDE	0.037	-0.041
CROTAMITON	-0.146	-0.042
CHLOROQUINE_DIPHOSPHATE	-0.384	-0.042
RITODRINE_HYDROCHLORIDE	-0.141	-0.043
MEPRYLCAINE_HYDROCHLORIDE	-0.045	-0.043
HOMATROPINE_HYDROBROMIDE	-0.341	-0.043
LISINOPRIL	0.112	-0.045
VINBLASTINE_SULFATE	0.016	-0.046
CEPHRADINE	-0.096	-0.047
NORGESTREL	-0.174	-0.049
BECLOMETHASONE_DIPROPIONATE	-0.144	-0.05
CARNITINE_(dl)_HYDROCHLORIDE	0.226	-0.05
NATEGLINIDE	-0.049	-0.05
TEMOZOLAMIDE	-0.1	-0.051
URAPIDIL_HYDROCHLORIDE	-0.072	-0.053
BENURESTAT	-0.329	-0.054
FOLIC_ACID	-0.08	-0.054
FOSCARNET_SODIUM	-0.722	-0.055
ASPARTAME	0.004	-0.056
EDARAVONE	0.148	-0.056
DINITOLMIDE	0.19	-0.056
BITHIONATE_SODIUM	-0.091	-0.057
GUAIFENESIN	-0.265	-0.057
CISPLATIN	-0.597	-0.058
PROCAINAMIDE_HYDROCHLORIDE	-0.264	-0.059
PROPARACAINE_HYDROCHLORIDE	0.033	-0.059
EDROPHONIUM_CHLORIDE	-0.127	-0.061
MEPIROXOL	-0.053	-0.061
PYRITHYLDIONE	-0.017	-0.062
HYDROXYCHLOROQUINE_SULFATE	-0.055	-0.062
RONNEL	-0.357	-0.063
PYRITHIONE_ZINC	-0.556	-0.064
XYLOMETAZOLINE_HYDROCHLORIDE	-0.598	-0.065
DOMPERIDONE	-0.477	-0.065
AZATHIOPRINE	-0.315	-0.067
DOXIFLURIDINE	0.176	-0.069
ARTESUNATE	-0.222	-0.07
DIACERIN	0.558	-0.07
CAMPHOR_(1R)	0.006	-0.071
COTININE	0.165	-0.072
NICOPHOLINE	0.022	-0.073
MIZORIBINE	-1.095	-0.074
LEVOTHYROXINE	0.35	-0.076
CEPHALOTHIN_SODIUM	-0.159	-0.077
BROMOCRIPTINE_MESYLATE	-0.145	-0.078
DIACETAMATE	-0.005	-0.078
CYSTEAMINE_HYDROCHLORIDE	0.078	-0.079
CYROMAZINE	-0.101	-0.079

CAPSAICIN	-0.393	-0.08
OXCARBAZEPINE	-0.443	-0.081
VARDENAFIL_HYDROCHLORIDE	-0.36	-0.082
CHLORAMPHENICOL_PALMITATE	-0.272	-0.082
TOLPERISONE_HYDROCHLORIDE	0.09	-0.082
METHYLBENZETHONIUM_CHLORIDE	-0.686	-0.082
BURAMATE	-0.253	-0.082
CLAVULANATE_LITHIUM	0.079	-0.082
BITOSCANATE	-0.181	-0.083
LANATOSIDE_C	0.281	-0.085
PROMAZINE_HYDROCHLORIDE	-0.469	-0.085
ALLOPURINOL	-0.006	-0.087
TILORONE	-0.235	-0.087
BENZETHONIUM_CHLORIDE	-0.473	-0.088
FENOFIBRATE	-0.064	-0.088
FLUVOXAMINE_MALEATE	0.054	-0.09
MELENGESTROL_ACETATE	-0.51	-0.093
ACIPIMOX	0.141	-0.093
DROFENINE_HYDROCHLORIDE	0.14	-0.093
CYPROHEPTADINE_HYDROCHLORIDE	-0.467	-0.094
PHENYLBUTAZONE	-0.053	-0.096
SULISOBENZONE	-0.209	-0.098
OXYBENZONE	-0.282	-0.099
GRAMICIDIN_(gramicidin_A_shown)	-0.478	-0.099
DANAZOL	-0.351	-0.1
PREDNISONE	-0.259	-0.101
FUSIDIC_ACID	-0.178	-0.103
SALINOMYCIN_SODIUM	0.098	-0.105
ZIOPRONIN	0.119	-0.105
FORMESTANE	0.086	-0.107
AMINOLEVULINIC_ACID_HYDROCHLORIDE	0.152	-0.108
BACLOFEN	-0.261	-0.108
TRAMADOL_HYDROCHLORIDE	-0.073	-0.108
TOLAZOLINE_HYDROCHLORIDE	0.435	-0.109
METHSUXIMIDE	-0.186	-0.109
HEXETIDINE	0.337	-0.109
ENILCONAZOLE_SULFATE	-0.196	-0.109
CLOMIPRAMINE_HYDROCHLORIDE	-0.236	-0.109
CARVEDILOL	-0.815	-0.11
PIMOZIDE	-0.516	-0.112
COLISTIMETHATE_SODIUM	-0.005	-0.112
ZOLPIDEM	0.016	-0.112
ROPINIROLE_HYDROCHLORIDE	-0.762	-0.113
TIMONACIC	0.086	-0.113
ALBENDAZOLE	-0.336	-0.115
DEBRISOQUIN_SULFATE	0.181	-0.116
REBAMIPIDE	0.208	-0.116
CHLORTHALIDONE	-0.164	-0.116
CEFADROXIL	-0.164	-0.117
PINACIDIL	0.125	-0.117
ZAPRINAST	-0.3	-0.117
CHLOROBUTANOL	0.262	-0.118
TANNIC_ACID	-0.07	-0.119
AZLOCILLIN_SODIUM	-0.667	-0.12
PICOLAMINE	0.081	-0.12
KETOTIFEN_FUMARATE	-0.796	-0.12
BENFLUOREX_HYDROCHLORIDE	0.131	-0.12
IBANDRONATE_SODIUM	-0.196	-0.121
ACEGLUTAMIDE	0.13	-0.121
NORETHINDRONE_ACETATE	-0.315	-0.121
ATENOLOL	-0.198	-0.123
TRIAMCINOLONE_DIACETATE	-0.053	-0.123
CHLORAMINE-T	-1.78	-0.123
BETAMETHASONE_SODIUM_PHOSPHATE	-0.057	-0.123

PANTETHINE	0.12	-0.123
DIPERODON_HYDROCHLORIDE	-0.361	-0.123
BUSPIRONE_HYDROCHLORIDE	-0.557	-0.124
METARAMINOL_BITARTRATE	-0.466	-0.124
SEVOFLURANE	0.059	-0.124
ANISODAMINE_HYDROBROMIDE	-0.671	-0.127
TOPIRAMATE	-0.084	-0.13
NILUTAMIDE	0.169	-0.13
EXALAMIDE	-0.244	-0.13
PRIMAQUINE_PHOSPHATE	-0.677	-0.131
PIROMIDIC_ACID	0.255	-0.133
BUPROPION	-0.048	-0.133
NIFENAZONE	0.052	-0.134
LOFEXIDINE__HYDROCHLORIDE	-0.184	-0.134
PROPAFENONE_HYDROCHLORIDE	-0.493	-0.137
NOREPINEPHRINE	-0.054	-0.138
PIDOLIC_ACID	0.25	-0.138
MOXIDECTIN	-0.321	-0.139
MODALINE_SULFATE	-0.454	-0.139
N-METHYL_(-)EPHEDRINE_[1R_2S]	0.047	-0.139
ADENOSINE	-0.048	-0.141
SULFAMETHOXYPYRIDAZINE	-0.355	-0.141
XYLOSE	0.087	-0.142
CYCLOSERINE_(D)	-0.318	-0.142
PHENINDIONE	-0.157	-0.142
PROCODAZOLE	0.487	-0.143
MAPROTILINE_HYDROCHLORIDE	-0.157	-0.144
BENZALKONIUM_CHLORIDE	-0.854	-0.145
XYLAZINE	-0.199	-0.145
DEXPANTHENOL	-0.432	-0.147
UREA	0.081	-0.15
ETHOXZOLAMIDE	-0.481	-0.15
CINCHOPHEN	-1.059	-0.15
RACECADOTRIL	0.293	-0.15
NICERGOLINE	-0.974	-0.151
MOROXYDINE_HYDROCHLORIDE	0.013	-0.152
TENOFOVIR	-0.47	-0.153
CHLORPYRIFOS	-0.235	-0.155
FLUCONAZOLE	-0.542	-0.155
LACTOSE_MONOHYDRATE	0.26	-0.156
KETOPROFEN	-0.18	-0.156
SULFANILAMIDE	0.165	-0.157
FLUNISOLIDE	-0.163	-0.158
LOXOPROFEN	0.03	-0.158
MINOXIDIL	-0.4	-0.158
CHLORZOXAZONE	0.332	-0.158
ENOXOLONE	-0.694	-0.158
AMINOCAPROIC_ACID	-0.045	-0.158
PASINIAZID	-0.016	-0.16
DESOXYCORTICOSTERONE_ACETATE	-0.176	-0.16
IMIQUIMOD	0.055	-0.161
AMOXICILLIN	-0.175	-0.161
THIOTHIXENE	0.227	-0.162
NORETHYNODREL	-0.001	-0.162
TRIFLUOPERAZINE_HYDROCHLORIDE	-0.154	-0.163
NEFAZODONE_HYDROCHLORIDE	0.003	-0.165
CHLORPROPAMIDE	-0.188	-0.166
PHTHALYLSULFATHIAZOLE	-0.181	-0.166
DROPERIDOL	-0.438	-0.166
LIOTHYRONINE_(L-_isomer)_SODIUM	-0.518	-0.168
ESTRADIOL_BENZOATE	-0.576	-0.168
METHYLPREDNISOLONE_SODIUM_SUCCINATE	-0.133	-0.169
GLIPIZIDE	-0.049	-0.17
PODOFILOX	-0.107	-0.17

AMITRIPTYLINE_HYDROCHLORIDE	0.01	-0.17
OXOLINIC_ACID	0.182	-0.17
PANTOPRAZOLE	-0.08	-0.171
PENTOXIFYLLINE	-0.138	-0.172
SUCCINYLSULFATHIAZOLE	-0.006	-0.173
SULFACARBAMIDE	-0.1	-0.173
FOSFOMYCIN_CALCIUM	-0.36	-0.173
TRIMETHOBENZAMIDE_HYDROCHLORIDE	-0.701	-0.175
GUANFACINE_HYDROCHLORIDE	-0.143	-0.176
PHENSUCCIMIDE	-0.312	-0.177
NORFLOXACIN	0.094	-0.179
AMINOPTERIN	-0.599	-0.18
OXYBUTYNIN_CHLORIDE	-0.338	-0.18
TRICLABENDAZOLE	-0.156	-0.181
SULFAMETER	-0.498	-0.182
ALOIN	0.055	-0.183
AFALANINE	0.174	-0.184
BENZYL_ISOTHIOCYANATE	0.249	-0.185
INAMRINONE	-0.01	-0.186
NAFTIFINE_HYDROCHLORIDE	-0.12	-0.186
PHYSOSTIGMINE_SALICYLATE	-0.201	-0.187
OFLOXACIN	-0.167	-0.189
FAMPROFAZONE	-0.043	-0.19
BENZOXIQUINE	-0.064	-0.191
DANTHRON	0.028	-0.191
HOMOSALATE	-0.416	-0.191
HYDROXYAMPHETAMINE_HYDROBROMIDE	-0.065	-0.192
)IATRIZOIC_ACID	-0.338	-0.197
,'LUMETHASONE	-0.248	-0.197
MEFEXAMIDE_HYDROCHLORIDE	-0.497	-0.198
ERGONOVINE_MALEATE	-0.117	-0.2
NAFTOPIDIL	-1.025	-0.201
METAXALONE	-0.413	-0.201
ACEDOBEN	0.094	-0.201
GLUCONOLACTONE	-0.149	-0.201
ADRENOLONE_HYDROCHLORIDE	-0.021	-0.202
MIDODRINE_HYDROCHLORIDE	-0.28	-0.203
CLEMIZOLE_HYDROCHLORIDE	-0.149	-0.205
GENTAMICIN_SULFATE	-0.37	-0.206
AMINOSALICYLATE_SODIUM	0.148	-0.206
TOLAZAMIDE	-0.26	-0.207
PIPERONYL_BUTOXIDE	0.091	-0.208
LEVOCETIRIZINE_DIHYDROCHLORIDE	-0.065	-0.208
PREGABALIN	-0.033	-0.209
QUINIDINE_GLUCONATE	-0.731	-0.209
OXYPHENBUTAZONE	-0.036	-0.209
LETROZOLE	-0.084	-0.211
CHLORINDIONE	-0.001	-0.211
OXYPHENCYCLIMINE_HYDROCHLORIDE	-0.5	-0.211
PROCAINE_HYDROCHLORIDE	-0.475	-0.212
FLUOCINONIDE	-0.27	-0.213
FENBENDAZOLE	-0.21	-0.213
ACETYL-L-LEUCINE	-0.886	-0.215
CROMOLYN_SODIUM	-0.58	-0.215
GALANTAMINE	-0.206	-0.216
BERBERINE_CHLORIDE	0.118	-0.218
METYRAPONE	0.145	-0.218
CLARITHROMYCIN	-0.225	-0.218
ACEDAPSONE	-0.112	-0.22
DIAVERIDINE	-0.207	-0.221
CARBENOXOLONE_SODIUM	-0.845	-0.224
BICALUTAMIDE	-0.207	-0.226
SULFADIMETHOXINE	-0.667	-0.228
MELPERONE_HYDROCHLORIDE	0.214	-0.228

PENICILLIN_V_POTASSIUM	-0.061	-0.229
ARECOLINE_HYDROBROMIDE	-0.05	-0.229
TEPOXALIN	-0.442	-0.23
CHINIOFON	0.108	-0.231
MEPHENTERMINE_SULFATE	-0.628	-0.232
FULVESTRANT	-0.121	-0.232
GANCICLOVIR	-0.09	-0.232
CEFOTETAN	-0.107	-0.234
DABIGATRAN_ETEXILATE_MESYLATE	0.114	-0.236
SULFAGUANIDINE	0.059	-0.237
FIPEXIDE_HYDROCHLORIDE	-0.921	-0.238
EPRINOMECTIN	-0.307	-0.239
SALICYLANILIDE	-0.201	-0.239
FLUOROURACIL	-0.079	-0.24
FENSPIRIDE_HYDROCHLORIDE	-0.371	-0.24
ITRACONAZOLE	0.077	-0.244
MEPARTRICIN	-0.098	-0.244
2-THIOURACIL	0.14	-0.245
ACRISORCIN	-0.225	-0.246
MECLOFENOXATE_HYDROCHLORIDE	-0.097	-0.25
MEFENAMIC_ACID	-0.196	-0.251
NIFLUMIC_ACID	-0.12	-0.251
CEFOXITIN_SODIUM	-0.18	-0.251
ANTIPYRINE	-0.393	-0.251
AMANTADINE_HYDROCHLORIDE	-0.089	-0.253
PINDOLOL	-0.259	-0.253
CHLOROGUANIDE_HYDROCHLORIDE	-0.291	-0.254
BISMUTH_SUBSALICYLATE	-0.139	-0.254
AMEQUINOL	-0.812	-0.256
FLUFENAMIC_ACID	-0.219	-0.257
CEFSULODIN_SODIUM	-0.714	-0.258
ALGESTONE_ACETOPHENIDE	-0.254	-0.264
AMIODARONE_HYDROCHLORIDE	-0.398	-0.265
CEFALONIUM	-0.244	-0.266
SURAMIN_HEXASODIUM	-0.426	-0.267
ETHYL_VANILLIN	-0.078	-0.268
CLOMIPHENE_CITRATE	-0.492	-0.269
PROGLUMIDE	-0.185	-0.269
NALTREXONE_HYDROCHLORIDE	-0.351	-0.27
MEROPENEM	-0.111	-0.27
LONIDAMINE	-0.849	-0.272
CETYLPYRIDINIUM_CHLORIDE	-0.263	-0.272
PROPIOLACTONE	-0.146	-0.272
OXTRIPHYLLINE	-0.407	-0.274
DROPROPIZINE	0.169	-0.275
CARPROFEN	-0.277	-0.275
HEXAMETHONIUM_BROMIDE	0.18	-0.276
DOCETAXEL	-0.602	-0.276
CIANIDANOL	0.345	-0.277
PRASTERONE	0.111	-0.277
FLURANDRENOLIDE	-0.449	-0.28
CYCLAMIC_ACID	0.154	-0.281
NORTRIPTYLINE_HYDROCHLORIDE	-0.098	-0.281
LOMUSTINE	-0.163	-0.284
ROXATIDINE_ACETATE_HYDROCHLORIDE	-0.086	-0.284
AMPICILLIN_SODIUM	-0.302	-0.286
AMIKACIN_SULFATE	-0.136	-0.287
NAPROXEN(+)	-0.268	-0.288
AMSACRINE	0.071	-0.29
NADOLOL	-0.318	-0.293
RIFAXIMIN	-0.187	-0.293
LASALOCID_SODIUM	-0.256	-0.293
SPARTEINE_SULFATE	0.074	-0.296
AZTREONAM	-0.398	-0.296

ATOMOXETINE_HYDROCHLORIDE	-0.042	-0.297
PAMABROM	-1.942	-0.297
GATIFLOXACIN	-0.788	-0.299
NONOXYNOL-9	-0.252	-0.3
OXINIACIC_ACID	-0.057	-0.303
METRONIDAZOLE	-0.427	-0.303
CALCIUM_CHLORIDE	-0.36	-0.306
QUININE_ETHYL_CARBONATE	0.186	-0.306
ALVERINE_CITRATE	-0.053	-0.307
ZILEUTON	0.099	-0.31
TRIMEBUTINE_MALEATE	0.213	-0.311
CLOTRIMAZOLE	-0.408	-0.311
GUANADREL_SULFATE	-0.197	-0.314
TIMOLOL_MALEATE	0.363	-0.315
ATROPINE_OXIDE	0.324	-0.315
FLUBENDAZOLE	-0.491	-0.315
ALLYLTHIOUREA	-0.033	-0.316
TRIMETAZIDINE_DIHYDROCHLORIDE	0.114	-0.317
IPRONIAZID_SULFATE	0.323	-0.32
BALSALAZIDE_DISODIUM	-0.107	-0.32
TROXERUTIN	-0.58	-0.32
TRIAMTERENE	-0.328	-0.32
IRBESARTAN	-0.622	-0.324
MEXENEONE	0.066	-0.324
PHENYLEPHRINE_HYDROCHLORIDE	-0.313	-0.325
METHYLPHENIDATE_HYDROCHLORIDE	-0.377	-0.327
LUCYTOSINE	-0.482	-0.328
LOXYQUIN	0	-0.333
AMILORIDE_HYDROCHLORIDE	-0.089	-0.345
CEFAMANDOLE_NAFATE	-0.935	-0.346
ATORVASTATIN_CALCIUM	-0.885	-0.346
CEPHALOSPORIN_C_SODIUM	-0.037	-0.346
CAPOBENIC_ACID	-0.286	-0.347
PHENOTHRIN	0.21	-0.347
PYRIDOSTIGMINE_BROMIDE	-0.271	-0.349
OXYPHENONIUM_BROMIDE	-0.536	-0.352
BAMBUTEROL_HYDROCHLORIDE	-0.013	-0.352
PREGNENOLONE	0.111	-0.353
TRIAMCINOLONE_ACETONIDE	-0.237	-0.357
SALSALATE	-0.109	-0.357
AMPIROXICAM	-0.277	-0.357
BROMINDIONE	-0.233	-0.357
DIMETRIDAZOLE	0.031	-0.359
SPAGLUMIC_ACID	-0.03	-0.361
IPRATROPIUM_BROMIDE	-0.521	-0.362
DIMERCAPROL	-0.097	-0.363
TULOBUTEROL_HYDROCHLORIDE	0.151	-0.363
DAPTOMYCIN_(5_millimolar/DMSO)	-0.063	-0.365
ANTAZOLINE_PHOSPHATE	-0.549	-0.367
CLONIDINE_HYDROCHLORIDE	-0.341	-0.367
GUANIDINE_HYDROCHLORIDE	-0.357	-0.369
TRIOXSALEN	-0.019	-0.369
BRONOPOL	-0.715	-0.372
PHENACEMIDE	-0.179	-0.372
ARTENIMOL	0.289	-0.375
AMLEXANOX	-0.168	-0.376
PRIMIDONE	-0.603	-0.376
TARTARIC_ACID_(L)	-0.266	-0.379
BUTYLATED_HYDROXYTOLUENE	-0.212	-0.38
BETAZOLE_HYDROCHLORIDE	-0.349	-0.38
DIMPYLATE	-0.327	-0.38
CHLOROPYRAMINE_HYDROCHLORIDE	-0.309	-0.382
HYMECHROME	-0.555	-0.385
THIOPHANATE	0.131	-0.386

AVOBENZONE	-0.484	-0.388
ACECLIDINE	-0.219	-0.389
RISPERIDONE	-1.053	-0.39
MELPHALAN	-0.047	-0.392
ACEXAMIC_ACID	-0.382	-0.392
EFAROXAN_HYDROCHLORIDE	-0.014	-0.393
CITIOLONE	0.28	-0.394
ECAMSULE_TRIETHANOLAMINE	-0.314	-0.394
CORTISONE	-0.315	-0.403
LEFLUNOMIDE	-0.354	-0.404
MIANSERIN_HYDROCHLORIDE	-0.103	-0.404
PROPOXUR	0.088	-0.404
LABETALOL_HYDROCHLORIDE	-0.899	-0.405
FLUMETHAZONE_PIVALATE	-0.199	-0.405
TRICHLORMETHIAZIDE	-0.3	-0.407
TROPICAMIDE	-0.582	-0.409
DEXFOSFOSERINE	-0.068	-0.411
TESTOSTERONE_PROPIONATE	-0.253	-0.413
OROTIC_ACID	0.069	-0.413
TELENZEPINE_HYDROCHLORIDE	-0.13	-0.413
OCTISALATE	-0.166	-0.414
GABAPENTIN	-0.226	-0.416
HYDROCORTISONE	-0.131	-0.417
LOSARTAN	-0.881	-0.419
VERAPAMIL_HYDROCHLORIDE	-0.06	-0.42
PENICILLIN_G_POTASSIUM	0.045	-0.42
BROXYQUINOLINE	0.108	-0.42
GLAFENINE	-0.243	-0.421
RIBOSTAMYCIN_SULFATE	0.022	-0.428
PHYTONADIONE	0.528	-0.429
ISOBUTAMBEN	-0.101	-0.43
SULFAMONOMETHOXINE	0.057	-0.431
SULPIRIDE	-0.305	-0.432
PRIDINOL_METHANESULFONATE	0.09	-0.432
FLUOROMETHOLONE	0.027	-0.433
ERDOSTEINE	-0.406	-0.434
BROMOPRIDE	0.236	-0.435
CEFMENOXIME_HYDROCHLORIDE	-0.232	-0.442
OXANTEL_PAMOATE	-0.986	-0.442
LINDANE	0.163	-0.442
BUFEXAMAC	-0.315	-0.449
SULOCTIDIL	-0.357	-0.451
PHENOXYBENZAMINE_HYDROCHLORIDE	-0.133	-0.452
IRINOTECAN_HYDROCHLORIDE	-0.159	-0.453
BECLAMIDE	-0.58	-0.46
THEOBROMINE	-0.646	-0.463
OXACILLIN_SODIUM	0.161	-0.464
ISAXONINE	-0.594	-0.468
APOMORPHINE_HYDROCHLORIDE	-0.468	-0.469
FAMPRIDINE	-0.723	-0.471
ISOSORBIDE_DINITRATE	0.265	-0.474
NAPHAZOLINE_HYDROCHLORIDE	-0.874	-0.475
RAMELTEON	-0.509	-0.475
URACIL	-0.58	-0.479
ABACAVIR_SULFATE	-0.104	-0.48
CLIMBAZOLE	-0.158	-0.481
MEDRYSONE	-0.555	-0.481
INOSINE	0.228	-0.483
TESTOSTERONE	-0.313	-0.486
AMYLENE_HYDRATE	-0.046	-0.492
BENZOYLPAS	-0.145	-0.492
FENCLONINE	0.232	-0.499
NITROXOLINE	-0.336	-0.5
NOVOBIOCIN_SODIUM	-0.164	-0.501

ALEXIDINE_HYDROCHLORIDE	-0.266	-0.503
TRIHEXYPHENIDYL_HYDROCHLORIDE	-0.166	-0.505
OXEDRINE	0.171	-0.507
GLYBURIDE	-0.791	-0.509
DIFLOXACIN_HYDROCHLORIDE	-1.188	-0.51
GLIMEPIRIDE	-0.36	-0.511
BARBITAL	0.055	-0.511
DYCLONINE_HYDROCHLORIDE	-1.364	-0.516
D-(+)-MALTOSE	-0.215	-0.52
ANTHRALIN	-0.89	-0.521
ACEMETACIN	-0.466	-0.522
DIMETHYL_FUMARATE	-0.755	-0.523
CANDESARTAN_CILEXTIL	-2.569	-0.527
PRASUGREL	-0.136	-0.527
DESLORATADINE_HYDROCHLORIDE	0.081	-0.53
NIFURSOL	-0.456	-0.531
TEGASEROD_MALEATE	-0.098	-0.532
METHIMAZOLE	-0.742	-0.533
ROSIGLITAZONE_MALEATE	-0.578	-0.534
ETHACRIDINE_LACTATE	-0.524	-0.538
MECYSTEINE_HYDROCHLORIDE	0.022	-0.538
CHLOROXYLENOL	0.041	-0.538
FLUDROCORTISONE_ACETATE	-0.115	-0.54
ISRADIPINE	-0.835	-0.543
MITOTANE	-0.652	-0.544
alpha-TOCHOPHERYL_ACETATE	-1.238	-0.547
METAPROTERENOL	-0.78	-0.547
MEGESTROL_ACETATE	-0.268	-0.548
D-PANTOTHENIC_ACID(d)_Na_salt	-0.93	-0.55
DICHLOROPHEN	-0.063	-0.551
DACTINOMYCIN	-0.121	-0.553
CLOFIBRIC_ACID	-0.803	-0.555
RITONAVIR	-0.254	-0.555
TRIAMCINOLONE	-0.368	-0.56
VALSARTAN	-0.435	-0.564
PRULIFLOXACIN	-0.346	-0.565
MUPIROCIN	0.021	-0.571
CLIDINIUM_BROMIDE	-0.439	-0.575
NADIFLOXACIN	-0.079	-0.576
OXOLAMINE_CITRATE	0.129	-0.576
NYLIDRIN_HYDROCHLORIDE	-0.175	-0.583
ACETAZOLAMIDE	0.115	-0.586
alpha-TOCHOPHEROL	-0.87	-0.589
ELETRIPTAN_HYDROBROMIDE	0.06	-0.592
ACETAMINOSALOL	-0.217	-0.595
BENFOTIAMINE	-0.659	-0.597
ERYTHROMYCIN	-0.771	-0.6
BROXALDINE	-0.393	-0.605
DEQUALINIUM_CHLORIDE	-0.909	-0.606
ANCITABINE_HYDROCHLORIDE	-0.029	-0.612
FASUDIL_HYDROCHLORIDE	-0.685	-0.612
ACETYLCYSTEINE	-1.076	-0.615
IDEBENONE	-0.611	-0.617
MILTEFOSINE	-0.054	-0.621
TOLMETIN_SODIUM	0.129	-0.621
TRYPTOPHAN	-0.457	-0.624
LORGLUMIDE_SODIUM	-0.008	-0.626
ACETOHYDROXAMIC_ACID	-0.382	-0.627
ACETYLCHOLINE_CHLORIDE	-0.537	-0.627
BUFLOMEDIL_HYDROCHLORIDE	0.253	-0.628
MECLOFENAMATE_SODIUM	-1.006	-0.633
FLURBIPROFEN	-0.981	-0.633
PEMPIDINE_TARTRATE	-0.121	-0.635
CHLORALOSE	0.111	-0.637

CLINDAMYCIN_HYDROCHLORIDE	-0.316	-0.641
ARIPIPRAZOLE	-0.101	-0.645
DIXANTHOGEN	0.151	-0.645
DEFERIPRONE	-0.618	-0.647
PYRONARIDINE_TETRAPHOSPHATE	-0.254	-0.651
PYRITINOL	0.134	-0.651
METHYLPREDNISOLONE	-0.771	-0.654
PALMIDROL	-0.284	-0.654
TEICOPLANIN_[A(2-1)_shown]	-0.742	-0.655
PIMETHIXENE_MALEATE	0.071	-0.655
LIOTHYRONINE	-0.791	-0.659
ORBIFLOXACIN	-0.542	-0.662
CARBIDOPA	-0.022	-0.666
BISOCTRIZOLE	-0.605	-0.668
TOLNAFTATE	-0.597	-0.676
THYMOPENTIN	-0.772	-0.676
ZOLMITRIPTAN	-0.264	-0.677
HEPTAMINOL_HYDROCHLORIDE	0.232	-0.686
MAFENIDE_HYDROCHLORIDE	-0.971	-0.691
METITEPINE_MALEATE	-0.062	-0.7
LEVOMENTHOL	0.014	-0.701
COUMARIN	-0.19	-0.704
THIOCTIC_ACID	-0.619	-0.709
ACETAMINOPHEN	-0.095	-0.715
MEGLUMINE	-0.455	-0.723
CETRIMONIUM_BROMIDE	-1.481	-0.725
OCTODRINE	-0.658	-0.726
)EXTROMETHORPHAN_HYDROBROMIDE	-0.296	-0.73
ıIYDROXYTOLUIC_ACID	-0.022	-0.734
FENIPENTOL	-0.367	-0.739
SULFAPHENAZOLE	-0.178	-0.746
EQUILIN	-0.225	-0.748
ISOFLUPREDONE_ACETATE	-0.678	-0.751
PICONOL	0.07	-0.753
BETAMETHASONE_VALERATE	-1.161	-0.76
OLTIPRAZ	-0.249	-0.761
GLUTATHIONE	-0.205	-0.763
METERGOLINE	-3.273	-0.768
CHROMOCARB	-0.447	-0.777
BENZONATATE	-0.426	-0.781
CHOLINE_CHLORIDE	-0.518	-0.782
SANGUINARIUM_CHLORIDE	-0.995	-0.783
KHELLIN	-0.364	-0.783
HOMIDIUM_BROMIDE	-0.794	-0.79
PRANOPROFEN	-0.395	-0.791
RUFLOXACIN_HYDROCHLORIDE	-0.057	-0.793
CLORGILINE_HYDROCHLORIDE	-0.2	-0.795
BUCLADESINE	-0.201	-0.8
CREATININE	-0.302	-0.803
THIODIGLYCOL	-0.41	-0.805
HYDRASTININE_HYDROCHLORIDE	-0.116	-0.806
EBSELEN	0.101	-0.81
MITOMYCIN	-0.488	-0.814
THEOPHYLLINE	-0.743	-0.815
PAZUFLOXACIN_MESYLATE	0.126	-0.82
CRESOPIRINE	-0.718	-0.823
GRISEOFULVIN	-0.198	-0.83
METHOPRENE_(S)	-0.005	-0.833
EPROBEMIDE	-0.175	-0.839
PITAVASTATIN_CALCIUM	-0.745	-0.843
DIMINAZENE_ACETURATE	-0.197	-0.85
CHLORQUINALDOL	0.115	-0.853
VINCAMINE	0.096	-0.853
BETAMIPRON	-0.423	-0.859

SULBENTINE	0.177	-0.861
RIBOFLAVIN	-1.508	-0.862
FLUOCINOLONE_ACETONIDE	0.298	-0.863
PAROXYPROPIONE	-0.33	-0.869
TENYLIDONE	-0.085	-0.875
IDAZOXAN_HYDROCHLORIDE	-0.579	-0.885
METHOCARBAMOL	-0.894	-0.887
ETOPOSIDE	-1.007	-0.89
OLANZAPINE	-0.885	-0.896
meta-CRESYL_ACETATE	-0.04	-0.901
SUXIBUZONE	-0.236	-0.901
ORNITHINE_HYDROCHLORIDE	-0.963	-0.903
CHLORPROMAZINE	-0.787	-0.908
RIBOFLAVIN_5-PHOSPHATE_SODIUM	-0.446	-0.91
AMBROXOL_HYDROCHLORIDE	-1.192	-0.91
GALLIC_ACID	0.062	-0.928
ACETARSOL	0.003	-0.931
GLYCOPYRROLATE	-0.122	-0.934
TIOXOLONE	-0.082	-0.935
MECLIZINE_HYDROCHLORIDE	-0.47	-0.941
DICHLORISONE_ACETATE	-0.476	-0.946
IDRAMANTONE	-0.287	-0.948
ACENEURAMIC_ACID	-0.082	-0.955
FENACLON	-0.097	-0.959
METHOXAMINE_HYDROCHLORIDE	-0.752	-0.96
AMANTADINE_HYDROCHLORIDE	-0.131	-0.964
CLENBUTEROL_HYDROCHLORIDE	-0.444	-0.968
AMINOTHIAZOLE	-0.19	-0.97
CHLORPHENIRAMINE_MALEATE	-0.754	-0.977
TOLFENAMIC_ACID	-0.833	-0.99
ASPIRIN	-0.185	-0.99
beta-NAPHTHOL	-1.433	-0.999
ANTIMONY_POTASSIUM_TARTRATE_TRIHYDRATE	-1.287	-1.002
CYTISINE	-0.233	-1.017
IRSOGLADINE_MALEATE	-0.007	-1.019
MOXISYLYTE_HYDROCHLORIDE	-0.027	-1.022
HYDROQUINONE	-0.437	-1.023
OMEGA-3-ACID_ESTERS_(EPA_shown)	-0.997	-1.032
PIDOTIMOD	-0.192	-1.039
ENALAPRILAT	-0.808	-1.041
LUFENURON	0.392	-1.044
RETINYL_ACETATE	-0.259	-1.055
NIMUSTINE	-0.657	-1.065
PRONETALOL_HYDROCHLORIDE	-0.424	-1.073
SILIBININ	-0.871	-1.101
DESVENLAFAXINE_SUCCINATE	-0.34	-1.102
BERGAPTEN	-0.844	-1.113
COUMOPHOS	-0.3	-1.123
ARMODAFINIL	-1.115	-1.127
MOGUISTEINE	-0.052	-1.137
CAPTAMINE	-0.319	-1.14
METHOTREXATE(+/-)	-0.832	-1.141
LOMERIZINE_HYDROCHLORIDE	0.099	-1.142
SELENOMETHIONINE	0.289	-1.162
TROPISETRON_HYDROCHLORIDE	-0.174	-1.17
PROTIONAMIDE	-0.224	-1.193
HYDROQUINIDINE	-0.738	-1.238
LACITOL	-0.039	-1.251
SODIUM_TETRADECYL_SULFATE	-2.094	-1.26
TOPOTECAN_HYDROCHLORIDE	-1.27	-1.322
CYPERMETHRIN	-0.495	-1.336
D-PHENYLALANINE	-0.335	-1.379
NEFOPAM	-0.797	-1.395
ITOPRIDE__HYDROCHLORIDE	-0.096	-1.432

HYCANTHONE	-2.05	-1.511
SECURININE	-0.464	-1.519
ARTEMISININ	0.175	-1.574
OCTOCRYLENE	-0.269	-1.598
CEFMETAZOLE_SODIUM	-1.047	-1.604
ESTRADIOL_VALERATE	-1.305	-1.647
MESTRANOL	-0.595	-1.823
TIRATRICOL	-0.011	-1.833
CLOFOCTOL	-1.509	-1.846
CHLOROCRESOL	-0.829	-1.982
CARMOFUR	-0.665	-2.037
RAMIFENAZONE	-0.873	-2.051
DIPYROCETYL	-0.526	-2.053
DICLAZURIL	-1.131	-2.082
ENALAPRIL_MALEATE	-0.458	-2.135
GABOXADOL_HYDROCHLORIDE	-0.046	-2.196
HYDROXYPROGESTERONE	-0.992	-2.278
PROXYPHYLLINE	-0.622	-2.323
TENATOPRAZOLE	-1.038	-2.422
CEPHARANTHINE	-1.079	-2.465
CARBIMAZOLE	-0.278	-2.493
ELLAGIC_ACID	-1.381	-2.585
SERATRODAST	-1.067	-2.693
GENISTEIN	-1.301	-2.795
ELTANOLONE	-0.492	-3.151
DEXAMETHASONE_SODIUM_PHOSPHATE	-0.15	-3.249
MONOBENZONE	-0.886	-4.171
PREGNENOLONE_SUCCINATE	-0.553	-8.344
MERBROMIN	-0.856	-8.819
TILETAMINE_HYDROCHLORIDE	-0.516	-9.088
CARBARIL	0.112	-11.08
TYROSINE	0.028	-11.24
PREDNISOLONE_SODIUM_PHOSPHATE	0.146	-11.55
EPIRUBICIN_HYDROCHLORIDE	0.029	-11.86
LEVOBUNOLOL_HYDROCHLORIDE	-0.105	-11.97
DULOXETINE_HYDROCHLORIDE	-0.267	-12.04
VECURONIUM_BROMIDE	0.084	-12.63
DESOXYMETASONE	-0.474	-12.72
ACAMPROSATE_CALCIUM	-0.386	-12.72
METHYLENE_BLUE	-0.764	-15.6
ACRIFLAVINIUM_HYDROCHLORIDE	-55.25	-53.45
FLUORESCEIN	-1.918	-56.42